ALTERNATIVE ROUTES TO ATOMIC LAYER DEPOSITION:

REACTOR DESIGN AND PROCESS DEVELOPMENT

A Dissertation

Presented to the Faculty of the Graduate School

of Cornell University

In Partial Fulfillment of the Requirements for the Degree of

Doctor of Philosophy

by

Jiun-Ruey Chen

August 2017

ALTERNATIVE ROUTES TO ATOMIC LAYER DEPOSITION:

REACTOR DESIGN AND PROCESS DEVELOPMENT

Jiun-Ruey Chen, Ph. D.

Cornell University 2017

Atomic layer deposition (ALD) is a powerful technique capable of depositing a variety of thin films with conformality and atomic-level control over film thickness. As a gas-phase deposition technique that has low processing temperature and applicability on substrates with high aspect ratios, ALD has been widely applied in semiconductor industry. Recently two emerging applications of ALD to manufacturing processes have drawn considerable attention. Those ALD chemistries possessing area selectivity are viewed as an alternative approach to existing patterning techniques; spatial ALD also holds promise as high-throughput, roll-to-roll processing by virtue of spatial separation of reactants.

Novel applications of ALD, like those mentioned above, involves development of new reactor design, process conditions, and most importantly, surface chemistries. The focus of the work presented here is the development of alternative approaches to selective area ALD by exploring all three aspects. The new reactor design provides us with abilities to produce industrially-relevant process conditions, to generate complex dosing sequences beyond conventional ALD, and to probe surface chemistry of the resulting ALD film *in situ*, without any air break. All these capabilities are exploited in a single chamber system.

We begin with the design and characterization of a micro-reactor for spatially-confined ALD that is integrated to our ultra-high vacuum (UHV) surface analysis chamber. The new reactor design allows deposition of ALD films at a reactor pressure in Torr range and *in situ* UHV surface analysis, including X-ray photoelectron spectroscopy (XPS) and low-energy ion scattering spectroscopy (LEISS). The micro-reactor design, which exhibits strong similarities to spatial ALD print head design, gives rise to spatial confinement of ALD films, as predicted by the computational fluid dynamics (CFD) models.

We investigate how an additional, third species in conventional ALD process affects the precursor-substrate interaction on dielectric and metal surfaces via competitive adsorption in our unique apparatus. Effects of a thiol, a phosphine and four amines as co-adsorbates on zirconia ALD (with a focus on the first half-cycle) are examined, and possible reaction mechanisms are discussed. Among the six co-adsorbates examined, triethylamine and 1,2 – ethanedithiol hold promise for selective deposition of continuous ALD zirconia films.

BIOGRAPHICAL SKETCH

Jiun-Ruey Chen was born and raised in Taipei, Taiwan. Taipei, the capital located at the northern Taiwan island, is the place where he lived for 23 years. Following an experimental elementary school, he attended Chien-Kuo Senior High School, an all-boy school in Taipei, and joined the marching band and the wind ensemble as a clarinetist. He then attended National Taiwan University (NTU), where he completed the bachelor degree in Chemical Engineering with four presidential awards. He worked with Prof. Nae-Lih Wu in NTU developing polypyrrole/LiFePO$_4$ hybrid as composite cathode material in lithium-ion batteries. Experiences of material processing and surface characterization using scanning electron microscope laid the foundation for his continued interest in material science. After a year of military service as a second lieutenant in Kinmen, a remote island 200 miles away from Taipei, he entered the PhD program at Cornell University in August, 2011 and moved to Ithaca, NY, where he lived for six years and exploited the natural resources by visiting wineries in the Finger Lakes region in summertime and snowboarding during winters. In his PhD career in Engstrom research group, he designed a micro-reactor system that allows fundamental examinations of selective area atomic layer deposition. After graduation he went on to work at Intel, at the component research group in Hillsboro, OR.

"A shimmering ocean, a beautiful island, the essential site

of our wise ancestors' destiny."

Dedicated to my parents, my family and my homeland, Taiwan

ACKNOWLEDGMENTS

There are so many people who guided and assisted me in many different ways during my time at Cornell. Their contributions are essential elements to the work presented here, and my PhD career would have been entirely different without them.

First I would like to take the opportunity to thank my advisor, Prof. James R. Engstrom. I was a total novice in surface science and vacuum technology when I first join the group in 2011, and my first task was to design, build and characterize a reactor for our UHV chamber in Olin 312. There was an enormous gap of knowledge and experience, with a steep learning curve to be filled. From our day-to-day discussions, I learned from him how to understand and explore the scientific world from thinking and doing critically and thoroughly. Looking back my Ph.D. career, everything I have learned from Jim is well summarized in the group motto: "Work Smart. Be thorough. Work as a team. Strive for quality.", and it is these words which at first seem simple but in fact challenging when putting into daily practice that now I still find invaluable. Jim has been an excellent mentor both in academic field and in casual life, which was in part manifested by our occasional meetings at Triphammer Wine and Spirits after working hours. On a side note, I also would like to thank Ms. Cheryl Stanley from the School of Hotel Administration for introducing me to the vast, intriguing world of wine during my time at Cornell.

I also would like to acknowledge my special committee. Prof. Tobias Hanrath, and his students Dr. Kevin Whitham and Ben Richards, have provided valuable insights on how the structure and the property of nanocrystal materials are closely related with their passion where all their fresh ideas originate. Prof. Frank Wise, his students Dr. Jun Yang and the post-doc Dr. Haitao Zhang, inspired me with their rigorous approach in understanding complex physical phenomena from a fundamental point of view.

Outside the realms of research, I would like to thank my friends in Ithaca, especially Po-Cheng, I-Tzu, Joyce, Julia and Henry for all our shared time and memories in this town. I also would like to thank those who are more intimate than families: Shang-Tian, Wei-Hsin, Yun-Fan, Yun-Ting, Chou-Song, Po-Hung and most importantly, Chih-Hao, for being the essential site for our destiny.

In the end, I would like to thank my parents and brother for their unconditional support.

TABLE OF CONTENTS

LIST OF FIGURES

1. Introduction

1.1 Atomic layer deposition: an introduction

Atomic layer deposition (ALD) is a powerful technique capable of depositing a variety of thin films with conformality and atomic-level control over film thickness [1]. As a gas-phase deposition technique that has low processing temperature and applicability on substrates with high aspect ratios, ALD has been widely applied in semiconductor industry [2]. ALD is comprised of sequential pulses of gas-phase reactants that cause complementary surface reactions on the substrate surface with self-limiting chemistry, as shown in Fig. 1-1 [3]. A full ALD cycle consists two half cycles for the metal precursor and the co-reactant, with purge steps in between. In this idealized scheme, a complete monolayer of the material of interest is deposited on the surface in every ALD cycle. In reality, an averaged, sub-monolayer growth (~ 1 Å) per cycle is experimentally observed [4]. Due to the self-limiting nature of the ALD process, one can precisely determine the thin film thickness at an atomic level by controlling the number of ALD cycles. ALD has been employed to deposit ultrathin films of many types of materials, including oxides, nitrides and noble metals [3], [5]. ALD has demonstrated advantages over existing thin-film deposition techniques such as physical vapor deposition (PVD) and chemical vapor deposition (CVD), due to the uniform, smooth and conformal films it produces, as shown in Fig. 1-2.

ALD cycles: metal | purge | co-reactant | purge

Expose to thin-film precursor (A)

Self-limiting reaction of A

Purge

Expose to co-reactant (B)

Self-limiting reaction of B

Purge
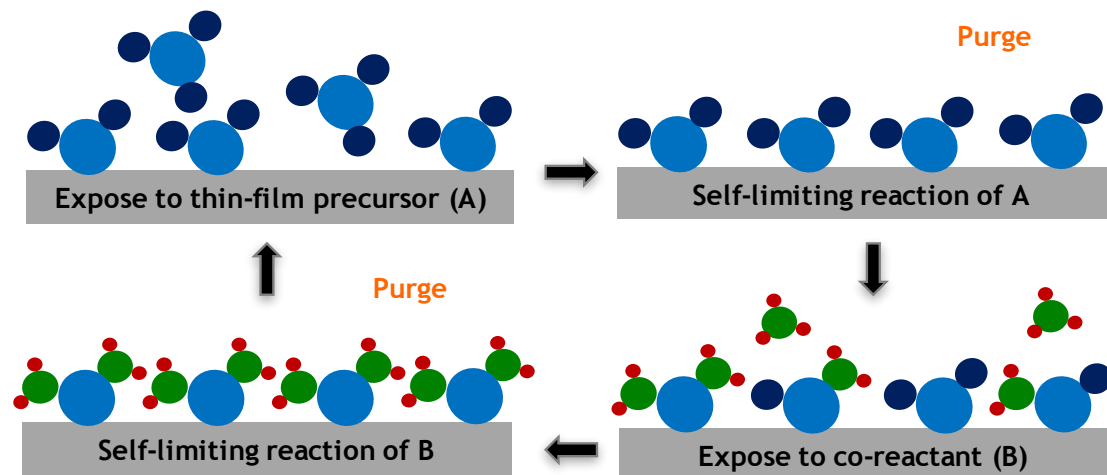
Figure 1-1: Schematic representation of an ALD process.
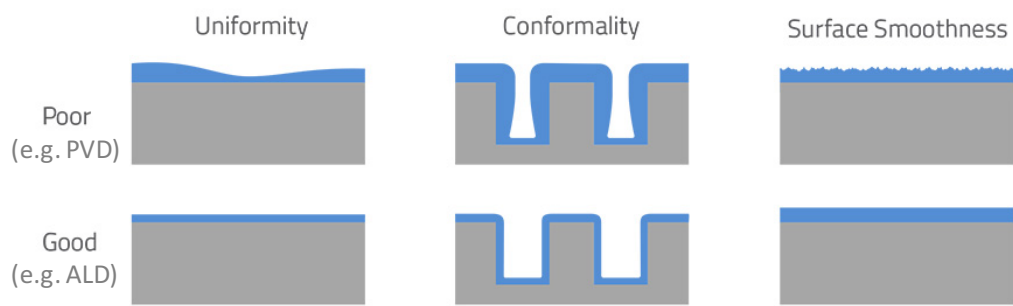
Figure 1-2: Schematic representation of characteristics of ALD films and films grown by other existing thin-film deposition techniques (source: Lam Research).

1.2 Atomic layer deposition: applications in microelectronics

These desirable characteristics of ALD has led to several applications in semiconductor industry. ALD was first introduced in transistor manufacturing processes in 45 nm node as a deposition tool for high-k gate dielectrics by Intel in 2007 [5]–[7]. ALD films were also utilized as diffusion barriers for interconnects, which require good conformality and precise thickness control to ensure effective separation of layers and to minimize undesirable effect of barrier layers on device performance [8], [9]. Several more applications of ALD in microelectronic fabrications are shown in Fig. 1-3 (upper panel). ALD was also utilized in a special patterning process, called spacer-defined double patterning, in which ALD spacers were formed after anisotropic etching of the ALD film deposited directly on patterned photoresist layers [10], [11]. Moreover, as a result of the inherent self-limiting chemistries of the precursors and all-gas-phase processes, precursors molecules can diffuse into the narrow gaps in the 3D stacked NAND structure after nitride layers are etched away for depositing conformal metal ALD word lines [12]. Depositing sidewalls for TriGate structures with high aspect ratios and gate dielectrics for the gate-all-around architecture also favors the use of ALD, as shown in Fig. 1-3 (lower panel) [13].
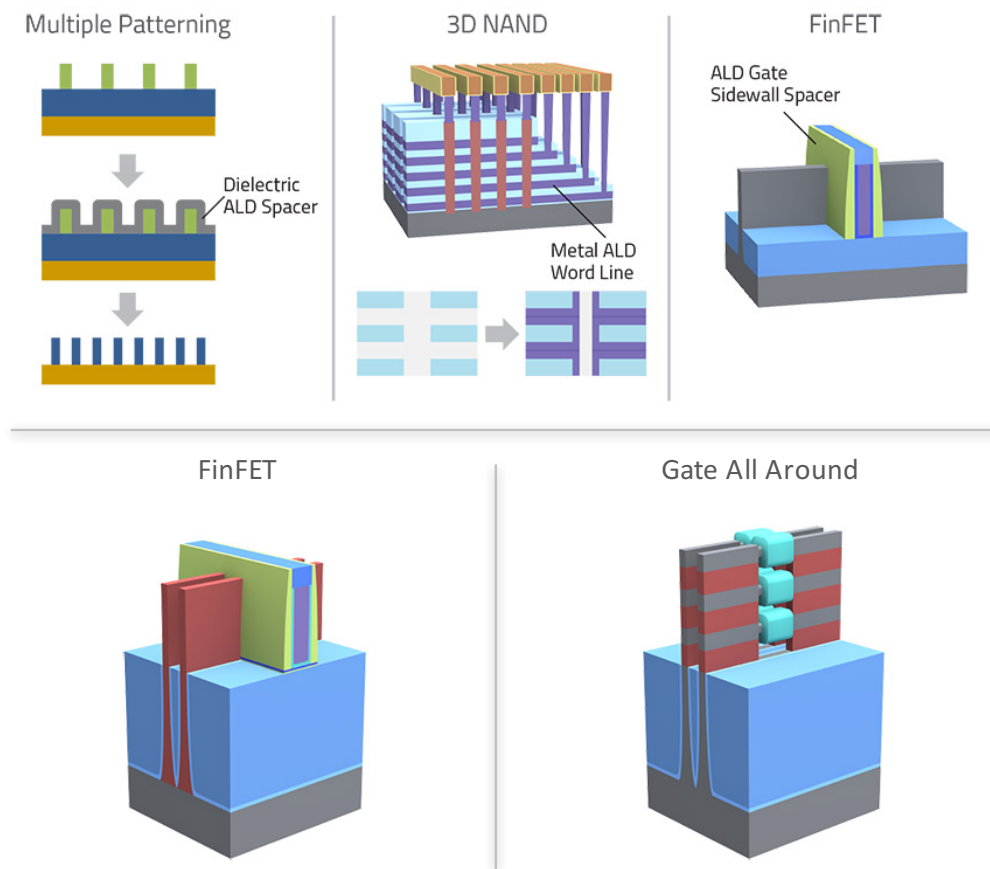
Figure 1-3: Upper panel: Schematic representation of applications of ALD in microelectronic industry. Lower panel: Schematic representation of FinFET and gate-all-around architectures. (source: Lam Research).

While ALD has many promising features, its low throughout prevents itself from extensive use at an industrial level. Many works on revising the reactor design to overcome the low deposition rates have been reported, ranging from reactors for traditional thermal and plasma-enhanced ALD to those for spatial or roll-to-roll ALD, as shown in Fig. 1-4 [14]. In spatial ALD, half cycles in a typical ALD cycle are separated in the spatial domain (instead of the time domain as in conventional ALD) [15], [16]. The spatial separation is achieved by implementing gas barriers (or "curtain gas") and exhaust lines in between the gas inlets in the print head design. An alternative design includes a rotating wafer holder and a reactor with many compartments for individual steps in an ALD cycle [17]. Spatial ALD has the advantages of depositing ALD films on confined regions [18] at atmospheric pressure [19] or with plasma treatment as a separate step [17], [20].

All of the applications in microelectronics mentioned above consist of both deposition and etching steps to pattern films in each layer. However, as the feature sizes keep shrinking according to Moore's law, the entire deposition/pattering/etching process has become immensely complicated, and accurate alignment of all these steps is essential to achieving correct structures and corresponding properties. Efforts have been made for overlay control, which reduces and eliminates overlay error such as variation of critical dimensions (CDs) and risk of shorting. Selective area ALD as an approach to self-aligned film growth, as a result, is even attractive to transistor manufacturers due to shorter patterning process flows (Fig. 1-5). Selective deposition of materials on a patterned substrate allows film growth on one surface but not on the other, without etching or patterning on the layer being deposited.
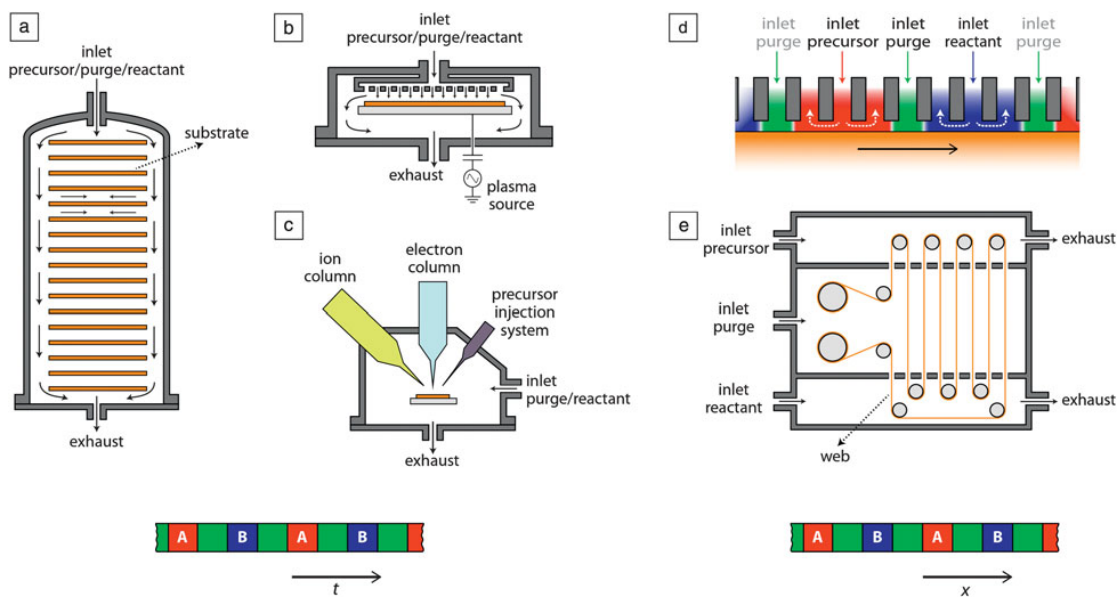
Figure 1-4: Schematic representation of various ALD Reactor designs at the industrial level [14].
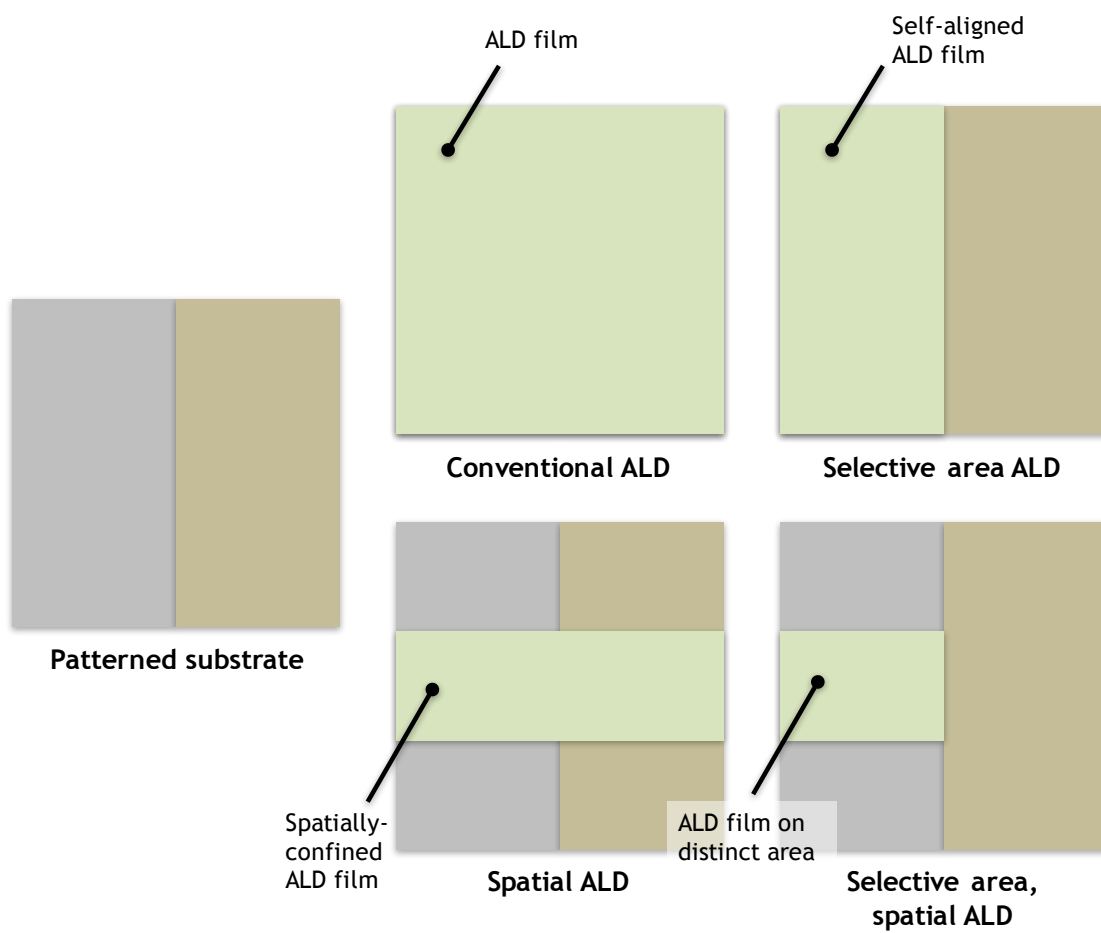
Figure 1-5: Schematic representation of two-dimensional spatial distribution of ALD film on patterned substrates resulting from various combinations of unconventional ALD processes.

Chemistries of all-vapor selective deposition using SAMs [21] or the alternative approaches we proposed and examined in Chapter 5 are expected to be compatible to the spatial ALD reactor design; therefore, deposition of ALD films at a distinct area could be possible (Fig. 1-5) when we combine the chemistry for area selectivity and the reactor design for spatial ALD. The apparatus we have developed, namely a micro-reactor for spatially-confined ALD (in Chapter 3) as well as an alternative approach to selective deposition using co-adsorbates, is one of the examples for this specific application.

1.3 Surface chemistry in atomic layer deposition

It has been pointed out that a better understanding and control over surface oxidation reactions (for oxides ALD), adsorption (physi- and chemi-sorption), nucleation, diffusion and removal (desorption and etching) is essential to robust selective area ALD processes [22]. Schematics of selected surface processes described in the classic model for nucleation is displayed in Fig. 1-6. Some of these processes, however, is unlikely to play an important role in ALD. For example, surface diffusion of chemisorbed precursor molecule may not be significant due to the bulky cluster size and the high cluster density during the precursor half cycle. On the other hand, desorption of the adsorbed species is not preferred due to their high binding energies.
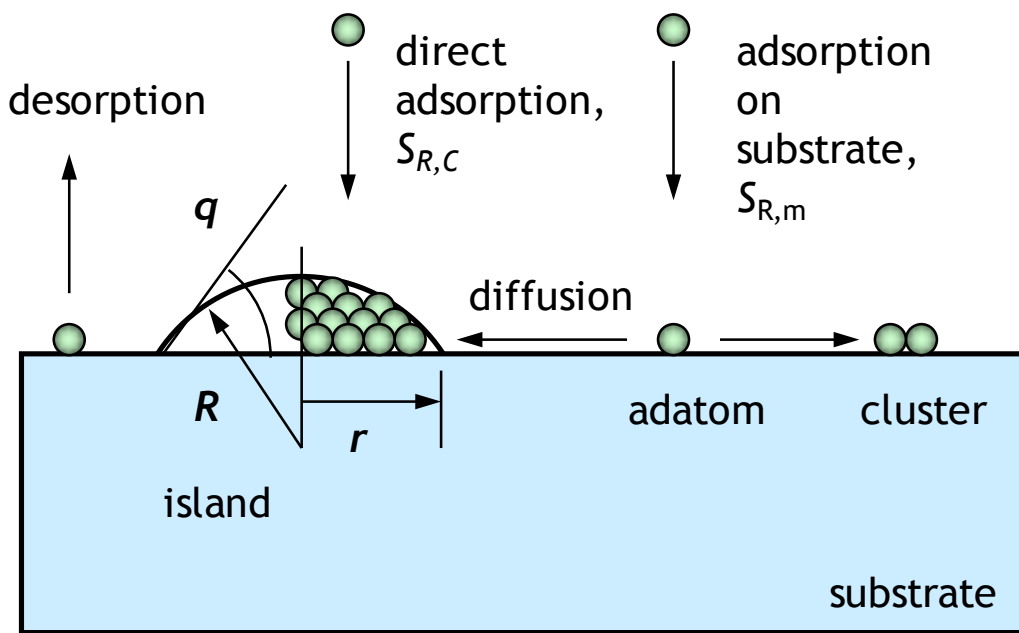
Figure 1-6: Atomistic processes considered in classic models for nucleation of a thin film on a foreign substrate.

To control nucleation in ALD it is clear that irreversible adsorption must occur on (and only on) the surface where growth is desired, and irreversible adsorption depends on the availability of active sites. A complete understanding of the nature of selective deposition requires extensive knowledge of chemical reaction kinetics and transport, surface chemistry and thin-film material science (particularly the initial stages of film growth).

1.4 Overview of dissertation

This dissertation revolves around two major topics regarding atomic layer deposition: reactor design (Chapters 3 and 4) and process development (Chapters 5 and 6). Chapter 2 describes the ultrahigh vacuum (UHV) chamber system in which almost all the experiments reported in subsequent chapters take place, as well as an outstanding surface characterization technique, X-ray photoelectron spectroscopy (XPS), that identifies surface species and provides quantitative information of the films grown using our custom-designed reactor. Chapter 3 reports the development of a micro-reactor probe for direct attachment to our UHV chamber and *in situ* surface analysis. The study is continued in Chapter 4, where we described an alternative probe head design that produces obround deposition spots potentially for terraced film growth based on a three-dimensional CFD model. Chapter 5 contains an initial work on achieving selective area ALD by virtue of competitive adsorption of a transitional metal precursor and an additional gas-phase species in the first half cycle. In Chapter 6 we extend the work and examine the effect of four co-adsorbates, including two promising molecules identified in Chapter 5, in multiple-cycle

ALD. Chapter 8 is composed of XPS studies on MOMBE (metal-organic molecular beam epitaxy) WSe$_2$ films and iodine-treated PbS nanocrystals as well as details on the addition of the micro-reactor probe system to an UHV chamber.

1.5 References

[1]   S. M. George, "Atomic layer deposition: An overview," *Chem. Rev.*, vol. 110, pp. 111–131, 2010.

[2]   R. W. Johnson, A. Hultqvist, and S. F. Bent, "A brief review of atomic layer deposition: from fundamentals to applications," *Mater. Today*, vol. 17, no. 5, pp. 236–246, Jun. 2014.

[3]   M. Leskelä and M. Ritala, "Atomic layer deposition (ALD): from precursors to thin film structures," *Thin Solid Films*, vol. 409, no. 1, pp. 138–146, Apr. 2002.

[4]   H. Van Bui, F. Grillo, and J. R. van Ommen, "Atomic and molecular layer deposition: off the beaten track," *Chem. Commun.*, vol. 53, no. 1, pp. 45–71, 2017.

[5]   M. Leskelä and M. Ritala, "Atomic Layer Deposition Chemistry: Recent Developments and Future Challenges," *Angew. Chemie Int. Ed.*, vol. 42, no. 45, pp. 5548–5554, Nov. 2003.

[6]   K. Mistry, C. Allen, C. Auth, B. Beattie, D. Bergstrom, M. Bost, M. Brazier, M. Buehler, A. Cappellani, R. Chau, C.-H. Choi, G. Ding, K. Fischer, T. Ghani, R. Grover, W. Han, D. Hanken, M. Hattendorf, J. He, J. Hicks, R. Huessner, D. Ingerly, P. Jain, R. James, L. Jong, S. Joshi, C. Kenyon, K. Kuhn, K. Lee, H. Liu, J. Maiz, B. McIntyre, P. Moon, J. Neirynck, S. Pae, C. Parker, D. Parsons, C. Prasad, L. Pipes, M. Prince, P. Ranade, T. Reynolds, J. Sandford, L. Shifren, J. Sebastian, J. Seiple, D. Simon, S. Sivakumar, P. Smith, C. Thomas, T. Troeger, P. Vandervoorn, S. Williams, and K. Zawadzki, "A 45nm Logic Technology with High-k+Metal Gate Transistors, Strained Silicon, 9 Cu Interconnect Layers, 193nm Dry Patterning, and

100% Pb-free Packaging," in *2007 IEEE International Electron Devices Meeting*, 2007, pp. 247–250.

[7]   M. Ritala and J. Niinistö, "Industrial Applications of Atomic Layer Deposition," in *ECS Transactions*, 2009, vol. 25, no. 8, pp. 641–652.

[8]   O. van der Straten, S. M. Rossnagel, J. P. Doyle, and K. P. Rodbell, "Metal-Organic Atomic Layer Deposition of Metals for Applications in Interconnect Technology," in *ECS Transactions*, 2006, vol. 1, no. 10, pp. 51–56.

[9]   J. Nag, B. Cohen, S. Choi, A. Ogino, M. Oh, Y. Yan, J. Liang, C. Christiansen, A. Kim, B. Li, P. DeHaven, A. Madan, S. Krishnan, and A. H. Simon, "ALD TaN Barrier for Enhanced Performance with Low Contact Resistance for 14nm Technology Node Cu Interconnects," *ECS Trans.*, vol. 69, no. 7, pp. 161–169, Oct. 2015.

[10]   J. Beynet, P. Wong, A. Miller, S. Locorotondo, D. Vangoidsenhoven, T.-H. Yoon, M. Demand, H.-S. Park, T. Vandeweyer, H. Sprey, Y.-M. Yoo, and M. Maenhoudt, "Low temperature plasma-enhanced ALD enables cost-effective spacer defined double patterning (SDDP)," in *Proc. SPIE*, 2009, vol. 7520, p. 75201J.

[11]   A. J. M. Mackus, A. A. Bol, and W. M. M. Kessels, "The use of atomic layer deposition in advanced nanopatterning," *Nanoscale*, vol. 6, no. 2011, pp. 10941–10960, 2014.

[12]   R. S. Makala and J. Alsmeier, U.S. Patent No. 9,397,093 B2 (2016).

[13]   K. J. Kuhn, "Considerations for Ultimate CMOS Scaling," *IEEE Trans. Electron Devices*, vol. 59, no. 7, pp. 1813–1828, Jul. 2012.

[14]   W. M. M. Kessels and M. Putkonen, "Advanced process technologies: Plasma,

direct-write, atmospheric pressure, and roll-to-roll ALD," *MRS Bull.*, vol. 36, no. 11, pp. 907–913, 2011.

[15] P. Poodt, D. C. Cameron, E. Dickey, S. M. George, V. Kuznetsov, G. N. Parsons, F. Roozeboom, G. Sundaram, and A. Vermeer, "Spatial atomic layer deposition: A route towards further industrialization of atomic layer deposition," *J. Vac. Sci. Technol. A Vacuum, Surfaces, Film.*, vol. 30, no. 1, p. 10802, 2012.

[16] K. Sharma, R. A. Hall, and S. M. George, "Spatial atomic layer deposition on flexible substrates using a modular rotating cylinder reactor," *J. Vac. Sci. Technol. A Vacuum, Surfaces, Film.*, vol. 33, no. 1, p. 01A132, Jan. 2015.

[17] P. Poodt, R. Knaapen, A. Illiberi, F. Roozeboom, and A. van Asten, "Low temperature and roll-to-roll spatial atomic layer deposition for flexible electronics," *J. Vac. Sci. Technol. A Vacuum, Surfaces, Film.*, vol. 30, no. 1, p. 01A142, 2012.

[18] P. Ryan Fitzpatrick, Z. M. Gibbs, and S. M. George, "Evaluating operating conditions for continuous atmospheric atomic layer deposition using a multiple slit gas source head," *J. Vac. Sci. Technol. A Vacuum, Surfaces, Film.*, vol. 30, no. 1, p. 01A136, 2012.

[19] R. L. Z. Hoye, D. Muñoz-Rojas, S. F. Nelson, A. Illiberi, P. Poodt, F. Roozeboom, and J. L. MacManus-Driscoll, "Research Update: Atmospheric pressure spatial atomic layer deposition of ZnO thin films: Reactors, doping, and devices," *APL Mater.*, vol. 3, no. 4, p. 40701, Apr. 2015.

[20] L. Hoffmann, D. Theirich, S. Pack, F. Kocak, D. Schlamm, T. Hasselmann, H. Fahl, A. Räupke, H. Gargouri, and T. Riedl, "Gas Diffusion Barriers Prepared by Spatial Atmospheric Pressure Plasma Enhanced ALD," *ACS Appl. Mater. Interfaces*, vol. 9,

no. 4, pp. 4171–4176, Feb. 2017.

[21]   F. S. M. Hashemi and S. F. Bent, "Sequential Regeneration of Self-Assembled Monolayers for Highly Selective Atomic Layer Deposition," *Adv. Mater. Interfaces*, p. 1600464, Sep. 2016.

[22]   S. E. Atanasov, B. Kalanyan, and G. N. Parsons, "Inherent substrate-dependent growth initiation and selective-area atomic layer deposition of TiO_2 using 'water-free' metal-halide/metal alkoxide reactants," *J. Vac. Sci. Technol. A Vacuum, Surfaces, Film.*, vol. 34, no. 1, p. 01A148, 2016.

2. Experimental techniques

2.1 Overview

This chapter provides a brief review and description on the materials and experimental techniques that are utilized in subsequent chapters. The chamber system in which almost all experiments were carried out and a prominent characterization technique, X-ray photoelectron spectroscopy (XPS), are described in more detail.

2.2 Materials

These materials were used in the course of substrate preparation, and were used as received: buffered oxide etch (6:1 aqueous solution of hydrofluoric acid buffered with ammonium fluoride, CMOS grade, Mallinckrodt Baker) and Nanostrip (mixture of hydrogen peroxide, sulfuric acid and peromonosulfuric acid, Cyantec, Fremont, CA). The following were used as transition metal precursors in thin-film deposition processes: Tetrakis(ethylmethylamido)zirconium(IV) $\{Zr[N(CH_3)(CH_2CH_3)]_4$, TEMAZ$\}$ (99.9999%, Air Liquide) and dicobalt hexacarbonyl tert-butylacetylene $\{Co_2(CO)_6[HC{\equiv}C(^tBu)]$, CCTBA$\}$. These materials were used as co-adsorbates, as-received: ethylenediamine [$H_2N(CH_2)_2NH_2$, EDA] (>99.5%, Sigma-Aldrich Corp.), diisopropylamine $\{[(CH_3)_2CH]_2NH$, DIPA$\}$ (>99.5%, Sigma-Aldrich Corp.), triethylamine [$N(CH_2CH_3)_3$, TEA] (>99.5%, Sigma-Aldrich Corp.), 1,2-ethanedithiol [$HS(CH_2)_2SH$, EDT] (>97%, Sigma-Aldrich Corp.), pyridine (C_5H_5N, >99.9%, Sigma-Aldrich Corp.) and

triethylphosphine [P(CH$_2$CH$_3$)$_3$, TEP] (99%, Strem Chemicals). Co-adsorbates were loaded into stainless steel bubblers (150 mL, Strem Chemicals or ~100 mL, of custom design) in a glove box to prevent any reaction and adsorption of moisture in the air. Chemical structures of these molecules are shown in Fig. 2-1.

2.3 Description of the vacuum system

Almost all the experiments involving thin-film deposition and *in situ* surface characterization in this dissertation were carried out in a multi-stage, ultra-high vacuum (UHV) system located at room 312, Olin Hall. A schematic of this system is shown in Fig. 2-2.

The chamber system is equipped with three deposition sources that are operated at different pressure regimes. First is the micro-reactor that allows gas-phase surface modification and vapor deposition, including chemical vapor deposition (CVD) and atomic later deposition (ALD) at $p \sim 10$ Torr. Second is a capillary array doser at $p \sim 10^{-5}$ Torr. Third is the supersonic molecular beam that causes a chamber pressure $\sim 10^{-7}$ Torr. Full details of the chamber setup and the operating procedures, focusing on the micro-reactor and X-ray photoelectron spectroscopy, are given in Chapter 3. Description of the design aspects to the micro-reactor system and its peripherals is provided in Chapter 8. Details of the operation of the supersonic molecular beam and associated nozzle position calibration are given in Chapter 4.
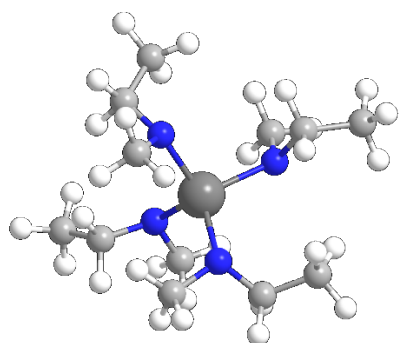
tetrakis(ethylmethylamido) zirconium(IV) (TEMAZ)
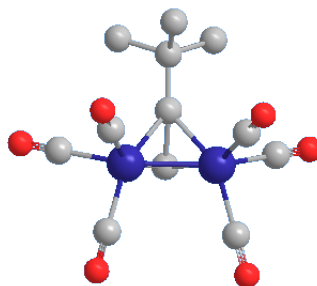
dicobalt hexacarbonyl *tert*-butylacetylene (CCTBA)
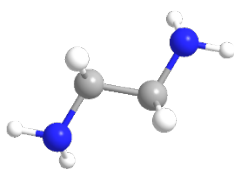
ethylenediamine (EDA)
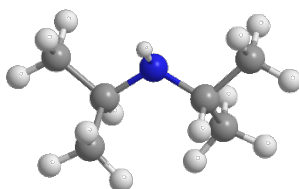
diisopropylamine (DIPA)
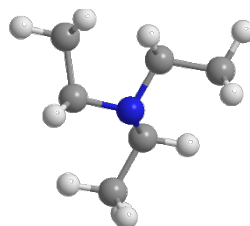
triethylamine (TEA)
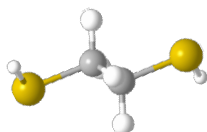
1,2-ethanedithiol (EDT)
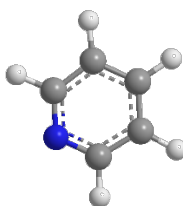
pyridine
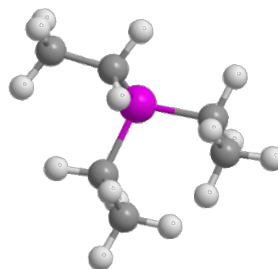
triethylphosphine (TEP)

Figure 2-1: Structures of molecules used in this dissertation.
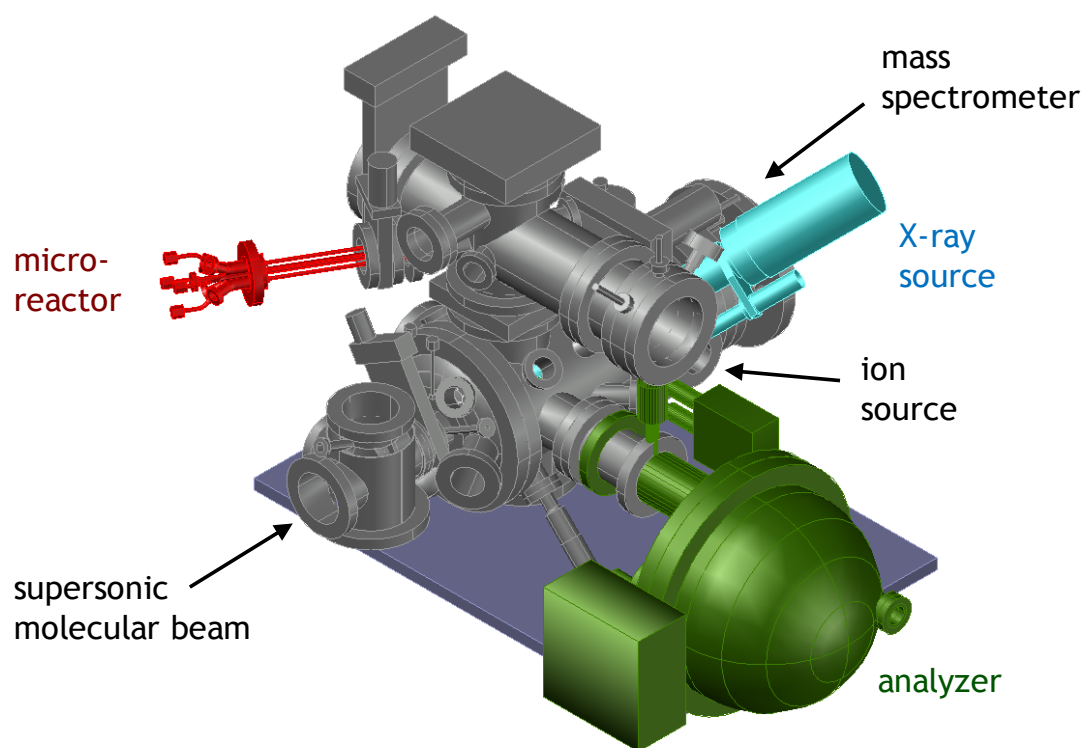
Figure 2-2: Schematic of the UHV system used for thin-film deposition and *in situ* surface characterization. Note that the gas delivery system of micro-reactor and other components for molecular beam generation, the QMS, and load-lock chamber are omitted for clarity.

A concentric hemispherical electron energy analyzer serves as an analyzer for both XPS (photoelectrons) and low-energy ion scattering spectroscopy (LEISS, scattered ions). A twin anode Mg/Al X-ray source and a differentially-pumped ion source (SPECS ion source IQE 12/38) are also located in the main chamber. The axis of the ion source is 40° off the axis the analyzer, resulting in an effective scattering angle for LEISS of 140°. For LEISS samples were oriented such that they were normal to the ion beam, and all samples were exposed to the ion beam for two minutes before the start of data collection to ensure a stable and constant ion beam current. A typical scan over the range of kinetic energies (1-1000 eV) would take approximately 10 min. In addition to generating helium ions for LEISS, the ion source can also generate argon ions for sputter etch (and sputter depth profile when combined with XPS) on the sample in a 1×1 cm^2 rastered area. A quadrupole mass spectrometer (QMS, Hiden 3F/EPIC, Hiden Analytical, Warrington, UK), also mounted in the lower chamber, allows direct analysis to the molecular beam, residual gas analysis to the UHV chamber and helium leak check on any component attached to the UHV chamber.

Substrate temperature is an important parameter in thin film deposition. Sample heating in the UHV system in 312 includes a pyrolytic boron nitride heater (Invensys Eurotherm), located at the backside of the sample. Due to experimental constraints, the exact temperature of the substrate cannot be measured during experiments. However, a thermocouple near the heater is available as a reference temperature.

Three Molybdenum platens (Thermionics Northwest) of different designs that were compatible with the sample manipulator (Thermionics SMR-3, Thermionics Northwest, Port Townsend, WA) and sample transfer system (Thermionics STLC Series II) in 312 Olin system were used to hold samples for film deposition and analysis (Fig. 2-3). One of these platens (referred to as design A) was designed for holding a full 100-mm wafer, as shown in Fig. 2-3(a). The recess region (depth ~ 0.5 mm) on the back plate was machined for holding a 100-mm wafer with the primary flat in the circumference of the wafer (indicating {110}) aligned with a flat wall. Similar recess design was also on the front plate for holding a 76-mm wafer. There are two circular opening (diameter ~ 7.0 cm) at both front and back ends for processing/surface analysis and efficient radiative heating, respectively. Six tapped holes on the back plate were used to combine the two plates and keep the wafer in place. Relevant work includes the use of the "half-moon" sample [1] and that in Chapters 5 and 6. The second platen (referred to as design B) was designed by Kevin Hughes in 2008 for holding three 17×17 mm^2 coupon samples, as shown in Fig. 2-3(b). The three samples are in a column along the axis of rotation of the manipulator, which allows for angle-resolved XPS on each sample. Sample are held within a shallow well in the back plates by a retaining plate secured by three clips. Both sides of the front plate can be used to hold coupon samples with different thicknesses; the flat side is used to hold samples ~ 0.50 mm thick and the other side with recess can hold samples ~ 0.76 mm thick. With the exception of a narrow lip to prevent the sample from falling through, the well is open, so that the back of the sample is directly exposed to the sample heater, allowing efficient radiative heat transfer from the heating element in the manipulator and the back of the sample.
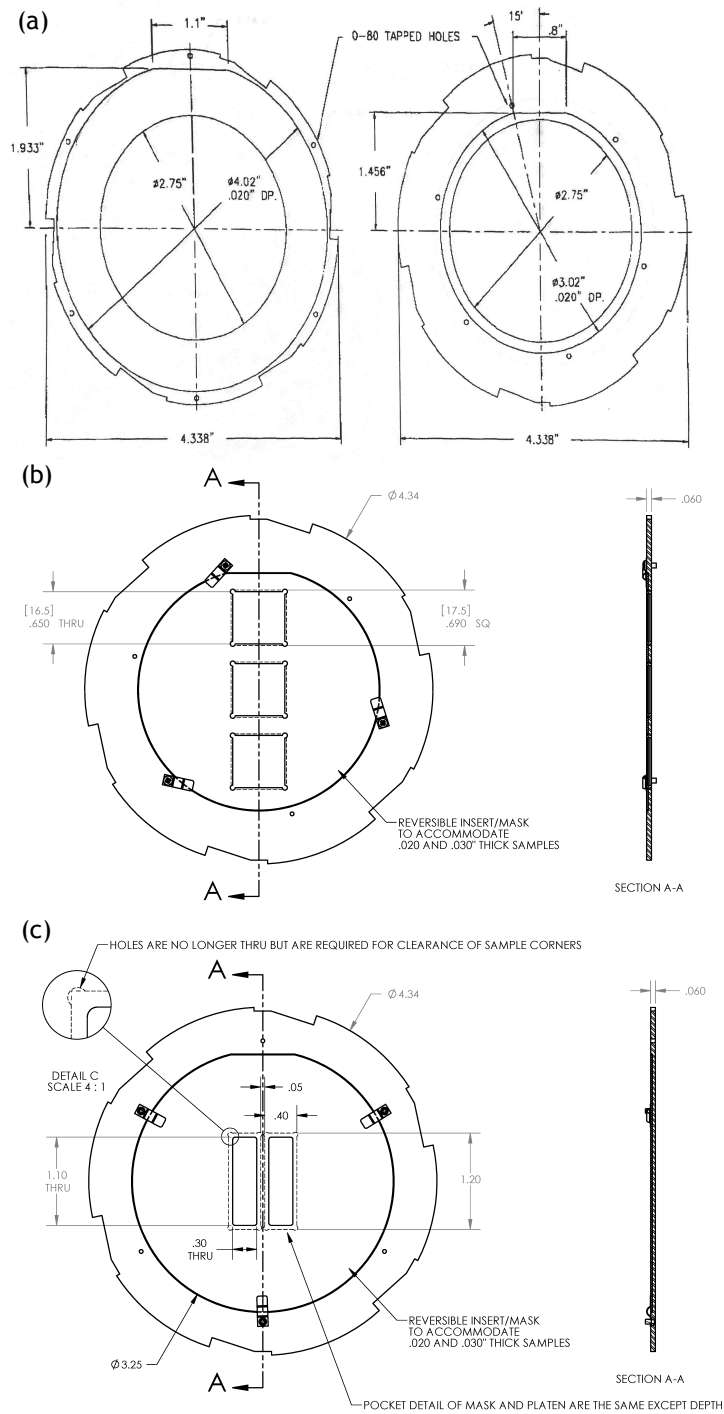
Figure 2-3: Drawing of three Mo sample platens: **(a)** design A for holding a 100-mm wafer.

(b) design B for holding up to three 17×17 mm^2 coupon samples. **(c)** design C for holding

up to two 10×25 mm^2 rectangular samples (courtesy Thermionics Northwest, Inc.).

Two tapped holes on the back plate that were close to the recess for the central sample allowed the use of two additional clips for holding samples of non-typical shape. Recent examples were the WSe_2 films from G-line chamber and the iodine-treated PbS nanocrystals described in Chapter 8. Selected work with the use of this platen includes characterizations of ALD films using the conventional ALD in an Oxford FlexAL reactor (Oxford Instruments, Oxfordshire, UK) at Cornell Nanofabrication Facility (CNF) [2]–[4], those using the supersonic molecular beam in the Olin 312 system [2] and those were analyzed as-received [5]. I designed a third generation of the sample platen (referred to as design C) for holding two 10×25 mm^2 rectangular samples in 2016, as shown in Fig. 2-3(c). This design allowed identical experimental conditions on the two samples using the micro-reactor probe when rectangular samples were oriented vertically and angle-resolved XPS on each sample when samples were oriented horizontally (rotating azimuthally the entire platen by 90°). Similar recess design as design B was adopted on both front and back plates. Recent examples were the studies described in Chapters 5 and 6.

It has been observed that the actual substrate temperature was lower than the reference temperature. Calibration of substrate temperature in each of the platens was therefore conducted for accurate control over conditions of film growth. Two different methods of obtaining actual substrate temperature were used. The sample platen was located at the intermediate chamber using both methods. The first (for design A) involved attaching a thermocouple (type K, chromel–alumel) onto the sample transfer arm so that the thermocouple and the substrate surface made physical contact, while the sample was being heated at different conditions. Thermocouple wires were connected via a 1.33" CF flange (#22), a nipple adaptor (1.33" to 2.75" CF), and a thermocouple feedthrough (MDC,

#9312013). The sample was oriented toward the load-lock chamber ($\theta = 123.5°$), and the transfer arm approached the sample through the load-lock chamber. The second (for designs B and C) involved attaching the thermocouple onto sample(s) using ceramic adhesive (Aremco products, Inc., Ultra-temp 516). This was done so as to simulate the actual deposition process at higher pressures, with the micro-reactor close to the sample surface. 2-8 ml of the ceramic adhesive was dropped onto the area where the sample and the thermocouple overlap, and immediately compacted to achieve a thin and conformal adhesion. After having dried in air overnight, the sample underwent a three-step anneal curing: 1 to 2 hours at 200 °F, 500 °F and 700 °F each followed by a cool down process (~100 °F every 30 minutes).

Temperature calibration of all three sample platens were carried out at high vacuum condition. For designs B and C the micro-reactor was retracted completely and the small gate valve was closed. Chamber was pumped down using the load-lock turbo pump, obtaining a chamber pressure of ~ 10^{-8} Torr. No gas flow was used in this case.

Temperature calibration of designs A and C were also conducted at high pressure (Torr range). For design A, the sample was loaded into the chamber and rotated toward the micro-reactor ($\theta = 183.5°$). The micro-reactor was then brought to approach the sample. After the position the sample and the micro-reactor, we started the curtain gas (100 sccm N_2) and reactant (10 sccm He, barometer reading: 23.7 Torr) flows. Chamber pressure was kept at ~ 18 Torr (throttle valve set point: 18.9 Torr). Equilibrium temperature readings were obtained at different heater powers (from 5.5 to 11.5%). For design C the calibration was performed at a reactor pressure of 10 Torr with a curtain gas flow of 75 sccm N_2.

In Fig. 2-4 we display reference and thermocouple temperatures as a function of heater power at the two pressure regimes. In the case of $p \sim 10^{-8}$ Torr [Fig. 2-4(a)] We first observed that all the temperature readings increase with the heater power. While all temperature readings increase with the heater power, different slopes were clearly seen in the sample temperature readings. We also observed that different sample holders have an effect on the heat transfer from heater to sample by comparing the curves from designs A and C. A greater slope from design B could result from the platen design and/or the method of measurement. Also, the reference temperature was higher than any of the thermocouple reading. This was attributed to longer distance to the boron nitride heater from the sample than that from the point of reference. Data points on the calibration curves were fit to third-order polynomials:

$$T_A = -275.5 + 101.1\,x - 5.475x^2 + 0.122x^3 \qquad (2-1)$$

$$T_B = 166.0 - 97.17\,x - 20.7x^2 - 0.861x^3 \qquad (2-2)$$

$$T_C = -2339 - 960.7\,x - 120.3x^2 + 5.217x^3 \qquad (2-3)$$

Where T_A, T_B and T_C are substrate temperatures (°C) at $p \sim 10^{-8}$ Torr in sample platen A, B and C, respectively and x is the heater power (%).

In the case of $p \sim 10^1$ Torr [Fig. 2-4(b)] all curves appeared to be much flatter than those at high vacuum, indicating less efficient sample heating. This was attributed to heat loss via convective transport from the curtain gas flow. Measurements with a wider range of the heater power were obtained so that the result can be used to predict the actual sample temperature in future experiments.

$$T'_A = -161.5 + 55.72\,x - 4.393x^2 + 0.211x^3 \qquad (2-4)$$

$$T'_C = -75.8 + 23.02\,x - 0.392x^2 + 0.0156x^3 \qquad (2-5)$$
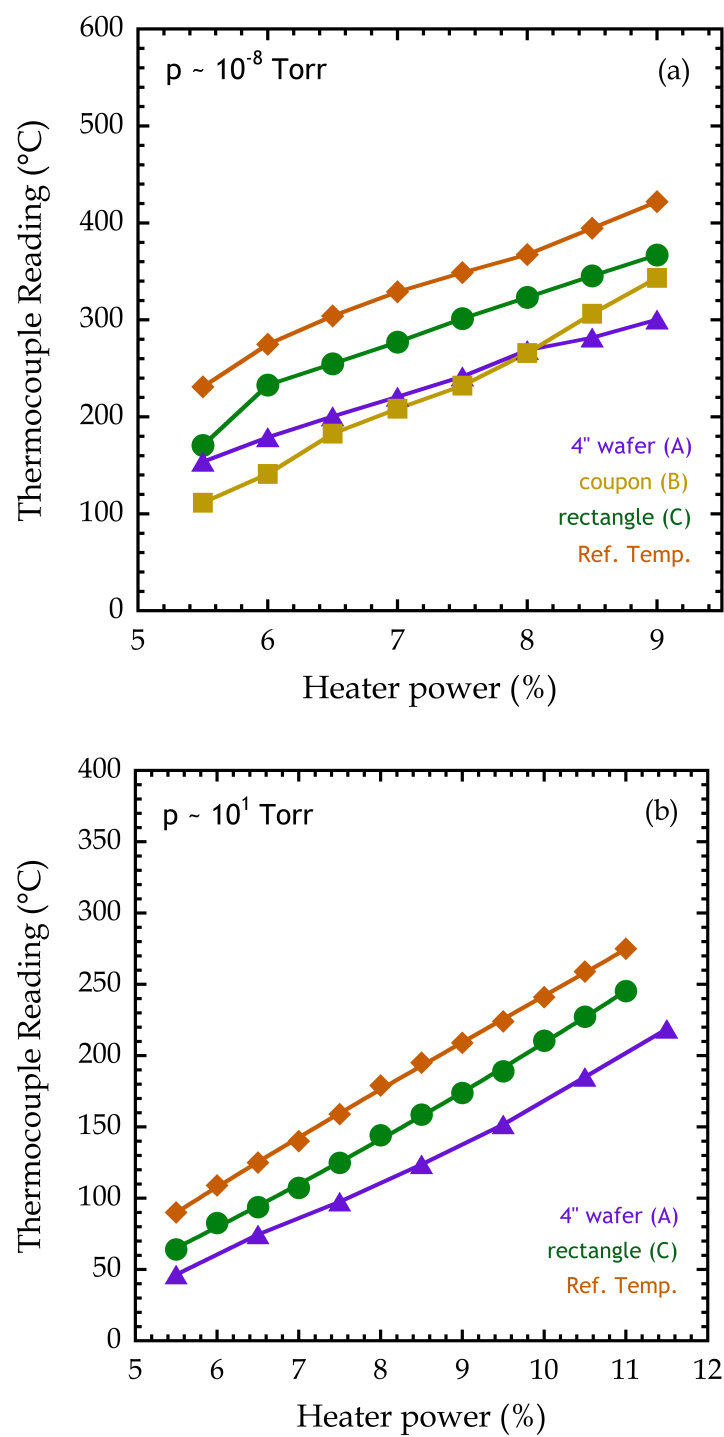
Figure 2-4: Thermocouple readings of samples in the three sample platens as a function of heater power at **(a)** $p \sim 10^{-8}$ Torr and **(b)** $p \sim 10^{1}$ Torr.

Where T'_A and T'_C are substrate temperatures (°C) at $p \sim 10^1$ Torr in sample platen A and C, respectively and x is the heater power (%).

2.4 X-ray photoelectron spectroscopy

X-ray photoelectron spectroscopy (XPS), also known as electron spectroscopy for chemical analysis (ESCA), is a surface-sensitive characterization technique that probes elemental composition and chemical states of the elements in the sample, as is suggested by its name of ESCA. In typical XPS experiments, spectra of photoelectrons of different kinetic energies were produced by irradiating s sample with soft X-rays ($\sim 1.3 - 1.5$ keV) that excites core electrons to escape from the solid.

The binding energy (BE) of a certain core level is calculated by subtracting the measured kinetic energy of the photoelectron from that level and the work function of the spectrometer from the incident photon energy, as displayed in Fig. 2-5. BE is an important figure that the interpretation of the elements in the sample relies heavily on. As a spatially averaging technique, XPS has a lateral resolution of $\sim$ μm (associated with the transfer lens fitted to the analyzer) and a depth of analysis $\sim$ nm [related to inelastic mean free path (IMFP, λ [6]–[11]) of the photoelectrons, $\sim 95\%$ of the signal in XP spectra comes from sample surface within a depth of 3λ] [12].

A typical XPS system comprises several key components, namely an X-ray source, an electron energy analyzer and detection system, and an ultrahigh vacuum chamber that contains all the rest of the components and the sample. A single X-ray source with a Mg/Al twin anode is the most common choice (same for 312 system). Such twin anode assemblies

are useful as they provide the ability to differentiate photoelectrons from Auger electrons (originated from Auger process involving energy transmission among three electrons) and to infer the structure of the film of interest [13]–[17].

Adding an X-ray monochromator to the source enhances the performance of XPS by lowering the background from Brensstralung radiation, reducing peak widths and removing satellite peaks of photoelectrons (Auger electrons do not show such features as their kinetic energy is unrelated to incident photons) originated from emission lines of less probable transition. Note that the twin source in 312 system is non-monochromatic. On the other hand, a common choice for the electron energy analyzer is a concentric hemispherical analyzer (CHA) as it provides good energy resolution that XPS requires with the addition of transfer lens and multi-channel detection [18]. A potential difference (ΔV) is applied across the two hemispheres (with radii of R_1 and R_2) in order to accurately select electrons reaching the detector with a specific kinetic energy (pass energy, E) in the following form:

$$E = e\Delta V \left(\frac{R_1 R_2}{R_2^2 - R_1^2} \right) \qquad\qquad (2-6)$$

The analyzer can be operated in one of the two following modes: constant analyzer energy (CAE) and constant retard ratio (CRR) modes. By imposing constant potential difference to the hemisphere, pass energy is fixed across the entire energy range of the spectrum in CAE mode and so is the absolute energy resolution (ΔE) [Fig. 2-6] [19].
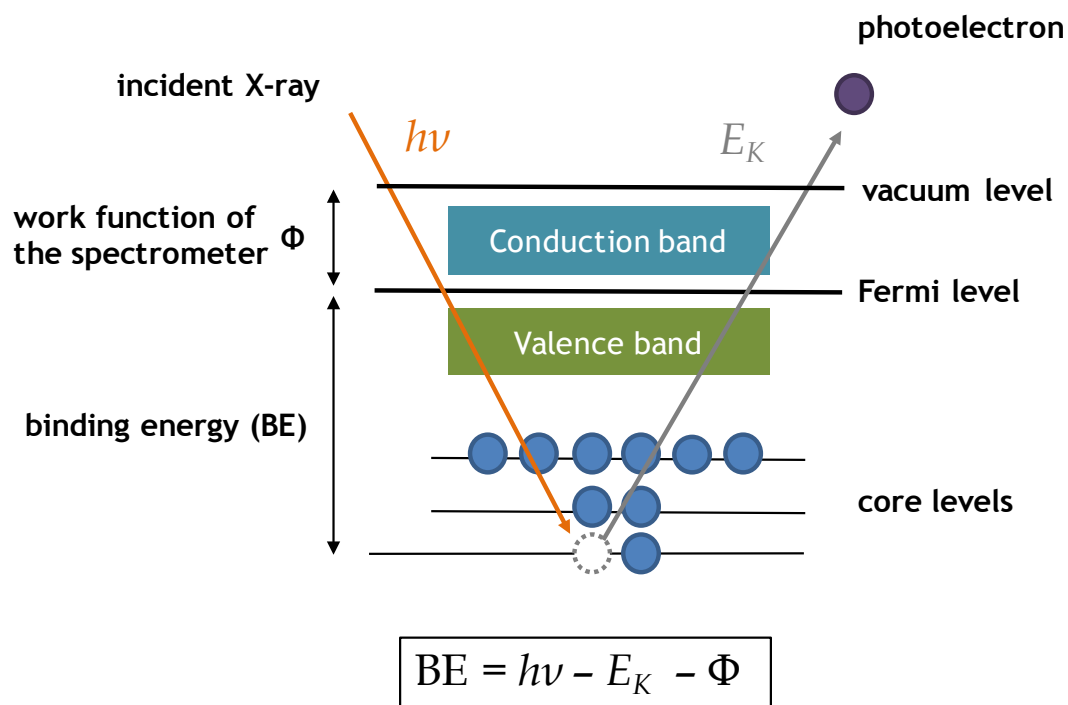
Figure 2-5: Schematic diagram of the XPS process comprising photoionization of a core-level electron and the energy levels involved.
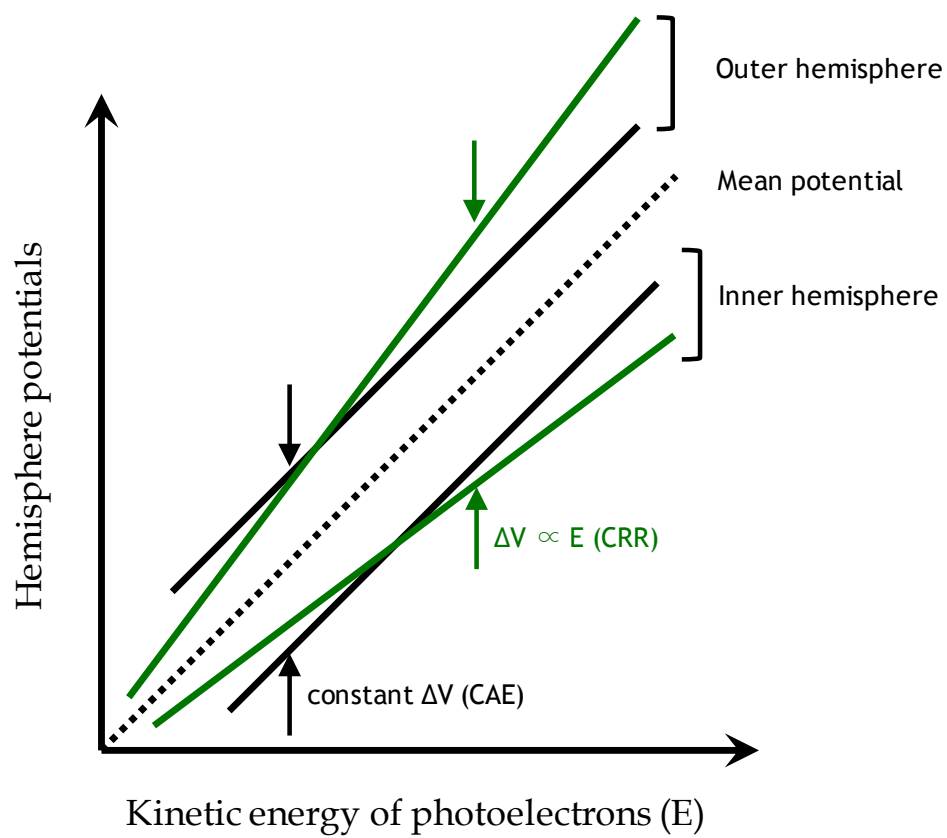
Figure 2-6: Operation of the concentric hemispherical analyzer (CHA) in constant analyzer energy (CAE) mode and constant retard ratio (CRR) mode.

Therefore, XP spectra are usually obtained in CAE mode as it ensures reliable quantification of the spectra at both low and high BEs (with sharp peaks and low count rates). A smaller pass energy results in higher resolution but poorer transmission, so a larger pass energy is normally used in the survey scan while a smaller one in the detailed scans.

In contrast, the retard ratio (= kinetic energy / pass energy) is kept constant when collecting XP spectra in CRR mode. As a result the pass energy (and thus the potential difference) is changing and is proportional to the kinetic energy of the electron [Fig. 2-6]. While the absolute resolution is dependent to the kinetic energy, the relative resolution ($\Delta E/E$) is unchanged across the energy window. It is normal practice to operate Auger electron spectroscopy (AES) in CRR mode. The transmission function of the analyzer is determined by the mode in which the analyzer is operated. Typically the transmission function of CHA under CAE mode is inversely proportional to the kinetic energy of the photoelectron. Lateral resolution is highly dependent to the transfer lens of which both the aperture size and the angle of acceptance are tunable. Higher lateral resolution can be achieved by reducing the aperture size and the angle of acceptance, but at the same time the data acquisition time becomes longer.

Before fitting the XP spectra, the background signal due to inelastic scattering and other energy loss events of the photoelectron is subtracted using the Shirley method, which produces a background in S-shape [20] . Shirley methods takes scattering events that cause energy loss of photoelectrons into consideration and therefore background signal increases as the kinetic energy decreases / as the binding energy increases. As core-level BEs are unique for every element, elemental information can be obtained by collecting BEs of

strong lines in a XP spectrum and compare them with theoretical and experimental values [21]. Also, the BE from a specific core level could shift up to several eV (the chemical shift) due to the chemical binding environment of the element of interest [22]–[27]. For the BE from a specific core level of an element, as the oxidation number increases and the nucleus becomes more positive, binding energy increases due to greater attraction of the nucleus to a core electron (or equivalently, a smaller radius) by the relative absence of outer valence electrons. The general rule is that core level BE of an element increases as the electronegativity of attached atoms or group increases.

XPS is also a powerful tool for evaluating the absolute amount of the elements on the samples using the signals from the film and/or the substrate [28]. An assumption to the film model / film structure further provides us with an estimated film thickness based on the signals from the film and/or the substrate, as shown in Fig. 2-7. Film models with various concentration profiles for analyzing XPS results are discussed in detail elsewhere [29].

With a known takeoff angle, inelastic mean free path of the photoelectron of interest through the film and the unattenuated intensity of the core level from the semi-infinite 2-d layer, one can estimate the film thickness given the assumed concentration profile. Film thickness can be derived from the film signal using the thin film (not buried) model and from the substrate signal using the buried substrate model. Thicknesses of ZrO_2 ALD films in multiple cycles are obtained using the above method.
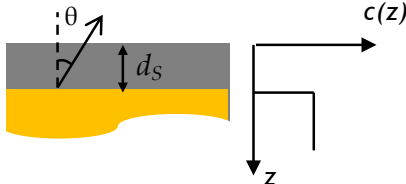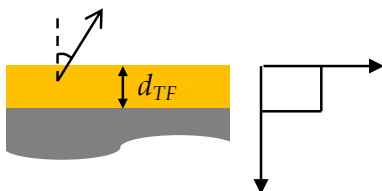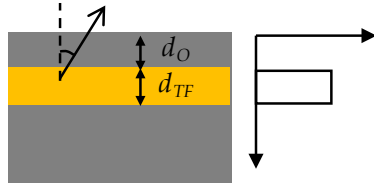
Concentration profile

Photoelectron Intensity

Buried substrate

θ $c(z)$ d_S z

$$I(\theta) = I_0 \exp\left(-\frac{d_S}{\lambda \cos\theta}\right)$$

Thin film (not buried)

d_{TF}

$$I(\theta) = I_0\left[1 - \exp\left(-\frac{d_{TF}}{\lambda \cos\theta}\right)\right]$$

Thin film (buried)

d_O d_{TF}

$$I(\theta) = I_0 \exp\left(-\frac{d_O}{\lambda_O \cos\theta}\right)\left[1 - \exp\left(-\frac{d_{TF}}{\lambda_{TF} \cos\theta}\right)\right]$$

Figure 2-7: Selected film models (left column) that are utilized for analyzing XPS results in this dissertation, and corresponding expressions for photoelectron intensities (right column). [29]

The absolute atomic density and the atomic ratio of a film can also be calculated by comparing the integrated intensity for the element of interest to each other (for atomic ratio) [30] and to an Au calibration standard (for density) [31]. The calibration standard consists of 1000 Å polycrystalline Au (e-beam evaporated) | 100 Å Cr | native SiO_2 | Si(100) was used. The calculation of the absolute atomic density is based on the atomic density of Au, $N_{Au} = 5.90 \times 10^{22}$ cm^{-3}, attenuation length of the Au(4f$_{7/2}$) photoelectrons in Au, $\lambda_{Au} = 15.5$ Å, photoelectron cross-sections (σ), and analyzer transmission functions of the photoelectrons of interest [T(E)], which in this case are inversely proportional to the photoelectron kinetic energy (E). The integrated intensity of the Au(4f$_{7/2}$) peak is proportional to $\sigma_{Au} N_{Au} \lambda_{Au} T(E_{Au})$, and that of the element of interest is dependent on the film structure.

In the case of a non-buried thin film model, the integrated intensity of the element of interest is proportional to $\sigma_{TF} N_{TF} \lambda_{TF} T(E_{TF}) \{1 - \exp[-d_{TF}/ (\lambda_{TF} \cos\theta)]\}$. If the film is very thin ($d_{TF} \ll \lambda_{TF}$), the expression can be simplified by replacing the exponential term with its form in Taylor expansion [i.e., $1 - d_{TF}/ (\lambda_{TF} \cos\theta)$] to $\sigma_{TF} N'_{TF} d_{TF} T(E_{TF})$, where $N'_{TF} d_{TF}$ is the absolute atomic density in atoms-cm^{-2} of the thin film. The ratio of the term before and after Taylor expansion represents the correction factor of the assumption of $d_{TF} \ll \lambda_{TF}$. Similarly, the atomic ratio (N_A/N_B) is calculated by combining the two expressions of the integrated intensities of the two elements (A and B) under a specific film model. In the case of a bilk film, the atomic ratio, N_A/N_B, has the form of $(I_A/I_B)(\sigma_A/\sigma_B)^{-1}[T(E_A)/T(E_B)](\lambda_A/\lambda_B)$, or equivalently, $(I_A/I_B)(\sigma_A/\sigma_B)^{-1}(E_A/E_B)^{0.5}$ (the IMFP of the photoelectrons scales with the square root of the kinetic energy).

2.5 Spectroscopic ellipsometry

Spectroscopic ellipsometry (SE) is a non-invasive, optical characterization technique that allows measurement of film thickness by detecting changes in polarization state of light of different wavelengths after reflection from the solid. Experiments involving SE in this dissertation was carried out on a Woollam VASE (J. A. Woollam Co., Inc. Lincoln, NE) in Cornell Nanoscale Science and Technology Facility (CNF). In the case of ZrO_2 | SiO_2 | Si reported in Chapter 3, we first measured ellipsometric thickness of the chemical oxide on Si substrate (d_1) by assuming a film model of SiO_2 (d_1, unknown) | Si (semi-infinite) and using the refractive index (n) and the extinction coefficient (k) values for SiO_2. We then measured the thickness of ZrO_2 (d_2) assuming a film model of ZrO_2 (d_2, unknown) | SiO_2 (d_1) | Si (semi-infinite) and using optical properties of ZrO_2. Cauchy model with three Cauchy fit parameters was used when the refractive index of the material of interest are not known. Data was analyzed using WVASE32 software.

2.6 References

[1]   S. E. Roadman, N. Maity, J. N. Carter, and J. R. Engstrom, "Study of thin film deposition processes employing variable kinetic energy, highly collimated neutral molecular beams," *J. Vac. Sci. Technol. A Vacuum, Surfaces, Film.*, vol. 16, no. 6, p. 3423, Nov. 1998.

[2]   K. J. Hughes, A. Dube, M. Sharma, and J. R. Engstrom, "Initial Stages of Atomic Layer Deposition of Tantalum Nitride on SiO_2 and Porous Low-κ Substrates Modified by a Branched Interfacial Organic Layer: Chemisorption and the Transition to Steady-State Growth," *J. Phys. Chem. C*, vol. 116, no. 41, pp. 21948–21960, Oct. 2012.

[3]   W. Zhang and J. R. Engstrom, "Effect of substrate composition on atomic layer deposition using self-assembled monolayers as blocking layers," *J. Vac. Sci. Technol. A Vacuum, Surfaces, Film.*, vol. 34, no. 1, p. 01A107, Jan. 2016.

[4]   K. J. Hughes and J. R. Engstrom, "Nucleation delay in atomic layer deposition on a thin organic layer and the role of reaction thermochemistry," *J. Vac. Sci. Technol. A Vacuum, Surfaces, Film.*, vol. 30, no. 1, p. 01A102, 2012.

[5]   W. Zhang, R. K. Nahm, P. F. Ma, and J. R. Engstrom, "Probing ultrathin film continuity and interface abruptness with X-ray photoelectron spectroscopy and low-energy ion scattering," *J. Vac. Sci. Technol. A Vacuum, Surfaces, Film.*, vol. 31, no. 6, p. 61101, 2013.

[6]   M. P. Seah and W. A. Dench, "Quantitative electron spectroscopy of surfaces: A standard data base for electron inelastic mean free paths in solids," *Surf. Interface*

Anal., vol. 1, no. 1, pp. 2–11, Feb. 1979.

[7]   M. P. Seah, "An accurate and simple universal curve for the energy-dependent electron inelastic mean free path," *Surf. Interface Anal.*, vol. 44, no. 4, pp. 497–503, Apr. 2012.

[8]   M. P. Seah, "Simple universal curve for the energy-dependent electron attenuation length for all materials," *Surf. Interface Anal.*, vol. 44, no. 10, pp. 1353–1359, Oct. 2012.

[9]   S. Tanuma, C. J. Powell, and D. R. Penn, "Calculations of electron inelastic mean free paths. III. Data for 15 inorganic compounds over the 50-2000 eV range," *Surf. Interface Anal.*, vol. 17, no. 13, pp. 927–939, Dec. 1991.

[10]   S. Tanuma, C. J. Powell, and D. R. Penn, "Calculations of electron inelastic mean free paths. V. Data for 14 organic compounds over the 50-2000 eV range," *Surf. Interface Anal.*, vol. 21, no. 3, pp. 165–176, Mar. 1994.

[11]   S. Tanuma, C. J. Powell, and D. R. Penn, "Calculations of electron inelastic mean free paths. IX. Data for 41 elemental solids over the 50 eV to 30 keV range," *Surf. Interface Anal.*, vol. 43, no. 3, pp. 689–713, Mar. 2011.

[12]   J. F. Watts, "X-ray photoelectron spectroscopy," *Vacuum*, vol. 45, no. 6–7, pp. 653–671, Jun. 1994.

[13]   P. K. Santra, R. Viswanatha, S. M. Daniels, N. L. Pickett, J. M. Smith, P. O'Brien, and D. D. Sarma, "Investigation of the Internal Heterostructure of Highly Luminescent Quantum Dot−Quantum Well Nanocrystals," *J. Am. Chem. Soc.*, vol. 131, no. 2, pp. 470–477, Jan. 2009.

[14]   J. Nanda and D. D. Sarma, "Photoemission spectroscopy of size selected zinc sulfide

nanocrystallites," *J. Appl. Phys.*, vol. 90, no. 5, p. 2504, 2001.

[15]   J. Nanda, B. Kuruvilla, and D. Sarma, "Photoelectron spectroscopic study of CdS nanocrystallites," *Phys. Rev. B*, vol. 59, no. 11, pp. 7473–7479, Mar. 1999.

[16]   K. Huang, R. Demadrille, M. G. Silly, F. Sirotti, P. Reiss, and O. Renault, "Internal Structure of InP/ZnS Nanocrystals Unraveled by High-Resolution Soft X-ray Photoelectron Spectroscopy," *ACS Nano*, vol. 4, no. 8, pp. 4799–4805, Aug. 2010.

[17]   H. Borchert, D. Dorfs, C. McGinley, S. Adam, T. Möller, H. Weller, and A. Eychmüller, "Photoemission Study of Onion Like Quantum Dot Quantum Well and Double Quantum Well Nanocrystals of CdS and HgS," *J. Phys. Chem. B*, vol. 107, no. 30, pp. 7486–7491, Jul. 2003.

[18]   C. R. Brundle, M. W. Roberts, D. Latham, and K. Yates, "An ultrahigh vacuum electron spectrometer for surface studies," *J. Electron Spectros. Relat. Phenomena*, vol. 3, no. 4, pp. 241–261, Jan. 1974.

[19]   J. F. Watts and J. Wolstenholme, *An Introduction to Surface Analysis by XPS and AES*. Chichester, UK: John Wiley & Sons, Ltd, 2003.

[20]   D. A. Shirley, "High-Resolution X-Ray Photoemission Spectrum of the Valence Bands of Gold," *Phys. Rev. B*, vol. 5, no. 12, pp. 4709–4714, Jun. 1972.

[21]   J. C. Fuggle and N. Mårtensson, "Core-level binding energies in metals," *J. Electron Spectros. Relat. Phenomena*, vol. 21, no. 3, pp. 275–281, Jan. 1980.

[22]   W. F. Egelhoff, "Core-level binding-energy shifts at surfaces and in solids," *Surf. Sci. Rep.*, vol. 6, no. 6–8, pp. 253–415, May 1987.

[23]   C. Papp and H.-P. Steinrück, "In situ high-resolution X-ray photoelectron spectroscopy – Fundamental insights in surface reactions," *Surf. Sci. Rep.*, vol. 68,

no. 3–4, pp. 446–487, Nov. 2013.

[24] R. Nyholm, A. Berndtsson, and N. Martensson, "Core level binding energies for the elements Hf to Bi (Z=72-83)," *Journal of Physics C: Solid State Physics*, vol. 13. pp. L1091–L1096, 1980.

[25] R. Nyholm and N. Martensson, "Core level binding energies for the elements Zr-Te (Z=40-52)," *J. Phys. C Solid State Phys.*, vol. 13, no. 11, pp. L279–L284, Apr. 1980.

[26] B. Johansson and N. Mårtensson, "Core-level binding-energy shifts for the metallic elements," *Phys. Rev. B*, vol. 21, no. 10, pp. 4427–4457, 1980.

[27] A. Lebugle, U. Axelsson, R. Nyholm, and N. Mårtensson, "Experimental L and M Core Level Binding Energies for the Metals ^{22}Ti to ^{30}Zn," *Physica Scripta*, vol. 23. pp. 825–827, 1981.

[28] M. P. Seah, "Data compilations: their use to improve measurement certainty in surface analysis by AES and XPS," *Surf. Interface Anal.*, vol. 9, no. 2, pp. 85–98, Jul. 1986.

[29] K. J. Hughes, Ph. D. dissertation, Cornell University, 2011.

[30] K. J. Hughes and J. R. Engstrom, "Interfacial organic layers: Tailored surface chemistry for nucleation and growth," *J. Vac. Sci. Technol. A Vacuum, Surfaces, Film.*, vol. 28, no. 5, p. 1033, 2010.

[31] A. S. Killampalli, P. F. Ma, and J. R. Engstrom, "The reaction of tetrakis(dimethylamido)titanium with self-assembled alkyltrichlorosilane monolayers possessing -OH, -NH$_2$, and -CH$_3$ terminal groups.," *J. Am. Chem. Soc.*, vol. 127, no. 17, pp. 6300–10, May 2005.

3. Design and characterization of a micro-reactor for spatially-confined atomic layer deposition and *in situ* UHV surface analysis

3.1 Overview

We report the design and characterization of a micro-reactor probe that enables gas-phase reactions such as atomic layer deposition (ALD) at low-to-medium vacuum, which is coupled directly to an ultra-high vacuum (UHV) analysis chamber for subsequent *in situ* surface characterization without an air break. Avoiding this air break is critical to developing a complete understanding of the growth of ultrathin films, particularly in the early stages of growth. Making use of a precisely defined gap between the micro-reactor probe and the substrate surface, the reactants are well confined in the reaction zone (total volume ~ 1 cm^3) by the use of "curtain gas" flow. Computational fluid dynamics was used to simulate both the steady-state and transient operations of the micro-reactor and surrounding UHV chamber in which fluid flow, heat transport and mass transport were considered. We provide two examples of the efficacy of the design by considering exposure of a Cu substrate to $I_2(g)$ vapor, and conducting the ALD of ZrO_2 using $Zr[N(C_2H_5)(CH_3)]_4$ and H_2O as reactants, the latter at a total pressure of 18 Torr. In both cases we achieve excellent confinement of the reactants to the central reaction zone, as confirmed by *in situ* spatially resolved X-ray photoelectron spectroscopy.

3.2 Introduction

Atomic layer deposition (ALD) is a technique for depositing thin films by exposing a substrate to alternating pulses of a thin film precursor and a co-reactant, with purge steps in between [1]. Due to the self-limiting nature of the ALD process, one can precisely determine the thin film thickness at an atomic level by controlling the number of ALD cycles. ALD has been employed to deposit ultrathin films of many types of materials, including oxides, nitrides and noble metals [2]. ALD also has the advantage of depositing conformal, ultrathin films on the surfaces present on 3D features, such as trenches and fins with high aspect ratios. Because of these and other features, ALD has been widely applied in semiconductor manufacturing for several different applications, such as high-k dielectrics [3], [4], diffusion barriers for interconnect [5] and spacers in double patterning [6], [7].

ALD, similar to other technologically important processes such as chemical vapor deposition (CVD) and plasma etching, is typically performed under medium vacuum conditions, or pressures ranging from 10^{-3} to 10 Torr. In contrast, many of the most powerful surface characterization methods, such as electron and ion based spectroscopies and diffraction techniques, are performed under ultra-high vacuum (UHV, $p < 10^{-9}$ Torr) conditions. Conducting surface analyses post-deposition and *ex situ* is always an option, however this approach is susceptible to the occurrence of undesirable reactions such as surface oxidation, reactions with adsorbed species, and contamination. This is particularly true in the case of the ultrathin films one most often seeks to deposit using ALD, where post-deposition reactions occurring upon exposure to atmospheric air could totally obscure

the composition and microstructure the deposited thin film. This situation is entirely analogous to the so-called "pressure gap" that has plagued the use of surface science approaches to examine reactions occurring in heterogeneous catalysis [8]. Recent innovations in spectrometer design have resulted in techniques such as near ambient pressure X-ray photoelectron spectroscopy (NAP-XPS), where ALD has been examined *in situ* at partial pressures of $\sim 7.5 \times 10^{-2}$ Torr [9]. Use of this technique at present, however, essentially requires the use of synchrotron X-ray radiation, thus significantly limiting its impact.

Historically, to overcome the pressure gap between the process and characterization conditions, two main approaches have been developed that involve employing separate chambers/zones for "high" pressure reaction and/or deposition and UHV surface analysis in a single apparatus [10]. One approach is to "bring the substrate to the gas source", where the substrate is transferred to and from the reaction chamber via a sample transfer mechanism to and from the analysis chamber for surface characterization [11]. An early example of this approach was provided by Goodman *et al*. [12]. Another approach is to "bring the gas source to the substrate": a translatable cup-like device, typically fitted with integrated lines for the introduction of reactive gases, makes contact with the substrate/substrate holder to form a small volume that acts as a small chemical micro-reactor, with the substrate surface providing one of the walls of the reactor. In this scheme, the micro-reactor is evacuated after the completion of the reactions, and surface characterization can be conducted once the chamber is brought back to UHV. Somorjai and co-workers were the first to utilize this design to study heterogeneous catalysis [13],

[14], and more recently George and co-workers applied this type of design to investigate ALD [15]–[17].

In addition to the issue of the design of the reaction chamber/zone, a number of probes have been employed for *in situ* characterization of the thin films deposited by ALD, including techniques such as spectroscopic ellipsometry [18], X-ray photoelectron spectroscopy (XPS) [19]–[21] and X-ray fluorescence (XRF) [22]. Rubloff and co-workers have described a system that utilizes a micro-reactor enclosed in an UHV chamber, similar to those employed by Somorjai and co-workers, where the gases leaving the reactor are sampled using quadrupole mass spectroscopy (QMS) [23], [24].

We present here the design and characterization of a micro-reactor that draws from both of the two main strategies discussed above: it uses a cup-like device to define the reaction zone inside of a larger chamber, and this larger chamber is coupled by a gate valve to another chamber possessing tools for UHV surface analysis. In our case an important criterion was that the design must be compatible with an existing sample holder and manipulator. In addition, another criterion we have invoked is that the design must not involve a physical seal (i.e., a gasket) to define the reaction zone, which essentially all previous designs have employed. The design we present here exhibits strong similarities to spatial ALD print head designs [25], [26], where the reaction zone is defined by the use of a "curtain gas" to limit the out-diffusion of reactive species into the surrounding larger chamber. In this paper, we will first provide a detailed description of our surface analysis system and how the probe is incorporated into the chamber and employed in experiments. We will describe a selected set of simulations at relevant reaction conditions using computational fluid dynamics (CFD) to evaluate the predicted performance of the micro-

reactor probe. Finally, to demonstrate the functionality and performance of the micro-reactor system, we have conducted a gas-surface reaction between $I_2(g)$ and Cu and ALD of thin films of ZrO_2 deposited on SiO_2 substrates, where the thin films have been analyzed *in situ* and without air break using XPS.

3.3 Design and construction

3.3.1 Surrounding and adjacent chambers and sample manipulator

The micro-reactor we describe here has been incorporated into an existing custom-designed, multiple-stage stainless steel UHV chamber as illustrated schematically in Fig. 3-1(a), which we have described in detail previously [27], [28]. For the experiments described here, the intermediate chamber plays an important role, as it is coupled to the main UHV surface analysis chamber via a gate valve, a load-lock chamber via a gate valve, and the micro-reactor, which can also be isolated in its own chamber by a gate valve. The main analysis chamber (volume ~ 22 L) is pumped by both a 400 L-s^{-1} magnetically levitated high-throughput turbomolecular pump and a titanium sublimation pump. A base pressure of ~ 9×10^{-10} Torr is routinely achieved after a 24-36 h bakeout at ~150 °C. The sample manipulator, mounted on the intermediate chamber, is designed to accept sample holders that can accommodate either full 100 mm wafers or smaller "coupon" size (e.g., 1.8×1.8 cm^2) substrates. The substrates are introduced using a magnetically coupled transfer arm mounted to the load-lock chamber, which is separately pumped by a 60 L s^{-1} turbomolecular pump. The substrates are mounted on a precision sample manipulator that

allows for motion of the sample along three linear axes as well as polar and azimuthal rotation. Translation of the sample along the long axis of the manipulator takes the sample from the intermediate chamber to the main analysis chamber. The substrates are heated radiatively by a pyrolytic boron nitride heating element that is incorporated in the manipulator and possesses a maximum power output of 3 kW. This sample stage can heat Si substrates to a peak temperature of 1200 °C and continuous working temperatures of 1000 °C, although much lower substrate temperatures are employed for the experiments we describe here.

The main analysis chamber houses a concentric hemispherical electron energy analyzer, which serves as an analyzer for both XPS (photoelectrons) and low-energy ion scattering spectroscopy (LEISS, scattered ions) [29], [30]. A twin anode Mg/Al X-ray source and an ion source (SPECS ion source IQE 12/38) are also located in the main chamber. The main analysis chamber is also coupled to a doubly differentially pumped supersonic molecular beam, and there is also a quadrupole mass spectrometer mounted on this chamber that can analyze both the molecular beam itself and residual gases in the chamber [27].
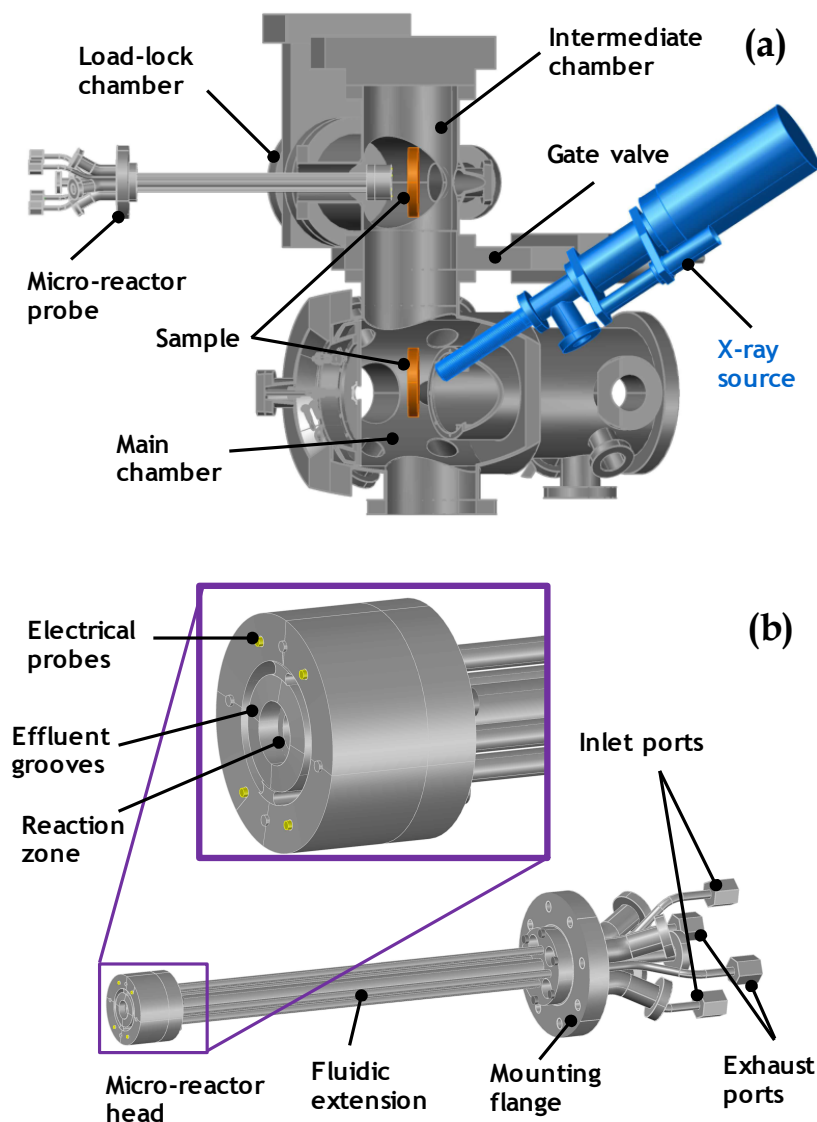
Figure 3-1: (a) Schematic drawing of the UHV chamber, indicating the position of the micro-reactor, and the sample in the two positions: for gas-surface reaction, and surface analysis using XPS. A number of components on the UHV chamber have been omitted for clarity. **(b)** Schematic drawing of the micro-reactor probe.

3.3.2 Micro-reactor probe configuration and hardware

As may be seen in Fig. 3-1(b), the micro-reactor probe, consisting of a precision machined head, a fluidic extension piece and a fluidic and electrical feedthrough is mounted on the intermediate chamber. The assembly is mounted on a linear translator, which affixed to a gate valve that is attached to the intermediate chamber. A key goal is to minimize any possible contamination to the UHV chamber when the probe is not in use (e.g., due to outgassing), which is achieved in our design by retracting the probe into its own sub-chamber and closing the gate valve. For experiments involving thin film deposition, the micro-reactor probe is translated into the intermediate chamber where it combines with the sample holder to form the reaction zone. The exact geometry of this reaction zone (and the probe head) is critical concerning the performance of the micro-reactor, and we consider these issues below in Section 3.4.2, where we describe results from CFD calculations designed to optimize these dimensions. In the actual construction, the optimized values were appropriately modified by considering limitations associated with machining and other practical constraints.

The micro-reactor probe consists of several components, as indicated above. The mounting flange has five fluidic feedthroughs for gas inlets or exhausts, and four mini-CF flanges for electrical feedthroughs (e.g., for heating elements and thermocouples). One of the feedthroughs, intended for use as a gas inlet and lying on the central axis of the probe, can double as a viewport, providing optical axis to the substrate surface. The five fluidic feedthroughs are connected to the probe head using an extension piece ($\sim$ 36 cm long). The probe head itself is a cylindrical machined piece of stainless steel, $\sim$ 5.6 cm in dia., and 2.5

cm in height. In the probe head the central fluid line combines with two of the other gas fluid lines in a cylindrical space at the end of the probe, which, along with the substrate surface, defines the reaction zone. This reaction zone has a height above the substrate surface of ~ 0.5 cm, and a diameter of ~ 1.5 cm, equivalent to a volume of ~ 1 cm^3. These three gas lines provide the ability to control the introduction of three independent species to the reaction zone. The final two gas lines are connected to two peripheral semi-circular grooves (tracing an arc of 150°) that are machined into the end of the probe, and these are ~ 1.5 cm from the centerline, ~ 0.3 cm wide. The two lines act together to provide the exhaust lines for the micro-reactor. Four physical "stops" are located on the surface of the end of the probe head, and these act to ensure a precise gap (~ 0.05-0.1 cm) between the probe head and the substrate surface. The micro-reactor system is constructed entirely of bakeable materials so that it can undergo a long bake (> 24 h) at ~ 150 °C. A closed-loop PID control system is employed to control the pressure in the reactor during thin film deposition, which includes the main process mechanical pump, a capacitance monometer, and an exhaust throttle valve.

3.3.3 Reactant delivery system

We have designed a gas delivery system that can deliver the reactive species to the micro-reactor and provide the needed performance for ALD, including fast switching between reactive species and inert purge gases, and this is displayed in Fig. 3-2. All gases (reactive and inert) are connected to the micro-reactor feedthrough using stainless steel tubes and VCR connections. In all cases we make use of a "vent-run" configuration for

both the reactive and purge streams, where each stream flows continuously, but the two streams alternate in sequence between being directed to a micro-reactor inlet and a bypass line to a pump. The volumetric flows of the reactive and purge streams are essentially the same, which minimizes any fluctuations of the reactor pressure. Each "toggling" network comprises four pneumatic valves driven by fast-switching solenoids (response time of 1.5-3.4 ms). A compact DAQ chassis with a power source sends 24 V DC signals to solenoids, as determined by a computer-programmed dosing sequence. The delivery lines of the reactants are heat-traced from the outlet of the bubbler (if present) to the micro-reactor probe feedthrough. In the case of vapors delivered by an inert carrier gas, these lines are heated to a temperature of ~ 20 °C higher than the temperature used for the bubbler.
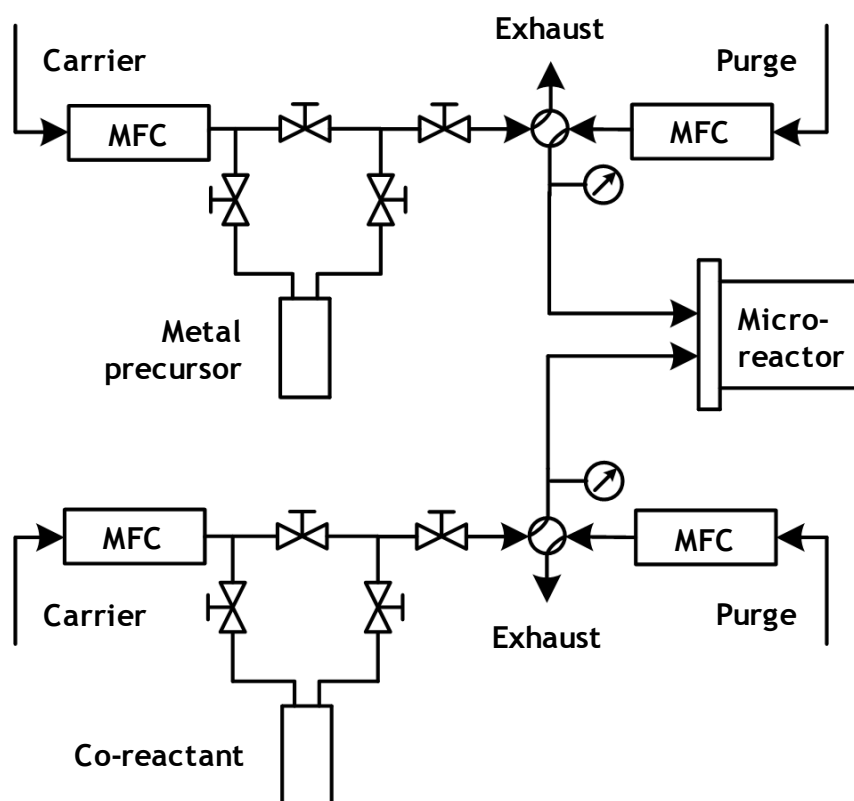
Figure 3-2: Schematic drawing of the reactant manifold employed here for studies of atomic layer deposition. The components that control the flow of the curtain and carrier gas are not shown in this diagram.

3.4 Simulation and optimization of the design of the micro-reactor probe

3.4.1 Simplified model for the micro-reactor probe and CFD calculations

We have conducted simulations of the micro-reactor probe at relevant reaction conditions using computational fluid dynamics (CFD) to model the flow, diffusion and heat transfer. As indicated above, confinement of the reactive gases to the reaction zone is an important design goal, and it will depend on both geometric factors and the reaction conditions (flow and pressure). The geometry of the reactor-substrate system was reduced to a two-dimensional, axisymmetric coordinate system to reduce the computation time. The simplified model consists of a cylindrical planar substrate (thickness ~ 0.076. cm), and a cylindrical sample heater (thickness ~ 0.51 cm) that are separated by a gap of ~ 0.25 cm. Both of these have a radius of ~ 5.1 cm. The micro-reactor probe head (outside radius ~ 3.25 cm, height of ~ 2.1 cm) includes one common cylindrical central feed (inside radius ~ 0.6 cm) for all input species (reactants, carrier and purge) and an annular exhaust channel (inside radius of 1.2 cm, outside radius of 1.4 cm). There is a cylindrical chamber (~ 14.4 cm in height, ~ 9.5 cm in radius) that surrounds the substrate holder and micro-reactor probe head, which represents the intermediate chamber on our actual system. There are two inlets for an inert gas inlet on this surrounding chamber, which represent the injection points of the curtain gas. One of these is at the top of the surrounding chamber, on-axis, with an opening radius of ~ 1.0 cm. The other is an annular region with an inner radius of ~ 3.25 cm, and an outside radius of ~ 4.25 cm. In this approach, the curtain gas flows radially inward between the small gap (~ 0.05-0.1 cm) between the substrate surface, and

flows out the annular region in the probe head to the exhaust, along with the reactant and purge flows.

We carried out CFD calculations based on the finite element method, which involved numerically solving all the governing equations that describe the physics, namely multi-component, non-isothermal, compressible flow. The domain was discretized into many triangular subdomains in which simple trial functions are used to approximate the true function, and the numerical solution was found across the whole domain at any given time with proper boundary conditions. Heat and mass transport and fluid flow are coupled due to the composition dependence of the viscosity and the thermal conductivity, and the temperature and pressure dependence of the diffusivity.

3.4.2 Results at steady-state

We first carried out CFD calculations under the assumption that the flow is time-independent, seeking to understand the behavior of the flow at the steady state, using the dimensions given above. In these simulations, heater power was set to produce a substrate temperature of 150 °C, which is within the process temperature "window" for a number of ALD chemistries. The flow rate of the reactant gas (assumed to be pure O_2) through the common central tube was set to 10 sccm, while the flow at the two inlets for the curtain gas (assumed to be pure N_2) were set to be 50 sccm each. The reactor pressure was set to be at ~ 1 Torr by fixing the exhaust pressure at the end of the effluent groove to be exactly 1 Torr.

In this calculation we sought to determine the effectiveness of reactant delivery to the substrate surface, and the confinement of these reactants to the central reaction zone, with minimal out-diffusion of reactants to surrounding sub-chamber. We first examined the effect of the dimension of the gap between the probe head and the substrate surface. An examination of the pressure distribution across the simulation cell revealed a pressure drop of ~ 0.5 Torr associated with the flow of the curtain gas inwards from the edge of the micro-reactor probe head to the annular exhaust groove. A somewhat larger pressure drop (~ 0.6 Torr) was associated with the flow of the reactant outwards from the reaction zone to the annular exhaust groove. Concerning the temperature distribution we found that it was uniform across the substrate surface (~ 150 °C), apparently unaffected by the flow of gases, even though the temperatures of the input reactant and carrier gases were set to 25 °C. A calculation of the mole fractions of each species indicated excellent segregation of the two components. For example, we calculate an spatially averaged mole fraction for the reactant gas, O_2, of 0.84 at the substrate surface. In contrast, the spatially averaged mole fraction for the reactant gas at the walls of the surrounding chamber of 7.4×10^{-4}, which corresponds to a 3 order-of-magnitude decrease in the amount of the reactant reaching those surfaces. These steady-state concentrations of O_2 represent a worst case scenario in terms of using this probe for ALD, as in ALD typically the reactant pulses are short, followed by much longer purge pulses. Thus, we expect that the concentration of reactant species reaching the walls of the surrounding chamber walls will be much lower in a transient mode, as compared to steady state.

We also examined the effect of the shape of the surface of the probe head, and the placement of the annular region. In particular, we have considered three cases concerning

shape variations: (i) a flat planar end surface, (ii) one where the surfaces are dished in a way such that the gap is greatest at the annular exhaust region, and (iii) one where the surfaces are dished such that the gap is smallest at the annular exhaust region. Of the three cases, the design where the gap is the largest at the annular exhaust region, and smallest at the edge of the probe and the edge of the reaction zone produced the best results in terms of minimizing the out-diffusion of the gaseous reactant. We also examined the effect of the placement of the annular region, by varying the relative length of radial travel from the reaction zone to the annular region, and from the annular region to the edge to the probe, where we considered the ratio of these lengths to be 1:3, 1:1, and 3:1. We found that the first of these produced the best result in terms of minimizing the out-diffusion of the gaseous reactant.

3.4.3 Results under conditions of sequential, periodic flows

In order to examine the effectiveness of the micro-reactor for operating conditions more representative of ALD, we have conducted CFD calculations under transient conditions. A two-step calculation was used to simulate the reactor flows for multiple cycles of ALD. The first step calculates the steady state that is reached for the flow of single-component species (e.g., the inert purge and curtain gases), which acts to establish the initial temperature distribution (including that of the substrate) and the reactor pressure. During this first step no reactant are introduced, so it is equivalent to flows of N_2 for both the reactant inflow and the curtain gas. Following this initiation step, we next consider the calculation of the time-dependent flows from the reactant inlet: alternating pulses of the

thin film precursor (or surrogate) and the co-reactant (e.g., H_2O), separated by flow of the purge gas (N_2). Xe was chosen as a surrogate of organometallic precursors because the transport properties (or collision cross-sections and intermolecular potentials) of such molecules are generally not known. We consider the following sequence of inlet flow compositions and cycle times: Xe (0.2 s), N_2 (0.6 s), H_2O (0.2 s), and N_2 (0.6 s), for a total ALD cycle time of 1.6 s. We found that the calculations had difficulty converging if we assumed that the initial concentrations of the reactant species (Xe and H_2O) in the surrounding chamber were set identically to zero. Instead, we set the initial concentrations of these species to be 10 ppb (mole fractions of 10^{-8} for each reactant) in the surrounding chamber. Transport properties in this calculation were dependent on the composition of the ternary mixture, as well as temperature and pressure.

The outputs of the calculations that we are most interested are the concentrations/partial pressures/fluxes reaching the surface of the substrate, and those reaching the surfaces of the surrounding chamber. In Fig. 3-3(a) we plot the partial pressure of the two reactants as a function of time, averaged over the substrate surface. We see that the peak partial pressure is $\sim$ 7.6-7.7 Torr for H_2O, while that for Xe is 6.9-7.8 Torr, compared to the total pressure of $\sim$ 10 Torr (with N_2 making up the balance). We see that there is minimal overlap between the two species. This suggests that CVD reactions (co-exposure to both reactants) are unlikely for this dosing sequence, although increasing the purge time would certainly be an option. If we integrate the date presented in Fig. 3-3(a), we can produce the results we present in Fig. 3-3(b), where we plot the cumulative exposure of the substrate to the two reactants. As may be seen we observe a staircase-like increase in the cumulative exposure for both H_2O and Xe, but that for H_2O approaches the absolute

limit (20 Torr-s) closer given the number of cycles simulated (10) and the inlet partial pressure (10 Torr) and cycle time (0.2 s). The cumulative precursor exposure reaches only 70% of the theoretical limit. This may reflect a difference in diffusivities of the two species (the diffusivity of Xe in N_2 is about ½ of that for H_2O in N_2).

The behavior at the surfaces of the surrounding chamber is quite different, which is of course a major objective of the design of the micro-reactor. In Fig. 3-3(c) we plot the partial pressure of the two reactants as a function of time, averaged over the surfaces of the surrounding chamber. As indicated above, we set the mole fractions of the reactants at zero time to be 10^{-8} in the surrounding chamber, or a partial pressure of 10^{-7} Torr. First, concerning the partial pressure of Xe, it exhibits a continuous decrease with time, exhibiting no periodicity, and in fact is fit extremely well by a simple exponential decay. This indicates that no Xe that enters the micro-reactor probe via the reactant inlet reaches the surrounding chamber—it is perfectly confined in the volume defined by the reaction zone and the gap leading to the annular effluent channel. The partial pressure of H_2O is quite different, as may be seen—it shows clear oscillations, but the peak partial pressure seems to be approaching a constant value. Indeed these peak values are very well described by an exponential decay to a constant value of ~ 1.8×10^{-6} Torr. This value is still an approximately 8 orders-of-magnitude reduction in the amount of H_2O reaching those surfaces as compared to that on substrate surface. It would seem that the inward radial flow of the curtain gas is sufficient to confine Xe, but not H_2O, due to a difference in their diffusivities.
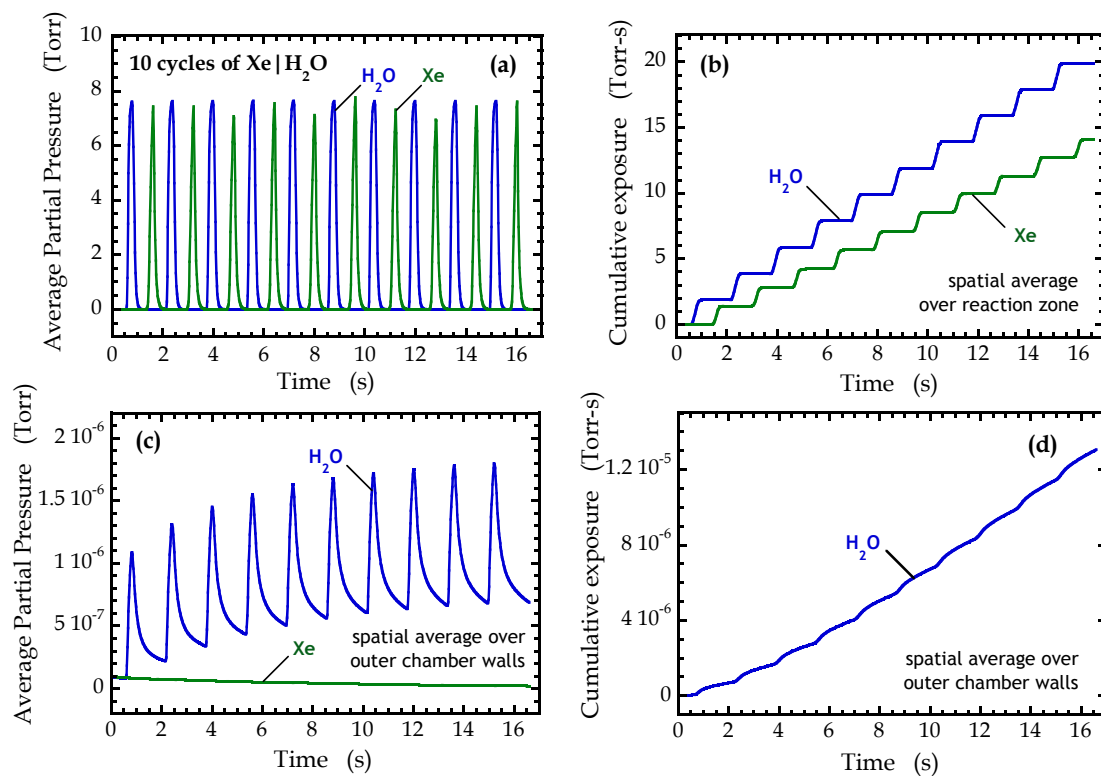
Figure 3-3: (a) Partial pressure of the two reactants (H_2O and the thin film precursor surrogate, Xe) produced at the sample surface as predicted by the CFD model for 10 cycles of ALD. **(b)** Partial pressures of the two reactants at the outer chamber walls for the same conditions. **(c)** Cumulative exposure of the sample surface to the two reactants for the same conditions. **(d)** Cumulative exposure of the outer chamber walls to the H_2O reactant for the same conditions.

In Fig. 3-3(d) we plot the cumulative exposure of the surfaces of the surrounding chamber to H_2O as a function of time. Consistent with results shown in Fig. 3-3(c), after an initial transient period of ~ 10 s, the increase in the exposure becomes approximately constant, reaching a value of ~ 1.3×10^{-5} Torr-s after 10 ALD cycles. This would represent a 13 Langmuir (L) exposure of the surfaces of the surrounding chamber to H_2O, which should not sufficiently degrade the ability to reach UHV after pump-out.

In summary, the CFD calculations indicate that using this design one can produce short pulses of reactant species, separated sufficiently by purge streams. The use of a curtain gas predicts that large molecules such as typical thin film precursors should be effectively confined to the reaction zone. On the other hand, smaller molecules, including typical co-reactants such as H_2O, may be present at trace levels in the surrounding chamber, but at levels that may be compatible with achieving UHV conditions after pump-out.

3.5 System performance

To evaluate the performance of the micro-reactor we have conducted two sets of experiments: (*i*) a gas-surface reaction between a single reactant [$I_2(g)$] and a substrate surface (Cu); and (*ii*) ALD of a thin film (ZrO_2) on a substrate surface (SiO_2). In the first experiment we have examined the reaction of $I_2(g)$ vapor with a thin film of Cu. The Cu substrate in this case was a thin film of Cu (900 Å thick, sputter deposited onto a SiO_2 substrate possessing also an intermediate thin film of Ta, several Å thick), mounted on a metal (Mo) platen capable of holding a wafer of 10 cm in diameter. Before inserting a sample, the sample manipulator is positioned in the intermediate chamber and the gate

valve separating the main surface analysis chamber and the intermediate chamber is closed. The sample is first placed in the load-lock chamber and is then transferred onto the sample manipulator in the intermediate chamber when the pressure in the load-lock chamber is below 1×10^{-6} Torr. Once mounted, the sample platen stays on the manipulator during thin-film deposition as well as surface analysis.

To begin an experiment, the gate valve isolating the micro-reactor probe is opened and the probe is translated into the intermediate chamber with a probe-substrate gap of ~ 1.5 cm. Next, the flow of the curtain gas (N_2 at 50-75 sccm) is initiated, and the sample is heated to the appropriate temperature for reaction or deposition. Once the sample temperature has stabilized, using a precision linear translator the probe is positioned in front of the sample, which produces the small gap (~ 0.05-0.1 cm) between the probe and the sample surface, and flow of the reactant (and purge for ALD) gas stream (N_2) is started. Spring-loaded electrical probes aid in the precise positioning of the probe, as contact with the conducting sample holder produces a change in resistance.

For the reaction of $I_2(g)$ with a Cu surface, we have delivered the $I_2(g)$ as a vapor using a carrier gas (N_2 at 20 sccm). The vessel containing solid I_2 was cooled to a temperature of 0 °C (vapor pressure ~ 11 mTorr [31]), while the lines downstream leading to the micro-reactor were kept at room temperature. The Cu substrate was exposed to the vapor for 30 s. Following reaction, the intermediate chamber was evacuated, the micro-reactor was retracted and isolated by closing a gate valve, the gate valve separating the intermediate chamber and the main surface analysis chamber was opened, and the sample was lowered into the position for analysis using XPS. In Fig. 3-4 we display results from XPS where we have translated the substrate such as to produce a line scan, i.e., the

integrated intensity of the I(3d) peak as a function of position. For this experiment the area sampled by XPS was 0.12 cm dia., and the line scan step size was 0.254 cm so there is no overlap between neighboring data points. As may be seen, we observe a flat-top profile, and over the reaction zone the mean of the measured integrated intensity is 1.920×10^5 eV-counts-s^{-1}, with a standard deviation of 5,800 eV-counts-s^{-1} (~ 3% of the mean). Outside of the reaction zone, we observe a smooth drop in intensity, reaching a value of zero at the centerline of the annular exhaust region. These results indicate that we have achieved excellent confinement of the $I_2(g)$, with uniform substrate modification over the reaction zone, and essentially no evidence of reaction beyond the annular exhaust region.

We have examined the ALD of ZrO_2 using as reactants tetrakis(ethylmethylamino) zirconium, $Zr[N(CH_2CH_3)(CH_3)]_4$ (purity 99.9999%, Air Liquide) and water vapor on SiO_2. The SiO_2 substrates were prepared starting from single-side polished, Si(100) wafers (B doped, resistivity 38-63 Ω cm). The native SiO_2 layer was removed from the substrates by dipping in buffered oxide etch (BOE) for 2 minutes. The substrates were then re-oxidized by dipping in Nanostrip for 15 min at a temperature of ~ 75 °C. The BOE/Nanostrip treatment was then repeated. This method is known to produce a 15-20 Å layer of chemical oxide with surface Si-OH density of ~5×10^{14} cm^{-2} [28], [32].
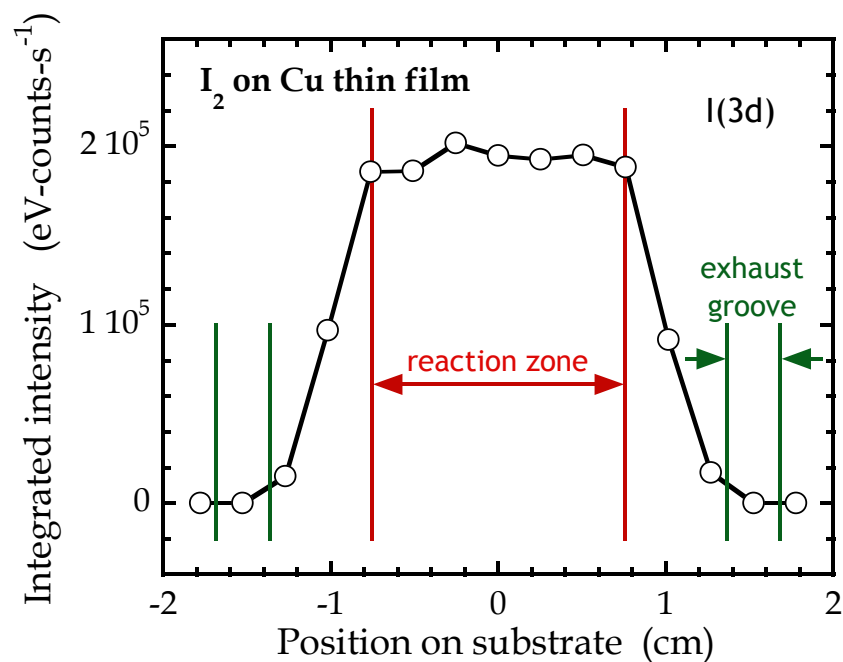
Figure 3-4: Intensity of the I(3d) peak from XPS as a function of the position on the sample, after a Cu surface was exposed to $I_2(g)$ vapor. The size of the central reaction zone, and the surrounding effluent exhaust grooves are also shown.

Once the Si substrate has been loaded, and the micro-reactor has been placed in position, the flows of the curtain and carrier gases are initiated and the substrate is heated to the temperature for ALD. First we conducted a series of ½ cycle experiments to verify that for the conditions examined that they were in the so-called ALD window. For these experiments the combined gas flow rate was 50 sccm (35 sccm N_2 curtain gas, 5 sccm (He) carrier/(N_2) purge gas for the (Zr) reactant and 5 sccm N_2 each in the other two inlets), and the total pressure in the micro-reactor was 5 Torr. The substrate temperature was set to T_s = 180 °C. The temperature of the bubbler containing the $Zr[N(CH_2CH_3)(CH_3)]_4$ precursor was held at 40 °C, producing a vapor pressure of ~ 30 mTorr [33]. In Fig. 3-5 we display the integrated intensity of the Zr(3d) peak as a function of the exposure time of the SiO_2 surface to the $Zr[N(CH_2CH_3)(CH_3)]_4$ precursor. As may be seen, saturation is reached after an exposure time of ~ 1 min. This time is not totally the effect of the kinetics of adsorption, rather it is mostly associated with the length of the feed lines between the bubbler and the micro-reactor, and may also include effects due to passivation of these feed lines.
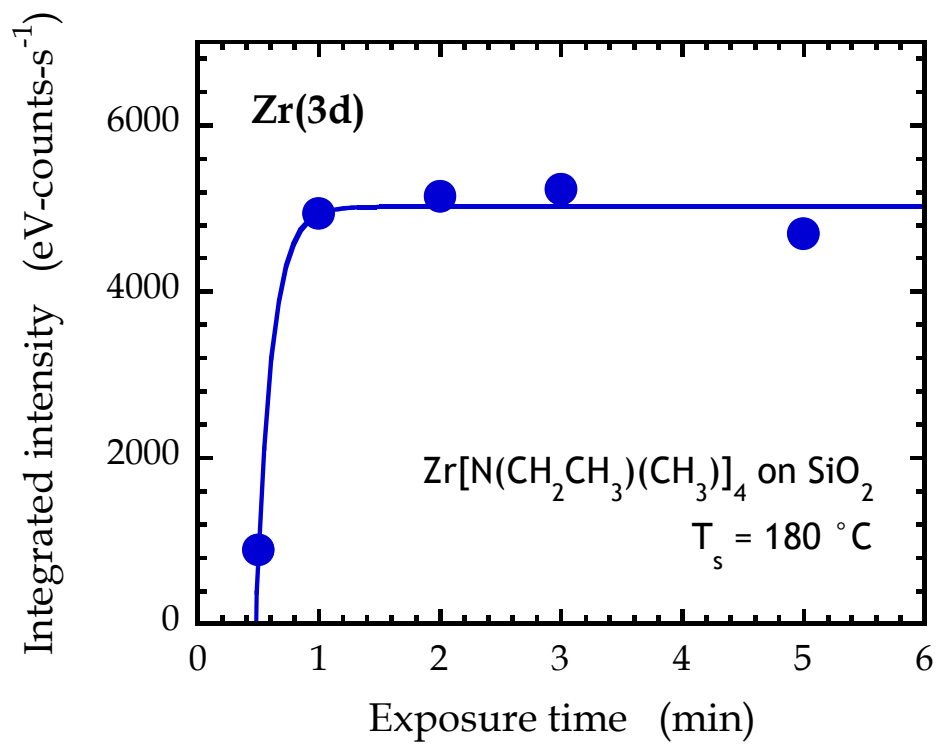
Figure 3-5: Integrated intensity of the Zr(3d) peak from XPS as a function of exposure to the Zr thin film precursor. The line is a fit to a decaying exponential, with an offset in the exposure time.

We next conducted ALD of ZrO_2 using as reactants $Zr[N(CH_2CH_3)(CH_3)]_4$ as the precursor (bubbler temperature of 40 °C) and H_2O as the co-reactant (held at 0 °C in a stainless steel bubbler). For these experiments, we used a total flow of 95 sccm (curtain, carrier and purge gases), which resulted in an operating pressure of 18 Torr. The dosing sequence was as follows: $Zr[N(CH_2CH_3)(CH_3)]_4$ for 2 min (delivered using 10 sccm of a He carrier gas), purge for 2 min with N_2, H_2O for 2 min (delivered using 10 sccm of a N_2 carrier gas), and finally purge for 2 min with N_2. The combined flow of purge (N_2) and carrier (He or N_2) gases through the two reactant inlet lines was always 20 sccm (the balance being 75 sccm of curtain gas N_2 flow). Once we had conducted the desired number of ALD cycles, the intermediate chamber was pumped down, first to a pressure of < 100 mTorr by a roughing pump, and then to < 10^{-6} Torr by a turbomolecular pump. During this time period the micro-reactor probe is also retracted and isolated from the intermediate chamber by closing a gate valve. The sample was then transferred to main chamber using the precision sample manipulator for surface analysis using XPS.

In Fig. 3-6 we consider a series of XP spectra taken on thin films of ZrO_2 deposited by ALD, where the samples were examined directly after growth, and no air-exposure of the samples had occurred. XPS is of course a surface-sensitive technique that probes the elemental composition and chemical states of the elements in a material. In Fig. 3-6(a) we display the XP spectrum of the Zr(3d) region for a thin film of ZrO_2 deposited on SiO_2 at 150 °C after 10 cycles of ALD. As may be seen, we clearly observe the $Zr(3d_{5/2})$ and $Zr(3d_{3/2})$ peaks with a spin-orbit doublet splitting of 2.4 eV [34], [35]. In addition, we find a binding energy for the $Zr(3d_{5/2})$ peak of 183.3 ± 0.1 eV, which is in good agreement with previous reports for ZrO_2 [36].
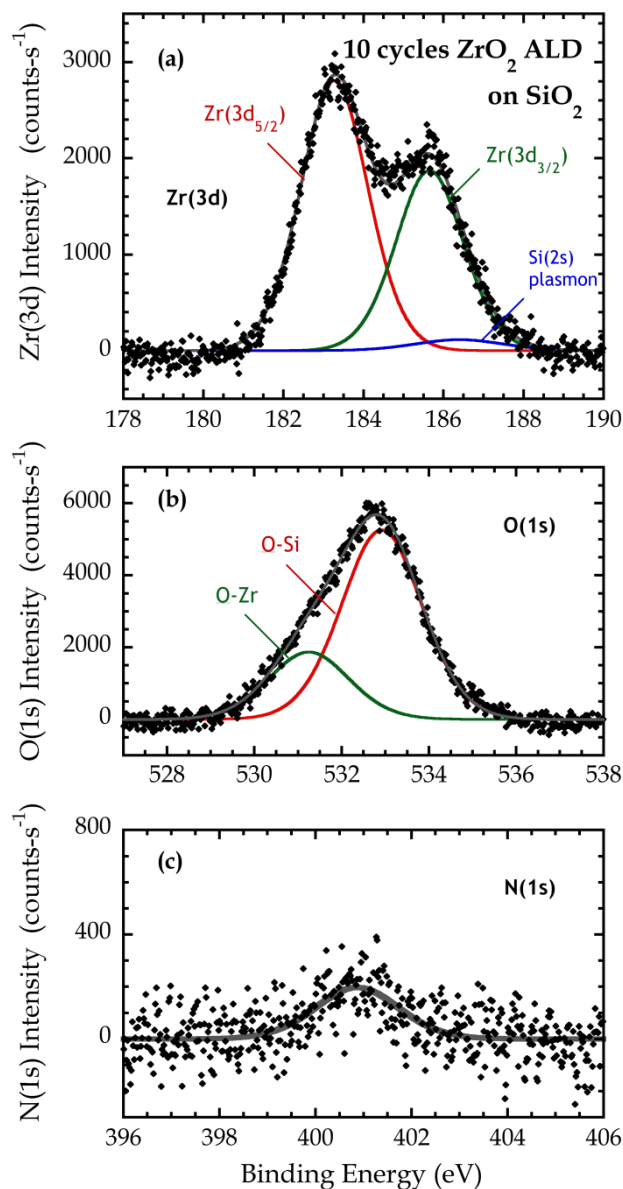
Figure 3-6: XP spectra of a SiO_2 surface after 10 cycles of ZrO_2 ALD, using $Zr[N(C_2H_5)(CH_3)]_4$ and H_2O as reactants. In **(a)** the $Zr(3d)$ peak is fit well to a doublet defined by a single binding energy. In **(b)** we fit the $O(1s)$ feature to two peaks, one representing O bound to Si in the substrate, and the other representing O bound to Zr in the thin film. In **(c)** we fit the $N(1s)$ feature to a single peak.

In Fig. 3-6(b) we display the XP spectrum of the O(1s) region for this same thin film of ZrO_2 deposited on SiO_2 at 150 °C after 10 cycles of ALD. As may be seen, the O(1s) feature is fit with two peaks, one at higher binding energy (532.9 ± 0.1 eV) and representing the underlying SiO_2 substrate, and another at lower binding energy (531.2 ± 0.1 eV) representing the ZrO_2 thin film. These values are in good agreement with previously reported values for the O(1s) peak for SiO_2 [37] and ZrO_2 [34]. We also have examined the N(1s) feature and these data are displayed in Fig. 3-6(c), and we observe a single peak at a binding energy of 399.5 ± 0.3 eV. Although detectable, this amount of N represents a sub-monolayer coverage of about ~ 0.07 ML if we compare this to the density of O found in crystalline ZrO_2.

In Fig. 3-7 we plot the integrated intensity of the Zr(3d) feature as a function of positon on the sample, similar to the procedure we used in connection with the data shown in Fig. 3-4. Here the step size varied between 0.254 and 0.508 cm. In Fig. 3-7 we have also indicated by the dashed line the results shown above in Fig. 3-4. As may be seen, here also we observe a flat top profile, and a drop in the intensity moving from the perimeter of the reaction zone to the effluent groove, indicating excellent confinement of the reaction to the central zone.

We have also examined thin films of ZrO_2 deposited on SiO_2 at 150 °C after 20 and 40 cycles of ALD, and we consider these results in Fig. 3-8. Here we plot the integrated intensities of the peaks representing the deposited thin film [Zr(3d)] and the substrate [Si(2p)] as a function of the number of ALD cycles.
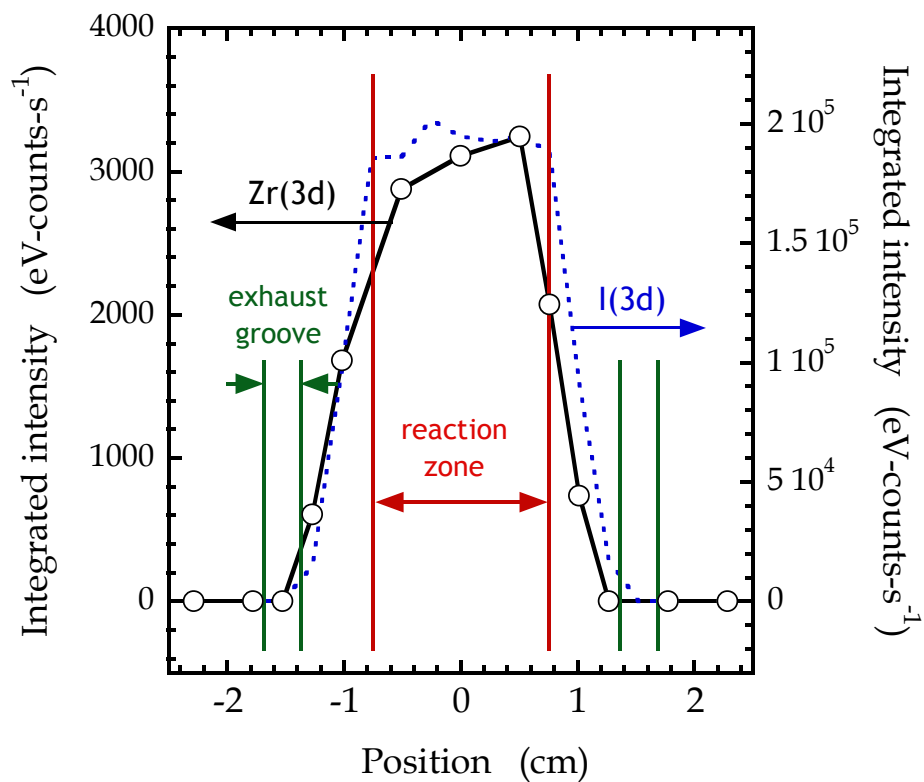
Figure 3-7: Intensity of the Zr(3d) peak from XPS as a function of the position on the sample, after 10 cycles of ZrO_2 ALD on a SiO_2 surface. The size of the central reaction zone, and the surrounding effluent exhaust grooves are also shown. We also duplicate the results shown in Figure 3-4 with the dashed line.
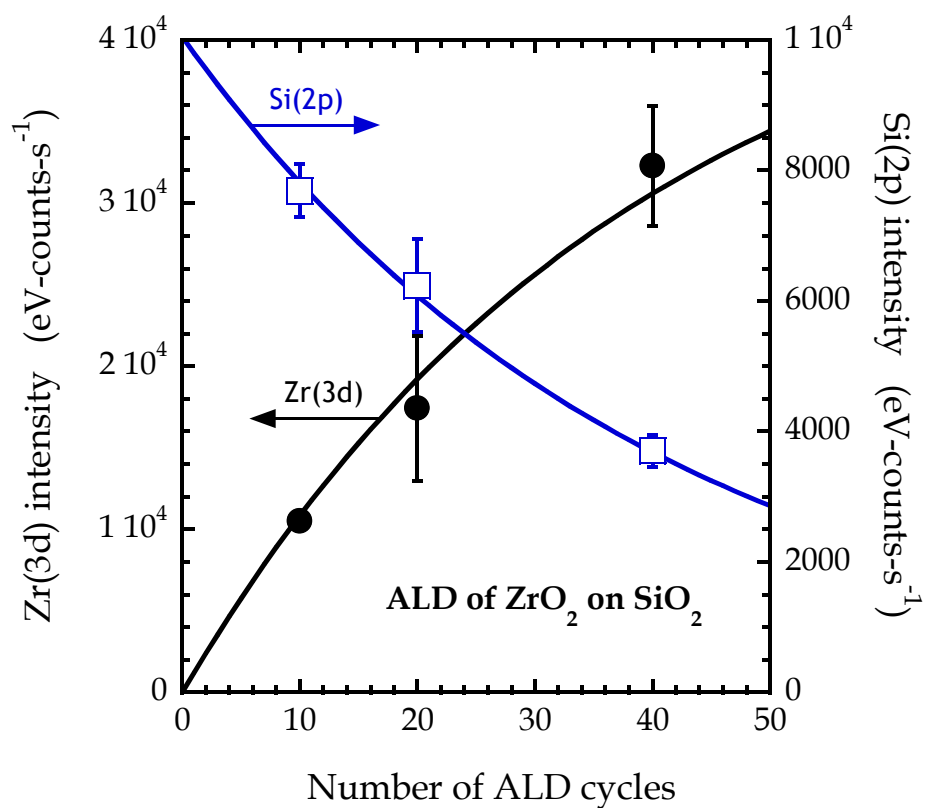
Figure 3-8: Integrated intensities of the Zr(3d) and Si(2p) peaks from XPS as a function of the number of ZrO_2 ALD cycles. The lines are a fit to a model that assumes growth of the ZrO_2 thin film is smooth and uniform over the SiO_2 surface.

As may be seen there is a continuous increase in the intensity of the Zr(3d) feature, and a continuous decrease in the intensity of the Si(2p) feature, consistent with expectations. We have fit these data to a simple model that assumes the growth rate per cycle is constant, and that a uniform 2D thin film of ZrO_2 is deposited on the SiO_2 substrate. In this case the integrated intensities will exhibit opposing exponential decays, and the decay constant for the two peaks will differ only by a factor that depends on the inelastic mean free path (IMFP) of the photoelectrons (which scales with the square root of the kinetic energy). The fit to this model is shown by the smooth curves in Fig. 3-8, and as may be seen this model describes the data quite well.

In addition to analysis by XPS similar to those shown in Fig. 3-6 and 3-8, we have also determined the thicknesses of the ZrO_2 thin films by employing *ex situ* spectroscopic ellipsometry (SE, Woollam VASE ellipsometer) after the samples were unloaded from the UHV chamber. The thickness of ZrO_2 film on SiO_2 was determined by the difference in the ellipsometric thickness between a bare chemical oxide and the $ZrO_2|SiO_2$ film. This analysis made use of the *n* and *k* values for ZrO_2 and SiO_2. We plot these results in Fig. 3-9 where we display the thickness of ZrO_2 films deposited on SiO_2 as a function of ALD cycles, measured by *ex situ* spectroscopic ellipsometry. We also plot the thicknesses predicted by the integrated intensities of both the Zr(3d) and Si(2p) peaks, using the same assumptions that went into the fit we displayed in Fig. 3-8.
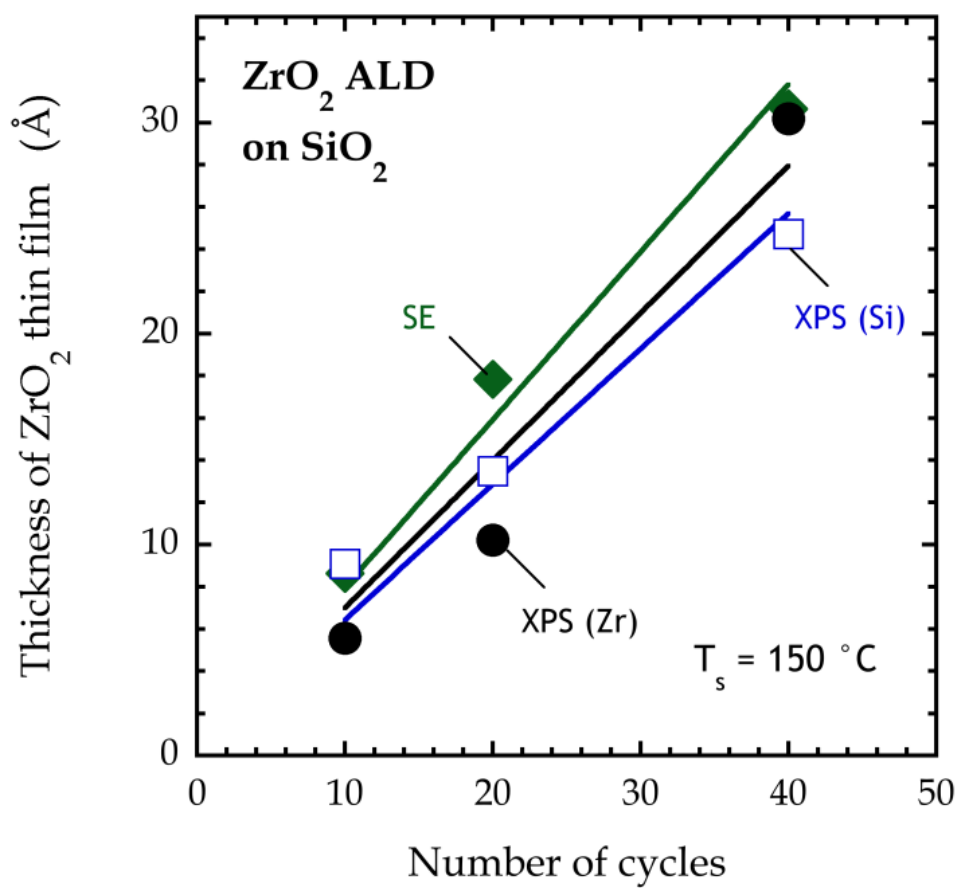
Figure 3-9: Thickness of the ZrO_2 thin film as a function of the number of ALD cycles, as measured by *ex situ* spectroscopic ellipsometry (green diamonds) and by *in situ* XPS of the thin film component (Zr, black circles) and the substrate component (Si, open blue squares). The lines are straight line fits that pass through the origin.

As may be seen, for all sets of data the thickness of ZrO_2 deposited grows linearly with the number of ALD cycles, and there is no indication of a nucleation delay[28], as the results are well described by a linear function passing through the origin. From SE, we find a rate of ~ 0.80 Å-cycle^{-1}, where from XPS we find rates of ~ 0.64-0.70 Å-cycle^{-1}. These values are similar to those reported previously for this same ALD process conducted under similar conditions, i.e., rates of ~ 0.9-1.1 Å-cycle^{-1} [38]–[41].

3.6 Conclusions

We have described the design, construction and performance evaluation of a micro-reactor probe that enables the study of gas-surface reactions at pressures on the order of 10 Torr, and subsequent *in situ* analysis of the surface under UHV conditions with no air-break. Our design makes use of the flow of a curtain gas to spatially confine the reactant species to a well-defined area on the substrate surface. Calculations using computational fluid dynamics determined the critical dimensions of the probe under typical reaction conditions necessary to achieve confinement and minimize out-diffusion of the reactant species to the surrounding UHV chamber. We evaluated the performance of the probe by examining two gas-surface reactions: (i) the adsorption of I_2 on a Cu surface, and (ii) the atomic layer deposition of ZrO_2 using a Zr amido compound and H_2O as the co-reactant. Confinement of the reactant species was verified by the use of *in situ* XPS, and the thickness of ZrO_2 deposited per cycle was consistent with results reported using conventional reactors designed for ALD. We anticipate that this design could be replicated

and retrofitted onto a variety of UHV systems that possess tools for *in situ* surface analysis,

but the lack the ability to study gas-surface reactions at low-to-medium vacuum conditions.

3.7 References

[1]   S. M. George, "Atomic layer deposition: An overview," *Chem. Rev.*, vol. 110, pp. 111–131, 2010.

[2]   M. Leskelä and M. Ritala, "Atomic layer deposition (ALD): from precursors to thin film structures," *Thin Solid Films*, vol. 409, no. 1, pp. 138–146, Apr. 2002.

[3]   C. Auth, C. Allen, A. Blattner, D. Bergstrom, M. Brazier, M. Bost, M. Buehler, V. Chikarmane, T. Ghani, T. Glassman, R. Grover, W. Han, D. Hanken, M. Hattendorf, P. Hentges, R. Heussner, J. Hicks, D. Ingerly, P. Jain, S. Jaloviar, R. James, D. Jones, J. Jopling, S. Joshi, C. Kenyon, H. Liu, R. McFadden, B. McIntyre, J. Neirynck, C. Parker, L. Pipes, I. Post, S. Pradhan, M. Prince, S. Ramey, T. Reynolds, J. Roesler, J. Sandford, J. Seiple, P. Smith, C. Thomas, D. Towner, T. Troeger, C. Weber, P. Yashar, K. Zawadzki, and K. Mistry, "A 22nm high performance and low-power CMOS technology featuring fully-depleted tri-gate transistors, self-aligned contacts and high density MIM capacitors," in *2012 Symposium on VLSI Technology (VLSIT)*, 2012, no. 2003, pp. 131–132.

[4]   C. H. Tsai, C. W. Yang, C. H. Hsu, C. M. Lai, K. Y. Lo, C. G. Chen, R. M. Huang, C. T. Tsai, L. S. Hung, J. W. You, W. H. Hung, T. F. Chen, O. Cheng, J. Y. Wu, S. F. Tzou, C. W. Liang, and I. C. Chen, "Characteristics of $HfZrO_x$ gate stack engineering for reliability improvement on 28nm HK/MG CMOS technology," in *Proceedings of Technical Program of 2012 VLSI Technology, System and Application*, 2012, pp. 1–2.

[5]   O. van der Straten, S. M. Rossnagel, J. P. Doyle, and K. P. Rodbell, "Metal-Organic

Atomic Layer Deposition of Metals for Applications in Interconnect Technology," in *ECS Transactions*, 2006, vol. 1, no. 10, pp. 51–56.

[6]   J. Beynet, P. Wong, A. Miller, S. Locorotondo, D. Vangoidsenhoven, T.-H. Yoon, M. Demand, H.-S. Park, T. Vandeweyer, H. Sprey, Y.-M. Yoo, and M. Maenhoudt, "Low temperature plasma-enhanced ALD enables cost-effective spacer defined double patterning (SDDP)," in *Proc. SPIE*, 2009, vol. 7520, p. 75201J.

[7]   A. J. M. Mackus, A. A. Bol, and W. M. M. Kessels, "The use of atomic layer deposition in advanced nanopatterning," *Nanoscale*, vol. 6, no. 2011, pp. 10941–10960, 2014.

[8]   D. W. Goodman, "Model Studies in Catalysis Using Surface Science Probes," *Chem. Rev.*, vol. 95, no. 3, pp. 523–536, May 1995.

[9]   A. R. Head, S. Chaudhary, G. Olivieri, F. Bournel, J. N. Andersen, F. Rochet, J.-J. Gallet, and J. Schnadt, "Near Ambient Pressure X-ray Photoelectron Spectroscopy Study of the Atomic Layer Deposition of TiO_2 on RuO_2 (110)," *J. Phys. Chem. C*, vol. 120, no. 1, pp. 243–251, Jan. 2016.

[10]   C. T. Campbell, "Studies of Model Catalysts with Well-Defined Surfaces Combining Ultrahigh Vacuum Surface Characterization with Medium- and High-Pressure Kinetics," *Adv. Catal.*, vol. 36, no. 1, pp. 1–54, 1989.

[11]   K. J. Park, D. B. Terry, S. M. Stewart, and G. N. Parsons, "In Situ Auger Electron Spectroscopy Study of Atomic Layer Deposition: Growth Initiation and Interface Formation Reactions during Ruthenium ALD on Si−H, SiO_2 , and HfO_2 Surfaces," *Langmuir*, vol. 23, no. 11, pp. 6106–6112, May 2007.

[12]   D. Goodman, R. D. Kelley, T. E. Madey, and J. T. Yates, "Kinetics of the

hydrogenation of CO over a single crystal nickel catalyst," *J. Catal.*, vol. 63, no. 1, pp. 226–234, May 1980.

[13]   D. W. Blakely, E. I. Kozak, B. A. Sexton, and G. A. Somorjai, "New instrumentation and techniques to monitor chemical surface reactions on single crystals over a wide pressure range (10^{-8} –10^5 Torr) in the same apparatus," *J. Vac. Sci. Technol.*, vol. 13, no. 5, pp. 1091–1096, Sep. 1976.

[14]   A. L. Cabrera, N. D. Spencer, E. Kozak, P. W. Davies, and G. A. Somorjai, "Improved instrumentation to carry out surface analysis and to monitor chemical surface reactions in situ on small area catalysts over a wide pressure range (10^{-8}– 10^5 Torr)," *Rev. Sci. Instrum.*, vol. 53, no. 12, pp. 1888–1893, Dec. 1982.

[15]   O. Sneh and S. M. George, "Sample manipulator employing a gas-thermal switch designed for high pressure experiments in an ultrahigh vacuum apparatus," *J. Vac. Sci. Technol. A Vacuum, Surfaces, Film.*, vol. 13, no. 2, pp. 493–496, Mar. 1995.

[16]   J. W. Elam, C. E. Nelson, R. K. Grubbs, and S. M. George, "Nucleation and growth during tungsten atomic layer deposition on SiO_2 surfaces," *Thin Solid Films*, vol. 386, no. 1, pp. 41–52, May 2001.

[17]   R. K. Grubbs, C. E. Nelson, N. J. Steinmetz, and S. M. George, "Nucleation and growth during the atomic layer deposition of W on Al_2O_3 and Al_2O_3 on W," *Thin Solid Films*, vol. 467, no. 1–2, pp. 16–27, Nov. 2004.

[18]   E. Langereis, S. B. S. Heil, H. C. M. Knoops, W. Keuning, M. C. M. van de Sanden, and W. M. M. Kessels, "In situ spectroscopic ellipsometry as a versatile tool for studying atomic layer deposition," *J. Phys. D. Appl. Phys.*, vol. 42, no. 7, p. 73001, Apr. 2009.

[19] R. Methaapanon, S. M. Geyer, C. Hagglund, P. A. Pianetta, and S. F. Bent, "Portable atomic layer deposition reactor for in situ synchrotron photoemission studies," *Rev. Sci. Instrum.*, vol. 84, no. 1, p. 15104, Jan. 2013.

[20] S. K. Selvaraj, G. Jursich, and C. G. Takoudis, "Design and implementation of a novel portable atomic layer deposition⁄chemical vapor deposition hybrid reactor," *Rev. Sci. Instrum.*, vol. 84, no. 9, p. 95109, Sep. 2013.

[21] T. Weiss, M. Nowak, U. Mundloch, V. Zielasek, K. Kohse-Höinghaus, and M. Bäumer, "Design of a compact ultrahigh vacuum-compatible setup for the analysis of chemical vapor deposition processes," *Rev. Sci. Instrum.*, vol. 85, no. 10, p. 104104, Oct. 2014.

[22] J. Dendooven, E. Solano, M. M. Minjauw, K. Van de Kerckhove, A. Coati, E. Fonda, G. Portale, Y. Garreau, and C. Detavernier, "Mobile setup for synchrotron based in situ characterization during thermal and plasma-enhanced atomic layer deposition," *Rev. Sci. Instrum.*, vol. 87, no. 11, p. 113905, Nov. 2016.

[23] W. Lei, L. Henn-Lecordier, M. Anderle, G. W. Rubloff, M. Barozzi, and M. Bersani, "Real-time observation and optimization of tungsten atomic layer deposition process cycle," *J. Vac. Sci. Technol. B Microelectron. Nanom. Struct.*, vol. 24, no. 2, p. 780, 2006.

[24] L. Henn-Lecordier, W. Lei, M. Anderle, and G. W. Rubloff, "Real-time sensing and metrology for atomic layer deposition processes and manufacturing," *J. Vac. Sci. Technol. B Microelectron. Nanom. Struct.*, vol. 25, no. 1, p. 130, 2007.

[25] P. Ryan Fitzpatrick, Z. M. Gibbs, and S. M. George, "Evaluating operating conditions for continuous atmospheric atomic layer deposition using a multiple slit

gas source head," *J. Vac. Sci. Technol. A Vacuum, Surfaces, Film.*, vol. 30, no. 1, p. 01A136, 2012.

[26] P. Poodt, D. C. Cameron, E. Dickey, S. M. George, V. Kuznetsov, G. N. Parsons, F. Roozeboom, G. Sundaram, and A. Vermeer, "Spatial atomic layer deposition: A route towards further industrialization of atomic layer deposition," *J. Vac. Sci. Technol. A Vacuum, Surfaces, Film.*, vol. 30, no. 1, p. 10802, 2012.

[27] S. E. Roadman, N. Maity, J. N. Carter, and J. R. Engstrom, "Study of thin film deposition processes employing variable kinetic energy, highly collimated neutral molecular beams," *J. Vac. Sci. Technol. A Vacuum, Surfaces, Film.*, vol. 16, no. 6, p. 3423, Nov. 1998.

[28] K. J. Hughes and J. R. Engstrom, "Nucleation delay in atomic layer deposition on a thin organic layer and the role of reaction thermochemistry," *J. Vac. Sci. Technol. A Vacuum, Surfaces, Film.*, vol. 30, no. 1, p. 01A102, 2012.

[29] W. Zhang, R. K. Nahm, P. F. Ma, and J. R. Engstrom, "Probing ultrathin film continuity and interface abruptness with x-ray photoelectron spectroscopy and low-energy ion scattering," *J. Vac. Sci. Technol. A Vacuum, Surfaces, Film.*, vol. 31, no. 6, p. 61101, 2013.

[30] W. Zhang and J. R. Engstrom, "Effect of substrate composition on atomic layer deposition using self-assembled monolayers as blocking layers," *J. Vac. Sci. Technol. A Vacuum, Surfaces, Film.*, vol. 34, no. 1, p. 01A107, Jan. 2016.

[31] D. R. Stull, "Vapor Pressure of Pure Substances. Organic and Inorganic Compounds," *Ind. Eng. Chem.*, vol. 39, no. 4, pp. 517–540, Apr. 1947.

[32] L. T. Zhuravlev, "Concentration of hydroxyl groups on the surface of amorphous

silicas," *Langmuir*, vol. 3, no. 3, pp. 316–318, 1987.

[33] D. Monnier, I. Nuta, C. Chatillon, M. Gros-Jean, F. Volpi, and E. Blanquet, "Gaseous Phase Study of the Zr-Organometallic ALD Precursor TEMAZ by Mass Spectrometry," *J. Electrochem. Soc.*, vol. 156, no. 1, p. H71, 2009.

[34] C. Morant, J. M. Sanz, L. Galán, L. Soriano, and F. Rueda, "An XPS study of the interaction of oxygen with zirconium," *Surf. Sci.*, vol. 218, no. 2–3, pp. 331–345, Aug. 1989.

[35] D. Majumdar and D. Chatterjee, "X-ray photoelectron spectroscopic studies on yttria, zirconia, and yttria-stabilized zirconia," *J. Appl. Phys.*, vol. 70, no. 1991, pp. 988–992, 1991.

[36] Y. Zhou, N. Kojima, H. Sugiyama, K. Ohara, and K. Sasaki, "Preparation of ZrO2 ultrathin films as gate dielectrics by limited reaction sputtering — On growth delay time at initial growth stage," *Appl. Surf. Sci.*, vol. 254, no. 19, pp. 6131–6134, Jul. 2008.

[37] D. S. Jensen, S. S. Kanyal, N. Madaan, M. A. Vail, A. E. Dadson, M. H. Engelhard, and M. R. Linford, "Silicon (100)/SiO$_2$ by XPS," *Surf. Sci. Spectra*, vol. 20, no. 1, pp. 36–42, Dec. 2013.

[38] D. M. Hausmann, E. Kim, J. Becker, and R. G. Gordon, "Atomic layer deposition of hafnium and zirconium oxides using metal amide precursors," *Chem. Mater.*, vol. 14, no. 14, pp. 4350–4358, 2002.

[39] B. Lee, K. J. Choi, A. Hande, M. J. Kim, R. M. Wallace, J. Kim, Y. Senzaki, D. Shenai, H. Li, M. Rousseau, and J. Suydam, "A novel thermally-stable zirconium amidinate ALD precursor for ZrO$_2$ thin films," *Microelectron. Eng.*, vol. 86, no. 3,

pp. 272–276, Mar. 2009.

[40]   T. Keuter, G. Mauer, F. Vondahlen, R. Iskandar, N. H. Menzler, and R. Vaßen, "Atomic-layer-controlled deposition of TEMAZ/O$_2$–ZrO$_2$ oxidation resistance inner surface coatings for solid oxide fuel cells," *Surf. Coatings Technol.*, vol. 288, pp. 211–220, Feb. 2016.

[41]   J. Provine, P. Schindler, J. Torgersen, H. J. Kim, H.-P. Karnthaler, and F. B. Prinz, "Atomic layer deposition by reaction of molecular oxygen with tetrakisdimethylamido-metal precursors," *J. Vac. Sci. Technol. A Vacuum, Surfaces, Film.*, vol. 34, no. 1, p. 01A138, Jan. 2016.

4. Three-dimensional modeling and the design of a high-throughput micro-reactor by computational fluid dynamics

4.1 Overview

Spatial confinement with the use of supersonic molecular beam and a custom micro-reactor of the Engstrom research group design has been previously reported. A comparison between the two deposition techniques that can be carried out in a shared ultrahigh vacuum chamber system was presented concerning the cause of the spatial confinement, the spot size and the range of the operating pressure. A revised probe head design in the micro-reactor system for an obround deposition spot based on the concentric model was simulated in a three-dimension modeling using computational fluid dynamics. We confirmed that relevant reaction conditions were produced on the substrate surface with suppressed out-diffusion by 3-4 orders of magnitudes in the new design. We also adopted a probe head design with a flat, planar end surface, as compared to that with a chamfered surface, due to an improved operating efficiency. The new probe head design holds promise for terraced film growth at an operating pressure ~ 10 Torr.

4.2 Introduction

While most commercial tools for thin film deposition provides uniform growth across the entire substrate, spatially-confined thin-film deposition, combined with the system geometry, provides an efficient means to study the evolution of thin film growth.

Roadman and co-workers made use of the highly collimated nature of the supersonic molecular beam for a set of terraces of Si thin film of varying thickness on a "half-moon" wafer, a Si wafer with half of the area thermally oxidized [1]. Hughes and co-workers continued the work that exploits the nature of the supersonic molecular beam and deposited terraced films of chemical vapor deposition (CVD) Co using dicobalt hexacarbonyl tert-butylacetylene (CCTBA) on Ta substrates for Co/Ta interficial studies [2]. We note that rigorous position calibration of the nozzle is essential to an ideal beam spot. CCTBA has been readily utilized in CVD processes for depositing Co metal films [3], [4] and cobalt silicides films [5], [6]. ALD chemistries for cobalt oxide and Co metal films are also reported [7], [8]. Thompson and co-workers recently revealed selective area Co ALD on metals over dielectrics with the use of alcohol pre-treatment on a pattern substrate [9].

In addition to the supersonic molecular beam, we recently unveiled a design of a micro-reactor (see Chapter 3) that incorporates with an ultra-high vacuum chamber for spatially-confined atomic layer deposition (ALD) at ~ 10 Torr and *in situ* surface characterization with a potential for depositing terraced ALD films. The schematics of the two thin-film deposition systems are illustrated in Fig. 4-1. While the supersonic molecular beam can generate highly collimated beam and can be used for terraced film growth at high vacuum ($p \sim 10^{-6}$ Torr), there exist some kinetics that cannot be observed at such a low pressure. By contrast, the current, concentric design of the micro-reactor allows for spatially-confined thin-film deposition at a reactor pressure of ~ 10 Torr.

Moreover, a custom platen that can hold two adjacent, rectangular substrates (~ 3.0 cm × 1.0 cm) has been designed and used for depositing thin films on two surfaces simultaneously (i.e. with identical experimental conditions) using the custom-designed

micro-reactor. With proper modification of the spot generated, terraced films on two surfaces could be deposited at 'high' pressure ($p \sim$ 1-10 Torr) by the micro-reactor and be characterized by *in situ* XPS. Furthermore, we only need to re-design the micro-reactor head while keeping all other components unchanged in renovating the micro-reactor system, which could save significant cost and time, because the micro-reactor system comprises three individual components: a precision machined head, a fluidic extension piece and a fluidic and electrical feedthrough.

We first demonstrate and contrast the spatial confinement effect in the two systems, supersonic molecular beam and the micro-reactor, using a CVD Co process, followed by a new obround probe design and the evaluation of its performance using computational fluid dynamics (CFD) method.
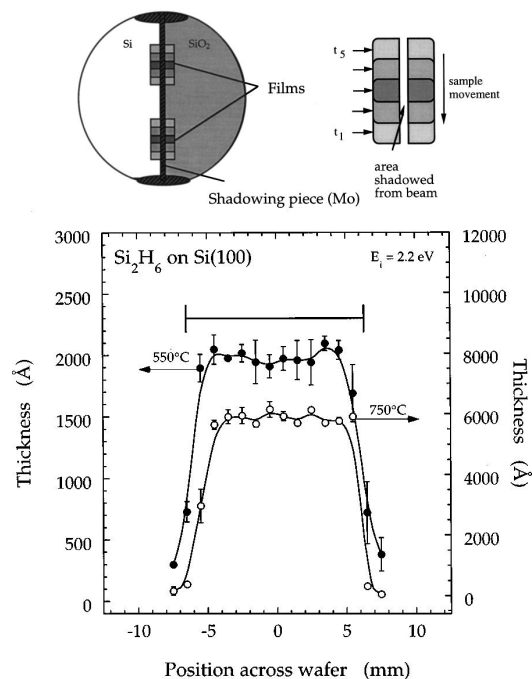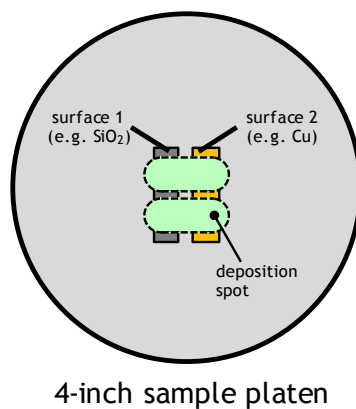
Figure 4-1: (a) Upper panel: Arrangement employed to measure the kinetics of thin film growth. Sample shown here is patterned to expose half of the underlying silicon of a thermally oxidized wafer, a so-called ''half moon'' sample. Lower panel: Lateral thickness distribution of a thin film deposited at fixed incident beam kinetic energy [1]. **(b)** Schematic representation of deposition of confined obround spots on two adjacent substrates using the micro-reactor system.

4.3 Spatially-confined CVD Co films: a case study

Recent work on calibrating the supersonic molecular beam of the 312 chamber system for generating confined beam spots of CVD Co using CCTBA as Co precursor is reported. A collimated molecular beam of CCTBA was generated by passing ultra-high purity 35 sccm He through a stainless steel bubbler that contains CCTBA (bubbler temperature set at 40 °C) and expanding the resulting mixture through a heated 150 μm nozzle into the lower chamber in the 312 system. Beam exposure time was set at 10 mins using the shutter. The schematic of the setup of the supersonic molecular beam in the 312 chamber system is displayed in Fig. 4-2. Before careful calibration of the nozzle position, an off-centered CVD Co film was deposited inhomogeneously at the lower-left corner of the Ta substrate, determined both experimentally by *in situ* XPS and visually in Fig. 4-3 and Fig. 4-4(a).
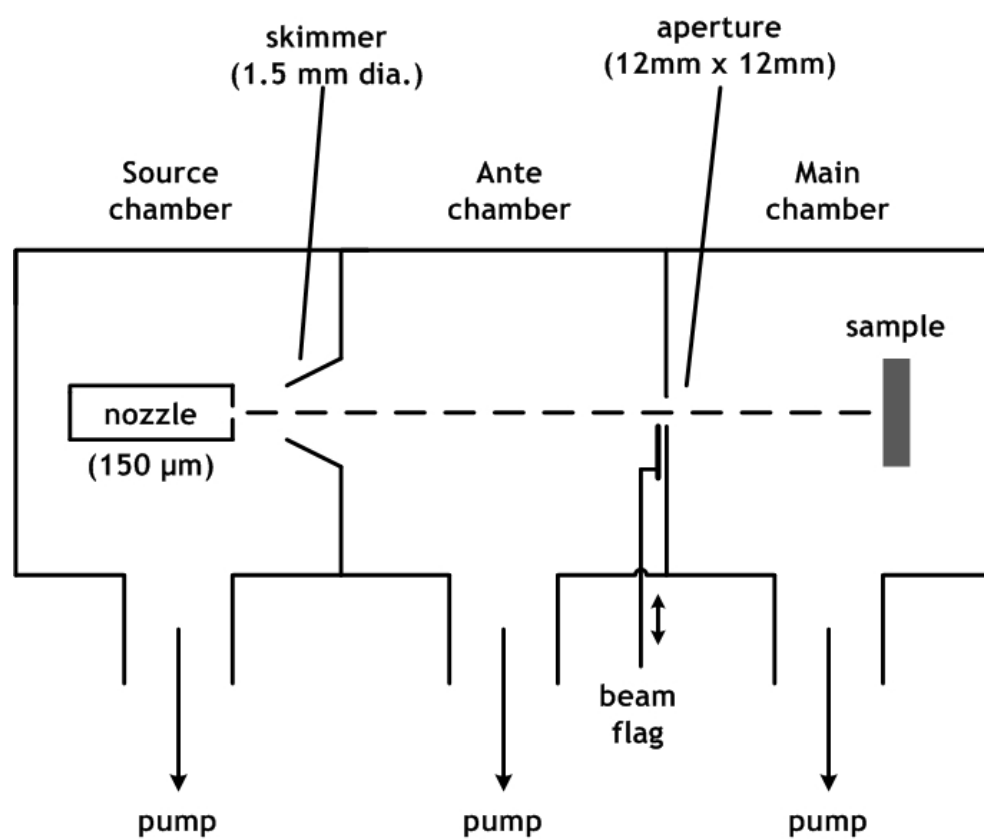
Figure 4-2: Schematic representation of the supersonic molecular beam system.
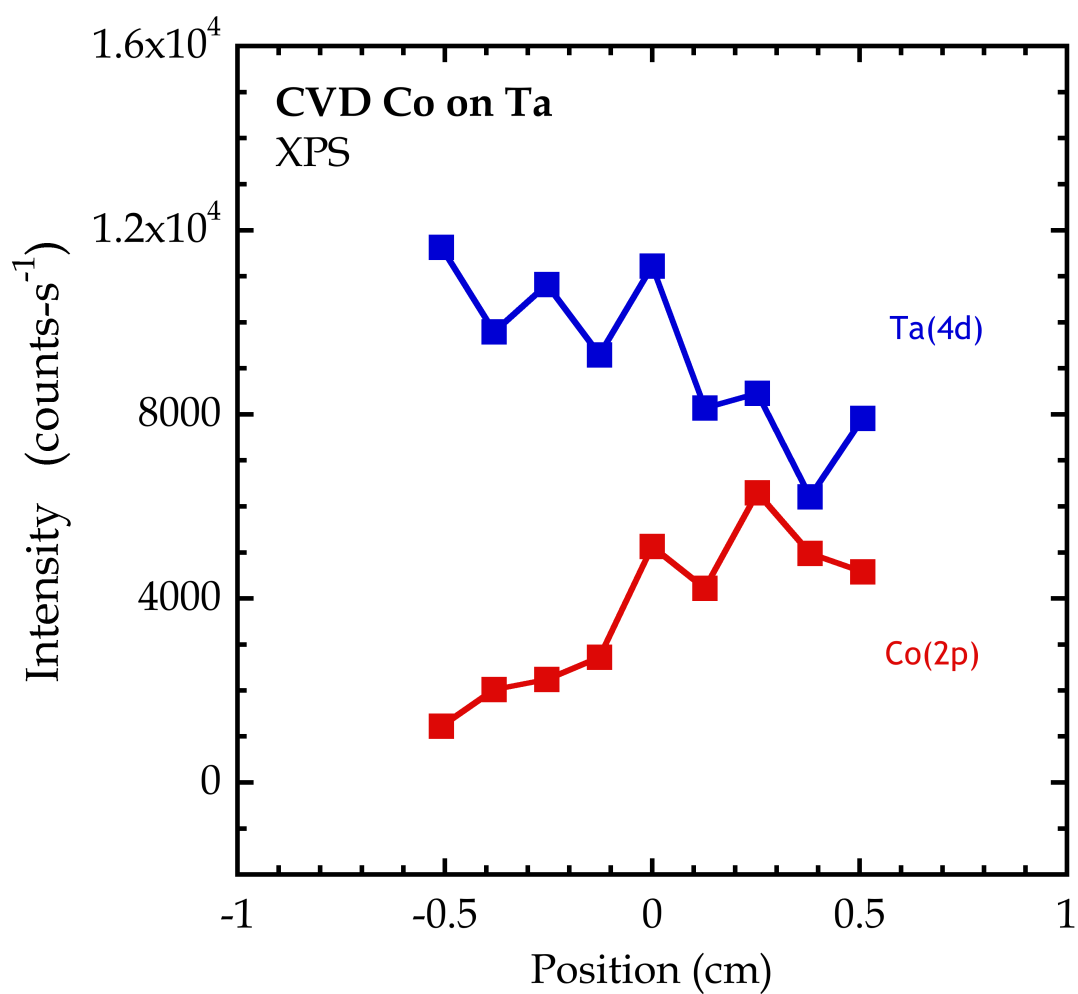
Figure 4-3: XPS for CVD Co on Ta: line scan across the substrate surface displaying Co(2p) and Ta(4d) integrated intensity as a function of position.
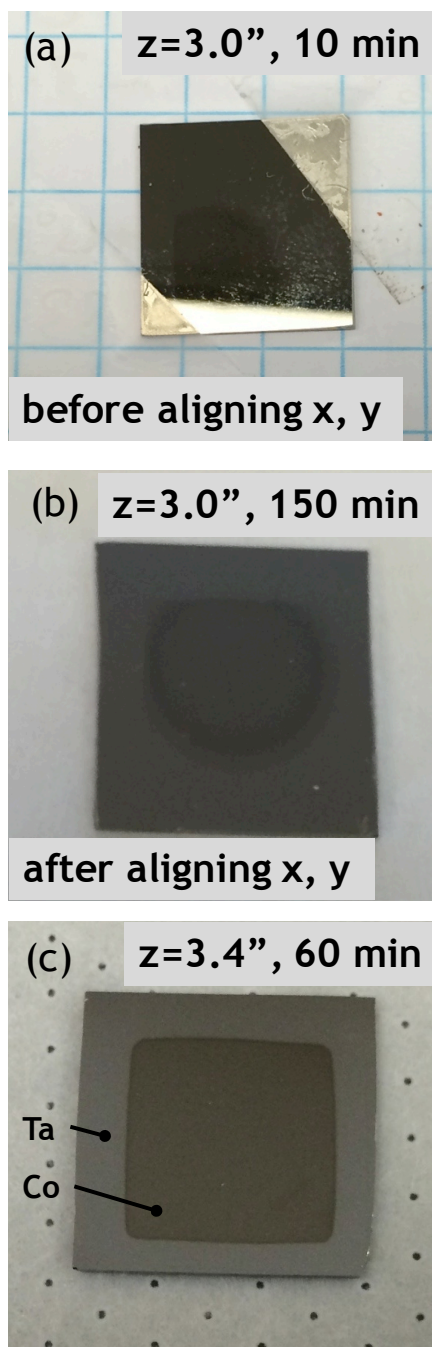
Figure 4-4: photographs of the CVD Co deposition spot using supersonic molecular beam. **(a)** 10 mins exposure at $Z = 3.0$ and uncalibrated X and Y positions. **(b)** 150 mins exposure at $Z = 3.0$ and calibrated X and Y positions. **(c)** 60 mins exposure at $Z = 3.4$ and calibrated X and Y positions.

We first calibrated X and Y axes of the supersonic molecular beam in mass spectrometry experiments. A beam of 15 sccm Ar, aligned with the ionized region of the mass spectrometer, is generated with QMS intensity at monitored m/z = 40. X and Y positions are determined by maximizing the signal from the Ar beam. This method is more accurate than monitoring/maximizing the chamber pressure, which could lead to imprecise calibration. Z position has to do with the nozzle-skimmer distance and therefore changing it results in different signal-to-background ratio in QMS. As a result, Z position of the supersonic molecular beam was calibrated using modulated Ar direct beam in another set of mass spectrometry experiments. The modulation of the Ar beam by the shutter was confirmed by tracking the QMS intensity of Ar at m/z = 40 while opening then closing the shutter. When the shutter is closed (t < 2.5 mins and t > 6 mins), the 'background' QMS intensity is low because the beam access is terminated and only a fraction of Ar due to scattering is detected by mass spectrometer. The plateau intensity when the shutter is open represents the contribution from both the direct beam and the background scattering. The intensities with the shutter open and closed are recorded with different Z positions [shown in Fig. 4-5(b)], and the beam-to-background ratios are calculated in each case [shown in Fig. 4-5(c)].
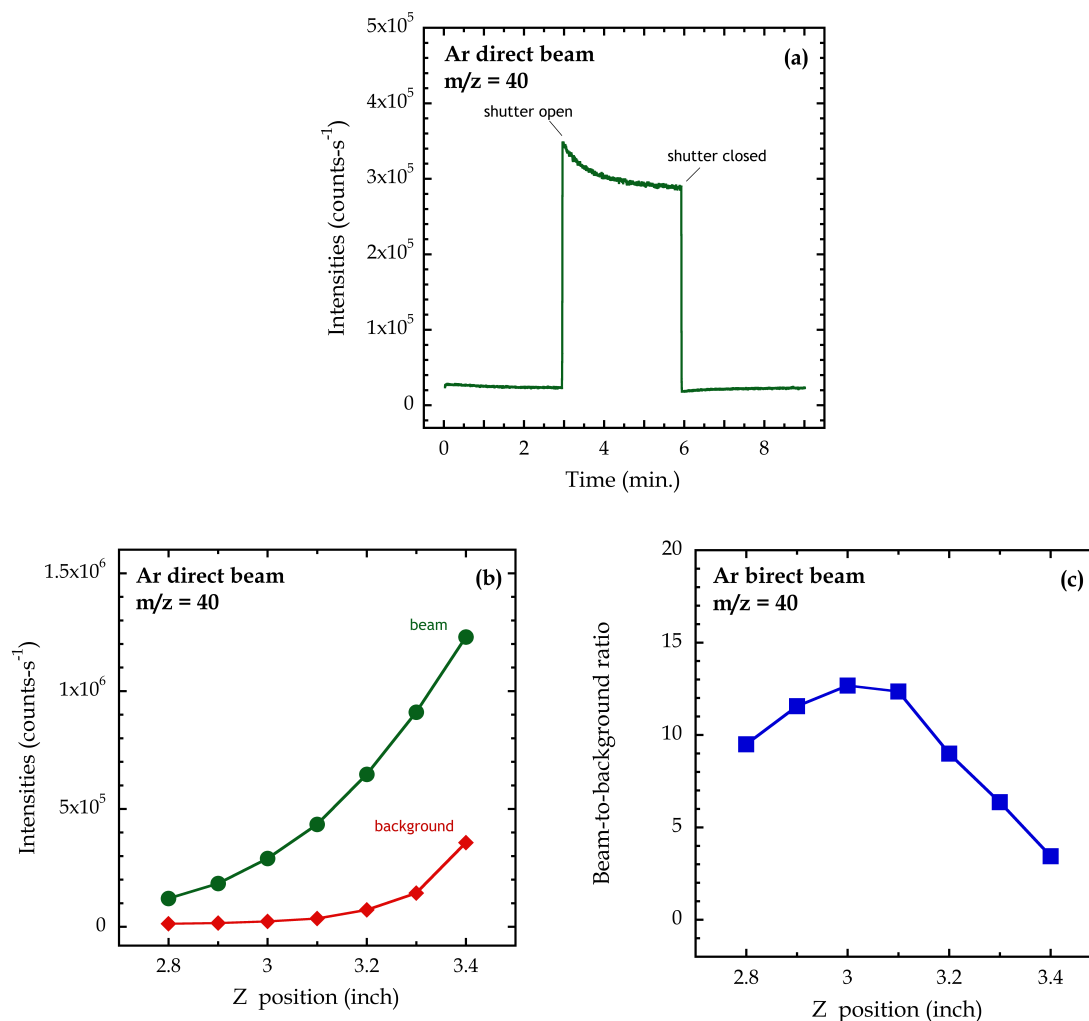
Figure 4-5: (a) QMS intensity at m/z = 40 (Ar) as a function of time. In this experiment the beam shutter was opened from ~ 3 min to 6 min. **(b)** QMS intensities at m/z = 40 in the case of shutter on ("beam intensity") and of the shutter off ("background intensity") as a function of Z position (on axis) of the nozzle. **(c)** Beam-to-background ratio as a function of Z position (on axis) of the nozzle.

After position calibration, deposition of CVD Co film on a Ta substrate (T_s = 160 °C) was conducted using a collimated beam of CCTBA (T_b = 40 °C) seeded in 35 sccm He for 150 mins. The 1.7×1.7 cm^2 Ta substrate, prepared by depositing ~ 1200 Å PVD Ta on cleaned SiO_2/Si(100) via sputtering, is pre-annealed at 350 °C for an hour before the experiment. The spatial confinement of the beam spot, shown in Fig. 4-4(b) is visually examined. While the beam spot is centered, the deposited Co film is inhomogeneous, as can be seen from the gradient at the lower half of the substrate. This could result from the insufficient dose of CCTBA as the beam gets through the skimmer. We inspected the Co film deposited with a shorter nozzle-skimmer distance (moving the nozzle toward the skimmer by ~ 1 cm, at a final Z position of 3.4") and compared to that at Z = 3.0". In Fig. 4-4(c) we can clearly see a spatially-confined beam spot of CVD Co in uniform color (~ 1.2 cm × 1.2 cm).

For example, CVD Co film that is spatially confined on ~1200 Å PVD Ta substrate can be carried out using the micro-reactor for delivering CCTBA | 35 sccm He flow for 1 min at a reactor pressure of ~18 Torr. In Fig. 4-6 we display results from XPS where we have translated the substrate such as to produce a line scan, i.e., the integrated intensity of the Co(2p) peak as a function of position. We can clearly see that the deposition of CVD Co is confined within the exhaust groove and has a plateau region within the reaction zone (~ 1.5 cm in diameter).
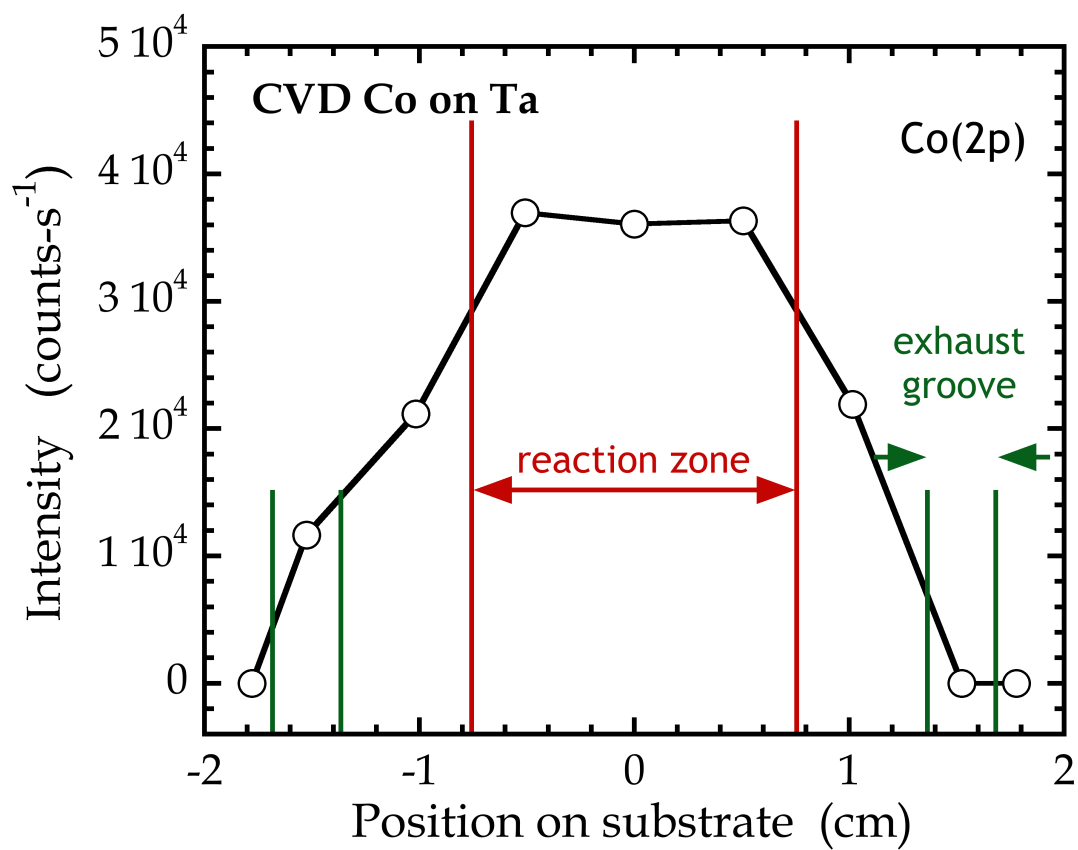
Figure 4-6: XPS Co(2p) integrated intensity as a function of vertical position on the Ta sample.

4.4 Design and construction

The hardware upgrade in this work only includes the revised design of the micro-reactor head, and the rest of the micro-reactor / UHV chamber system stays the same. It is therefore important to have the new probe head compatible to the sample platen and the central fluidic feedthrough. As a result, the position and the height of the four physical stops at the end face is identical to the first-generation concentric design. The side that is in contact with the central fluidic feedthrough has the same dimension as that in the previous design. Tapped holes for vented screws, empty space for spring-loaded electrical probes and the overall dimension of the head (~ 5.6 cm in dia., and 2.5 cm in height) are unchanged in order to preserve all the desired functions.

In Fig. 4-7 detailed dimensions and the three-dimensional model (constructed in AutoCAD 2017) of the new obround probe are displayed. This reaction zone has a height above the substrate surface of ~ 0.5 cm, an obround base with a width of 1.0 cm (along the "short axis") and a length of 2.5 cm (along the "long axis"), equivalent to a volume of ~ 1.2 cm^3. These three gas lines provide the ability to control the introduction of three independent species to the reaction zone. The final two gas lines are connected to two peripheral grooves (with an arc of 15° as a separator at each side) that are machined into the end of the probe. The two lines act together to provide the exhaust lines for the micro-reactor. The central, obround cylinder (referred to as the reaction zone) within the probe head is surrounded by a thin wall of ~ 0.3 cm thick (outer dimension ~ 2.8 cm × 1.3 cm), an exhaust region of ~ 0.6 cm wide (outer dimension ~ 3.4 cm × 1.9 cm) and a region with chamfered or flat surfaces of the probe of ~ 2.5 cm wide (outer dimension ~ 5.9 cm × 4.3

cm). Details of the central fluidic feedthrough, the mounting flange and the reactant delivery system are thoroughly described in Chapter 3.

4.5 Simulation and optimization of the design of the micro-reactor probe

4.5.1 Simplified model for the micro-reactor probe and CFD calculations

A three-dimensional CFD model was constructed for the second generation of the micro-reactor head design, in contrast to the two-dimensional model reported in Chapter 3. While a horizontal band that are long enough to cover both surfaces and wide enough to overlap is of the most ideal shape, it is very different from the circular spot out of the current setup of a cylindrical reaction zone. An obround, consisting of a rectangle bracketed by two semicircles, is used as an alternative to the ellipse in the CFD model. A reactor design that produces an obround spot has all the advantages from the rectangular spot as well as the feasibility to model in computational fluid dynamics (CFD) as it is geometrically closer to the circular shape we previously modeled. However, constructing an obround cylinder as the reaction zone in COMSOL Multiphysics breaks the radial symmetry that was assumed in the current design of the micro-reactor. Expanding the geometry into a three-dimensional one requires more computationally expensive calculation for numerical solutions that describe the flow behaviors within the new design of the reactor.
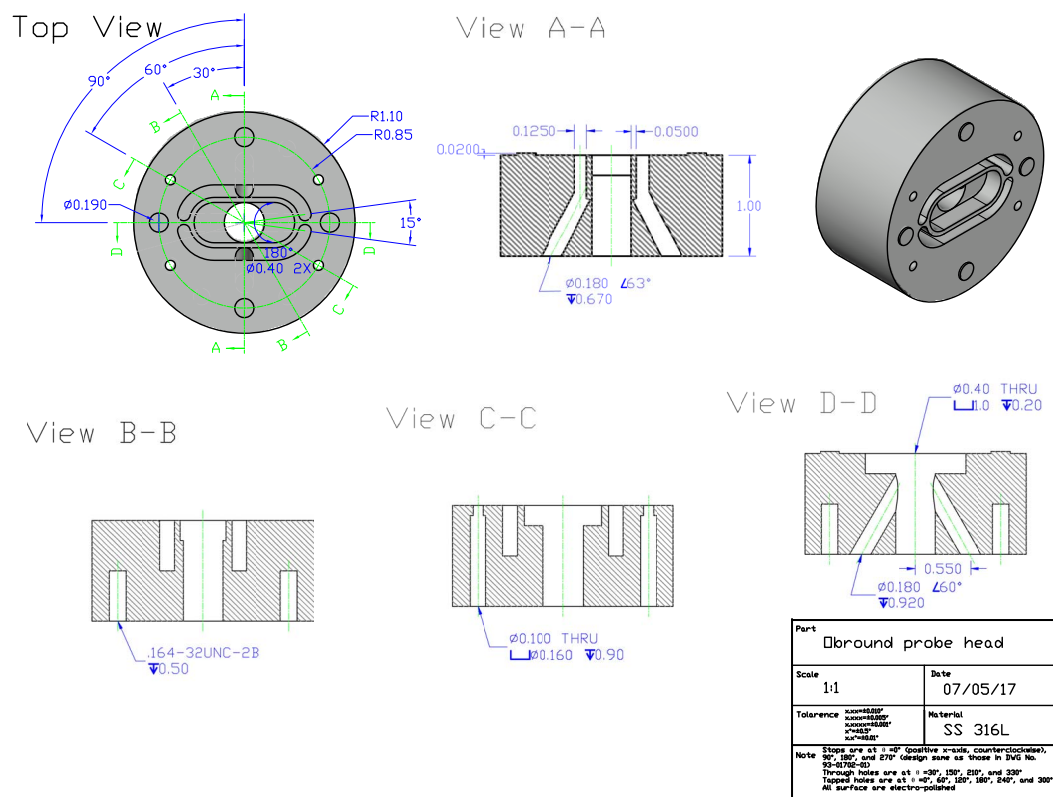
Figure 4-7: Schematic representation and cross-sectional diagrams of the new obround probe

A design of a micro-reactor head for an obround spot that has a height of 1.0 cm and a width of 2.5 cm was constructed in AutoCAD (version 2017), illustrated in Fig. 4-8. The simplified model consists of a cylindrical planar substrate, a cylindrical sample heater and a cylindrical chamber that surrounds the former two (all of same dimensions as the concentric model described). The AutoCAD model was reduced to a quarter for more efficient meshing and computation by introducing two planes of symmetry with proper symmetric boundary conditions. The micro-reactor probe head (outside radius ~ 3.25 cm, height of ~ 2.1 cm) includes one common central feed (an obround cylinder, width of ~2.5 cm and height of ~1.0 cm) for all input species (reactants, carrier and purge) and an annular exhaust channel (width of ~ 0.3 cm). There are two inlets for inert gas on this surrounding chamber, which represent the injection points of the curtain gas (of same dimensions as the concentric model). In this approach, the curtain gas flows radially inward between the small gap (~ 0.1 cm) between the substrate surface, and flows out the annular region in the probe head to the exhaust, along with the reactant and purge flows.

Dimensions of the core region consisting of the obround cylinder, the exhaust region and the region with chamfered or flat surfaces are fully described in Section 4.4. The chamfered surface is dished in a way such that the gap is greatest (~ 0.3 cm) at the annular exhaust region, whereas the flat surface has a constant gap of ~ 0.1 cm between the probe head and the planar substrate. We first constructed the three-dimensional model of two different geometries: one with chamfering and one without. The effect of chamfering is first evaluated by the performance of the models in steady states. We then operate the transient models in the two geometries for the first ALD cycle at various reactor pressures and compare the results to those in the steady states.
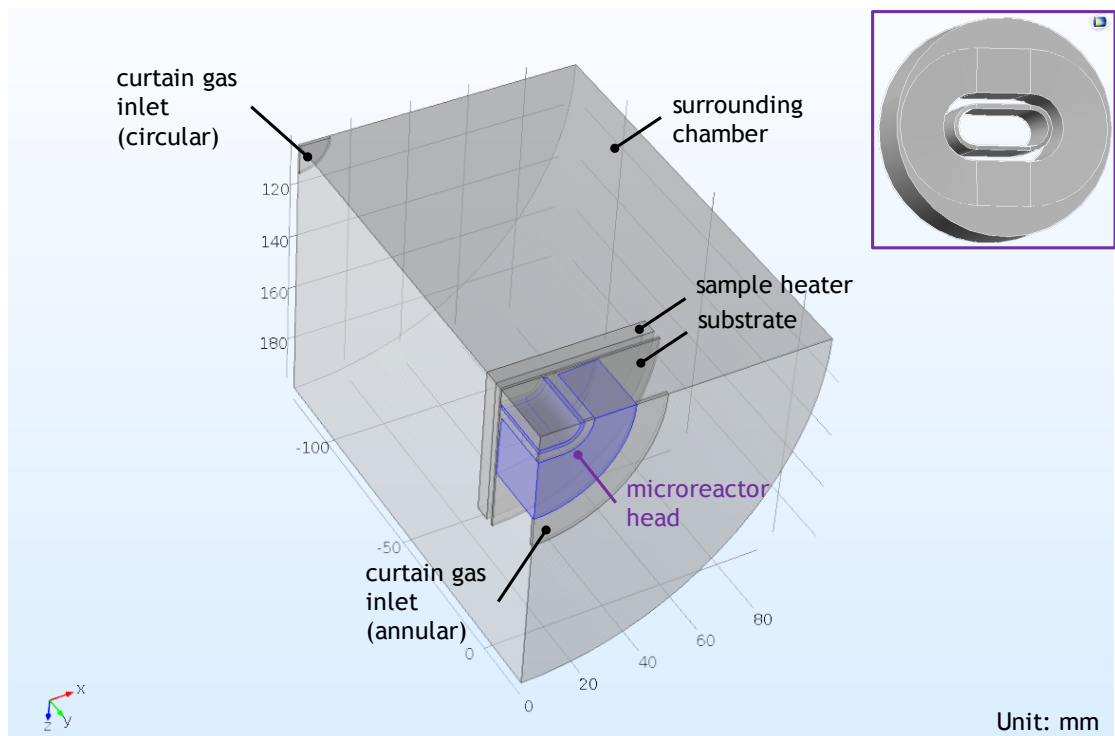
Figure 4-8: Three-dimensional CFD model in COMSOL Multiphysics. Inset: the chamfered end face of the obround probe head design.

COMSOL Multiphysics (version 4.5), a CFD package based on finite element method, is used to simulate the behavior of the multi-component, isothermal, compressible laminar flow in the obround probe. "Transport for concentrated species" is chosen as the module that describes the mass transport phenomena. Mass transport and fluid flow are coupled due to the composition dependence of the viscosity and the pressure dependence of the diffusivity [10]. The domain was discretized into many triangular subdomains that are physical-defined.

4.5.2 Results at steady-state

We first carried out CFD calculations that are assumed to be time-independent with the flat or the chamfered surface of the probe. The flow rate of the reactant gas (assumed to be pure H_2O) through the common central tube was set to 10 sccm, while the flow at the two inlets for the curtain gas (assumed to be pure N_2) were set to be 50 sccm each. The entire system is set at a fixed temperature of 150 °C, and the reactor was operated at ~ 10 Torr by fixing the exhaust pressure at the end of the effluent groove to be exactly 10 Torr. In this calculation we evaluated the effectiveness of the design of the micro-reactor probe by the two following criteria: (i) is the gas-phase reactant well-confined within the reaction zone and produces partial pressure for vapor deposition? (ii) is the out-diffusion of the reactants to the surrounding sub-chamber minimized? In Fig. 4-9 we displayed the surface plot of the steady-state mole fraction of water on the substrate surface for the case with the chamfered surface [Fig. 4-9(a)] and for the case with the flat surface [Fig. 4-9(b)].
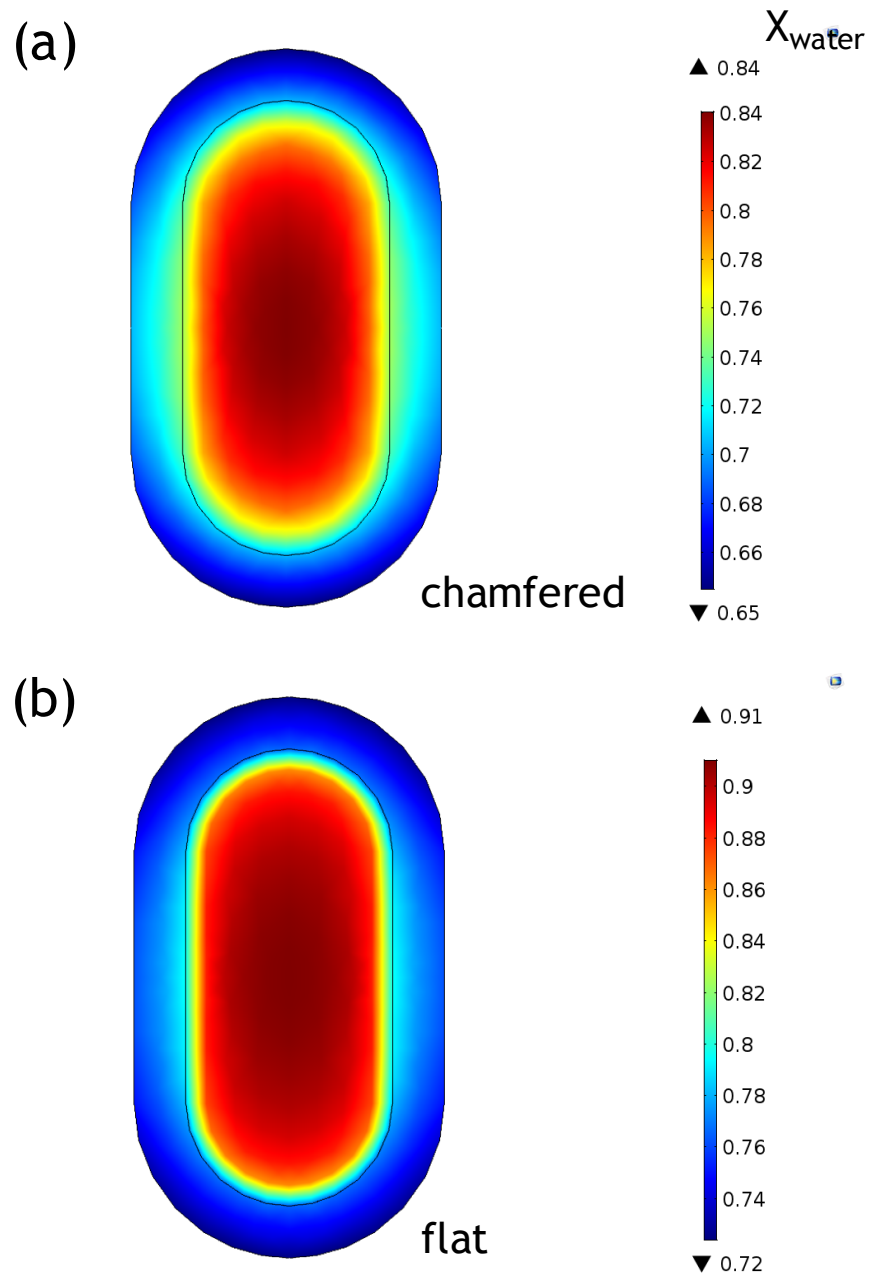
Figure 4-9: Simulated steady-state water mole fraction profiles on the substrate surface in the probe head design of **(a)** a chamfered surface and **(b)** of a flat surface.

The two regions on the substrate area corresponded to the reaction zone (and the thin wall) and the exhaust region of the probe, respectively. As may be seen in both cases the mole fraction within the reaction zone was sufficiently high (> 0.8), and it started to drop near the boundary of the two regions. The case of a flat surface has a greater maximum value of mole fraction of water (0.91) than that in the case of a chamfered surface (0.84), and the average mole fraction in the reaction zone indicated the same (0.89 for the flat surface vs. 0.81 for the chamfered surface). Moreover, the average mole fraction of water at the surface of the surrounding chamber is 3.6×10^{-3} for the chamfered surface and 6.0×10^{-3} for the chamfered surface, which also indicated that the design with a flat surface is favored due to less out-diffusion ($\sim 40\%$ lower) of the gas reagent that could contaminate the UHV chamber and a 3 orders-of-magnitude reduction in the amount of water reaching chamber walls as compared to that on substrate surface.

4.5.3 Results under conditions of sequential flows

We also have conducted CFD calculations in a transient mode that is more representative of the ALD processes. Like in the concentric model, the transient, obround model includes two steps: the first step calculates the steady-state velocity of the inert flow, and the second step considers the calculation of the alternating flows from the central feed line. The following sequence of inlet flow compositions is adopted: N_2 (1 s), Xe (1 s), N_2 (2 s), H_2O (1 s) and N_2 (2 s), to represent one full ALD cycle. We note that the dosing pattern of short pulses of the reactants followed by long purge pulses is expected to lower the amount of out-diffusion to the walls of the surrounding chamber, as compared to steady state. In Fig. 4-10(a) we display the mole fraction of the two reactants as a function of time,

average over the substrate surface in a 2×2 matrix of the process conditions (the reactor pressure of 1 Torr / 10 Torr $\times$ the geometry of flat / chamfered surface). As may be seen, we observe square-wave like profiles of water and xenon fractions at 1 Torr, as compared to curves with profound dynamics at 10 Torr. This suggests that a longer dose time may be required for operating at 10 Torr, due to a lower rate of mass transport. We note that this pressure effect is regardless of the detailed geometry (i.e. chamfered or flat surfaces), and this could be explained by an enhanced rate of diffusion due to the pressure dependence of the diffusivity (inversely proportional to pressure). The peak values of water and xenon fractions in each half cycle are augmented in the case of low reactor pressure and of flat surface.

Although there are observable differences concerning the mole fractions of the gas reagents on the substrate surface, exposures in all four cases displayed here are of the same order of magnitude (~ 0.5 to 0.8 for Xe and ~ 0.7 to 1.0 for H_2O) and are efficient for vapor deposition processes to the substrate. Moreover, the fact that a greater exposure is achieved in the water dose than in the xenon dose can be justified also by different rate of diffusion: a $\sim 50\%$ higher diffusivity of H_2O in N_2 than that for Xe in N_2.

In Fig. 4-10(b) we display the mole fraction of the two reactants as a function of time, average over the surfaces of the surrounding chamber in the same matrix of the process conditions. We observed oscillation of water and xenon fractions in all four cases, which was also the case for the water partial pressure in the concentric model. The peak values of the fractions in the first cycle are $\sim 10^{-3} - 10^{-4}$ among the four cases studied here. 3-4 orders of magnitude reduction in the amount of reactants, in contrast to ~ 8 orders of magnitude in the concentric model could be partially explained by a longer dose time in

the obround model. However, the reduced diffusion barrier along the 'long axis' of the obround probe is more probable to be held responsible to a less desired performance. As a result, the path of least resistance for the curtain gas flowing in toward the exhaust is along the long axis. This did not occur in the concentric model because of the radial symmetry.

Peak values of water and xenon fractions in each half cycle are reduced in the case of high reactor pressure and of flat surface. The adverse effect of the chamfering on the performance of the obround micro-reactor at the both the substrate surface and surrounding chamber walls strongly suggests that a reactor design with chamfered surfaces is unfavored. Also, 10 Torr is chosen as the operating pressure as the amount of out-diffusion of xenon and water is ~10 times lower than that in 1 Torr. In Fig. 4-11 we displayed the surface plot of the mole fraction of water on the substrate surface during the xenon pulse [Fig. 4-11(a)] and during the water pulse [Fig. 4-11(b)] for the case with the flat surface. As may be seen well-confined, efficient partial pressures of the reactants were established within the reaction zone, which allows for effective surface reactions.
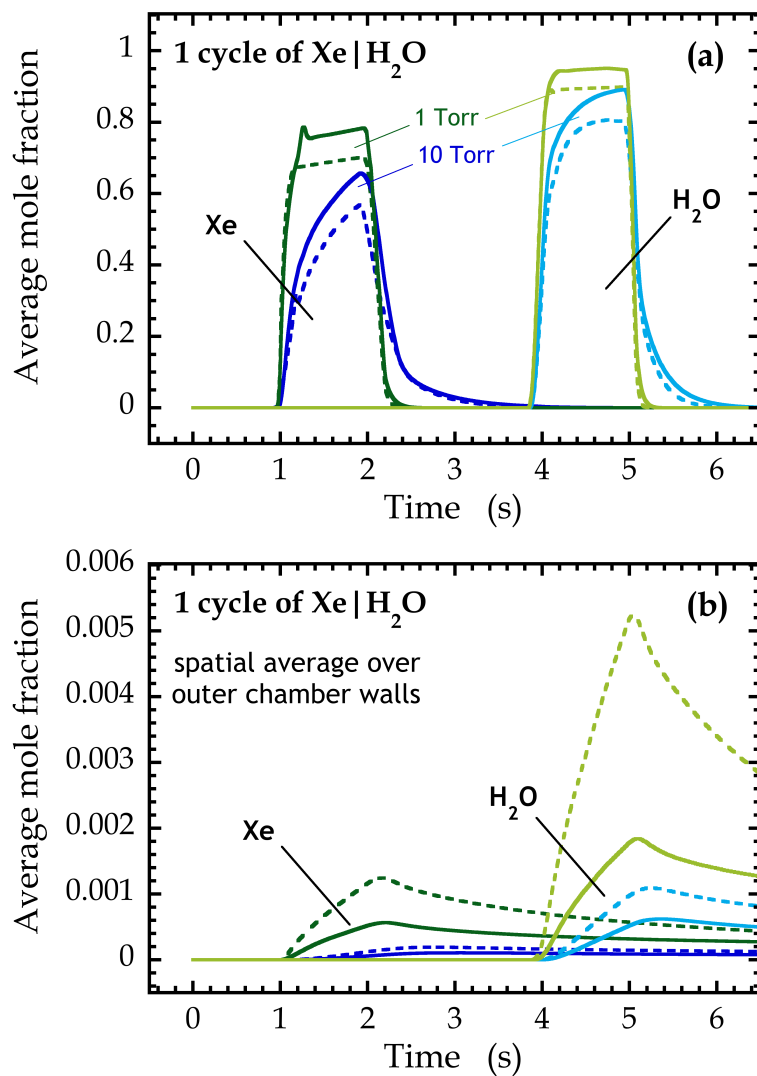
Figure 4-10: Average mole fraction of xenon and water **(a)** on substrate surface and **(b)** on surrounding chamber walls under various experimental conditions. Blue curves represents models operated at a pressure of 10 Torr (blue curves for xenon and light-blue for water), and green curves represents models operated at 1 Torr. Solid and dashed lines represent results of "no chamfering" and "with chamfering", respectively.
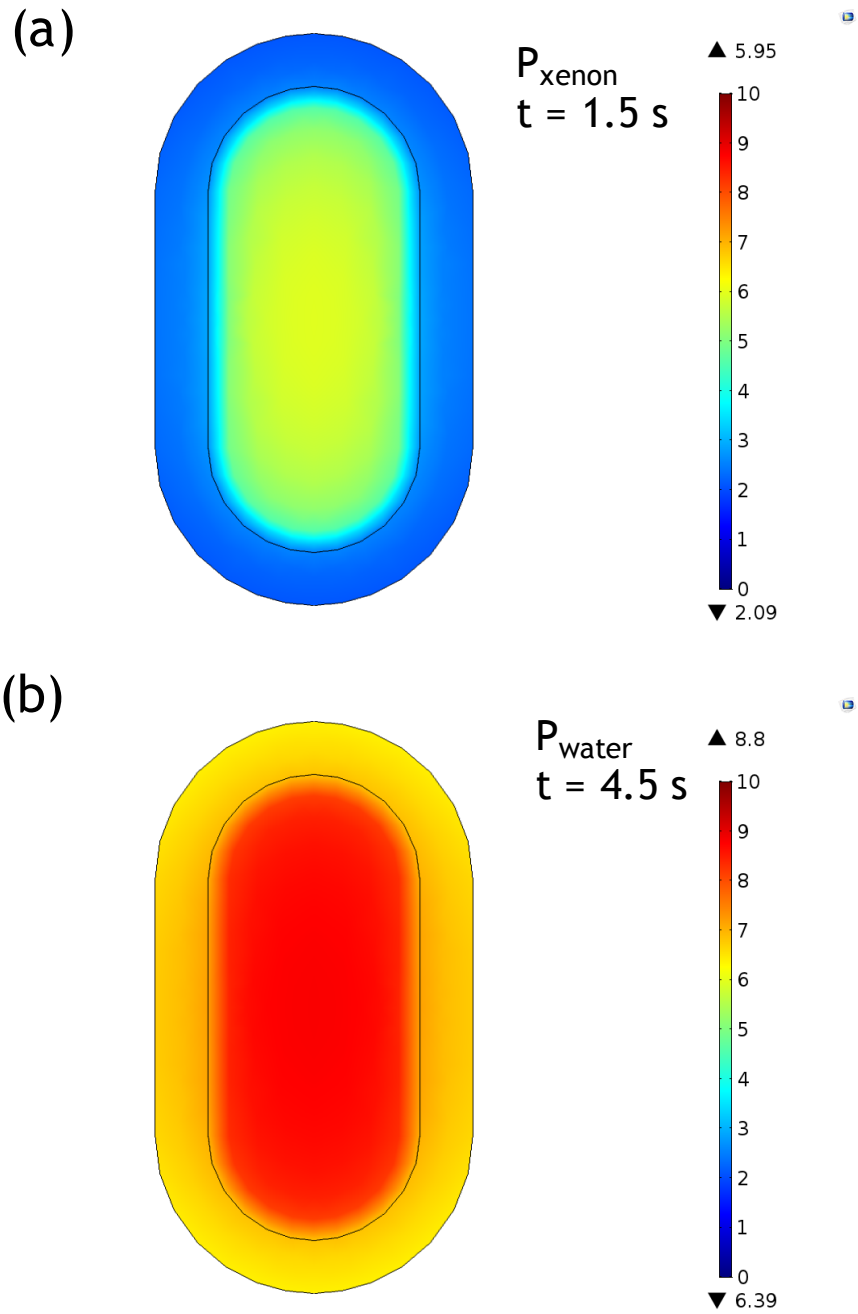
Figure 4-11: (a) Simulated xenon mole fraction profile on the substrate surface in the xenon half cycle (t = 1.5 min) in the probe head design of a flat surface. **(b)** Simulated water mole fraction profile on the substrate surface in the water half cycle (t = 4.5 min) in the probe head design of a flat surface.

4.6 Conclusions

The experimental setup for spatially-confined film growth using two different *in situ* deposition techniques in 312 chamber system are reviewed. We exploited the highly-collimated behavior of the hyperthermal molecular beam from the supersonic molecular beam technique and spatial confinement from the micro-reactor for terraced film growth. A CVD Co process is carried out using both deposition techniques, and confined Co spots are observed on Ta substrate by *in situ* XPS in both cases. A micro-reactor head for an obround deposition spot (2.5 cm × 1.0 cm) and for terraced film growth has been designed and simulated in a three-dimensional model using a CFD commercial package. We showed a 3-4 orders-of-magnitude reduction in the amount of the reactant reaching to the surrounding chamber as compared to that on substrate surface in both stationary and transient modes. A probe head design with a flat, planar end surface is preferred for an enhanced exposure to the substrate surface and a reduced out-diffusion to surrounding chamber walls, as compared to that with a chamfered surface. Future work could include multiple ALD cycles in the transient model rather than just the one cycle, inclusion of the heating element and non-isothermal flow, and further optimization of the probe geometry.

4.7 References

[1] S. E. Roadman, N. Maity, J. N. Carter, and J. R. Engstrom, "Study of thin film deposition processes employing variable kinetic energy, highly collimated neutral molecular beams," *J. Vac. Sci. Technol. A Vacuum, Surfaces, Film.*, vol. 16, no. 6, p. 3423, Nov. 1998.

[2] K. J. Hughes, Ph. D. dissertation, Cornell University, 2011.

[3] H. K. Jung, H. B. Lee, M. Tsukasa, E. Jung, J. H. Yun, J. M. Lee, G. H. Choi, S. Choi, and C. Chung, "Formation of highly reliable Cu/low-k interconnects by using CVD Co barrier in dual damascene structures," *IEEE Int. Reliab. Phys. Symp. Proc.*, pp. 307–311, 2011.

[4] T. Nogami, J. Maniscalco, A. Madan, P. Flaitz, P. DeHaven, C. Parks, L. Tai, B. St. Lawrence, R. Davis, R. Murphy, T. Shaw, S. Cohen, C.-K. Hu, C. Cabral, S. Chiang, J. Kelly, M. Zaitz, J. Schmatz, S. Choi, K. Tsumura, C. Penny, H.-C. Chen, D. Canaperi, T. Vo, F. Ito, O. Straten, A. Simon, S.-H. Rhee, B.-Y. Kim, T. Bolom, V. Ryan, P. Ma, J. Ren, J. Aubuchon, J. Fine, P. Kozlowski, T. Spooner, and D. Edelstein, "CVD Co and its application to Cu damascene interconnections," in *2010 IEEE International Interconnect Technology Conference*, 2010, no. 111, pp. 1–3.

[5] B. Lee, K. J. Choi, A. Hande, M. J. Kim, R. M. Wallace, J. Kim, Y. Senzaki, D. Shenai, H. Li, M. Rousseau, and J. Suydam, "A novel thermally-stable zirconium amidinate ALD precursor for ZrO_2 thin films," *Microelectron. Eng.*, vol. 86, no. 3, pp. 272–276, Mar. 2009.

[6] S. B. Kang, H. S. Kim, K. J. Moon, W. H. Sohn, G. H. Choi, S. H. Kim, N. J. Bae,

U. I. Chung, and J. T. Moon, "CVD-cobalt for the next generation of source/drain salicidation and contact silicidation in novel MOS device structures with complex shape," *IEEE Int. Electron Devices Meet. 2003*, p. 20.6.1-20.6.4, 2003.

[7]   K. Bernal Ramos, M. J. Saly, and Y. J. Chabal, "Precursor design and reaction mechanisms for the atomic layer deposition of metal films," *Coord. Chem. Rev.*, vol. 257, no. 23–24, pp. 3271–3281, Dec. 2013, and references therein.

[8]   B. Han, K. H. Choi, K. Park, W. S. Han, and W.-J. Lee, "Low-Temperature Atomic Layer Deposition of Cobalt Oxide Thin Films Using Dicobalt Hexacarbonyl tert-Butylacetylene and Ozone," *Electrochem. Solid-State Lett.*, vol. 15, no. 2, pp. D14–D17, Jan. 2011.

[9]   F. Q. Liu, M. Chang, and D. Thompson, U.S. Patent No. 145,738 A1 (2016).

[10]   E. N. Fuller, P. D. Schettler, and J. C. Giddings, "A New Method for Prediction of Binary Gas-Phase Diffusion Coefficients," *Ind. Eng. Chem.*, vol. 58, no. 5, pp. 18–27, May 1966.

5. Effects of co-adsorbates on chemisorption of tetrakis(ethylmethylamino) zirconium on SiO$_2$ and Cu in atomic layer deposition of zirconium oxide

5.1 Overview

Selective area atomic later deposition (ALD) can play an important role in addressing numerous challenges as the downscaling of semiconductor devices continues. In this study we investigate how an additional, third species in conventional ALD process, with a focus on the first half cycle, affects the precursor-substrate interaction on dielectric and metal surfaces via competitive adsorption. A kinetic model of competitive adsorption suggests that higher partial pressure of the co-adsorbate and lower substrate temperature facilitate the suppression of metal precursor adsorption. Among several amines and thiols employed as co-adsorbates, half of these show promise concerning selective area growth. For example, 1,2-ethanedithiol [HS(CH$_2$)$_2$SH, EDT] can effectively block the nucleation of Zr, resulting from chemisorption of tetrakis(ethylmethylamido)zirconium(IV), on Cu surface, while having moderated nucleation on a SiO$_2$ surface under the same reaction conditions. Post-reaction analysis using XPS shows that a sulfur-containing species is present on the Cu surface, capable of blocking nucleation, whilst this species is absent on SiO$_2$. Co-exposure of TEMAZ with triethylamine [N(CH$_2$CH$_3$)$_3$, TEA] also produces a desirable result concerning selectivity: nucleation is observed on SiO$_2$, somewhat attenuated, while no nucleation is observed on Cu surface. In this case, analysis by XPS shows no evidence for irreversibly adsorbed species on the Cu surface; thus, the effect of TEA is transient in nature. From the TEA / TEMAZ co-exposure experiments at different

substrate temperatures, the observed temperature dependence of competitive adsorption, less nucleation of TEMAZ as the substrate temperature increases, further corroborates the proposed mechanism of adsorption reversal. The process space of TEA / TEMAZ ratio and substrate temperature is established and may suggest a route to future selective area ZrO_2 ALD studies.

5.2 Introduction

Atomic layer deposition (ALD) is a thin-film deposition technique which provides precise and conformal growth of oxides, nitrides and noble metals by alternating exposure of the substrate to thin film precursor with self-limiting chemistry and the co-reactant at a relatively low substrate temperature compared to other existing deposition techniques. The desired properties of ALD films give rise to various applications of ALD in fabrication of nanoscale semiconductor devices. For example, ALD chemistries for high-k dielectric materials such as ZrO_2 have been developed as an outstanding candidate for gate dielectrics with low leakage current [1]–[3].

Recently the development of selective area growth has been identified as an important challenge concerning single-digit nanometer technologies in 2015 International Technology Roadmap for Semiconductors. Over the past several years a number of groups have been pursuing a variety of approaches for selective chemical vapor deposition [4], [5], selective ALD [6], [7] (Fig. 5-1) and selective epitaxial growth [8]–[10].
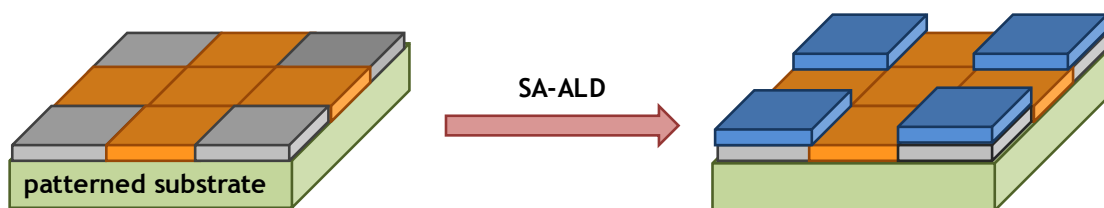
Figure 5-1: Schematics of selective area ALD on a patterned substrate.

The most traditional approach is perhaps to employ etch step following the deposition step. Lift-off, like other methods discussed below, eliminates etching steps and achieve selective growth by depositing thin film on the pre-patterned photoresist layer. Most approaches taken to date concerning selective area growth have involved the use of masking layers consisting of photoresists or self-assembled monolayers (SAMs) that can be prepared in both liquid phase [11]–[14] and vapor phase [15]–[19] and by microcontact printing [20]–[22]. While some success has been achieved with this approach, there are a number of disadvantages intrinsic to these methods. First, it is very difficult for SAMs to form a defect-free layer due to both intrinsic (e.g., dynamics of SAM deposition) and extrinsic factors (e.g., substrate preparation) [23]. It has been shown that the defects in the SAM layer serve as the nucleation sites for the subsequent ALD film growth [24]. Previous studies also reported takes long preparation time (> hrs) in liquid phase to form good quality of closely-packed SAMs on a planar surface [14], [24], [25]. Complex topography of a non-planar substrate, such as that of finEFTs, makes the formation of SAMs with a high packing density even more challenging. Ekerdt and co-workers showed that defects of SAMs are formed at the corners of the fabricated nanoline that has an aspect ratio of ~1.5, resulting in nucleation of TiN ALD films on HfO_2 surface [26]. Compatibility of SAMs to current manufacturing processes in the semiconductor industry, such as plasma-enhanced and high-temperature processes, is poor, and post-deposition treatment, such as sputter etch [27] and/or thermal desorption [28], is required to remove all the SAMs from the surface before the succeeding steps. Finally, and perhaps more important, these masking layers themselves must be patterned or deposited selectively.

111

A second approach to selective area ALD relies on intrinsic differences of reactivities between starting surfaces. While this approach is, to a certain degree, manifested by substrate-dependent growth rates of several ALD chemistries reported [29]–[31], it, unfortunately, may be limited to a few special cases [32]–[36]. Cho *et al.* reported selective TiO_2 ALD on SiO_2 over H-terminated Si based on the innate chemical differences, which are supported by the DFT calculations that revealed unfavored energetics of chemisorption of Ti precursor on H-terminated Si [30]. Fundamental understanding of the interfacial phenomena is crucial to developing techniques for selective film growth beyond the intrinsic reactivity / selectivity. It is well recognized that nucleation is the key process in the early stages of ALD film growth on different surfaces. Interfacial chemistry, the film growth mode and its growth rate in the initial nucleation period (*aka* heterodeposition) can be very different from those in the steady-state growth of bulk film (*aka* homodeposition) [29]. Therefore, charaterization of the surface / interface *in situ* is crucial to understanding the early stages of heterodeposition, for instance the nucleation, adhesion and island growth [37]. It is also pointed out that the size and the density of the nanoparticle is controlled by the SAM formation time (and thus the density of active sites) during the nucleation period of Platinum ALD [24].

Interestingly, Elam and co-workers reported similar behavior in substrate pre-treatment of trimethylaluminum, a third species that is not involved in the conventional Palladium ALD cycles [38]. Yanguas-Gil et al. reported a reduction of density of active sites by surface functionalization that modulates the precursor-substrate reactivity via pre-dosing the surface inhibitor, including alcohols, ketones and carboxylic acids, during ALD reactions [39].

112

The idea of co-dosing an additional inhibitor species in the gas phase during the reaction for surface site blocking can also be applied in tuning CVD growth characteristics. Abelson and co-workers showed that vinyltrimethylsilane is used to block CVD Cu growth on thermal SiO_2 [5], [40], [41]. Ekerdt and co-workers proposed that competitive adsorption of the Ru precursor and an additional species (carbon monoxide or ammonia) is the underlying cause for resulting smoother Ru CVD films [42]–[44]. These observations are essentially representation of the phenomenon of competitive adsorption that Langmuir discovered in 1922 [45]. There have been previous studies on the modulation and area selectivity of the ZrO_2 ALD processes with a third species involved. Elam and co-workers reported a 50% reduction in the growth rate of ZrO_2 ALD by incorporating an additional step of pre-dosing ethanol in a conventional ALD cycle comprising of tetrakis(dimethylamido)zirconium(IV) and water pulses [39]. Takoudis and co-workers replaced the co-reactant of ZrO_2 ALD [tris(dimethylamido)cyclopentadienyl zirconium(IV) as the precursor] with ethanol from which selective deposition on SiO_2 over Cu is achieved [46]. To the best of our knowledge, no selective area ZrO_2 ALD using tetrakis(ethylmethylamido) zirconium(IV) has been reported.

Here we report investigation of alternative approaches to selective, self-aligned ALD, where we seek to develop processes that are fast, exclusively vapor phase, involving "zero-thickness / zero residue" modification layers. Selective substrate attachment of the precursor, either intrinsic or induced, could be possible under certain conditions given the chemical specificity of the ALD surface reactions. In our approach we employ a mode of atomic layer deposition involving the use of molecular blocking agents and adsorption

reversal agents, both of which exploit the effects of co-adsorption and competitive adsorption.

We will present an analysis of competitive adsorption based on Langmuir kinetic model and the experimental results concerning the first half cycle of transition metal (Zr) oxides ALD on a metal (Cu) and a dielectric surface (SiO$_2$), where we seek to deposit the oxide thin film on the dielectric, but not on the metal.

We are examining two specific approaches to the surface chemistry: (*i*) the use of adsorption reversal agents; and (*ii*) the use of molecular blocking agents, as shown in Fig. 5-2. Here for a thin film precursor we examine transition metal complexes with the generic structure, $M(XR_m)_n$, where M is the transition metal and XR_m is the coordinating ligand. In pursuing strategy (*i*) we examine the introduction of a second species in the first half-cycle that can act as a coordinating ligand, e.g., HXR'_m, or $HXR'_{m-1}R''$, etc. In pursuing strategy (*ii*) species (Y) are selected that can effectively compete for adsorption sites, dependent on the composition of the substrate. Concerning strategy (*i*) we are currently investigating reactions between transition metal amido compounds and a series of amines ($X = N$).

Tetrakis(ethylmethylamido)zirconium(IV) {Zr[N(CH$_3$)(CH$_2$CH$_3$)]$_4$, TEMAZ}is chosen as the transition metal precursor, and we initially focus on the first half-cycle of ZrO$_2$ ALD, where demonstrating selectivity for this part of the ALD process is a necessary, but not sufficient condition for selective area growth. Three amines, including ethylenediamine [H$_2$N(CH$_2$)$_2$NH$_2$, EDA], diisopropylamine {[(CH$_3$)$_2$CH]$_2$NH, DIPA}, triethylamine [N(CH$_2$CH$_3$)$_3$, TEA] and a thiol, 1,2-ethanedithiol [HS(CH$_2$)$_2$SH, EDT], are examined for their effects on how TEMAZ is adsorbed on the two surfaces by competitive adsorption. We have examined no less than 5 thin film precursor/co-adsorbate

combinations, where we employ a custom designed micro-reactor that is coupled to an ultrahigh vacuum system for post-reaction surface analysis, avoiding complications due to air breaks. We find that at least half of the studied co-adsorbates show promise concerning selective area growth, and the possible mechanisms that are likely operative are examined making use of *in situ* measurements involving X-ray photoelectron spectroscopy are discussed.

5.3 Experimental Procedures

5.3.1 Chamber setup and sample preparations

Experiments reported here are carried out in a custom designed ultrahigh vacuum system (UHV) coupled with a micro-reactor for *in situ* ALD. The chamber/reactor design and the operating procedures are described in detail elsewhere. SiO_2 substrates were prepared starting from single-side polished, Si(100) wafers (B doped, resistivity 38-63 Ω cm) The native SiO_2 layer was removed from the substrates by submerging in buffered oxide etch (BOE) for 2 minutes. The substrates were then re-oxidized by dipping in Nanostrip for 15 min at a temperature of ~75 °C. The BOE/Nanostrip treatment was then repeated. This method is known to produce a 15-20 Å layer of chemical oxide with surface Si-OH density ~ 4 - 6 $\times 10^{14}$ cm^{-2} [47], [48]. The Cu substrate in this work is Cu thin film deposited on SiO_2 via physical vapor deposition.

Figure 5-2: Schematics of selective area ALD by **(a)** reversible adsorption with the use of co-adsorbates and **(b)** competitive adsorption with the use of co-adsorbates.

5.3.2 Experiments for screening co-adsorbates

We examined the effect of the four different organic molecules (three amines and one thiol) individually on the competitive adsorption with TEMAZ on the two surfaces: the dielectric (SiO_2) and the metal (Cu). A gas delivery system that allows for independent dose control of the two reagents is designed to integrate with the micro-reactor, as shown in Fig. 5-3. TEMAZ and co-adsorbates are stored in stainless steel bubblers, and the dosage can be controlled by the bubbler temperature, carrier gas flow rate and the extent of dilution with an inert gas flow (nitrogen in this work).

This set of experiments were conducted under an operating pressure of 18 Torr. The SiO_2 or Cu substrate, loaded on a custom platen for a 4" wafer, is thermalized to ~150 °C for an hour prior to the exposure. The first step of an experiment involves exposing the substrate to the co-adsorbate in order to achieve its steady-state coverage, followed by a co-exposure to both the co-adsorbate and the metal precursor. After that we terminate the metal precursor flow while keeping the co-adsorbate flow. It is aimed to prevent the active sites from possible reactions with lingering metal precursor molecules. Flow sequence utilized in this set of experiments is summarized in Table 5-1. For each co-adsorbate examined, the experiments are conducted with two different effective vapor pressures with a ~5X to ~10X difference for examining the effect of the partial pressure ratio A/B_2, summarized in Table 5-2 [49], [50]. After the exposure, the samples were then transferred to the main chamber in UHV for *in situ* XPS.
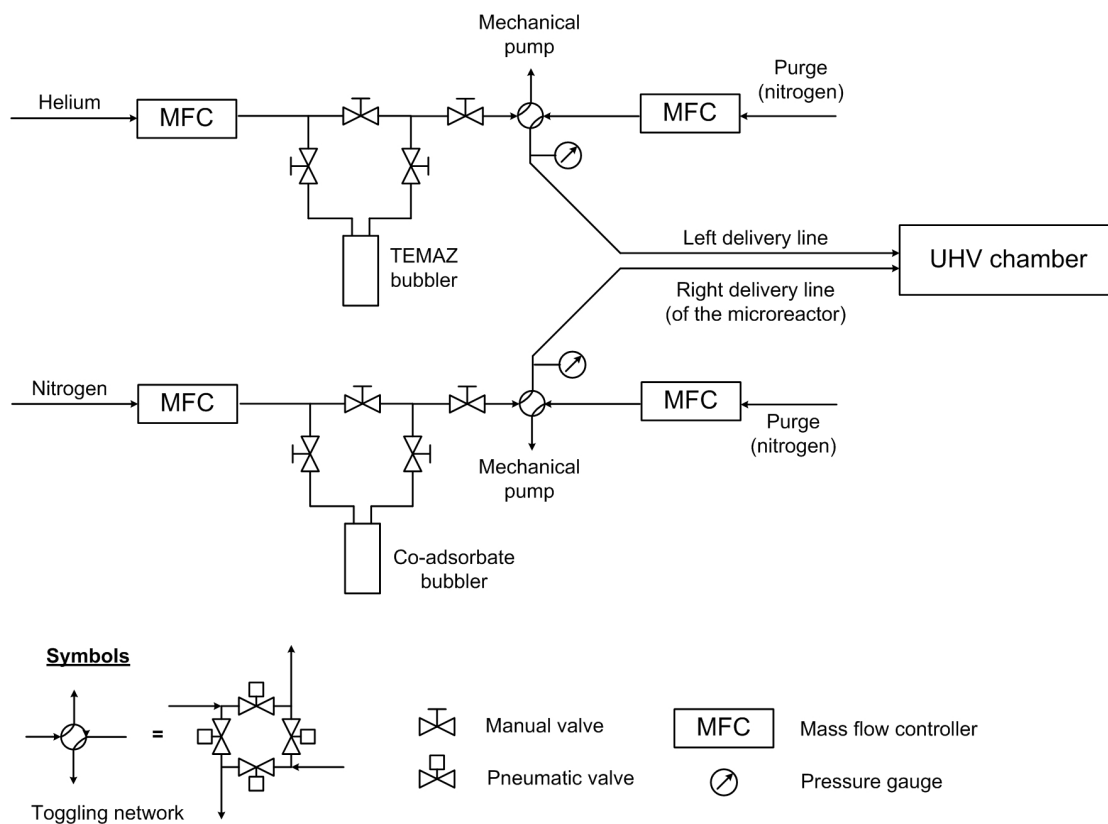
Figure 5-3: Schematic representation of the reactant delivery system.

Table 5-1: Flow setup in each step of Experiments for screening of co-adsorbates

	Flow from the precursor manifold	Flow from the co-adsorbate manifold
Pre-dose (co-adsorbate)	10 sccm N_2 or He	Co-adosrbate | 10 sccm N_2 (with or without dilution)
Co-dose (metal precursor and co-adsorbate)	TEMAZ (~40 °C) | 10 sccm He	
Post-dose (co-adsorbate)	10 sccm N_2 or He	
Note: the dose time for each step is 5 mins		

Table 5-2: The effective partial pressures ratio of the co-adsorbate to the metal precursor

	Effective partial pressures of co-adsorbates	
	low concentration	high concentration
Ethylenediamine (EDA)	6.22	69.8
Diisopropylamine (DIPA)	77.8	389
Triethylamine (TEA)	23.9	119
1,2-ethanedithiol (EDT)	2.96	32.9

5.3.4 *In situ* XPS

XPS data were collected using an Omicron Sphera U5 concentric hemispherical electron energy analyzer (Omicron Nanotechnology USA, Eden Prairie, MN), operated at a constant pass energy of 50 eV. Nonmonochromated MgKα X-rays (1253.6 eV excitation energy) and Al Kα x-rays (1486.7 eV excitation energy) were produced using an Omicron DAR 400 twin anode source operated at 300 W (15 kV anode potential × 20 mA emission current). CasaXPS software (version 2. 3. 15) was used for analyzing XP spectra. Zr(3d) spectra were fit assuming a spin-orbit doublet separation of 2.4 eV with a fixed ratio of 2:3 for the $3d_{3/2}$ to $3d_{5/2}$ peak area [51], [52]. S(2p) spectra were fit assuming a spin-orbit doublet separation of 1.2 eV with a fixed ratio of 1:2 for the $2p_{1/2}$ to $2p_{3/2}$ peak area [53]. BE difference of Si(2s)/Si(2p) parent and plasmonic peaks is fixed with a plasmonic energy of 17.8 eV [54]. Background subtraction was carried out using the Shirley method [55]. Peak areas were calculated by fitting spectra to a Gaussian/Lorentzian product formula with a mixing ratio of 0.7. Binding energies of all spectra were referenced to peaks originated from the substrates, which were assigned to 99.5 eV for Si(2p) on SiO_2 and 932.6 eV on Cu, to correct for the substrate charging effect [56].

5.4 Results

5.4.1 A kinetic model of competitive adsorption on a single surface

A kinetic model of competitive adsorption was constructed for examining the effect of the introduction of co-adsorbate on the nucleation of the metal precursor in the transient regime. The Langmuir model applies to the two species, the co-adsorbate (A) and the metal precursor (B_2), so that both the adsorption and desorption reactions for the two species are allowed in this model. The adsorption reactions are spontaneous, while the desorption reactions include energy barriers to be overcome. It is also assumed that on the surface modeled there is only one binding state of the active sites for which the two species compete. The governing equations in this kinetic model are a set of first-order ordinary differential equations:

$$\frac{d\theta_A}{dt} = \frac{S_A F_A}{n_s}(1 - \theta_A - \theta_B) - k_{d,A}\theta_A \qquad (5-1)$$

$$\frac{d\theta_B}{dt} = \frac{S_B F_B}{n_s}(1 - \theta_A - \theta_B)^2 - k_{d,B}\theta_B^2 \qquad (5-2)$$

where θ_i is surface coverage of the species i (the co-adsorbate or metal precursor), S_i is the probability of adsorption of species i, F_i is the impinging flux of the species i onto the surface, n_s is the surface density of the active sites and $k_{d,i}$ is the rate constant of desorption reaction of the species i. The rate constant of desorption reaction is in the form of Arrahenius equation: $k_{d,i} = A_0 \cdot exp(-E_{d,i}/RT)$ where A_0 is the pre-exponential factor, $E_{d,i}$ is the desorption energy of the species i. Reaction orders and desorption energies of the co-adsorbate or the metal precursor are adopted from previous works on ammonia and metal

alkylamide precursors on Si(100) by density functional theory (DFT) calculation [57], [58]. All parameters used in the model are summarized in Table 5-3. The set of differential equations is solved simultaneously for numerical solutions.

In order to minimize the possibility for the chemisorption of the metal precursor, the surface is first introduced to the co-adsorbate of high exposure for achieving the steady-state coverage of the co-adsorbate where only a small fraction of the active sites is accessible. The final coverage of A on the surface, as a function of substrate temperature, is shown in Fig. 5-4(a). A decreasing final coverage when the substrate temperature increases coincides with both a greater rate constant of desorption and a reduced impinging flux in the adsorption term. The surface is then exposed to both the co-adsorbate or the metal precursor under a pre-defined ratio of the two species. The coverage of B at various pressure ratios of A to B_2 as a function of the exposure of B_2, from 0 to 2 mTorr-s (or 2,000 Langmuir) is shown in Fig. 5-4(b). We found that the final coverage of B after an exposure of 2 mTorr-s decreased significantly due to the introduction of A (see Table 5-4). We also found that a greater pressure ratio of A to B_2 leads to a lower final coverage of B. This observation is consistent with the scheme of competitive adsorption where the more abundant species dominates the active sites on a surface. The effect of the co-adsorbate is not only demonstrated by the decreased coverage of the metal precursor but also by how fast the metal precursor is essentially chemisorbed.

Table 5-3: Parameters used in the kinetic model for competitive adsorption

Parameters	Values
Pre-exponential factor, A	10^{13} (s^{-1})
Probability of adsorption, S_A and S_B	1, 0.002
Surface density of active sites, n_S	10^{19} (m^{-2})
Energy of desorption, $E_{d,A}$ and $E_{d,B}$	19.9, 25.7 (kcal mol^{-1})
Molecular weight, M_A and M_B	0.017, 0.282 (kg mol^{-1})
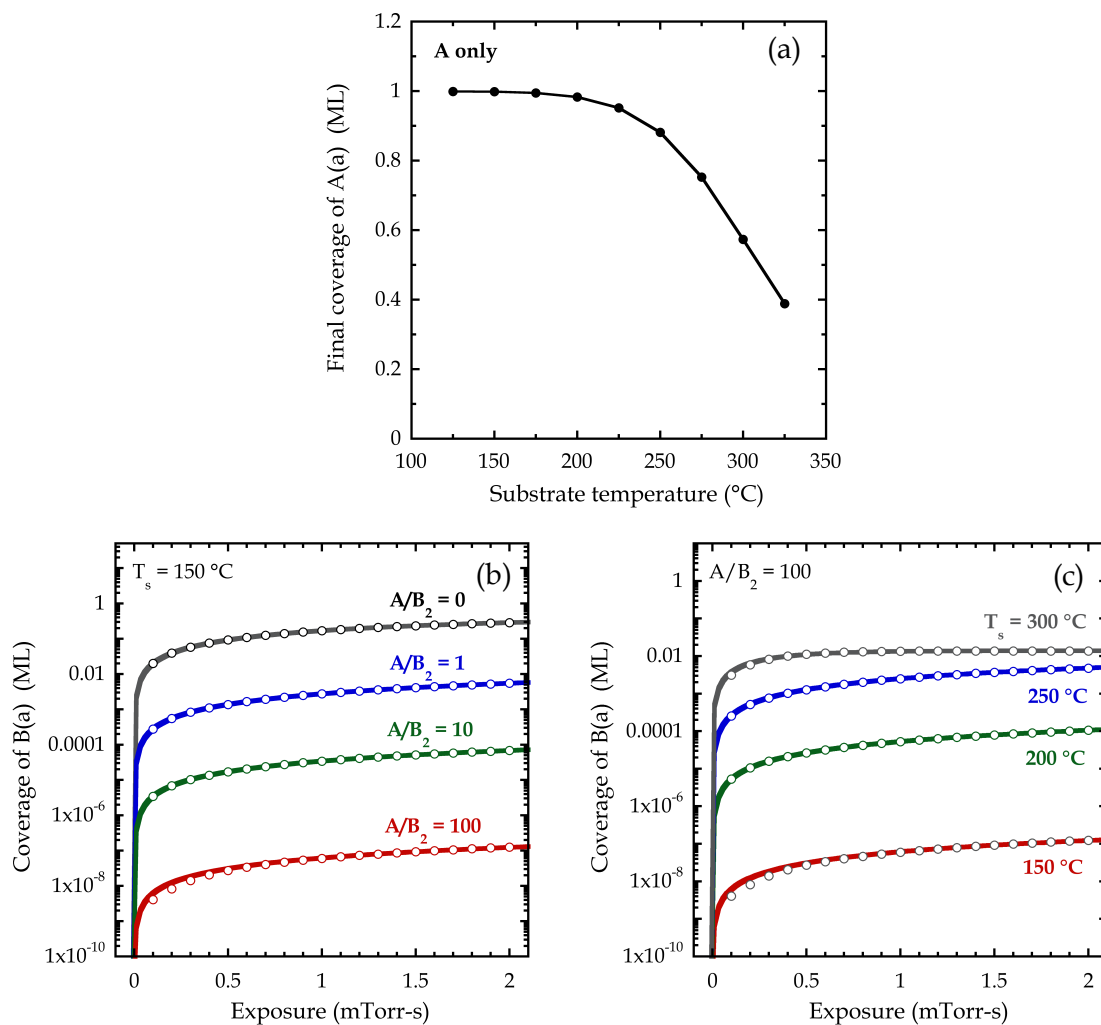
Figure 5-4: Results of a kinetic model for competitive adsorption: **(a)** Final coverage of A as a function of substrate temperature. **(b)** The coverage of B at various pressure ratios of A to B_2 as a function of the exposure **(c)** The coverage of B at various substrate temperatures as a function of the exposure. The solid lines in (b) and (c) are fits of the numerical solution from the model.

Table 5-4: Summary of coverage of B after an exposure of 2 mTorr-s, the steady-state coverage of B and time constants derived from the fits to the coverage of B under various pressure ratios of A to B_2.

A/B_2	θ_B after an exposure of 2 mTorr-s	θ_B^{SS}	τ (s)
0	2.86×10^{-1}	6.57×10^{-1}	0.2742 ± 0.0012
1	5.47×10^{-3}	1.82×10^{-1}	16.99 ± 2.748
10	6.81×10^{-5}	2.42×10^{-2}	104.6 ± 82.22
100	1.25×10^{-7}	2.51×10^{-3}	1242 ± 854.6

We compared the final coverage of B after the exposure to the steady-state coverage of B by solving the governing equations analytically:

$$\theta_B^{SS} = \frac{\sqrt{\dfrac{S_B F_B}{k_{d,B} n_s}}}{1 + \dfrac{S_A F_A}{k_{d,A} n_s} + \sqrt{\dfrac{S_B F_B}{k_{d,B} n_s}}} \qquad (5-3)$$

While the final coverage is very close to the steady-state value in the case of no co-adsorbate, it is 4 orders of magnitude lower than the steady-state value case with the A/B_2 ratio of 100. We can also see from the analytical expression of the steady-state coverage that the introduction of the co-adsorbate (increasing F_A) helps suppress the adsorption of the metal precursor (decreasing θ_B^{SS}). Moreover, the time constants (τ), retrieved by fitting the coverage-exposure curves in the following form: $\theta_B = \theta_B^{SS} \left[1 - exp\left(-\dfrac{t}{\tau}\right)\right]$, are used to further assess the suppressive effect of the co-adsorbates. The time constant for the case with the A/B_2 ratio of 100 (=1242 s) is ~5000 times greater than that with no co-adsorbate (= 0.2742 s).

The effect of substrate temperature on the nucleation of metal precursor is also examined with the use of the kinetic model. We displayed the coverage of B at various substrate temperatures as a function of the exposure with a fixed pressure ratio of A to B_2 of 100 in Fig. 5-4(c), and the competitive adsorption is favored at a lower substrate temperature. This can be explained by the fact that the desorption energy of the metal precursor is greater than that of the co-adsorbate, so the adsorption/desorption behavior of the metal precursor is more sensitive to temperature. Therefore, higher substrate temperature causes lower coverage of B in the case of co-exposure, as we have seen in the

case of B only [see the above discussion of final coverage of a single species and Fig. 5-4(a)].

5.4.2 XPS results for the co-adsorbate screening experiments

5.4.2.1 Ethelynediamine

We first consider the TEMAZ / EDA co-exposure to SiO_2 and Cu surfaces at a substrate temperature of $T_s = 150\ °C$ in which EDA, a primary amine, is chosen as the co-adsorbate. In Fig. 5-5(a) we display the XP spectra from the Zr(3d) region for three different cases on SiO_2: (*i*) the case of no EDA (i.e., 10 sccm N_2 in the co-adsorbate line); (*ii*) the case of low concentration of EDA; and (*iii*) the case of high concentration of EDA. In this specific system, Zr(3d) peaks from the film overlap with the second plasmonic peak of the Si(2s) peak originated from the substrate, SiO_2. In case (*i*) we find that TEMAZ is adsorbed on SiO_2 surface at the given substrate temperature of 150 °C as we observed the Zr(3d) doublets. $Zr(3d_{5/2})$ binding energy of ~183 eV is in good agreement with the report values of BE of the ZrO_2 film [59]–[61]. In case (*ii*) we also observed both Zr(3d) and the plasmonic peaks. While the Zr(3d) peaks in case (*ii*) are smaller than those in case (*i*) (decreased by 67%), the plasmonic peak in case (*ii*) is bigger than that in case (*i*). This is consistent to a simple film structure comprising a thin adsorbed layer of Zr on top of the planar substrate of SiO_2. As the coverage of Zr layer decreases [which can be seen from the decrease of Zr(3d) peak area], the attenuation effect of the Zr-containing over layer to the photoelectrons from the underlying substrate of SiO_2 therefore decreases, resulting in

stronger Si peaks, including the Si(2s) plasmonic peak. In case (*iii*) we see no appearance of Zr(3d) peak(s) out of a strong Si peak, so no adsorption of TEMAZ on SiO_2 is observed with a EDA / TEMAZ partial pressure ratio of 140.

Considering all three cases, we can clearly see a monotonic trend from case (*i*) extended to case (*iii*): the amount of Zr observed on the surface is the highest without the use of the co-adsorbate, EDA in case (*i*). When we introduce a modest amount of EDA in case (*ii*), the amount of Zr adsorbed on the surface is reduced by $\sim$ 67% due to the suppressing effect of the co-adsorbate. As we introduce EDA with ~11X higher in terms of the EDA / TEMAZ partial pressure ratio, the nucleation of Zr on SiO_2 is completely blocked by the use of the co-adsorbate. This effect of the EDA partial pressure on the adsorption of Zr (along with the evolution of Si plasmonic peaks) is consistent to the conclusion from the kinetic model of competitive adsorption that the more the co-adsorbate is introduced, the lower the coverage of the adsorbed metal precursor on the surface is.

Figure 5-5: XP Spectra of Zr(3d) of TEMAZ / EDA co-exposure experiments **(a)** on SiO_2 and **(b)** on Cu and spectra of N(1s) **(c)** on SiO_2 and **(d)** on Cu.

In Fig. 5-5(b) we display the XP spectra from the Zr(3d) region for the three cases on Cu. We first observe that without EDA the amount of Zr on Cu [black curve in Fig. 5-5(b)] is almost the same as that on SiO$_2$ [black curve in Fig. 5-5(a)] given a long dose of TEMAZ. An attenuated adsorption of Zr is observed in case (*ii*), and a complete suppression of Zr is observed in case (*iii*). That is, in all four cases that involve the use of EDA discussed above, the addition of EDA affected the chemisorption of TEMAZ on either substrate. The experimental observation coincides with the effect of the partial pressure of the co-adsorbate on the adsorption of the metal precursor predicted by the kinetic model, regardless of the choice of the substrate (SiO$_2$ or Cu). Moreover, a side-by-side comparison of the results on SiO$_2$ and on Cu allow us to examine the effect of the substrate composition. In case (*ii*), Zr(3d) peak area on Cu is slightly greater than that on SiO$_2$, despite that the 'starting' peak area [i.e. case (*i*)] is almost the same (<1%, and has therefore no preference as to which surface to deposit on). In this case the chemisorption of TEMAZ on Cu is preferred than on SiO$_2$ in the presence of EDA. By contrast, in case (*iii*) Zr nucleation is completely suppressed on both surfaces, so there is no preference for the starting surface.

In Fig. 5-5(c) we displayed the N(1s) spectra on SiO$_2$. With no EDA, we observed a N(1s) peak at 401.0 eV, which is most likely to be from the chemisorbed metal precursor that has some remaining ligands. N(1s) peak at 399.7 eV assigned to the ligand is also seen on Cu under the same experimental conditions [case (*i*), shown as the black curve] in Fig. 5-5(d). The 1.3 eV difference is attributed to different molecular environments of the transitional metal bound to SiO$_2$ vs. Cu. However, with a high partial pressure of EDA, there is no Zr nucleation on SiO$_2$. The N(1s) peak is therefore most likely from the

interaction of the SiO$_2$ surface and EDA. With a low partial pressure of EDA the N(1s) peak is most likely from the two possible binding environments discussed above. In sharp contrast to N(1s) region of SiO$_2$, we observed a N(1s) peak at ~ 398.7 eV and of a greater peak area on Cu with a high partial pressure of EDA. This suggests a very different binding environment than the amido-ligands on TEMAZ. The peak could be assigned to N strongly bound to Zr or Cu in the substrate [62], [63].

5.4.2.2 Diisopropylamine

The second candidate for the co-adsorbate examined is DIPA, a secondary amine that is the most volatile among the four molecules reported in this study. In Fig. 5-6(a) we display the XP spectra from the Zr(3d) region for three different cases on SiO$_2$: (*i*) the case of no DIPA; (*ii*) the case of low concentration of DIPA; and (*iii*) the case of high concentration of DIPA. We observe a suppressive effect of the DIPA partial pressure on the Zr(3d) region, which is in common for both EDA and DIPA. The amount of Zr is decreased by 44% and 97% in case (ii) and case (iii), respectively. The fact that the more DIPA is used, the less TEMAZ is chemisorbed on SiO$_2$ is supported by the correlated changes in the Zr(3d) doublet and the Si plasmonic peak. The behavior on Cu also follows the same trend on SiO$_2$ (decreased by 38% and 100%, respectively).

Figure 5-6: XP Spectra of Zr(3d) of TEMAZ / DIPA co-exposure experiments **(a)** on SiO_2 and **(b)** on Cu and spectra of N(1s) **(c)** on SiO_2 and **(d)** on Cu.

The substrate effect on the nucleation of Zr in the co-exposure scheme is examined when we juxtapose Fig. 5-6(a) and (b). In case (*ii*) we can see that the amounts of Zr on SiO_2 and Cu are quite similar with a DIPA / TEMAZ partial pressure ratio of 77.8 and at a substrate temperature of $T_s = 150$ °C. In case (*iii*) the nucleation of Zr on either surface is completely blocked with the use of greater amount of the co-adsorbate (DIPA / TEMAZ partial pressure ratio of 389). There is no inherent substrate dependence of TEMAZ adsorption due to the self-limiting chemical nature as a ALD precursor. However, even with the introduction of DIPA into the first half-cycle of ZrO_2 ALD, no derived substrate dependence is observed in either case (*ii*) or case (*iii*): in case (*ii*) similar amount of Zr precursor is chemisorbed on SiO_2 and Cu, and in case (*iii*) no TEMAZ adsorption is observed on SiO_2 or Cu. This suggests that DIPA is not a good choice of the co-adsorbate because of the lack of the ability to introduce substrate dependence. At this point, no selective chemisorption of the metal precursor is induced by either EDA or DIPA. The authors, however, would like to point out that in all four cases that involve the use of DIPA, the addition of DIPA affected the chemisorption of TEMAZ on either substrate despite that no substrate dependence is derived.

In Fig. 5-6(c) we display the N(1s) spectra of the three cases on SiO_2. While the N(1s) peak area do not change significantly with the partial pressure ratio, the binding energy of N(1s) in case (*iii*) was increased to 401.3 eV, from 401.8 eV in case (*i*). This indicates that while the amount of N found in all three cases is quite similar, N from the chemisorbed TEMAZ is most probable in case (*i*) and N from the co-adsorbate is in case (*iii*). Also, when DIPA is used [i.e. cases (*ii*) and (*iii*)] the N(1s) peak area is smaller compared to the counterpart of the TEMAZ / EDA study [see Fig. 5-5(a)], and this implies

less interaction in the DIPA/TEMAZ/SiO$_2$ system than that in the EDA/TEMAZ/SiO$_2$ system. In Fig. 5-6(d) we displayed the N(1s) spectra of the three cases on Cu, and the N(1s) bond at ~ 398.7 eV that can be identified in the EDA case was not observed here, so this again implies less interaction between DIPA and TEMAZ than that between DIPA and TEMAZ on both SiO$_2$ and Cu surface.

5.4.2.3 Triethylamine

TEA, the third amine molecule examined in this work, is a tertiary amine with three ethyl groups bound to the N atom center and with no N-H bond. In Fig. 5-7(a) we display the XP spectra from the Zr(3d) region for three cases on SiO$_2$ analogous to those in EDA and DIPA studies: (*i*) the case of no TEA; (*ii*) the case of low concentration of TEA; and (*iii*) the case of high concentration of TEA. The suppression of TEMAZ adsorption by competitive adsorption between TEA and TEMAZ is markedly demonstrated, in the order of increasing TEA/TEMAZ partial pressure ratio: first unhindered adsorption in the absence of the co-adsorbate [case (*i*), black curve] followed by suppressed adsorption of the metal precursor molecule [case (*ii*), blue curve] and finally a complete blockage of the TEMAZ adsorption [case (*iii*), red curve]. The relative signals of Zr(3d) and 2nd plasmonic peak of Si(2s) regions in XP spectra showed that the increase of Zr(3d) integrated intensity was coincident with the decrease in the integrated intensity of Si plasmonic peak. The amount of Zr is decreased by 52% and 99% in case (ii) and case (iii), respectively.
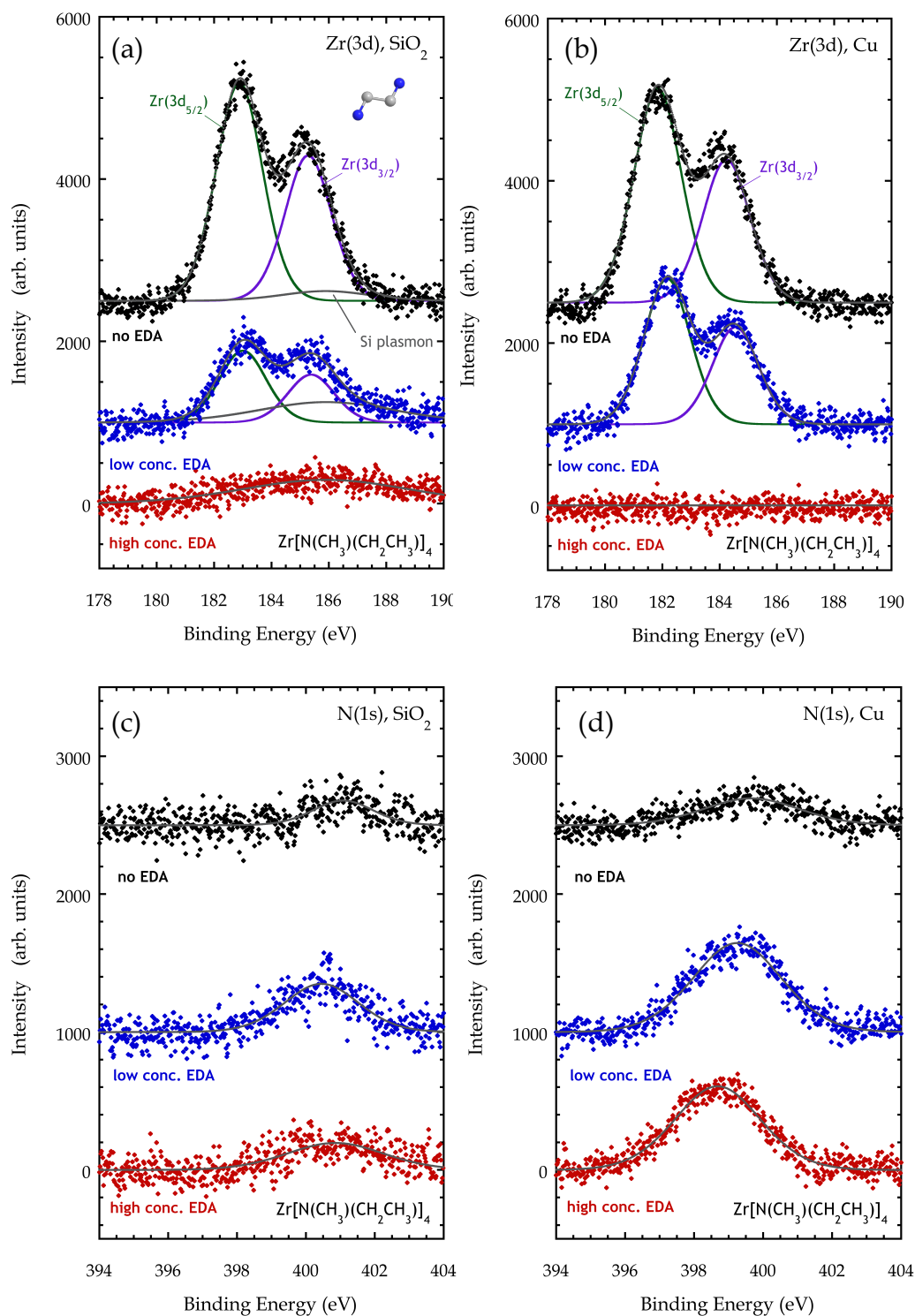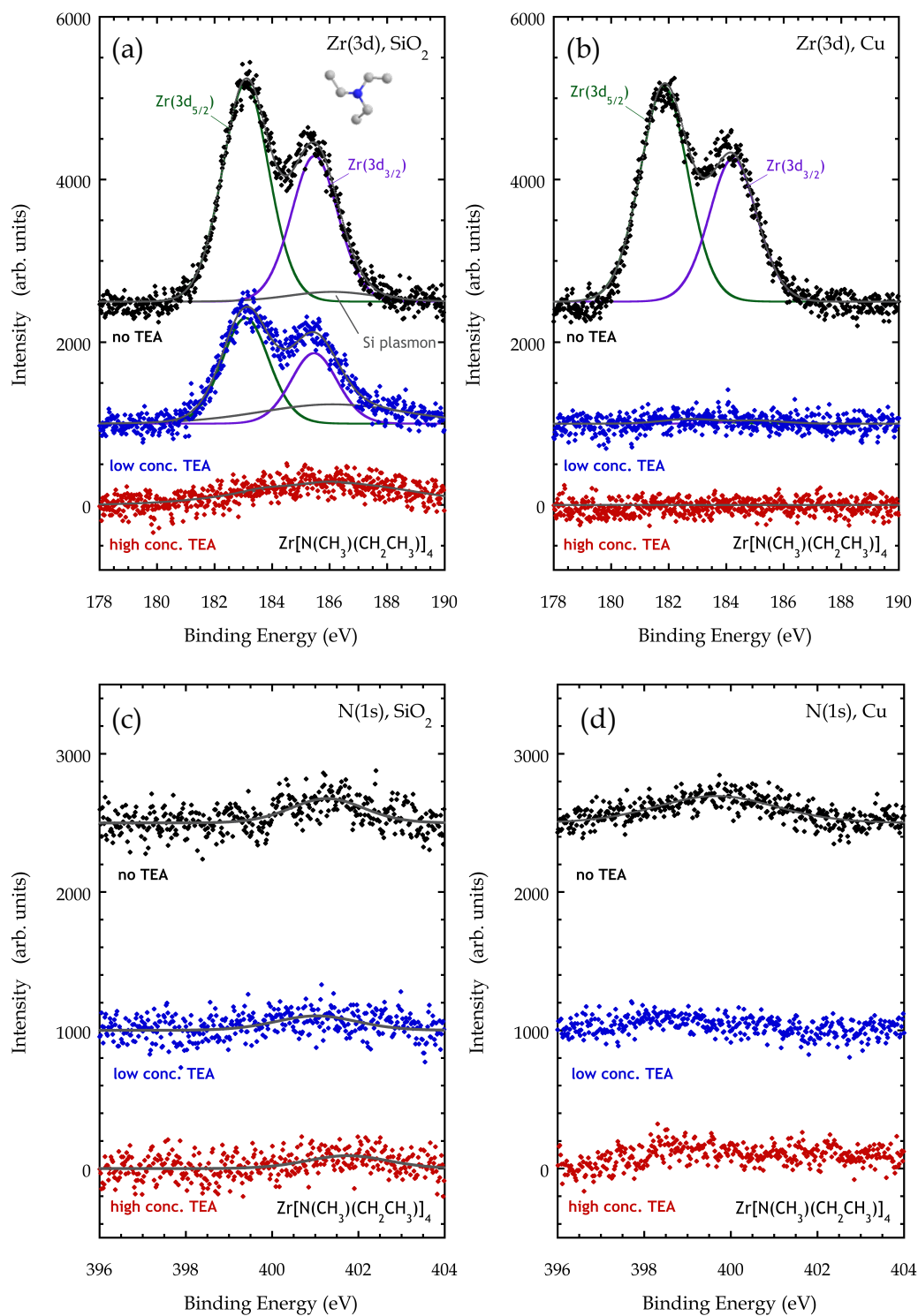
Figure 5-7: XP Spectra of Zr(3d) of TEMAZ / TEA co-exposure experiments **(a)** on SiO$_2$ and **(b)** on Cu and spectra of N(1s) **(c)** on SiO$_2$ and **(d)** on Cu.

The addition of TEA also suppresses the TEMAZ adsorption on the Cu surface in a somewhat interesting way, shown in Fig. 5-7(b). In contrast to the gradual change in the amount Zr on the surface with respect to the TEA concentration on SiO_2, the change with respect to the TEA concentration on Cu is abrupt compared to other cases of amines. In case (ii) and case (iii) TEA prevents the chemisorption of Zr on Cu for both partial pressures of TEA that were examined, and no partial suppression is observed. This result also means that the low concentration of TEA is sufficient for the total blockage of TEMAZ adsorption on Cu, and a higher concentration of TEA in case (*iii*) does sustain the complete blockage on Cu. Additionally, the substrate composition also plays an important role in competitive adsorption when we consider the results on SiO_2 and Cu altogether. Without the use of TEA an almost equal amount of Zr is detected on SiO_2 and Cu, shown as black curves in Fig. 5-7(a) and (b), and simply no selective adsorption of the metal precursor is observed. With the low concentration of TEA (TEA/TEMAZ ratio of 23.9), however, TEMAZ adsorption is only observed on SiO_2 but not on Cu (blue curves). That is, selective adsorption is achieved in case (*ii*) of the TEA/TEMAZ study. With the high concentration of TEA (TEA/TEMAZ ratio of 119), no Zr is detected on either surface and therefore the selective adsorption is not sustained. This manifests the synergistic effect of the partial pressure of the co-adsorbate and the substrate composition, and it also demonstrates that a dosage of the co-adsorbate under close control is crucial to the effectiveness of the competitive adsorption.

In Fig. 5-7(c) we displayed the N(1s) spectra of the three cases for TEA/TEMAZ co-adsorption on SiO_2. We observe that the N(1s) peak areas for case (*ii*) and (*iii*) are apparently smaller than that for case (*i*), and this suggests that while TEA helps suppress

TEMAZ adsorption on SiO$_2$ surface and therefore the contribution of N atoms from the amido-ligands of the metal precursor is greatly reduced, the amount of surface-bound N atoms resulting from the interaction between TEA and the surrounding is not significant. In fact, it is less significant than that of EDA or DIPA on SiO$_2$, and no (irreversible) interaction of TEA to the surrounding on Cu surface is observed in case (*ii*) and case (*iii*). Therefore TEA holds promises for the selective deposition of ZrO$_2$ ALD due to the selective adsorption of TEMAZ it introduces, although the mechanism is unclear at this point.

5.4.2.4 1,2-ethanedithiol

EDT has two thiol functional groups, which is a head group commonly found in self-assembled monolayers (SAMs), in its molecular structure; EDT is therefore chosen a candidate for molecular blocking agent that is expected to bind to the metal surface for blocking the ALD growth while keeping the dielectric surface intact. In Fig. 5-8(a) we display the XP spectra from the Zr(3d) region for three cases on SiO$_2$, analogous to the studies described above: (*i*) the case of no EDT; (*ii*) the case of low concentration of EDT; and (*iii*) the case of high concentration of EDT. In case (*ii*) the amount of chemisorbed Zr on SiO$_2$ is reduced by 24% with the use of low concentration of EDT whereas it is reduced by 96% on Cu [Fig. 5-8(b)], and this is the second experimental conditions (comprising the choice of co-adsorbate molecule and its dosage at a given set of surfaces at a fixed substrate temperature) that induce the selective chemisorption of TEMAZ on SiO$_2$ over Cu.
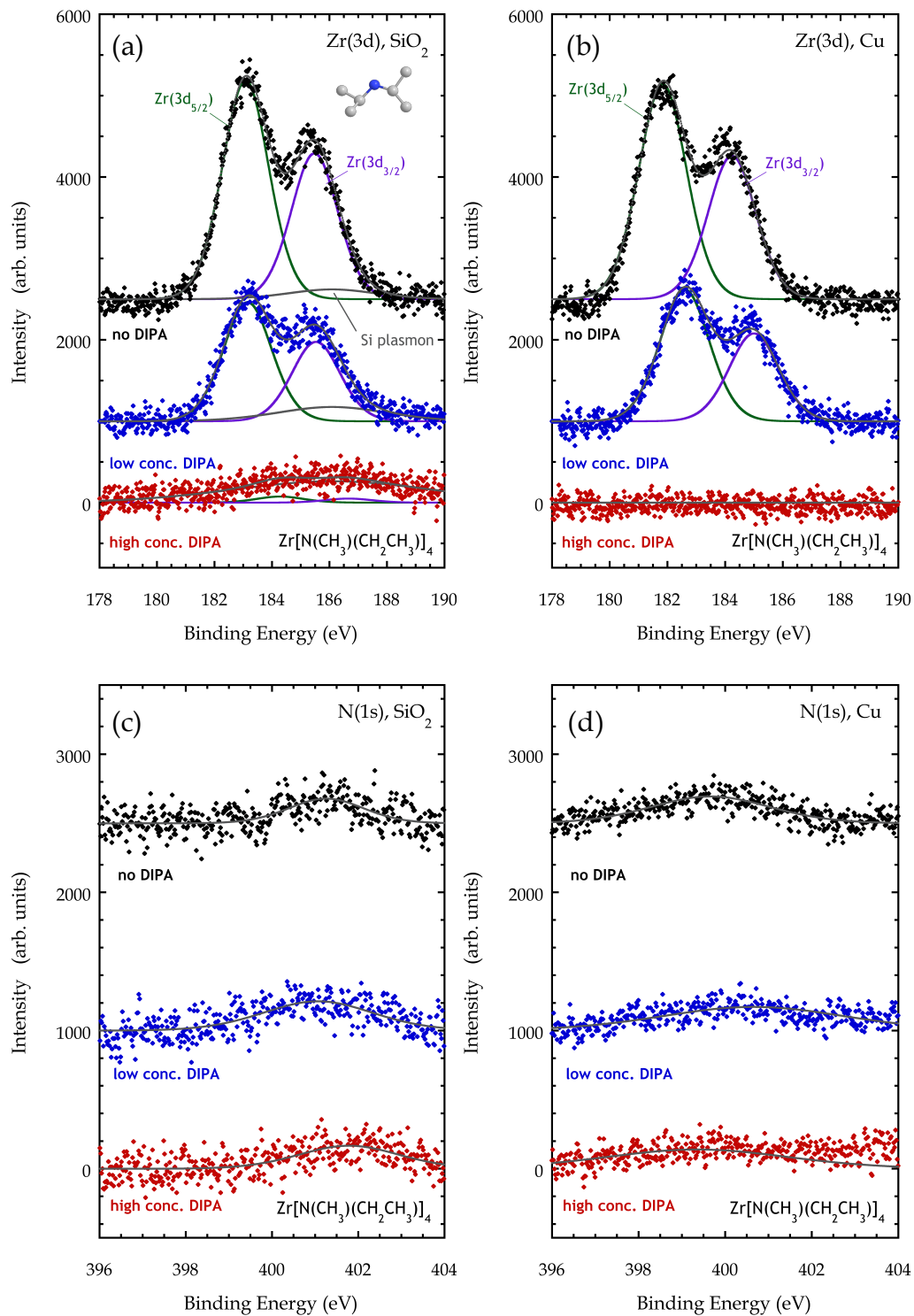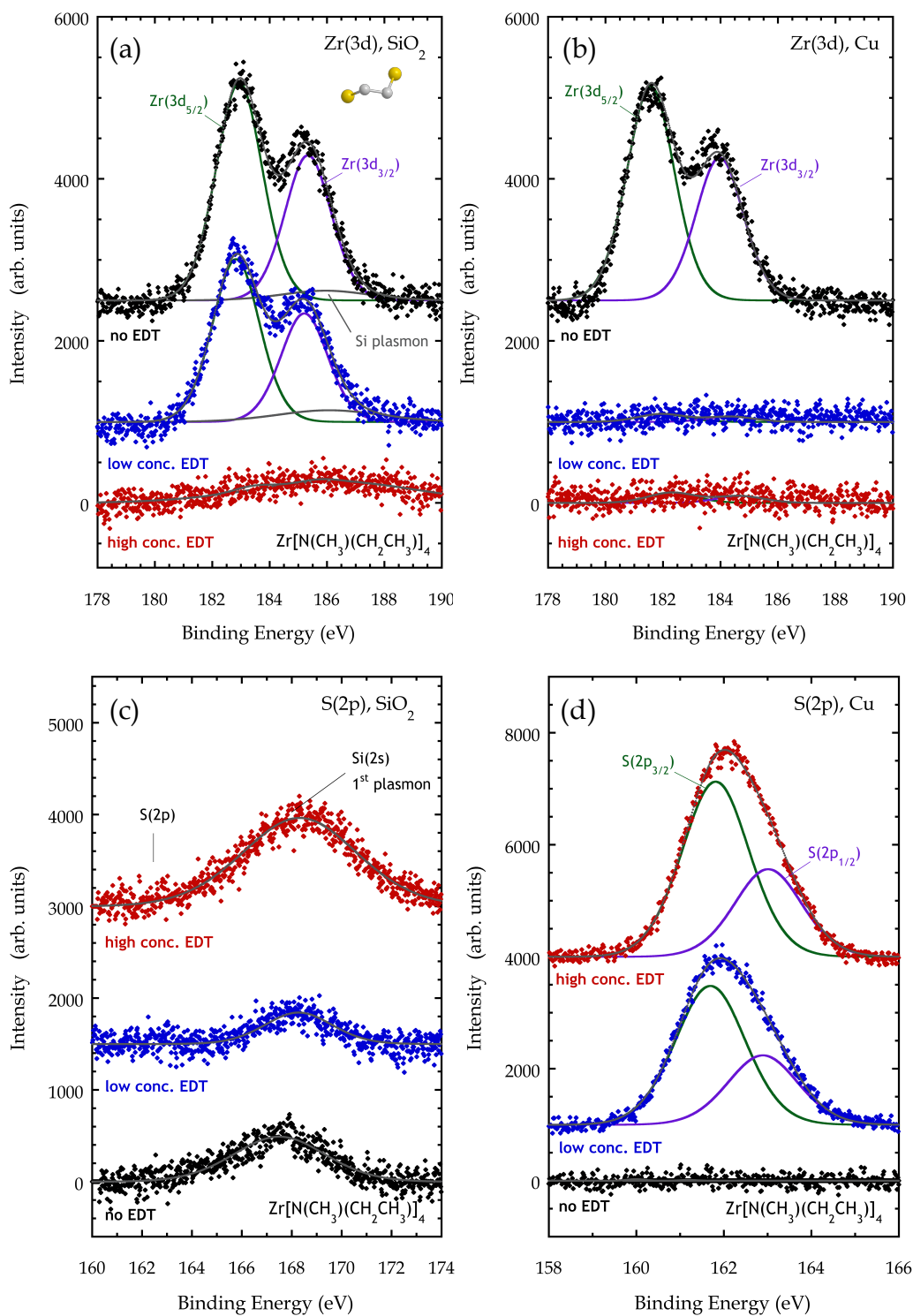
Figure 5-8: XP Spectra of Zr(3d) of TEMAZ / EDT co-exposure experiments **(a)** on SiO$_2$ and **(b)** on Cu and spectra of S(2p) **(c)** on SiO$_2$ and **(d)** on Cu.

Also, as we have learned from the studies of the amines, in case (*iii*) the TEMAZ chemisorption is extinguished on both surfaces due to the high concentration of co-adsorbate used despite the difference in chemical nature of the thiol (EDT) from that of the amines. In contrast to the results on SiO_2, EDT prevents the chemisorption of Zr on Cu for both partial pressures of EDT that were examined, so EDT more tends to suppress the adsorption of Zr complex on metal surface just like SAMs. Interpreting the three cases overall, we can see that a selectivity window in terms of the EDT concentration exists at the first ½ cycle of TEMAZ with EDT.

We also probe the "fate" of EDT molecules on both surfaces by quantifying the amount of S via *in situ* XPS. In Fig. 5-8(*c*), no signature of S(*a*) [i.e. S(2p) peak] is observed on SiO_2 in all cases. We note that while the S(2p) peak could partially overlap with the first plasmonic peak of Si(2s), no 'shoulder' that indicates the presence of small S(2p) peak is observed. In Fig. 5-8(*d*) we display the XP spectra from the S(2p) region for the three cases on Cu. The S(2p) peak is observed at ~162 eV representing the Cu-S thiolate binding in both case(*ii*) and case (*iii*), in contrast to the flat line in case (*i*) [64]. EDT can form Cu-S bonds through one of the thiol groups forming monodentate thiolate intermediate or thorough both thiol groups forming a bidentate metallocycle on metal surface [65]. Hence, the S(*a*) is present on Cu surface after the first ½ cycle exposure as S(*a*) acts to block chemisorption of Zr complex. The fact that EDT selectively binds to metal surface but not to SiO_2 is consistent to the interfacial properties of thiol-containing molecules like SAMs [18]. To calculate the atomic density of S we compare the integrated intensity of the S(2p$_{3/2}$) peak from S(*a*) to that of the Au(4f$_{7/2}$) peak from an evaporated thin film of Au [12], [48]. In addition, we need to account for the relative photoionization

cross-sections, σ_{Au}/σ_S=8.51 [66], analyzer transmission function, $T(E_{Au})/T(E_S)$=(1170 eV/ 1093 eV)$^{-1}$=0.93, the attenuation length of the Au(4f$_{7/2}$) photoelectrons, λ_{Au}=15.5 Å [67], and the atomic density of Au, N_{Au}=5.90 × 10^{22} cm^{-3} [68]. No photoelectron attenuation effects given the location of the S atoms is considered, because no overlayer of Zr complex is assumed. Using the above method, we calculate surface density of S of 2.21 × 10^{15} and 2.67 × 10^{15} atoms-cm^{-2} for cases (*ii*) and (*iii*), respectively.

5.4.3 XPS results of the temperature studies of TEMAZ / TEA co-exposure experiments

TEMAZ / TEA co-exposure experiments were conducted in a 3-by-3 matrix of TEA partial pressures and substrate temperatures. We first examine the effect of the TEA dosage on the chemisorption of TEMAZ molecule on SiO$_2$ and Cu surfaces at three different substrate temperatures. To calculate the atomic density of Zr we compare the integrated intensity of the Zr(3d$_{5/2}$) peak from chemisorbed TEMAZ to that of the Au(4f$_{7/2}$) peak from an evaporated thin film of Au, and the relative photoionization cross-sections, σ_{Au}/σ_{Zr}=2.26 [66] and analyzer transmission function, $T(E_{Au})/T(E_{Zr})$=(1170 eV/ 1071 eV)$^{-1}$=0.92 are accounted for. As a comparison, 9.2 × 10^{14} ZrO$_2$ cm^{-2} in an average monolayer is reported in ZrO$_2$ ALD process [3]. In Fig. 5-9(a) we display the Zr atomic density from the Zr(3d$_{5/2}$) peak area by *in situ* XPS on SiO$_2$, as a function of the concentration of TEA at various substrate temperatures: 120, 150, and 180 °C.
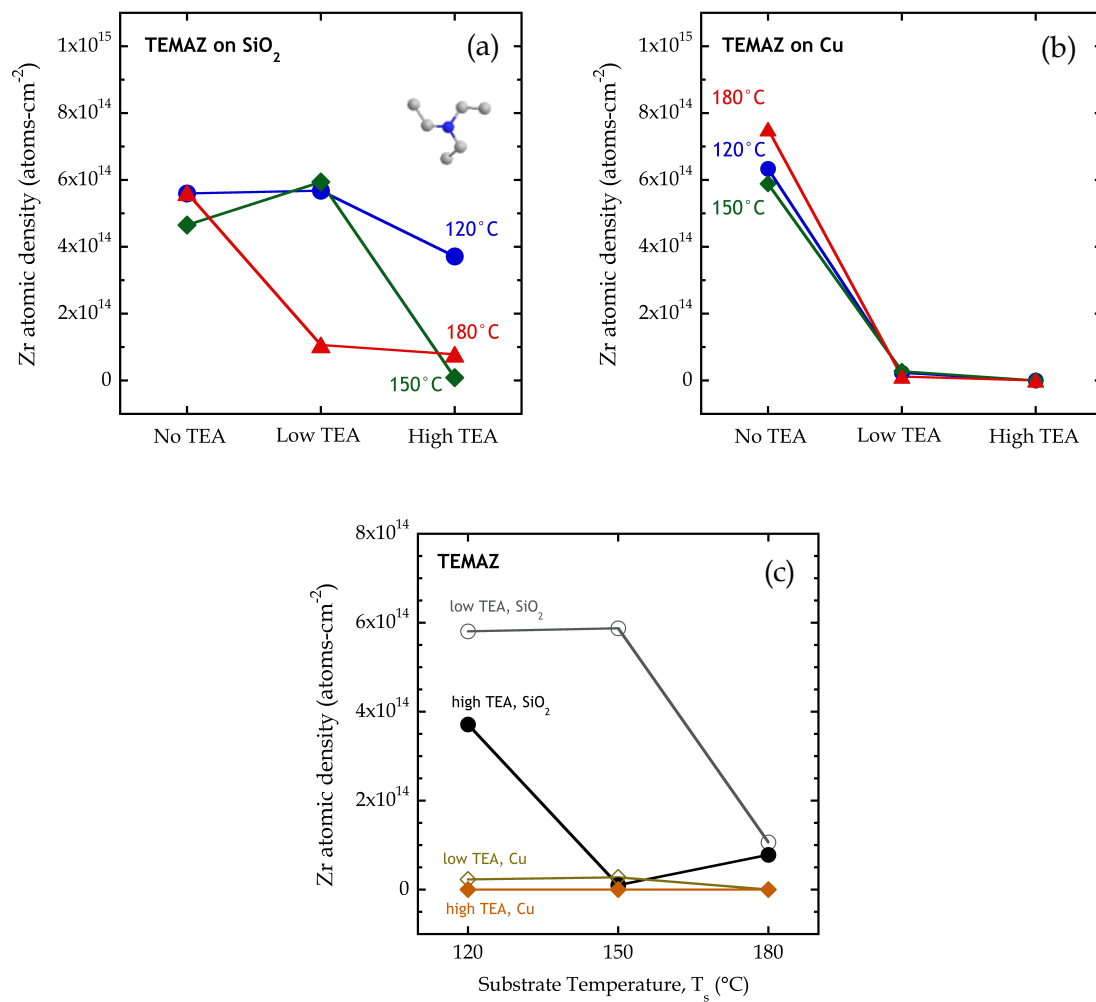
Figure 5-9: Zr density of the 6 TEMAZ / TEA co-exposure and 3 TEMAZ exposure experiments at various substrate temperatures with no TEA, with low and high concentration of TEA **(a)** on SiO$_2$ and **(b)** on Cu. **(c)** Zr density of the 12 TEMAZ / TEA co-exposure experiments as a function of substrate temperature at various experimental conditions.

The results at 120 and 180 °C showed the same monotonic trend, in which the greater the TEA dosage, the less adsorbed Zr on the surface, as what we observe in the screening experiments. At 150 °C a general trend of Zr suppression by the co-adsorbate (despite not a monotonic one) is observed as a function of TEA concentration.

Despite the TEA / TEMAZ ratios used in this set of experiments (0, 6.04 and 12.1) are lower than those in the screening experiments (0, 23.0 and 119), many factors including the reactor pressure, absolute dosage of TEMAZ and flow conditions, are changed so that it is unclear, when we directly compare the two sets of experiments at 150 °C, whether the ratio is the only factor that contributes to the TEMAZ chemisorption in case (*ii*) here but not in the earlier experiments. In Fig. 5-9(b) we display the atomic density of Zr(3d) from *in situ* XPS on Cu, as a function of the concentration of TEA at 120, 150 and 180 °C. With the use of TEA, no-to-minimal amount of chemisorbed Zr complex is observed regardless of the TEA / TEMAZ partial pressure ratios. This reveals that the concept of competitive adsorption is applied at a range of substrate temperature (120 – 180 °C) and TEA / TEMAZ ratios. Also, selective chemisorption of TEMAZ on SiO_2 over Cu is induced in three out of the six cases of TEA / TEMAZ co-exposure experiments. As can be seen, an appropriate combination of the experimental conditions such as substrate temperature, the choice of the co-adsorbate chemistry and the relative amount of the co-adsorbate to the metal precursor, is the key to selective deposition.

We also examine the effect of substrate temperature by replotting the data as a function of substrate temperature in Fig. 5-9(c). With a low concentration of TEA on SiO_2, we observe a Zr atomic density of $\sim 5.8 \times 10^{14}$ atoms-cm^{-2} starting from $T_s = 120$ °C to $T_s = 150$ °C and it drops to $\sim 1.1 \times 10^{14}$ atoms-cm^{-2} at $T_s = 180$ °C. With a high concentration

of TEA on SiO_2, Zr atomic density starts at $\sim 3.7 \times 10^{14}$ atoms-cm^{-2} at $T_s = 120$ °C drops to $\sim 7.8 \times 10^{13}$ atoms-cm^{-2} at $T_s = 180$ °C, although it almost reaches to 0 at $T_s = 150$ °C. The temperature dependence on Cu is less pronounced as on SiO_2 because the chemisorption of TEMAZ is appreciably suppressed.

In Fig. 5-10 we display the XP spectra from the Zr(3d) region for the case of low TEA and $T_s = 120$ °C with and without pre-annealing at 180 °C on Cu. As we discussed above, the chemisorption of Zr complex on Cu at $T_s = 120$ °C is completely suppressed on pre-annealed Cu. By contrast, nucleation of Zr is observed on Cu without pre-annealing. We proposed that in the latter case oxidized Cu that is not removed by pre-annealing has surface oxygen serving as active sites for TEMAZ to chemisorb [69].

5.5 Discussions

5.5.1 The effect of the order of the amine as co-adsorbates: the reactivity of N-H bonds

Interaction between the precursor and co-adsorbates molecules is not only limited to surface reactions. It is also possible that the two species undergo gas-phase reactions by which the chemical nature of both species are changed in an irreversible way. For example, a ligand-exchange reaction between ALD precursor (trimethylaluminum) and the surface inhibitor (ethanol) has been confirmed by *in situ* Fourier Transform Infrared Spectroscopy (FT-IR) [39].
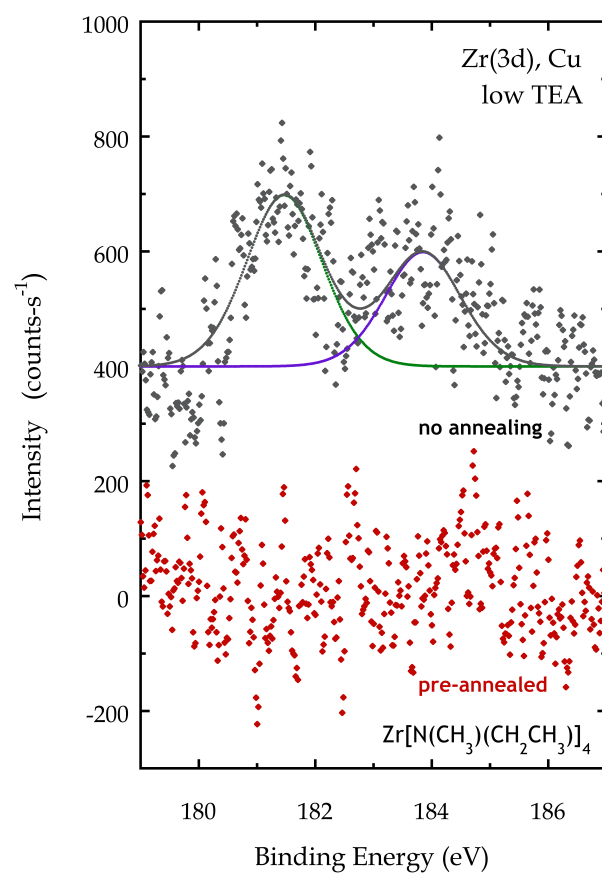
Figure 5-10: XP spectra of Zr(3d) for the case of low TEA and T_s = 120 °C with and without pre-annealing at 180 °C on Cu.

While we observed suppression of TEMAZ nucleation with high concentration of the co-adsorbate in the cases of all three amines, the interaction differed in the amount of N and Zr remained on the surface. We speculate that there is ligand exchange reaction in TEMAZ/EDA co-exposure experiments, in addition to the competitive adsorption. That is, multiple (surface and bulk) reactions mechanism occur simultaneously and compete with one another during co-exposure.

From the molecular structure point of view, EDA has two N-H bonds per N atom that could react with the metal precursor, while DIPA and TEA has one and zero N-H bond, respectively. Bradley reported that transition-metal alkylamides are readily reactive toward protic compounds in ligand exchange reactions involving the scission of the metal-nitrogen bonds [70]. It is therefore possible for EDA and DIPA to undergo ligand exchange reactions with TEMAZ in gas phase, but not for TEA due to the lack of N-H bond. EDA has more N-H bonds than DIPA, so TEMAZ is more prone to parasitic ligand exchanged reaction with EDA, by which a deprotonated EDA fragment [-NH(CH$_2$)$_2$NH$_2$] that still has three N-H bonds is bound to the Zr atom as a new ligand. This could open up more reaction pathways for intra-molecular and inter-molecular reactions (e.g. among Zr-containing molecules and the amines) in gas phase, and the self-limiting nature of the metal precursor could be lost after possible reactions. The products of the ligand exchange reaction, The Zr complex with EDA fragment(s) and ethylmethylamine, as well as EDA itself could result in the high N level on both SiO$_2$ and Cu. N densities on SiO$_2$ and Cu are 1.65 and 3.98×10^{14} atoms-cm^{-2} in case (*iii*) for TEMAZ / EDA co-exposure experiments where there is no chemisorbed TEMAZ on either surface. In contrast, ligand exchange reaction between TEMAZ and DIPA results in Zr complex with new ligand(s) {-N[CH(CH$_3$)$_2$]$_2$}

and ethylmethylamine. The resulting Zr complex does not have any N-H bond, and therefore no further reactions that requires N-H bond on the complex is possible. This is manifested by N densities on SiO_2 and Cu are 1.38 and 1.96×10^{14} atoms-cm^{-2} in case (*iii*) for TEMAZ / DIPA co-exposure experiments.

5.5.2 Possible mechanisms of selectivity: site blocking, reversible adsorption and surface modification

A co-adsorbed species may: (a) prevent the irreversible adsorption of the metal-containing thin film precursor (referred to as 'site blocking'); or (b) recombine with chemisorbed molecular fragments of the metal-containing thin film precursor (referred to as 'reversible adsorption'); or (c) modulate the reactivity of the surface by changing its oxidation state or surface microstructure (referred to as 'surface modification'). One or more of these mechanisms may contribute to substrate dependent chemisorption. *In situ* XPS is used to probe the chemical change of the surfaces that could be induced by a molecular blocking agent that is irreversibly bound to the surface (e.g. SAM) or a surface modifier. An adsorption reversal agent or a blocking agent that is reversibly bound to the surface, which cannot be probed by XPS because of the reversibility, could be identified by kinetic studies, DFT theoretical calculations, real time quadrupole mass spectroscopy (QMS) or FT-IR for understanding the species involved in the surface reactions. In the case of EDA and DIPA, surface modification is most likely to dominate due to residual N atoms observed on the two surfaces, to which the amine molecules contribute by modifying the SiO_2 and Cu surface. In the case of TEA, however, no residual N atom is observed when there is no chemisorbed TEMAZ on Cu in case (*ii*) and case (*iii*). Therefore surface

modification is not the mechanism held responsible here. It is more likely that the reversible adsorption and/or the reversible site blocking is the reaction mechanism for TEMAZ / TEA co-exposure experiments, and we can distinguish the two by interpreting the temperature dependence in the kinetic study of the TEMAZ / TEA co-exposure experiments. We can see from Section 5.4.3 that, in overall, higher substrate temperature helps prevent the chemisorption of the Zr complex, whereas the kinetic model of competitive adsorption based on (reversible) site blocking suggested otherwise. We can thus conclude that site blocking is also not the reaction mechanism behind the selective chemisorption in the TEMAZ / TEA study. While we rule out all options but the adsorption reversal, further studies by DFT calculation of adsorption reversal model and/or *in situ*, real time QMS study during the co-exposure experiments may provide insights into full understanding of the reaction kinetics.

We also further probe the "fate" of EDT molecules on both surfaces by converting the density into how many layers of S on Cu by considering the surface density of a monolayer of S on Cu(111) of 7.50×10^{14} atoms-cm^{-2} [71], and we get 2.94 and 3.55 monolayers (ML) of S for cases (*ii*) and (*iii*), respectively. This is then converted into, in spatial average, 1.47 and 1.78 EDT molecules adsorbed on the Cu surface. The fact that there is more than one dithiol molecule on the surface reveals the event of dimerization and/or polymerization of dithiol molecules [72], and we prove the existence of S(*a*) in the cases where the adsorption of Zr complex on Cu is completely blocked. Therefore no irreversible adsorption of EDT is found on SiO$_2$ surface in either case of EDT/TEMAZ co-exposure of SiO$_2$. However, the Zr adsorption on SiO$_2$ is, either partially or completely, suppressed with the use of EDT. Especially in the case of high partial pressure of EDT,

no S(a) detected on SiO$_2$ yet Zr adsorption is completely blocked. This suggests that while the surface mechanism of EDT on Cu is molecular site blocking, a different mechanism comes into play on SiO$_2$. It is possible that EDT could contribute to competitive adsorption via weak interaction with the hydroxyl functional group on the SiO$_2$ surface despite that no irreversible adsorption is observed.

5.5.3 Co-adsorbate chemistry and the process space of growth as a function of vapor pressure and substrate temperature

We consider further these effects of the choice of the co-adsorbate chemistry and its concentration in the form of a Zr-Zr density plot on SiO$_2$ vs. on Cu in Fig. 5-11, where we consider all the results at T$_s$ = 150 °C in the screening experiments. A 45° straight line passing the origin is shown in the figure for equal amount of growth on the two substrates. The 'pristine' case in which no co-adsorbate is used, shown as a black, filled circle, is practically on the 45° line. Four out of the eight co-exposure experiments are very close to the origin, which suggests that there is no-to-minimal growth on either substrate. These four conditions are of high concentration of the four chemistries examined. Two data points, low EDA and low DIPA, are above the 45° line, which represents that there is more Zr adsorbed on Cu than on SiO$_2$, an induced preference in an opposing direction of selective growth of ZrO$_2$ on SiO$_2$ over Cu. The last two data points, low TEA and low EDT, are below the 45° line, which shows preferred adsorption of Zr complex on SiO$_2$ on Cu. Furthermore, these two points nearly lie on the horizontal axis, which essentially represents the selective chemisorption of Zr complex on SiO$_2$ over Cu.   The diverse location of the

data points on the figure reveals how adsorption of Zr complex can be tuned by the chemistry and the exposure of the co-adsorbate. Although there is no data point in this study lying on the vertical axis that shows the preferred growth on Cu over SiO_2, there is a potential, implied by the two data points above the 45° line, for achieving it with a right choice of co-adsorbate chemistry and the experimental conditions.

In Fig. 5-12 we display a plot of growth characteristics of TEMAZ / TEA co-exposure experiments as a function of effective vapor pressure of TEA and the substrate temperature. Filled symbols represent chemisorption of Zr observed on both SiO_2 and Cu, half-filled represent Zr observed only on SiO_2, and empty represent no-to-minimal Zr observed on both SiO_2 and Cu. The 'pristine' experiments of the TEMAZ-only exposure at saturated dose at all three substrate temperatures are marked as filled symbol as the nucleation of Zr are found on both metal and dielectric surfaces. Three co-exposure experiments are marked as half-filled and the remaining are marked as empty symbols.

The two straight lines with negative slopes represent the dividing lines of chemisorption of the Zr complex on the two surfaces, and no adsorption is possible on a surface above the curve. The upper dividing line is for SiO_2 and the lower one for Cu. The negative slope is originated from the dependence of TEMAZ chemisorption on the two process variables: less chemisorption of Zr with increasing partial pressure of the co-adsorbate and increasing substrate temperature.

Figure 5-11: Zr density of the 8 TEMAZ / co-adsorbate co-exposure (with the 4 co-adsorbates examined in this work) and 1 TEMAZ exposure experiments on SiO_2 *vs.* Zr density on Cu. Filled symbols represents the co-exposure experiments with a high concentration of the co-adsorbate, and half-filled represents the co-exposure experiments with a low concentration of the co-adsorbate.

Figure 5-12: A plot of growth characteristics as a function of effective vapor pressure of TEA and the substrate temperature. Filled symbols represent TEMAZ adsorption observed on both SiO_2 and Cu, half-filled represents growth observed only on SiO_2, and open represents no-to-minimal growth observed on SiO_2 and Cu. The shaded areas represent the approximate regions of phase space for growth.

The process space is divided into three regions (with shaded areas) by the two straight lines, and the shaded areas represent the approximate regions of phase space for chemisorption of TEMAZ: the region in gray represents chemisorption of Zr observed on both SiO_2 and Cu, yellow represents Zr observed only on SiO_2, and blue represents no-to-minimal Zr observed on both SiO_2 and Cu. We note that these dividing lines could essentially be curves instead of simple, straight lines depending on the reaction mechanism on the surface. Moreover, the ALD substrate temperature window (shown as vertical, dashed lines) will further define a window for selective growth for multiple ALD cycles. For multiple ZrO_2 ALD cycles, it is recommended to operate at the yellow region that holds promise to selective area ALD.

5.6 Conclusions

The effect of four organic molecules as co-adsorbates on the chemisorption of tetrakis(ethylmethylamido)zirconium(IV) on SiO_2 and Cu has been examined in our custom designed ALD micro-reactor / *in situ* XPS system. In all the conditions examined in this work, the amount of Zr observed on the surfaces was modulated by the addition of the co-adsorbate. Among the four candidates, selective chemisorption of the Zr complex on SiO_2 over Cu is attained with the presence of triethylamine or 1,2-ethanedithiol. Competitive adsorption holds promise as a "generalized approach" to selective area/substrate composition dependent ALD, and the range of chemistries that can be explored is vast. We propose that the mechanism of selective chemisorption in the TEA / TEMAZ system is adsorption reversal, and the process space within which selective growth of ZrO_2 ALD could be possible is identified. These results demonstrate how our approach

could lead to the development of robust and versatile selective area ALD processes for a variety of systems. Further study will be required to distinguish the effects of co-adsorbates in each of the three stages (pre-dose, co-dose and post-dose) and elucidate the responsible mechanisms, including factors that might lead to loss of selectivity.

5.7 References

[1]   D. M. Hausmann, E. Kim, J. Becker, and R. G. Gordon, "Atomic layer deposition of hafnium and zirconium oxides using metal amide precursors," *Chem. Mater.*, vol. 14, no. 14, pp. 4350–4358, 2002.

[2]   S. J. Yun, J. W. Lim, and J.-H. Lee, "PEALD of Zirconium Oxide Using Tetrakis(ethylmethylamino)zirconium and Oxygen," *Electrochem. Solid-State Lett.*, vol. 7, no. 12, p. F81, 2004.

[3]   W. Weinreich, T. Tauchnitz, P. Polakowski, M. Drescher, S. Riedel, J. Sundqvist, K. Seidel, M. Shirazi, S. D. Elliott, S. Ohsiek, E. Erben, and B. Trui, "TEMAZ/O$_3$ atomic layer deposition process with doubled growth rate and optimized interface properties in metal–insulator–metal capacitors," *J. Vac. Sci. Technol. A Vacuum, Surfaces, Film.*, vol. 31, no. May, p. 01A123, 2013.

[4]   S. W. Ryu, S. Kim, J. Yoon, J. T. Tanskanen, H. Kim, and H. B. R. Lee, "Area-selective chemical vapor deposition of Co for Cu capping layer," *Curr. Appl. Phys.*, vol. 16, no. 1, pp. 88–92, 2016.

[5]   S. Babar, E. Mohimi, B. Trinh, G. S. Girolami, and J. R. Abelson, "Surface-Selective Chemical Vapor Deposition of Copper Films through the Use of a Molecular Inhibitor," *ECS J. Solid State Sci. Technol.*, vol. 4, no. 7, pp. N60–N63, Apr. 2015.

[6]   A. J. M. Mackus, A. A. Bol, and W. M. M. Kessels, "The use of atomic layer deposition in advanced nanopatterning," *Nanoscale*, vol. 6, no. 2011, pp. 10941–10960, 2014.

[7]   A. Sinha, D. W. Hess, and C. L. Henderson, "Transport behavior of atomic layer

deposition precursors through polymer masking layers: Influence on area selective atomic layer deposition," *J. Vac. Sci. Technol. B Microelectron. Nanom. Struct.*, vol. 25, no. 5, p. 1721, 2007.

[8]   B. D. Joyce and J. A. Baldrey, "Selective Epitaxial Deposition of Silicon," *Nature*, vol. 195, no. 4840, pp. 485–486, Aug. 1962.

[9]   K. Kamon, S. Takagishi, and H. Mori, "Selective epitaxial growth of GaAs by low-pressure MOVPE," *J. Cryst. Growth*, vol. 73, no. 1, pp. 73–76, Oct. 1985.

[10] L. Vescan, "Selective epitaxial growth of SiGe alloys -- influence of growth parameters on film properties," *Mater. Sci. Eng. B*, vol. 28, no. 1–3, pp. 1–8, Dec. 1994.

[11] R. Chen, H. Kim, P. C. McIntyre, and S. F. Bent, "Investigation of self-assembled monolayer resists for hafnium dioxide atomic layer deposition," *Chem. Mater.*, vol. 17, no. 3, pp. 536–544, 2005.

[12] A. S. Killampalli, P. F. Ma, and J. R. Engstrom, "The reaction of tetrakis(dimethylamido)titanium with self-assembled alkyltrichlorosilane monolayers possessing -OH, -NH$_2$, and -CH$_3$ terminal groups.," *J. Am. Chem. Soc.*, vol. 127, no. 17, pp. 6300–10, May 2005.

[13] O. Seitz, M. Dai, R. M. Wallace, and Y. J. Chabal, "Copper−Metal Deposition on Self Assembled Monolayer for Making Top Contacts in Molecular Electronic Devices," *J. Am. Chem. Soc.*, vol. 131, no. 50, pp. 18159–18167, 2009.

[14] R. Chen, H. Kim, P. C. McIntyre, and S. F. Bent, "Self-assembled monolayer resist for atomic layer deposition of HfO2 and ZrO2 high-k gate dielectrics," *Appl. Phys. Lett.*, vol. 84, no. 20, pp. 4017–4019, May 2004.

[15] H. Junsic, D. W. Porter, R. Sreenivasan, P. C. McIntyre, and S. F. Bent, "ALD resist formed by vapor-deposited self-assembled monolayers," *Langmuir*, vol. 23, no. 17, pp. 1160–1165, 2007.

[16] E. Färm, M. Vehkamäki, M. Ritala, and M. Leskelä, "Passivation of copper surfaces for selective-area ALD using a thiol self-assembled monolayer," *Semiconductor Science and Technology*, vol. 27. p. 74004, 2012.

[17] J. R. Avila, E. J. DeMarco, J. D. Emery, O. K. Farha, M. J. Pellin, J. T. Hupp, and A. B. F. Martinson, "Real-Time Observation of Atomic Layer Deposition Inhibition: Metal Oxide Growth on Self-Assembled Alkanethiols," *ACS Appl. Mater. Interfaces*, vol. 6, no. 15, pp. 11891–11898, Aug. 2014.

[18] F. S. Minaye Hashemi, B. R. Birchansky, and S. F. Bent, "Selective Deposition of Dielectrics: Limits and Advantages of Alkanethiol Blocking Agents on Metal-Dielectric Patterns," *ACS Appl. Mater. Interfaces*, vol. 8, no. 48, pp. 33264–33272, 2016.

[19] W. Zhang and J. R. Engstrom, "Effect of substrate composition on atomic layer deposition using self-assembled monolayers as blocking layers," *J. Vac. Sci. Technol. A Vacuum, Surfaces, Film.*, vol. 34, no. 1, p. 01A107, Jan. 2016.

[20] M. H. Park, Y. J. Jang, H. M. Sung-Suh, and M. M. Sung, "Selective Atomic Layer Deposition of Titanium Oxide on Patterned Self-Assembled Monolayers Formed by Microcontact Printing," *Langmuir*, vol. 20, no. 6, pp. 2257–2260, Mar. 2004.

[21] K. J. Park, J. M. Doub, T. Gougousi, and G. N. Parsons, "Microcontact patterning of ruthenium gate electrodes by selective area atomic layer deposition," *Appl. Phys. Lett.*, vol. 86, no. 5, p. 51903, Jan. 2005.

[22] X. Jiang and S. F. Bent, "Area-selective ALD with soft lithographic methods: Using self-assembled monolayers to direct film deposition," *J. Phys. Chem. C*, vol. 113, no. 41, pp. 17613–17625, 2009.

[23] J. C. Love, L. A. Estroff, J. K. Kriebel, R. G. Nuzzo, and G. M. Whitesides, "*Self-assembled monolayers of thiolates on metals as a form of nanotechnology*," vol. 105, no. 4. 2005.

[24] H.-B.-R. Lee, M. N. Mullings, X. Jiang, B. M. Clemens, and S. F. Bent, "Nucleation-Controlled Growth of Nanoparticles by Atomic Layer Deposition," *Chem. Mater.*, vol. 24, no. 21, pp. 4051–4059, Nov. 2012.

[25] C. R. Kessel and S. Granick, "Formation and Characterization of a Highly Ordered and Well- Anchored Alkylsilane Monolayer on Mica by Self-Assembly," *Langmuir*, vol. 7, no. 9, pp. 532–538, 1991.

[26] S. N. Chopra, Z. Zhang, C. Kaihlanen, and J. G. Ekerdt, "Selective Growth of Titanium Nitride on HfO_2 across Nanolines and Nanopillars," *Chem. Mater.*, vol. 28, no. 14, pp. 4928–4934, Jul. 2016.

[27] S. P. Chenakin, B. Heinz, and H. Morgner, "Angular and energy effects in sputtering of hexadecanethiol monolayers self-assembled on Ag(111)," *Surf. Sci.*, vol. 436, no. 1–3, pp. 131–140, Aug. 1999.

[28] N. Nishida, M. Hara, H. Sasabe, and W. Knoll, "Thermal Desorption Spectroscopy of Alkanethiol Self-Assembled Monolayer on Au(111)," *Jpn. J. Appl. Phys.*, vol. 35, no. Part 1, No. 11, pp. 5866–5872, Nov. 1996.

[29] R. Methaapanon and S. F. Bent, "Comparative Study of Titanium Dioxide Atomic Layer Deposition on Silicon Dioxide and Hydrogen-Terminated Silicon," *J. Phys.*

Chem. C, vol. 114, no. 23, pp. 10498–10504, Jun. 2010.

[30] R. C. Longo, S. McDonnell, D. Dick, R. M. Wallace, Y. J. Chabal, J. H. G. Owen, J. B. Ballard, J. N. Randall, and K. Cho, "Selectivity of metal oxide atomic layer deposition on hydrogen terminated and oxidized Si(001)-(2×1) surface," *J. Vac. Sci. Technol. B, Nanotechnol. Microelectron. Mater. Process. Meas. Phenom.*, vol. 32, no. 3, p. 03D112, May 2014.

[31] J. C. Hackley, T. Gougousi, and J. D. Demaree, "Nucleation of HfO_2 atomic layer deposition films on chemical oxide and H-terminated Si," *J. Appl. Phys.*, vol. 102, no. 3, p. 34101, Aug. 2007.

[32] Q. Tao, K. Overhage, G. Jursich, and C. Takoudis, "On the initial growth of atomic layer deposited TiO_2 films on silicon and copper surfaces," *Thin Solid Films*, vol. 520, no. 22, pp. 6752–6756, Sep. 2012.

[33] S. E. Atanasov, B. Kalanyan, and G. N. Parsons, "Inherent substrate-dependent growth initiation and selective-area atomic layer deposition of TiO_2 using 'water-free' metal-halide/metal alkoxide reactants," *J. Vac. Sci. Technol. A Vacuum, Surfaces, Film.*, vol. 34, no. 1, p. 01A148, 2016.

[34] S. McDonnell, R. C. Longo, O. Seitz, J. B. Ballard, G. Mordi, D. Dick, J. H. G. Owen, J. N. Randall, J. Kim, Y. J. Chabal, K. Cho, and R. M. Wallace, "Controlling the Atomic Layer Deposition of Titanium Dioxide on Silicon: Dependence on Surface Termination," *J. Phys. Chem. C*, vol. 117, no. 39, pp. 20250–20259, Oct. 2013.

[35] J. Kwon, M. Saly, M. D. Halls, R. K. Kanjolia, and Y. J. Chabal, "Substrate Selectivity of (^{t}Bu-Allyl)Co(CO)$_3$ during Thermal Atomic Layer Deposition of

Cobalt," *Chem. Mater.*, vol. 24, no. 6, pp. 1025–1030, Mar. 2012.

[36] Q. Tao, G. Jursich, and C. Takoudis, "Selective atomic layer deposition of HfO2 on copper patterned silicon substrates," *Appl. Phys. Lett.*, vol. 96, no. 19, 2010.

[37] S. D. Elliott, "Atomic-scale simulation of ALD chemistry," *Semicond. Sci. Technol.*, vol. 27, no. 7, p. 74008, Jul. 2012.

[38] H. Feng, J. A. Libera, P. C. Stair, J. T. Miller, and J. W. Elam, "Subnanometer palladium particles synthesized by atomic layer deposition," *ACS Catal.*, vol. 1, no. 6, pp. 665–673, 2011.

[39] A. Yanguas-Gil, J. A. Libera, and J. W. Elam, "Modulation of the Growth Per Cycle in Atomic Layer Deposition Using Reversible Surface Functionalization," *Chem. Mater.*, vol. 25, no. 24, pp. 4849–4860, Dec. 2013.

[40] A. Yanguas-Gil, N. Kumar, Y. Yang, and J. R. Abelson, "Highly conformal film growth by chemical vapor deposition. II. Conformality enhancement through growth inhibition," *J. Vac. Sci. Technol. A Vacuum, Surfaces, Film.*, vol. 27, no. 5, pp. 1244–1248, Sep. 2009.

[41] S. Babar, N. Kumar, P. Zhang, J. R. Abelson, a. C. Dunbar, S. R. Daly, and G. S. Girolami, "Growth Inhibitor To Homogenize Nucleation and Obtain Smooth HfB$_2$ Thin Films by Chemical Vapor Deposition," *Chem. Mater.*, vol. 25, no. 5, pp. 662–667, Mar. 2013.

[42] W. Liao and J. G. Ekerdt, "Effect of CO on Ru Nucleation and Ultra-Smooth Thin Film Growth by Chemical Vapor Deposition at Low Temperature," *Chem. Mater.*, vol. 25, no. 9, pp. 1793–1799, May 2013.

[43] W. Liao and J. G. Ekerdt, "Ru nucleation and thin film smoothness improvement

with ammonia during chemical vapor deposition," *J. Vac. Sci. Technol. A Vacuum, Surfaces, Film.*, vol. 34, no. 3, p. 31508, May 2016.

[44] W. Liao and J. G. Ekerdt, "Precursor dependent nucleation and growth of ruthenium films during chemical vapor deposition," *J. Vac. Sci. Technol. A Vacuum, Surfaces, Film.*, vol. 34, no. 4, p. 41514, Jul. 2016.

[45] I. Langmuir, "The mechanism of the catalytic action of platinum in the reactions $2CO + O_2 = 2CO_2$ and $2H_2 + O_2 = 2H_2O$," *Trans. Faraday Soc.*, vol. 17, no. 1905, p. 621, 1922.

[46] S. Kannan Selvaraj, J. Parulekar, and C. G. Takoudis, "Selective atomic layer deposition of zirconia on copper patterned silicon substrates using ethanol as oxygen source as well as copper reductant," *J. Vac. Sci. Technol. A Vacuum, Surfaces, Film.*, vol. 32, no. 1, p. 10601, 2014.

[47] L. T. Zhuravlev, "Concentration of hydroxyl groups on the surface of amorphous silicas," *Langmuir*, vol. 3, no. 3, pp. 316–318, 1987.

[48] K. J. Hughes and J. R. Engstrom, "Nucleation delay in atomic layer deposition on a thin organic layer and the role of reaction thermochemistry," *J. Vac. Sci. Technol. A Vacuum, Surfaces, Film.*, vol. 30, no. 1, p. 01A102, 2012.

[49] D. Monnier, I. Nuta, C. Chatillon, M. Gros-Jean, F. Volpi, and E. Blanquet, "Gaseous Phase Study of the Zr-Organometallic ALD Precursor TEMAZ by Mass Spectrometry," *J. Electrochem. Soc.*, vol. 156, no. 1, p. H71, 2009.

[50] C. L. Yaws and M. A. Satyro, "Vapor Pressure – Organic Compounds," in *The Yaws Handbook of Vapor Pressure*, 2nd ed., Burlington: Elsevier, 2015, pp. 1–314.

[51] C. Morant, J. M. Sanz, L. Galán, L. Soriano, and F. Rueda, "An XPS study of the

interaction of oxygen with zirconium," *Surf. Sci.*, vol. 218, no. 2–3, pp. 331–345, Aug. 1989.

[52] D. Majumdar and D. Chatterjee, "X-ray photoelectron spectroscopic studies on yttria, zirconia, and yttria-stabilized zirconia," *J. Appl. Phys.*, vol. 70, no. 1991, pp. 988–992, 1991.

[53] S. Svensson, A. Naves de Brito, M. P. Keane, N. Correia, and L. Karlsson, "Observation of an energy shift in the S $2p_{3/2}$ -S $2p_{1/2}$ spin-orbit splitting between x-ray photoelectron and Auger-electron spectra for the H2S molecule," *Phys. Rev. A*, vol. 43, no. 11, pp. 6441–6443, Jun. 1991.

[54] T. L. Barr, "An XPS study of Si as it occurs in adsorbents, catalysts, and thin films," *Appl. Surf. Sci.*, vol. 15, no. 1–4, pp. 1–35, Apr. 1983.

[55] D. A. Shirley, "High-Resolution X-Ray Photoemission Spectrum of the Valence Bands of Gold," *Phys. Rev. B*, vol. 5, no. 12, pp. 4709–4714, Jun. 1972.

[56] T. L. Barr and S. Seal, "Nature of the use of adventitious carbon as a binding energy standard," *J. Vac. Sci. Technol. A Vacuum, Surfaces, Film.*, vol. 13, no. 3, p. 1239, May 1995.

[57] C. Mui, G. T. Wang, S. F. Bent, and C. B. Musgrave, "Reactions of methylamines at the Si(100)-2×1 surface," *J. Chem. Phys.*, vol. 114, no. 22, pp. 10170–10180, Jun. 2001.

[58] J. C. F. Rodríguez-Reyes and A. V. Teplyakov, "Mechanisms of adsorption and decomposition of metal alkylamide precursors for ultrathin film growth," *J. Appl. Phys.*, vol. 104, no. 8, p. 84907, Oct. 2008.

[59] J. Liu, M. Liao, M. Imura, A. Tanaka, H. Iwai, and Y. Koide, "Low on-resistance

diamond field effect transistor with high-k ZrO_2 as dielectric.," *Sci. Rep.*, vol. 4, p. 6395, 2014.

[60]   C. Sleigh, A. P. Pijpers, A. Jaspers, B. Coussens, and R. J. Meier, "On the determination of atomic charge via ESCA including application to organometallics," *J. Electron Spectros. Relat. Phenomena*, vol. 77, no. 1, pp. 41–57, Feb. 1996.

[61]   Y. Zhou, N. Kojima, H. Sugiyama, K. Ohara, and K. Sasaki, "Preparation of ZrO_2 ultrathin films as gate dielectrics by limited reaction sputtering — On growth delay time at initial growth stage," *Appl. Surf. Sci.*, vol. 254, no. 19, pp. 6131–6134, Jul. 2008.

[62]   K. J. Hughes, A. Dube, M. Sharma, and J. R. Engstrom, "Initial Stages of Atomic Layer Deposition of Tantalum Nitride on SiO_2 and Porous Low-κ Substrates Modified by a Branched Interfacial Organic Layer: Chemisorption and the Transition to Steady-State Growth," *J. Phys. Chem. C*, vol. 116, no. 41, pp. 21948–21960, Oct. 2012.

[63]   G. Soto, J. A. Díaz, and W. de la Cruz, "Copper nitride films produced by reactive pulsed laser deposition," *Mater. Lett.*, vol. 57, no. 26–27, pp. 4130–4133, Sep. 2003.

[64]   R. Scheer and H. J. Lewerenz, "Photoemission study of evaporated $CuInS_2$ thin films. II. Electronic surface structure," *J. Vac. Sci. Technol. A Vacuum, Surfaces, Film.*, vol. 12, no. 1, pp. 56–60, Jan. 1994.

[65]   C. L. Roe, "Reaction of 1,2-ethanedithiol on clean, sulfur-modified, and carbon-modified Mo (110) surfaces," *Journal of Vacuum Science & Technology A: Vacuum, Surfaces, and Films*, vol. 16, no. 110. p. 1066, 1998.

[66]   J. Scofield, "Hartree-Slater Subshell Photoionization Cross-Sections at 1254 and

1487 eV," *J. Electron Spectros. Relat. Phenomena*, vol. 8, pp. 129–137, 1976.

[67]   C. J. Powell and A. Jablonski, "Consistency of calculated and measured electron inelastic mean free paths," *J. Vac. Sci. Technol. A Vacuum, Surfaces, Film.*, vol. 17, no. 4, p. 1122, 1999.

[68]   Haynes W. M., *CRC Handbook of Chemistry and Physics, 97th Edition*, 97th ed. Boca Raton, FL.: CRC Press/Taylor & Francis, 2017.

[69]   A. Gharachorlou, M. D. Detwiler, X.-K. Gu, L. Mayr, B. Klötzer, J. Greeley, R. G. Reifenberger, W. N. Delgass, F. H. Ribeiro, and D. Y. Zemlyanov, "Trimethylaluminum and Oxygen Atomic Layer Deposition on Hydroxyl-Free Cu(111)," *ACS Appl. Mater. Interfaces*, vol. 7, no. 30, pp. 16428–16439, Aug. 2015.

[70]   D. C. Bradley and M. H. Chisholm, "Transition-metal dialkylamides and disilylamides," *Acc. Chem. Res.*, vol. 9, no. 7, pp. 273–280, Jul. 1976.

[71]   F. Wiame, V. Maurice, and P. Marcus, "Reactivity to sulphur of clean and pre-oxidised Cu(1 1 1) surfaces," *Surf. Sci.*, vol. 600, no. 18, pp. 3540–3543, 2006.

[72]   S. W. Joo, S. W. Han, and K. Kim, "Multilayer formation of 1,2-ethanedithiol on gold: surface-enhanced Raman scattering and ellipsometry study," *Langmuir*, vol. 16, no. 12, pp. 5391–5396, 2000.

6 Effects of co-adsorbates on atomic layer deposition of zirconium oxide on SiO$_2$ and Cu: fundamental examinations of alternative approaches to self-aligned, selective area atomic layer deposition

6.1 Overview

We reported a continued study on alternative approaches to self-aligned, selective area atomic layer deposition (ALD) that are fast, exclusively vapor phase, involving "zero-thickness / zero residue" modification layers by means of introducing a third species, called co-adsorbates, in a conventional ALD cycle. Triethylamine (TEA) and 1,2 – ethanedithiol (EDT), two out of the four co-adsorbates molecules that were proved to be promising in the selective chemisorption study, were further examined in multiple cycles of ZrO$_2$ ALD. Area selectivity was found to be extended into multiple cycle regime: for TEA 1½ cycle seem to have very similar mechanism as in the case of ½ cycle; for EDT an estimated onset of film growth on Cu $\sim$ 9½ cycles. We also screened two additional co-adsorbates, pyridine and triethylphosphine (TEP), using modified 5-cycle ZrO$_2$ ALD. Enhanced growth of ZrO$_2$ with the presence of pyridine or TEP, and we postulated that one possible mechanism is catalytic reactions involving hydrogen bond or lone pair electrons.

6.2 Introduction

We have identified two out of four co-adsorbate molecules that have potential for selective deposition of ZrO$_2$ ALD based on the results of selective chemisorption described

in Chapter 5. Selective chemisorption of the transitional precursor in the first half-cycle of an ALD process is a necessary, but not sufficient condition for selective area growth. In this chapter, we extended the scheme of competitive adsorption of the transition metal precursor and the co-adsorbate from the first half-cycle to multiple ALD cycles.   Two significant challenges were involved in the extending work reported here. First, competitive adsorption took place multiple times during the ALD process, as compared to only once in the first half-cycle. The cumulative exposure of the transition metal precursor was therefore multiplied, and precursor molecules could start to nucleate in an extended period of dose time. More importantly the co-reactant was introduced in the full ALD cycle, so the number of reactants increased from two to three. More pathways to gas-phase and surface reactions consequently became possible due to increased combinations of species in the system. Reactions between the substrate surface and the co-reactant, such as oxidation reaction of metal surfaces, could affect the nucleation of precursor molecules considerably. We first extended the competitive adsorption study of 1,2-ethanedithiol (EDT) / triethylamine (TEA) and Tetrakis(ethylmethylamido)zirconium(IV) $\{Zr[N(CH_3)(CH_2CH_3)]_4$, TEMAZ$\}$to multiple cycles of ZrO_2 ALD.   Two additional candidates for co-adsorbates, pyridine and triethylphosphate (TEP), are examined for their effects on ZrO_2 ALD on the two surfaces (SiO_2 and Cu) by competitive adsorption using *in situ* X-ray photoelectron spectroscopy (XPS).

6.3 Experimental Procedures

Experiments reported here are carried out in a custom designed ultrahigh vacuum system (UHV) coupled with a micro-reactor for *in situ* ALD. The chamber/reactor design and the operating procedures are described in detail in Chapter 3. SiO_2 substrates were prepared starting from single-side polished, Si(100) wafers (B doped, resistivity 38-63 Ω cm) The native SiO_2 layer was removed from the substrates by submerging in buffered oxide etch (BOE) for 2 minutes. The substrates were then re-oxidized by dipping in Nanostrip for 15 min at a temperature of ~75 °C. The BOE/Nanostrip treatment was then repeated. This method is known to produce a 15-20 Å layer of chemical oxide with surface Si-OH density ~ 5 ×10^{14} cm^{-2} [1], [2]. The Cu substrate in this work is a 900 Å thick Cu thin film deposited on SiO_2 via physical vapor deposition.

TEMAZ, water and co-adsorbates are stored in stainless steel bubblers, and the dosage can be controlled by the bubbler temperature, carrier gas flow rate and the extent of dilution with an inert gas flow. The TEMAZ bubbler is kept at 40 °C, producing a vapor pressure of ~ 30 mTorr [3]. Vapor pressure ratio of the co-adsorbate to TEMAZ are 2.96 and 23.9 for the case of EDT and TEA, respectively. The water bubbler is maintained at 0 °C, producing a vapor pressure of ~ 4.6 Torr. Experiments involving EDT and TEA were conducted under an operating pressure of 18 Torr. The SiO_2 or Cu substrate, loaded on a custom platen for a 4" wafer, is thermalized *in vacuo* to ~150 °C for an hour prior to the exposure. Experiments involving TEMAZ/H_2O/EDT have dosing sequences of [AB]$_{×20}$ and [AB]$_{×40}$, where A denotes the first half cycle [EDT (120 s), TEMAZ + EDT (120 s), EDT (120 s) and N_2 (120 s)] and B denotes the second half cycle [H_2O (120 s) and N_2 (120

s)]. Experiments involving TEA has a dosing sequence of ABA (1.5 cycle), where A

denotes the first half cycle [TEA (180 s), TEMAZ + TEA (180 s), TEA (180 s) and N_2 (180

s)] and B denotes the second half cycle [O_2 (180 s) and N_2 (180 s)].

Experiments involving pyridine and TEP were conducted under an operating

pressure of 5 Torr. Two rectangular samples (1.02×2.54 cm^2) was designed to create

identical experimental conditions on the two surfaces (SiO_2 and Cu) and to enable side-by-

side surface characterization. Both SiO_2 and Cu substrates are vacuum annealed at ~180

°C for an hour before the exposure to ensure the initial conditions of the surfaces are well-

controlled. The TEMAZ bubbler is kept at 47 °C, producing a vapor pressure of ~ 60

mTorr [3]. Vapor pressure ratio of the co-adsorbate to TEMAZ are 3.89 and 6.03 for the

case of pyridine and TEP, respectively. Three inflows (a precursor stream, a co-adsorbate

stream and 10 sccm of N_2 as the third inflow) are arranged for this set of experiments.

Experiments involving TEP has a dosing sequence of [AB]$_{\times 20}$, where A denotes the first

half cycle [TEP (120 s), TEMAZ + TEP (120 s), TEP (120 s) and N_2 (120 s)] and B denotes

the second half cycle [O_2 (1 s) and N_2 (120 s)], and the dose sequence for pyridine is

analogous to the that for TEP.

6.4 Results and Discussions

6.4.1 ZrO$_2$ ALD experiments extended from selective chemisorption

6.4.1.1 1,2-ethanedithiol

We observed selective chemisorption on TEMAZ on SiO_2 over Cu with an EDT/TEMAZ ratio of 2.96 (described in Chapter 5). Here we conducted multiple-cycle ZrO_2 ALD experiments with the same EDT / TEMAZ ratio. We also retained the dosing pattern in the TEMAZ half cycle, namely EDT pre-dose followed by co-dose of TEMAZ and EDT, and EDT post-dose. While the dose time in each step decreased from 5 mins to 2 mins, the total TEMAZ dose time for 20 and 40 ALD cycles are 8 and 16 times longer than that in previous experiments, respectively. Water was used as the co-reactant / oxidizer, and a growth rate per cycle of ~0.7 Å-cycle^{-1} for the TEMAZ/H_2O chemistry using the micro-reactor system was reported in Chapter 3.

In Fig. 6-1(a) and (b) we display the XP spectra from the Zr(3d) region of 20 and 40 cycles of EDT-modified ZrO_2 ALD on SiO_2 and Cu. Zr(3d) spectra were fit assuming a spin-orbit doublet separation of 2.4 eV with a fixed ratio of 2:3 for the $3d_{3/2}$ to $3d_{5/2}$ peak area [4], [5]. Zr($3d_{5/2}$) binding energy (BE) for the case of SiO_2 ~ 183 eV is in good agreement with the report values of BE of the ZrO_2 film, including our previous work [6]–[8]. Zr($3d_{5/2}$) binding energy (BE) for the case of Cu ~ 182.3 eV was closer to that of chemisorbed TEMAZ on Cu (described in Chapter 4) than that of a bulk ZrO_2 film. As may be seen there was a considerable delay in the growth of ZrO_2 ALD film on Cu as compared to that on SiO_2 for both 20 and 40 cycles. As is evidenced by reduced amounts of Zr and BEs lower than typical values, we postulated that ZrO_2 ALD film growth on Cu was attenuated by EDT and, as a result, was before its formation of continuous thin film.
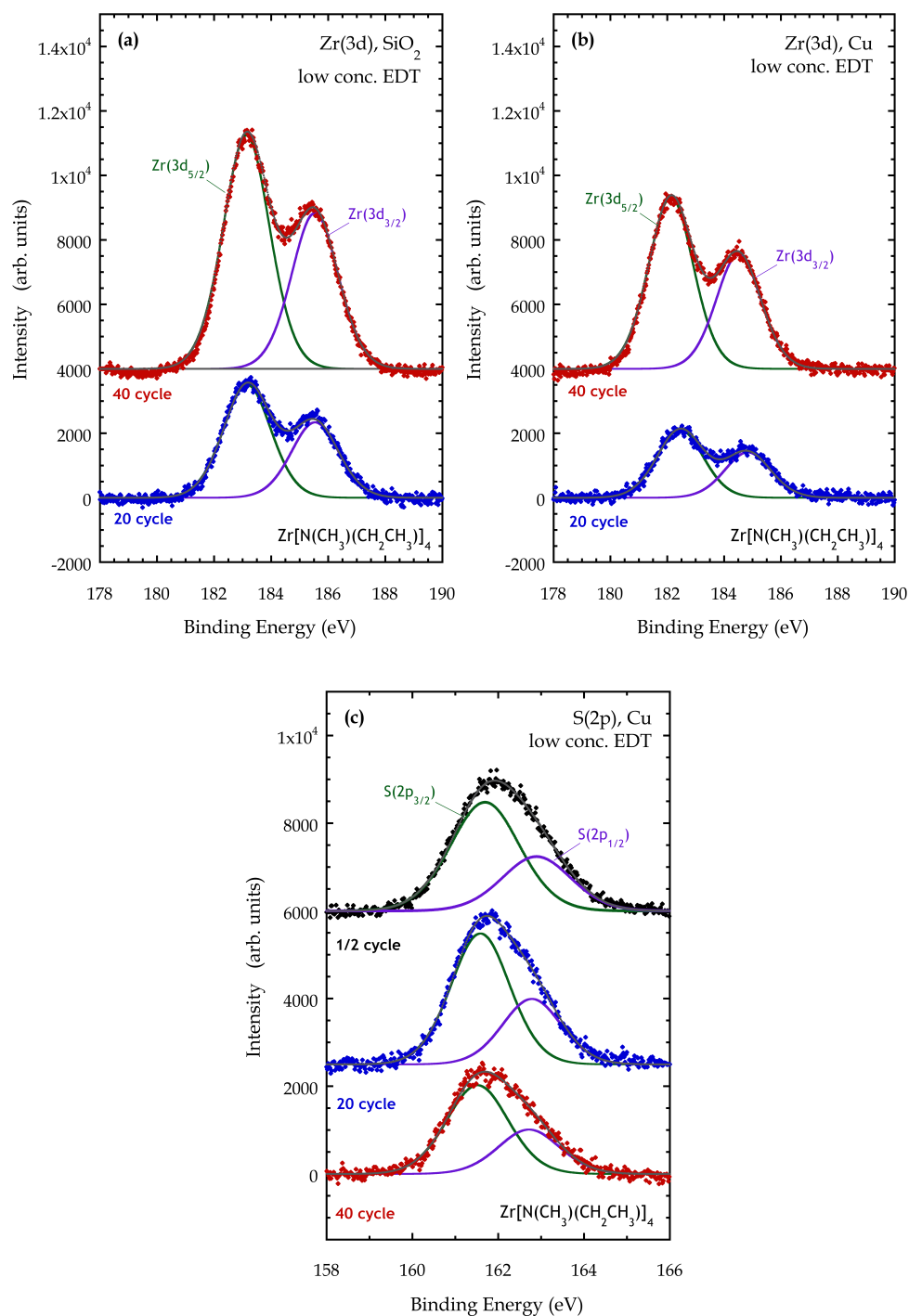
Figure 6-1: X-ray photoelectron spectrum of a SiO_2 and Cu surface after 20 and 40 cycles of ZrO_2 ALD using $Zr[N(C_2H_5)(CH_3)]_4$ and H_2O as reactants and $HS(CH_2)_2SH$ as the co-adsorbate. In **(a)** and **(b)** the Zr(3d) peak on SiO_2 or Cu is fit well to a doublet defined by a single binding energy. In **(c)** we fit the S(2p) feature on Cu also to a doublet.

In Fig. 6-1(c) we displayed the XP spectra from the S(2p) region of ½, 20 and 40 cycles of EDT-modified ZrO_2 ALD on Cu. As may be seen the amount of sulfur for all three cases were quite similar, with the amount of 40 cycles slightly lower than those of ½ and 20 cycles.

We further quantify thicknesses of ZrO_2 ALD films on both surfaces using the following simple equations describing a 2D thin film on top of a buried substrate:

$$I_{film}(\theta) = I_{0,film}\left(1 - \exp\left(-\frac{d_{film}}{\lambda_{f,film}\cos\theta}\right)\right) \qquad (6-1)$$

$$I_{subs}(\theta) = I_{0,subs}\left(\exp\left(-\frac{d_{film}}{\lambda_{s,film}\cos\theta}\right)\right) \qquad (6-2)$$

where d_{film} is the thickness of the 2D film, and θ is the takeoff angle in the setup of XPS. Integrated intensities from the film and the substrates (I_{film} and I_{subs}) are Zr(3d) integrated intensities and those of Cu(2p$_{3/2}$) and Si(2p) peaks from buried substrates in the EDT-modified ZrO_2 ALD experiments, respectively. Unattenuated intensities from the film and the substrates ($I_{0,film}$ and $I_{0,subs}$) were obtained by fitting XPS results (at a takeoff angle of 0°) from a large number of TEMAZ experiments to the following equation that described the relation of the two intensities (shown in Fig. 6-2) by combining equations (6-1) and (6-2):

$$I_{subs}(\theta) = I_{0,subs}\left(1 - \frac{I_{film}(\theta)}{I_{0,film}}\right)^{\frac{\lambda_{f,film}}{\lambda_{s,film}}} \qquad (6-3)$$

Ratios of inelastic mean free paths ($\lambda_{f,\,film}/\lambda_{s,\,film}$) were calculated from an empirical formula suggested by Tanuma, Powell and Penn [9].
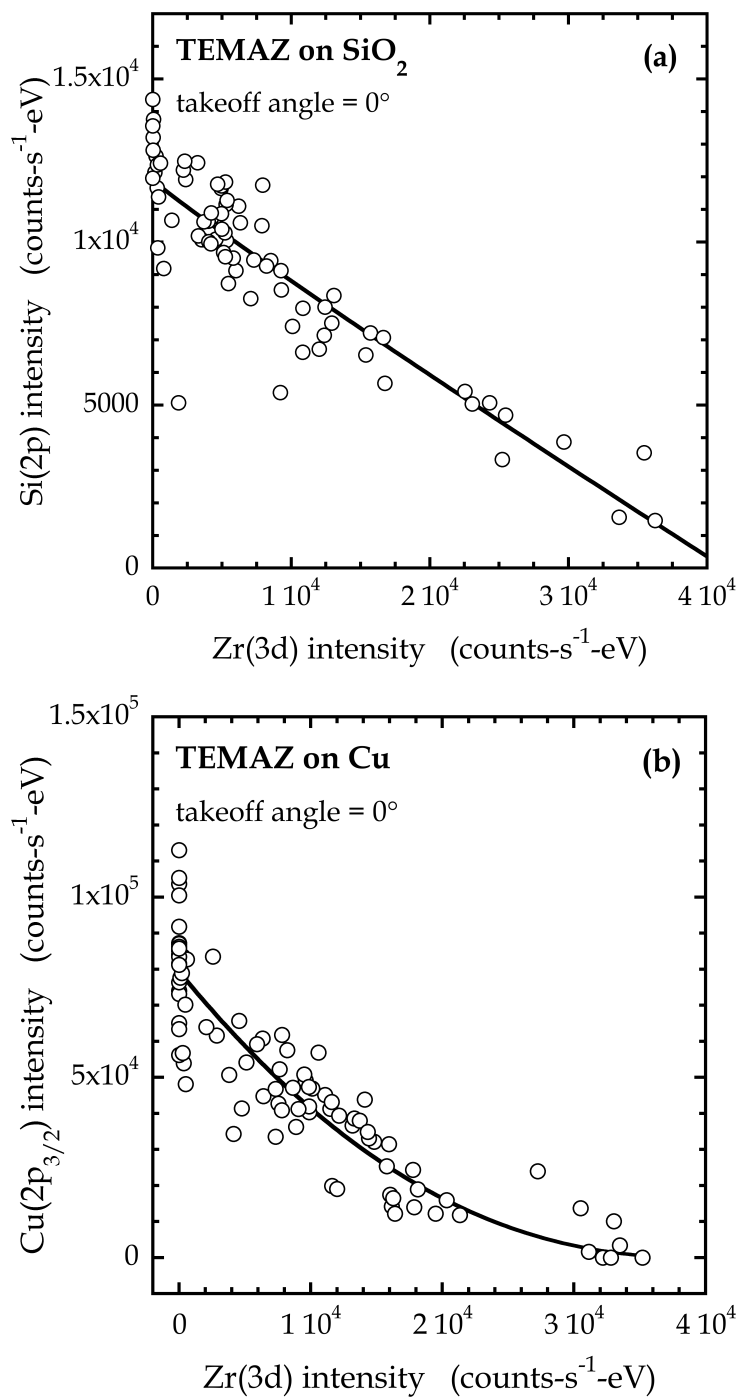
Figure 6-2: (a) The intensity of the Si(2p) XPS feature and (b) the intensity of the Cu(2p) feature versus the intensity of Zr(3d) feature for experiments in which $Zr[N(C_2H_5)(CH_3)]_4$ is one of the reactants, with a photoelectron takeoff angle of 0° (referred to as "universal curves").

In Fig. 6-3 we display estimated film thicknesses of ZrO_2 from film and substrate intensities for pristine ZrO_2 ALD on SiO_2 as well as EDT-modified ZrO_2 ALD on SiO_2 and Cu. As may be seen ZrO_2 ALD films with the use of EDT (on both SiO_2 and Cu) were thinner than pristine ZrO_2 ALD film. By a linear fit to thicknesses from both film and substrate signals, average growth rate per cycle of pristine ALD on SiO_2, EDT-modified ALD on SiO_2, and EDT-modified ALD on Cu were estimated to be 0.67, 0.52 and 0.31 Å-cycle^{-1}, respectively. Modulation of ZrO_2 ALD film growth with the introduction of the co-adsorbate (EDT) was demonstrated by a ~ 22% decrease in the growth rate on SiO_2 and a ~ 53% decrease on Cu. We also observed that the growth of ZrO_2 ALD on SiO_2 is preferred than that on Cu despite almost identical Zr(3d) intensities on SiO_2 and Cu were observed in the TEMAZ chemisorption experiments without any co-adsorbate (see Chapter 5). Moreover, an onset at ~ 9.5 cycles as we extrapolated ZrO_2 film thickness on Cu estimated by Zr(3d) signals to the vertical axis. This provided us with a clearer picture as to when the selectivity was lost between the first and the twentieth ALD cycle.

We also quantify the amount of sulfur in the $ZrO_2|Cu$ system. To calculate the atomic density of S we compare the integrated intensity of the $S(2p_{3/2})$ peak from S(a) to that of the $Au(4f_{7/2})$ peak from an evaporated thin film of Au [2], [10]. In addition, we account for the relative photoionization cross-sections, σ_{Au}/σ_S=8.51 [11], analyzer transmission function, $T(E_{Au})/T(E_S)$=(1170 eV/ 1093 eV)$^{-1}$=0.93, the attenuation length of the $Au(4f_{7/2})$ photoelectrons, λ_{Au}=15.5 Å [12], and the atomic density of Au, N_{Au}=5.90 × 10^{22} cm^{-3} [13]. We further assumed a sulfur interfacial layer in between ZrO_2 and Cu, and

the S(2p) intensity was corrected by the attenuation effect of an ZrO_2 overlayer with an estimated thickness from Fig. 6-3.

After correction to the attenuation effect, S densities for 20 and 40 cycles were 2.64 and 2.60×10^{15} atoms-cm^{-2}. This suggests that absolute amount of sulfur on Cu seems to reach a maximum after a sufficient dose of EDT. To compare, a calculated surface density of S of 2.67×10^{15} atoms-cm^{-2} for the case of TEMAZ / high conc. EDT was also very close to the maximum.
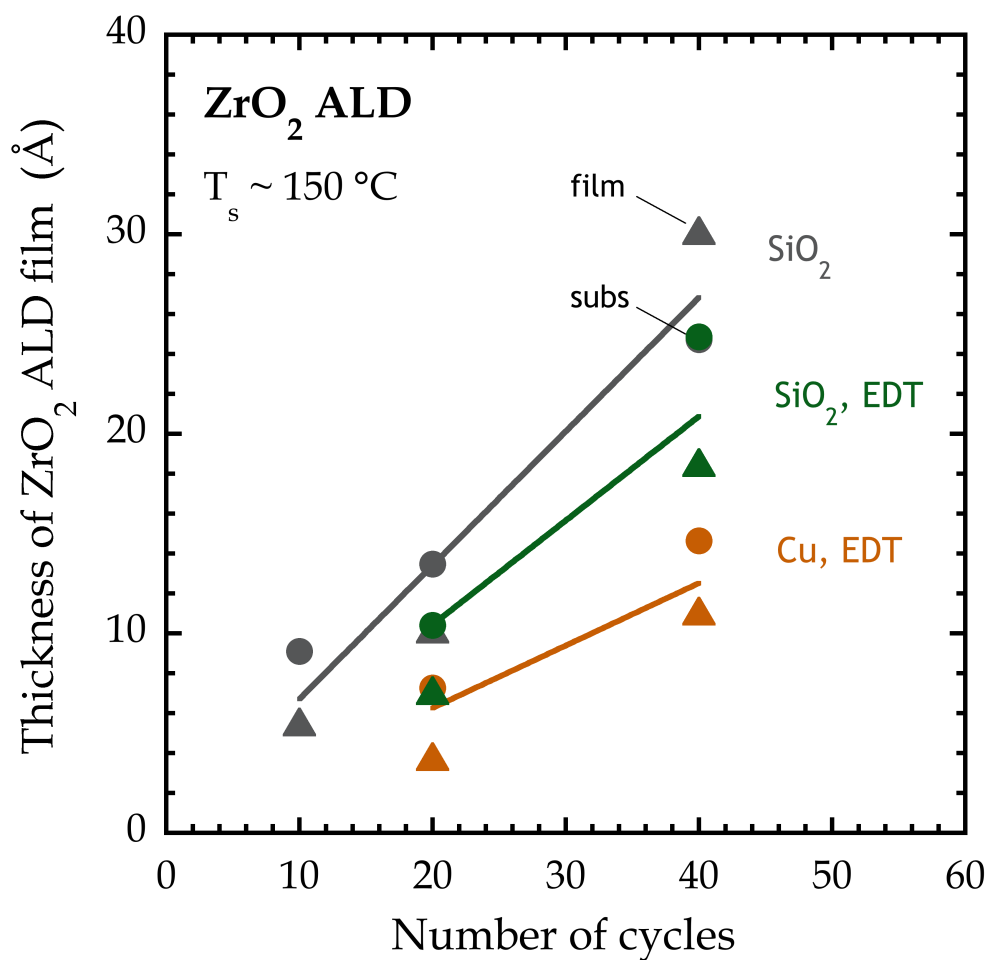
Figure 6-3: Thickness of the ZrO_2 thin films (regular ALD on SiO_2, gray symbols; EDT-modified ALD on SiO_2, green symbols; EDT-modified ALD on Cu, orange symbols) as a function of the number of ALD cycles, as measured by *in situ* XPS of the thin film component (Zr, triangles) and the substrate component (Si/Cu, circles). The lines are straight line fits that pass through the origin.

6.4.1.2 Triethylamine

We conducted 1.5-cycle ZrO_2 ALD experiments with the TEA / TEMAZ ratio in which selective chemisorption on TEMAZ on SiO_2 over Cu was observed. Here oxygen, instead of water, was used as co-reactant. Keuter *et al.* reported ALD chemistry of ZrO_2 using TEMAZ and molecular oxygen with a growth rate of ~ 1.0 Å-cycle^{-1} and a narrow ALD window of 200 – 220 °C [14]. In Fig. 6-4 we display estimated film thicknesses from film and substrate intensities for ZrO_2 ALD using TEMAZ and O_2 by the method described in Section 6.4.1.1.. Unattenuated intensities in this case were obtained by fitting XPS results at a takeoff angle of 38.5°, as shown in Fig. 6-5. An average growth rate per cycle of ~ 1.2 Å-cycle^{-1} using all data was in good agreement with the reported value.

In Fig. 6-6 we display the Zr densities (calculated from XPS results) for 1.5-cycle, regular and TEA-modified ZrO_2 ALD on SiO_2 and Cu as well as their half-cycle counterparts. We can clearly see that Zr densities of 1.5 cycles for all four cases almost doubled from those of half cycle. All Zr densities were not corrected for the attenuation effect under the assumption that these ZrO_2 'films' were very thin.
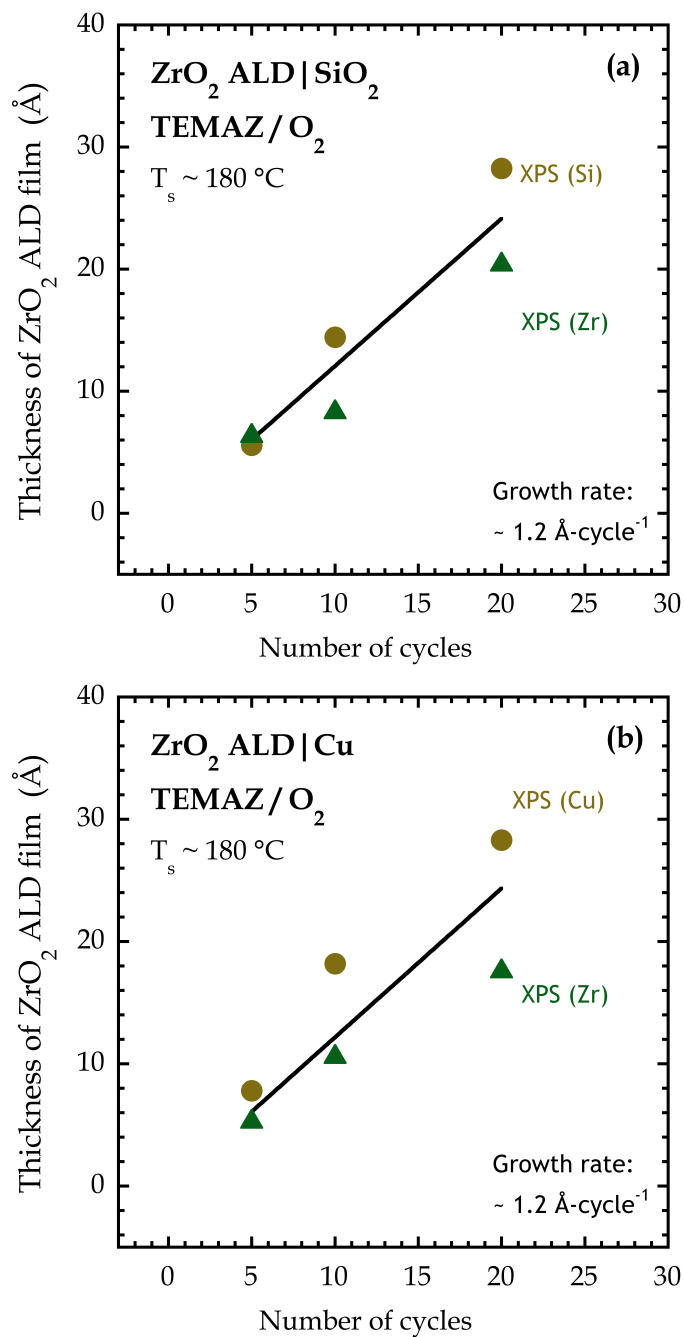
Figure 6-4: Thickness of the ZrO_2 thin film using $Zr[N(C_2H_5)(CH_3)]_4$ and O_2 as reactants as a function of the number of ALD cycles, as measured by *in situ* XPS of the thin film component (Zr, green triangles) and the substrate component (Si/Cu, brown circles) on **(a)** SiO_2 and **(b)** Cu. The lines are straight line fits of all the data points that pass through the origin.
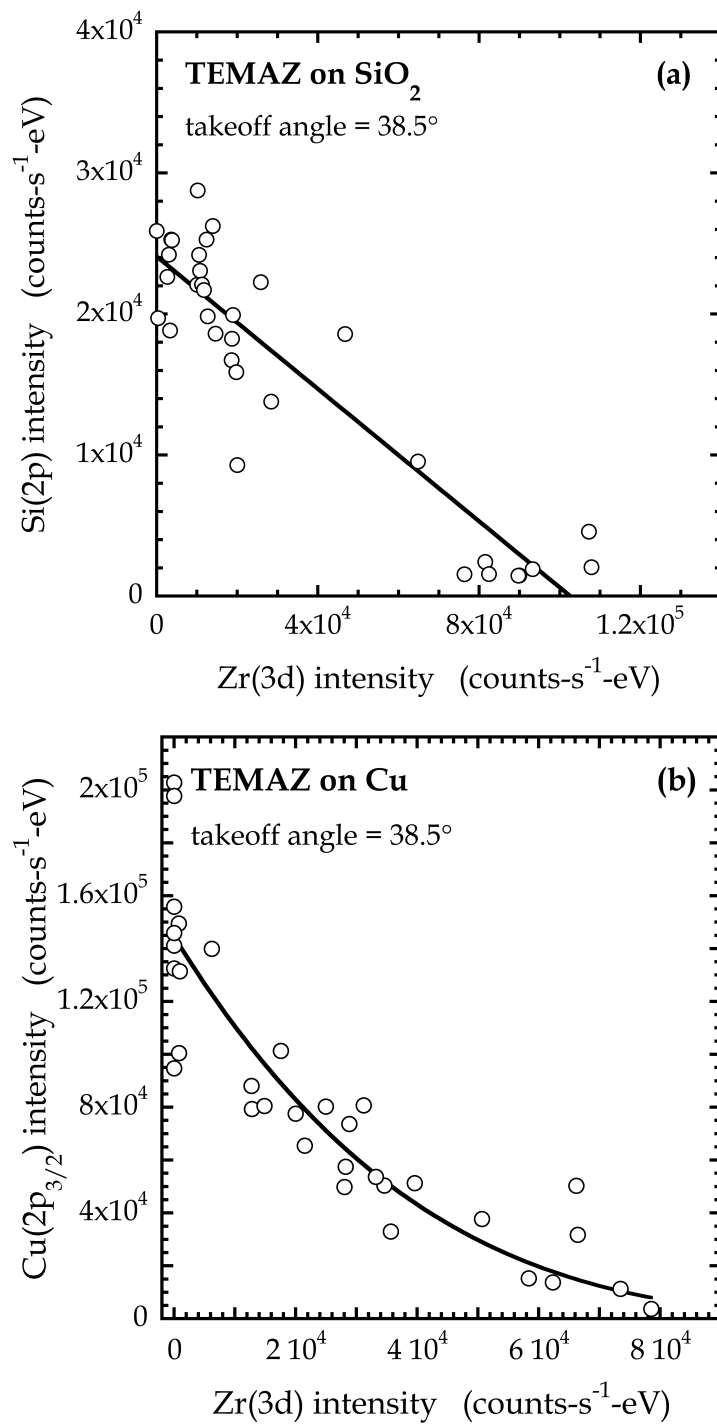
Figure 6-5: (a) The intensity of the Si(2p) XPS feature and **(b)** the intensity of the Cu(2p) feature versus the intensity of Zr(3d) feature for experiments in which $Zr[N(C_2H_5)(CH_3)]_4$ is one of the reactants, with a photoelectron takeoff angle of 38.5°.
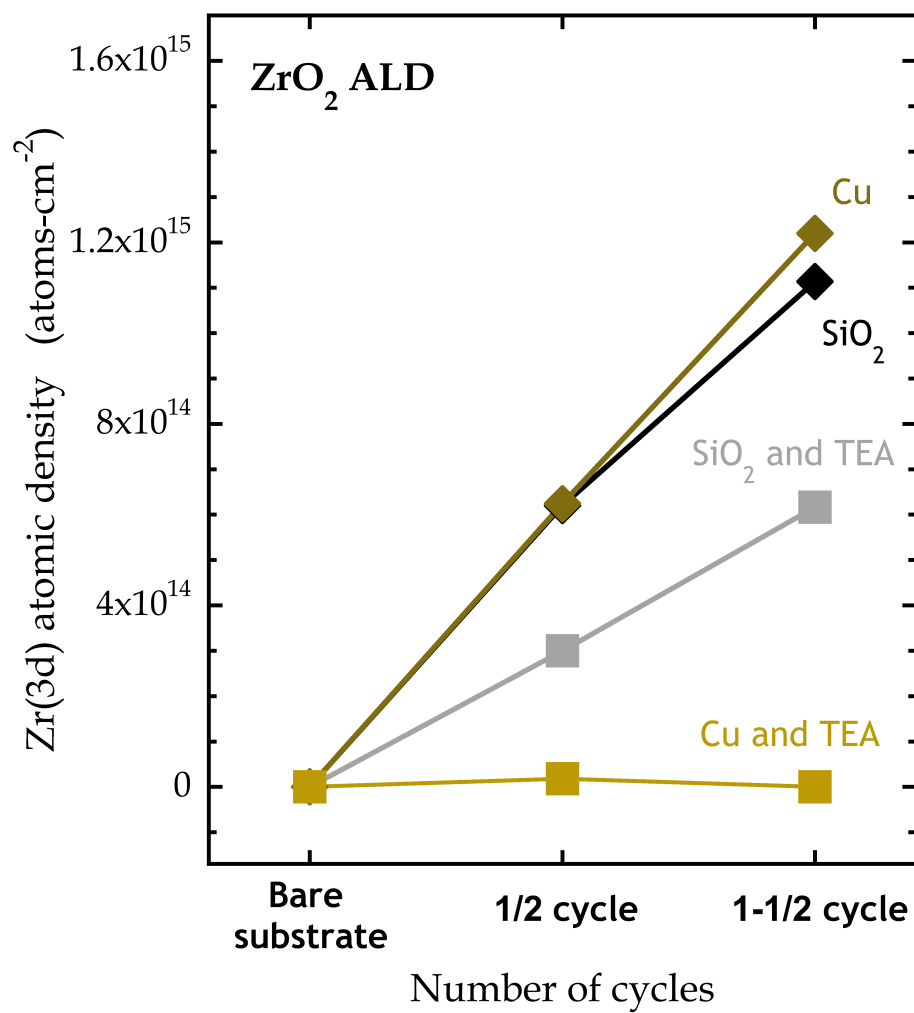
Figure 6-6: Zr atomic density from the Zr(3d) XPS feature of SiO$_2$ and Cu surfaces after

1.5 cycles of regular and TEA-modified ZrO$_2$ ALD using Zr[N(C$_2$H$_5$)(CH$_3$)]$_4$ and O$_2$ as

reactants versus the number of ALD cycles.

Zr densities of regular ZrO_2 ALD (regardless of the substrate surface) were $\sim 6.0 \times 10^{14}$ atoms-cm^{-2} for the half cycle and $\sim 1.2 \times 10^{15}$ atoms-cm^{-2} for 1.5 cycles. By contrast, Zr densities for TEA-modified ZrO_2 ALD was reduced by $\sim$50% on SiO_2 ($\sim 3.0 \times 10^{14}$ atoms-cm^{-2} for half cycle and $\sim 6.0 \times 10^{14}$ atoms-cm^{-2} for 1.5 cycle). Additionally, the curve of Zr densities for TEA-modified ZrO_2 ALD was almost a flat line as shown in the figure; nucleation of TEMAZ on Cu was completely suppressed up to 1.5 cycle using TEA as the co-adsorbate. In Fig. 6-7 we display the XP spectra from the N(1s) region of 1.5-cycle regular and TEA-modified ZrO_2 ALD on SiO_2 and Cu. There was no observable N(1s) peaks for 1.5 cycles on SiO_2 and Cu (same as those for half cycle). This indicated that the suggested mechanism of adsorption reversal the causes selective chemisorption in the TEMAZ/TEA co-adsorption experiments was maintained up to 1.5 cycle in the TEMAZ/O_2/TEA system.

6.4.2 ZrO_2 ALD experiments for screening new co-adsorbates

Pyridine is a heterocyclic molecule and is very stable so that incorporation of impurities of N or C into ALD films can be minimized when it is used as the co-adsorbate. We calculated the surface coverage of pyridine on Cu(110) as function of substrate temperature, as shown in Fig. 6-8.
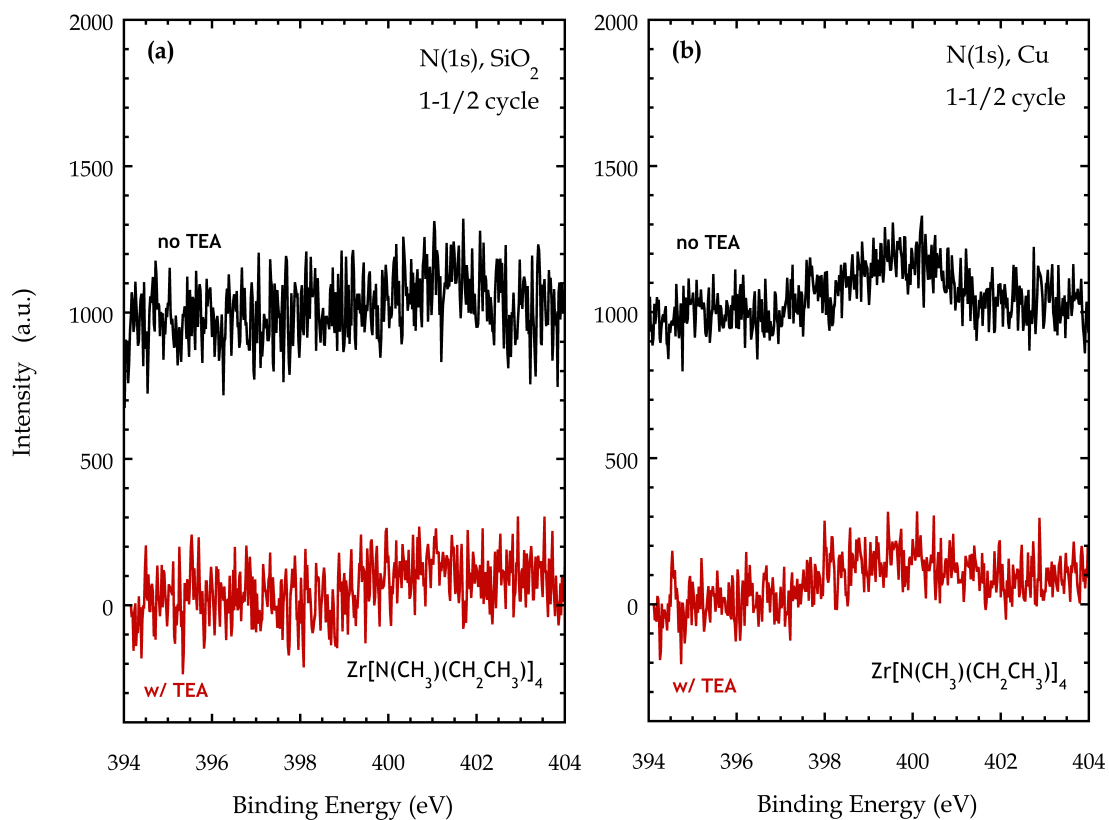
Figure 6-7: X-ray photoelectron spectrum of a SiO_2 and Cu surface after 1.5 cycles of **(a)** regular and **(b)** TEA-modified ZrO_2 ALD using $Zr[N(C_2H_5)(CH_3)]_4$ and H_2O as reactants.
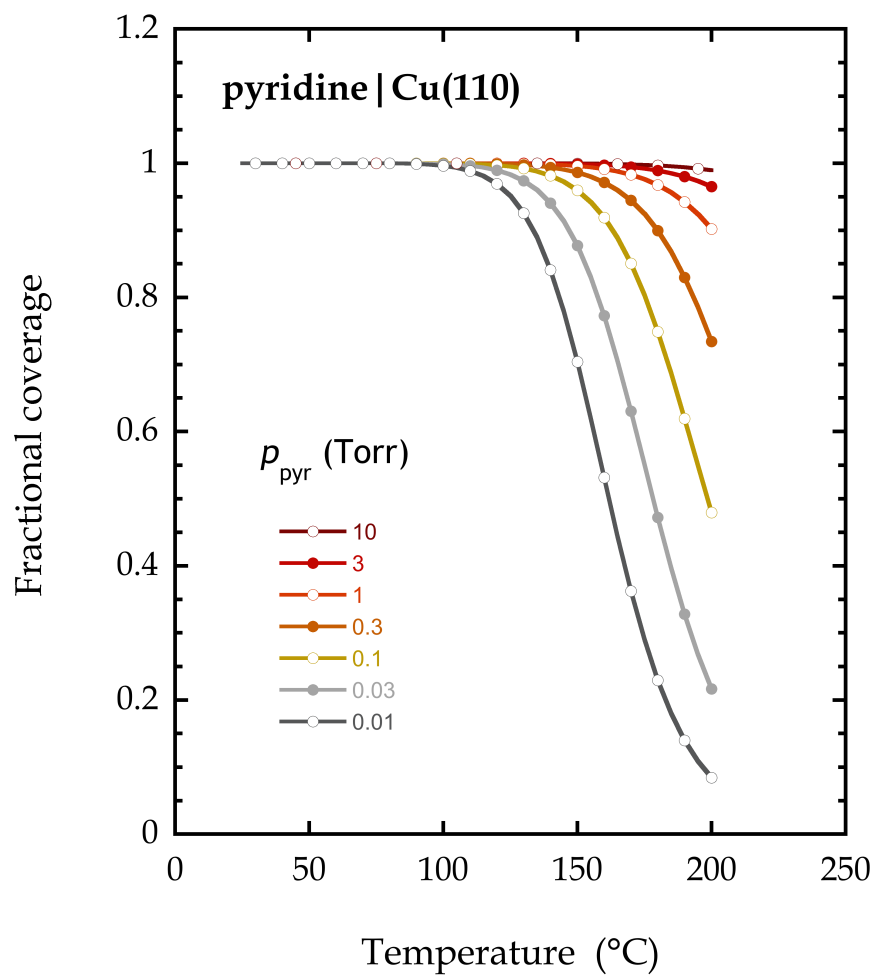
Figure 6-8: Fractional coverage at steady state of pyridine on Cu(110) with various partial pressures of pyridine as a function of substrate temperature. Zero-coverage desorption activation energy of ~ 22.4 kcal-mol[-1] was used in the calculation.

Steady-state coverage is calculated by balancing the adsorption and desorption reactions of pyridine on Cu(110):

$$\frac{d\theta}{dt} = \frac{SF}{n_s}(1-\theta) - k_d\theta \qquad (6-4)$$

where θ is the surface coverage of pyridine, S is the probability of adsorption, F is the impinging flux of pyridine, n_s is the surface density of the active sites, and k_d is the rate constant of desorption reaction [15].

The coverage at the steady-state is determined by setting the rate of change to zero:

$$\theta^{ss} = \left(1 + \frac{k_d n_s}{SF}\right)^{-1} \qquad (6-5)$$

The observation that a steady-state surface coverage under the experimental conditions is close to unity suggests pyridine could block the active sites on Cu during pyridine-modified ALD processes.

Phosphines, like many amines, could have possible interaction with dielectric surfaces via hydrogen bonding to lone pair. Its interaction with many transition metal surfaces is stronger those of other Lewis bases [16]. For example, the binding of trimethylphosphine (TMP) to Cu(110) is ~ 25 kcal-mol^{-1}.

5-cycle ZrO_2 ALD using TEMAZ and O_2 was used to quickly evaluate the effect of pyridine and TEP as co-adsorbate molecules. In Fig. 6-9 we display estimated film thicknesses from Zr(3d) intensities for pristine, pyridine-modified, and TEP-modified ZrO_2 ALD.
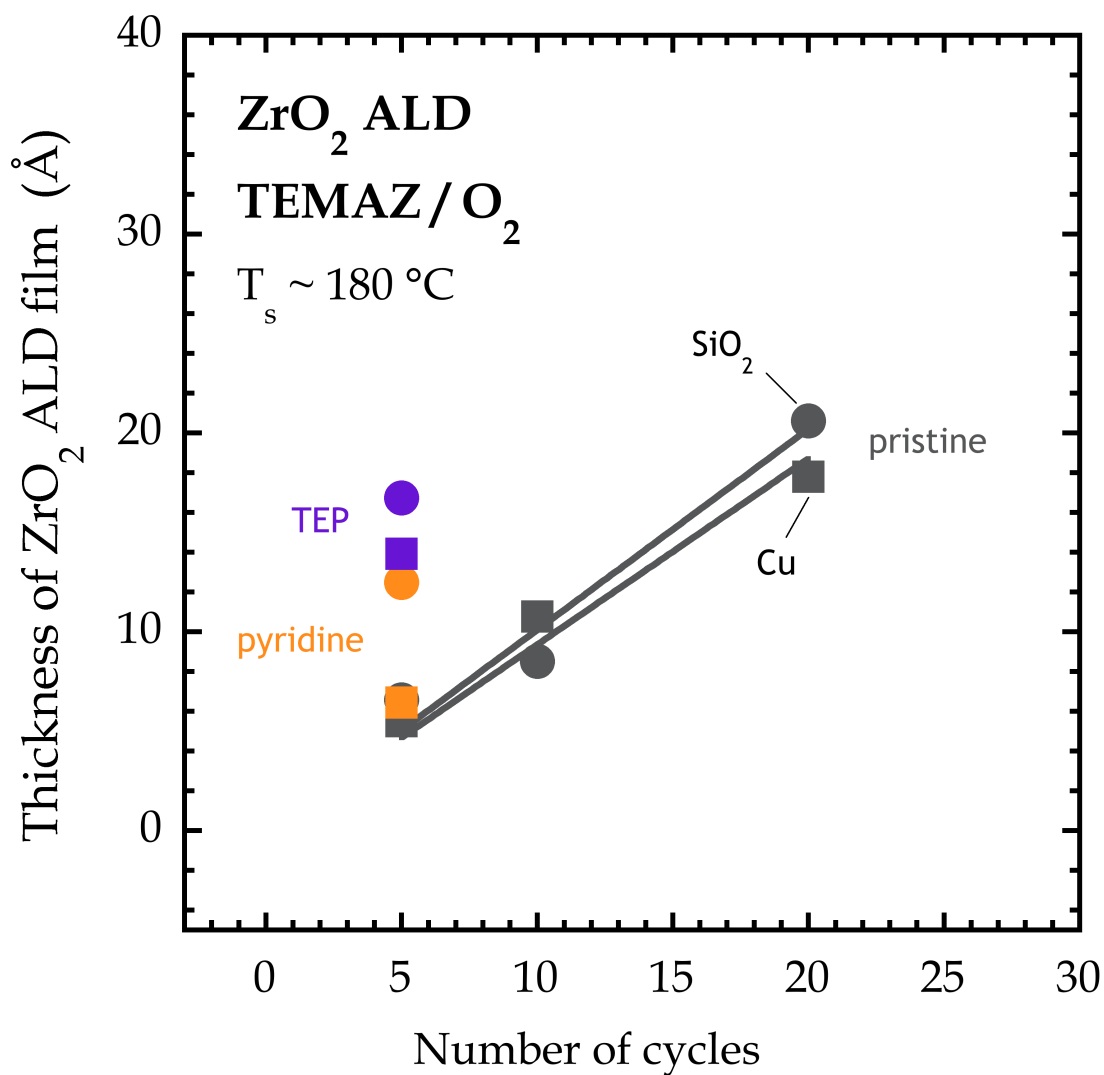
Figure 6-9: Thickness of ZrO_2 thin films (regular ALD, gray symbols; TEP-modified ALD, purple symbols; pyridine-modified, orange symbols) using $Zr[N(C_2H_5)(CH_3)]_4$ and O_2 as reactants as a function of the number of ALD cycles, as measured by *in situ* XPS of the thin film component on SiO_2 (circles) and Cu (squares). The lines are straight line fits that pass through the origin.

As may be seen both pyridine and TEP enhanced the growth rate of ZrO_2 on the two surfaces and therefore were not good candidates for co-adsorbates. In the pyridine case, the Zr(3d) binding energy ~ 182.6 eV was close to that of ZrO_2. N/Zr ratios ~ 0.06 for both SiO_2 and Cu indicated that no to little incorporation of pyridine and its fragments into the film. George and co-workers reported pre-dosed pyridine as the catalyst of SiO_2 ALD chemistry that results in a lower deposition temperature and an enhanced growth rate [17]. Catalytic reactions involving (1) hydrogen bond with surface hydroxyl group and (2) N long pair electrons were proposed based on findings in vibrational studies from Tripp and Hair [18] and Du *et al.* [19]. Similar reaction pathways could have applied to pyridine and chemisorbed TEMAZ molecules on surfaces.

For TEP, the Zr(3d) binding energy ~ 181.8 eV was lower than to that of ZrO_2. This could result from the reduction of Zr by TEP as alkylphosohines can act as reducing agents and remove oxides [20]. P/Zr ratios ~ 0.2 on both surfaces revealed incorporation of P into ZrO_2 film, consistent with the findings of the formation of phosphous on the Cu(110) surface after stepwise deethylation of TEP [16].

6.5 Conclusions and Future works

We examined effects of four molecules, including a thiol, two amines and a phosphine, as co-adorbates on ZrO_2 ALD processes. In the cases of an amine (pyridine) and triethylphosphine, growth rates of ZrO_2 ALD were enhanced by the use of co-adsorbates. In contrast, area selectivity of ZrO_2 on SiO_2 over Cu was demonstrated up to 1.5 cycle in the TEMAZ/O_2/TEA system. It was also predicted that selective growth on

SiO$_2$ over Cu last up to ~9.5 cycle in the TEMAZ/H$_2$O/EDT system. Improvement in the experimental protocol could alleviate the effect of the co-reactant on the starting surface and on the co-adsorbate. First, to remove any oxide that may have formed during the co-reactant step, an additional step of dosing a reducing agent (such as H$_2$) right after the co-reactant dose is suggested. Concerning gas-phase reactions that involve any possible combination of the three gas-phase reactants, reducing the reactor pressure could lead to significant decrease in the reaction rate. Modification to the micro-reactor probe and its exhaust is needed for dropping the reactor pressure by more than an order of magnitude. The overall reaction rate of a binary elementary reaction can be reduced by a factor of a hundred as a result.

We have finished a revised design of the central fluidic feedthrough in the micro-reactor system that increases the conductance of the exhaust line for lowering the reactor pressure, as shown in Fig. 6-10. In this design outer diameters of exhaust lines increase from ¼" to 3/8". We can also decrease the reactor pressure by replacing the current working mechanical pump in the micro-reactor system by a turbo pump, which has a much higher pumping speed. Also, doses of transition metal precursor for all the experiments so far were sufficiently long so that both surfaces were covered by chemisorbed precursor molecules of the maximum density. In some cases inherent selectivity was shown in the initial stages of film growth and was lost at a later time as the dose continued. We could exploit the inherent selectivity as well as reduce the exposure of the surfaces to metal precursor by shortening the precursor dose time.

effluents,
3/8" O.D.

central feedline,
3/8" O.D.

base plate
(probe head side)

base plate
(feedthrough side)
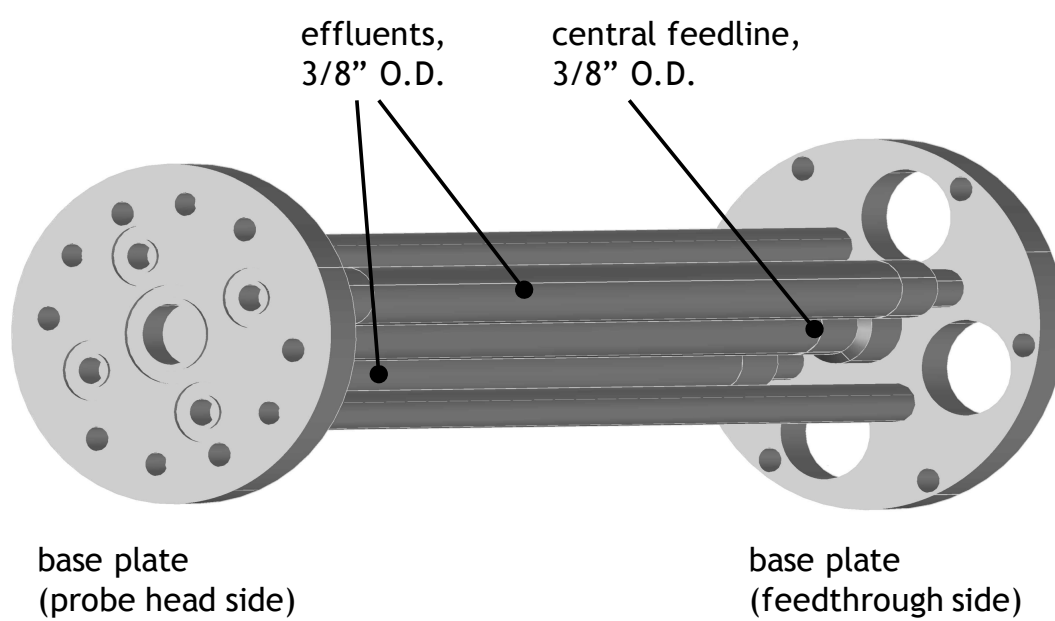
Figure 6-10: Schematic of a revised central fluidic extension design in the micro-reactor system.
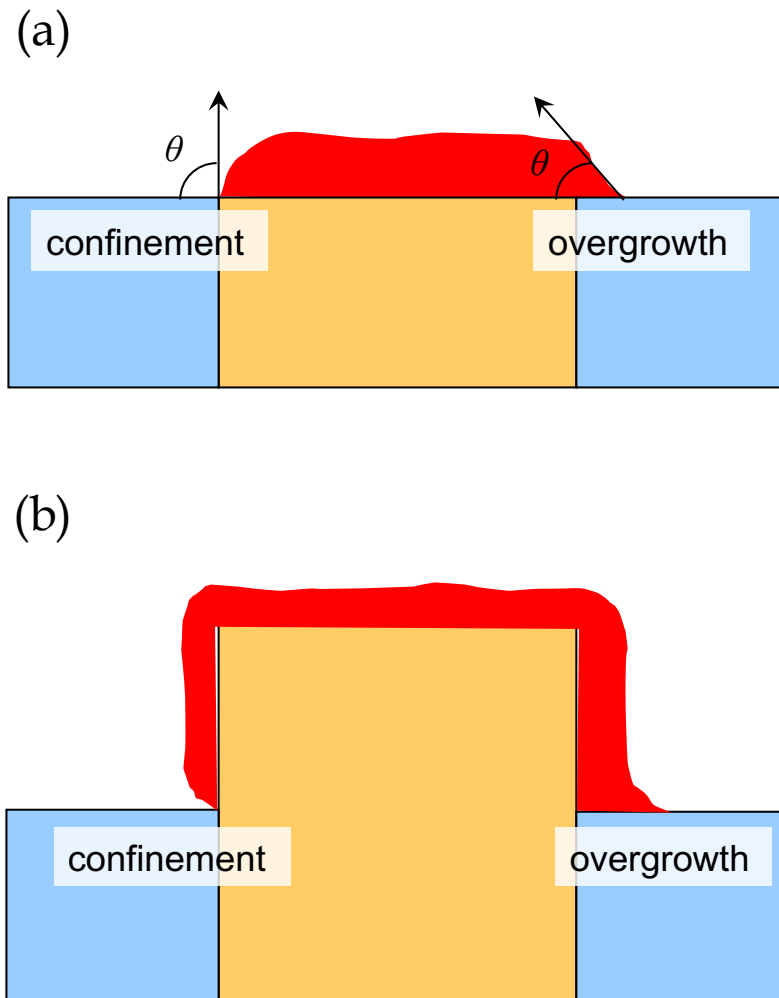
Figure 6-11: Schematic representations of possible outcomes of selective deposition on **(a)** a planar patterned substrate and **(b)** a patterned substrate with an aspect ratio with proximity effects.

Lastly, a mechanistic understanding of competitive adsorption reactions in our reactor system is needed. Fundamental studies using DFT calculations [21]–[30] could suggest possible reaction routes of the specific system comprising three has-phase species and two surfaces. Characterization techniques that allows probing of gas-phase and surface reactions *in situ* and real time during experiments such as quartz crystal microbalance (QCM) [31], [32] , quadrupole mass spectroscopy (QMS) [33], [34] and Fourier transform infrared spectroscopy (FT-IR) [35], [36] are essential experimental tools. Once a robust approach to selective growth of a continuous ALD film is achieved, growth characteristics on a patterned substrate and any possible proximity effect can be further investigated, as shown in Fig. 6-11.

6.6 References

[1] L. T. Zhuravlev, "Concentration of hydroxyl groups on the surface of amorphous silicas," *Langmuir*, vol. 3, no. 3, pp. 316–318, 1987.

[2] K. J. Hughes and J. R. Engstrom, "Nucleation delay in atomic layer deposition on a thin organic layer and the role of reaction thermochemistry," *J. Vac. Sci. Technol. A Vacuum, Surfaces, Film.*, vol. 30, no. 1, p. 01A102, 2012.

[3] D. Monnier, I. Nuta, C. Chatillon, M. Gros-Jean, F. Volpi, and E. Blanquet, "Gaseous Phase Study of the Zr-Organometallic ALD Precursor TEMAZ by Mass Spectrometry," *J. Electrochem. Soc.*, vol. 156, no. 1, p. H71, 2009.

[4] C. Morant, J. M. Sanz, L. Galán, L. Soriano, and F. Rueda, "An XPS study of the interaction of oxygen with zirconium," *Surf. Sci.*, vol. 218, no. 2–3, pp. 331–345, Aug. 1989.

[5] D. Majumdar and D. Chatterjee, "X-ray photoelectron spectroscopic studies on yttria, zirconia, and yttria-stabilized zirconia," *J. Appl. Phys.*, vol. 70, no. 1991, pp. 988–992, 1991.

[6] J. Liu, M. Liao, M. Imura, A. Tanaka, H. Iwai, and Y. Koide, "Low on-resistance diamond field effect transistor with high-k ZrO2 as dielectric.," *Sci. Rep.*, vol. 4, p. 6395, 2014.

[7] C. Sleigh, A. P. Pijpers, A. Jaspers, B. Coussens, and R. J. Meier, "On the determination of atomic charge via ESCA including application to organometallics," *J. Electron Spectros. Relat. Phenomena*, vol. 77, no. 1, pp. 41–57, Feb. 1996.

[8] Y. Zhou, N. Kojima, H. Sugiyama, K. Ohara, and K. Sasaki, "Preparation of ZrO2

ultrathin films as gate dielectrics by limited reaction sputtering — On growth delay time at initial growth stage," *Appl. Surf. Sci.*, vol. 254, no. 19, pp. 6131–6134, Jul. 2008.

[9]   S. Tanuma, C. J. Powell, and D. R. Penn, "Calculations of electron inelastic mean free paths. V. Data for 14 organic compounds over the 50-2000 eV range," *Surf. Interface Anal.*, vol. 21, no. 3, pp. 165–176, Mar. 1994.

[10]   A. S. Killampalli, P. F. Ma, and J. R. Engstrom, "The reaction of tetrakis(dimethylamido)titanium with self-assembled alkyltrichlorosilane monolayers possessing -OH, -NH2, and -CH3 terminal groups.," *J. Am. Chem. Soc.*, vol. 127, no. 17, pp. 6300–10, May 2005.

[11]   J. Scofield, "Hartree-Slater Subshell Photoionization Cross-Sections at 1254 and 1487 eV," *J. Electron Spectros. Relat. Phenomena*, vol. 8, pp. 129–137, 1976.

[12]   C. J. Powell and A. Jablonski, "Consistency of calculated and measured electron inelastic mean free paths," *J. Vac. Sci. Technol. A Vacuum, Surfaces, Film.*, vol. 17, no. 4, p. 1122, 1999.

[13]   Haynes W. M., *CRC Handbook of Chemistry and Physics, 97th Edition*, 97th ed. Boca Raton, FL.: CRC Press/Taylor & Francis, 2017.

[14]   T. Keuter, G. Mauer, F. Vondahlen, R. Iskandar, N. H. Menzler, and R. Vaßen, "Atomic-layer-controlled deposition of TEMAZ/O2–ZrO2 oxidation resistance inner surface coatings for solid oxide fuel cells," *Surf. Coatings Technol.*, vol. 288, pp. 211–220, Feb. 2016.

[15]   J.-G. Lee, J. Ahner, and J. T. Yates, "The adsorption conformation of chemisorbed pyridine on the Cu(110) surface," *J. Chem. Phys.*, vol. 114, no. 3, pp. 1414–1419,

Jan. 2001.

[16]   Y.-H. Lai, C.-T. Yeh, H.-J. Lin, C.-T. Chen, and W.-H. Hung, "Thermal Reaction of Trimethylphosphine and Triethylphosphine on Cu(110)," *J. Phys. Chem. B*, vol. 106, no. 7, pp. 1722–1727, Feb. 2002.

[17]   J. W. Klaus, O. Sneh, and S. M. George, "Growth of SiO2 at Room Temperature with the Use of Catalyzed Sequential Half-Reactions," *Science (80-.).*, vol. 278, no. 5345, pp. 1934–1936, Dec. 1997.

[18]   C. P. Tripp and M. L. Hair, "Chemical attachment of chlorosilanes to silica: a two-step amine-promoted reaction," *J. Phys. Chem.*, vol. 97, no. 21, pp. 5693–5698, May 1993.

[19]   Y. Du, X. Du, and S. M. George, "Mechanism of Pyridine-Catalyzed SiO2 Atomic Layer Deposition Studied by Fourier Transform Infrared Spectroscopy," *J. Phys. Chem. C*, vol. 111, pp. 219–226, 2007.

[20]   M. J. Hampden-Smith, T. T. Kodas, M. Paffett, J. D. Farr, and H. K. Shin, "Chemical vapor deposition of copper from copper(I) trimethylphosphine compounds," *Chem. Mater.*, vol. 2, no. 6, pp. 636–639, Nov. 1990.

[21]   A. V. Teplyakov and S. F. Bent, "Semiconductor surface functionalization for advances in electronics, energy conversion, and dynamic systems," *J. Vac. Sci. Technol. A Vacuum, Surfaces, Film.*, vol. 31, no. 5, p. 50810, Sep. 2013.

[22]   S. D. Elliott, G. Dey, Y. Maimaiti, H. Ablat, E. A. Filatova, and G. N. Fomengia, "Modeling Mechanism and Growth Reactions for New Nanofabrication Processes by Atomic Layer Deposition," *Adv. Mater.*, vol. 28, no. 27, pp. 5367–5380, Jul. 2016.

[23]   M. Shirazi and S. D. Elliott, "Cooperation between adsorbates accounts for the

activation of atomic layer deposition reactions," *Nanoscale*, vol. 7, no. 14, pp. 6311–6318, 2015.

[24] T. Weckman and K. Laasonen, "First principles study of the atomic layer deposition of alumina by TMA–H 2 O-process," *Phys. Chem. Chem. Phys.*, vol. 17, no. 26, pp. 17322–17334, 2015.

[25] A. S. Lisovenko, K. Morokuma, and A. Y. Timoshkin, "Initial Gas Phase Reactions between Al(CH 3) 3 /AlH 3 and Ammonia: Theoretical Study," *J. Phys. Chem. A*, vol. 119, no. 4, pp. 744–751, Jan. 2015.

[26] A. Gharachorlou, M. D. Detwiler, X.-K. Gu, L. Mayr, B. Klötzer, J. Greeley, R. G. Reifenberger, W. N. Delgass, F. H. Ribeiro, and D. Y. Zemlyanov, "Trimethylaluminum and Oxygen Atomic Layer Deposition on Hydroxyl-Free Cu(111)," *ACS Appl. Mater. Interfaces*, vol. 7, no. 30, pp. 16428–16439, Aug. 2015.

[27] J.-M. Lin, A. V. Teplyakov, and J. C. F. Rodríguez-Reyes, "Competing reactions during metalorganic deposition: Ligand-exchange versus direct reaction with the substrate surface," *J. Vac. Sci. Technol. A Vacuum, Surfaces, Film.*, vol. 31, no. 2, p. 21401, 2013.

[28] S. D. Elliott, "Atomic-scale simulation of ALD chemistry," *Semicond. Sci. Technol.*, vol. 27, no. 7, p. 74008, Jul. 2012.

[29] S. Shankar, H. Simka, and M. Haverty, "Density functional theory and beyond-opportunities for quantum methods in materials modeling semiconductor technology," *J. Phys. Condens. Matter*, vol. 20, no. 6, p. 64232, 2008.

[30] J. C. F. Rodríguez-Reyes and A. V. Teplyakov, "Mechanisms of adsorption and decomposition of metal alkylamide precursors for ultrathin film growth," *J. Appl.*

Phys., vol. 104, no. 8, p. 84907, Oct. 2008.

[31]   T. J. Larrabee, T. E. Mallouk, and D. L. Allara, "An atomic layer deposition reactor with dose quantification for precursor adsorption and reactivity studies.," *Rev. Sci. Instrum.,* vol. 84, no. 1, p. 14102, Jan. 2013.

[32]   J. W. Elam, M. D. Groner, and S. M. George, "Viscous flow reactor with quartz crystal microbalance for thin film growth by atomic layer deposition," *Rev. Sci. Instrum.,* vol. 73, no. 8, p. 2981, 2002.

[33]   W. Lei, L. Henn-Lecordier, M. Anderle, G. W. Rubloff, M. Barozzi, and M. Bersani, "Real-time observation and optimization of tungsten atomic layer deposition process cycle," *J. Vac. Sci. Technol. B Microelectron. Nanom. Struct.,* vol. 24, no. 2, p. 780, 2006.

[34]   L. Henn-Lecordier, W. Lei, M. Anderle, and G. W. Rubloff, "Real-time sensing and metrology for atomic layer deposition processes and manufacturing," *J. Vac. Sci. Technol. B Microelectron. Nanom. Struct.,* vol. 25, no. 1, p. 130, 2007.

[35]   A. Yanguas-Gil, J. A. Libera, and J. W. Elam, "Modulation of the Growth Per Cycle in Atomic Layer Deposition Using Reversible Surface Functionalization," *Chem. Mater.,* vol. 25, no. 24, pp. 4849–4860, Dec. 2013.

[36]   K. Li, S. Li, N. Li, D. a Dixon, and T. M. Klein, "Tetrakis(dimethylamido)hafnium Adsorption and Reaction on Hydrogen Terminated Si(100) Surfaces," *J. Phys. Chem. C,* vol. 114, no. 33, pp. 14061–14075, Aug. 2010.

7. Summary

This dissertation contains a comprehensive study on alternative routes to atomic layer deposition (ALD) by means of new reactor design and process development, and the results reported in this dissertation demonstrate the interweaving of reactor design, process conditions and surface chemistries.

In Chapter 3, we first begin with the design of a micro-reactor that enables ALD reactions and subsequent *in situ* UHV surface analysis in a single chamber system with no air break. This is essential to surface science studies on ultrathin films (particularly the early stages of film growth) as the surface functional groups, composition and microstructure of the films could change drastically after being exposed to air. Process development of alternative approaches to selective area ALD are made possible by the new reactor design as it minimizes exposure of ALD films to undesirable species such as oxygen and water before the analysis is employed. The primary task of this micro-reactor design is to bridge the "pressure gap" between vapor-phase deposition processes ($p \sim 10^{-3} - 10$ Torr) and UHV surface characterization ($p < 10^{-9}$ Torr) by confining the reactant in the reaction zone (total volume of ~ 1 cm^3) with the use of a "curtain gas" flow. Calculations using computational fluid dynamics determines the critical dimensions of the probe under typical reaction conditions necessary to achieve confinement and minimize out-diffusion of the reactant species to the surrounding UHV chamber. We demonstrated the efficacy of the micro-reactor probe by conducting ALD of ZrO_2 at $p = 18$ Torr using $Zr[N(C_2H_5)(CH_3)]_4$ and H_2O as reactants, as well as the capability for analyzing ZrO_2 ALD films *in situ*. Binding energies of Zr(3d) and O(1s) peaks, the evolution of Zr(3d) and Si(2p)

intensities with respect to the number of ALD cycles and growth rate per cycle of the spatially-confined films were consistent with results reported using conventional reactors designed for ALD, as confirmed by *in situ* X-ray photoelectron spectroscopy (XPS). Additional work presented in Chapter 4 involved a design a micro-reactor head for an obround deposition spot and for terraced film growth that has been simulated in a three-dimensional model using COMSOL Multiphysics, a CFD commercial package. We showed a 3-4 orders-of-magnitude reduction in the amount of the reactant (Xe and H_2O) reaching to the surrounding chamber as compared to that on substrate surface in both stationary and transient modes.

In Chapter 5 we investigate how an additional, third species in conventional ALD process, with a focus on the first half cycle, affects the precursor-substrate interaction on dielectric and metal surfaces via competitive adsorption. We produced a kinetic model of competitive adsorption that includes both adsorption and desorption kinetics of the two species, and the results suggested that higher partial pressure of the co-adsorbate and lower substrate temperature facilitate the suppression of metal precursor adsorption. In all the conditions experimentally examined, the amount of Zr observed on the surfaces was modulated by the addition of the co-adsorbate. Among the four candidates, selective chemisorption of $Zr[N(C_2H_5)(CH_3)]_4$ on SiO_2 over Cu is observed with the presence of $N(CH_2CH_3)_3$ or $HS(CH_2)_2SH$. From the $N(CH_2CH_3)_3$ / $Zr[N(C_2H_5)(CH_3)]_4$ co-exposure experiments at different substrate temperatures, the observed temperature dependence of competitive adsorption (less nucleation of $Zr[N(C_2H_5)(CH_3)]_4$ as the substrate temperature increases) further corroborates the proposed mechanism of adsorption reversal. The process space within which selective growth of ZrO_2 ALD could be possible is also

identified. However, selective chemisorption of the transitional metal precursor in the first half-cycle of an ALD process is a necessary, but not sufficient condition for selective area growth. We then extended the scheme of competitive adsorption of the transition metal precursor and the co-adsorbate from the first half-cycle to multiple ALD cycles in Chapter 6. Area selectivity of ZrO_2 on SiO_2 over Cu was demonstrated up to 1.5 cycle in the $Zr[N(C_2H_5)(CH_3)]_4/O_2/N(CH_2CH_3)_3$ system. It was also predicted that selective growth on SiO_2 over Cu last up to ~9.5 cycle in the $Zr[N(C_2H_5)(CH_3)]_4/H_2O/HS(CH_2)_2SH$ system. In contrast, growth rates of ZrO_2 ALD were enhanced by the use of new co-adsorbates, C_5H_5N and $P(CH_2CH_3)_3$, possibly due to catalytic reactions involving hydrogen bond or long pair electrons. Improvement in the experimental protocol, such as reducing reactor pressure and introducing an additional step of hydrogen dose, could alleviate the effect of the co-reactant on the starting surface and on the co-adsorbate.

8. Appendix

8.1 XPS on WSe$_2$ thin film

The growth of tungsten diselenide (WSe$_2$) films on highly ordered pyrolytic graphite (HOPG) by metal-organic molecular beam epitaxy (MOMBE) using tungsten hexacarbonyl [W(CO)$_6$, via supersonic molecular beam] and elemental selenium (via an effusive source) are characterized by a number of X-ray techniques. Film growth was monitored by real time, *in situ* X-ray fluorescence (XRF) using synchrotron radiation at the Cornell High Energy Synchrotron Source (CHESS). Elemental composition and chemical states of the elements in a material was analyzed by *ex situ* XPS.

We investigated the role that both precursors play during the growth of WSe$_2$ by gating one of the precursor flows using shutters that allow for controlled exposure of the substrate from both the supersonic beam and the effusive source. Films grown in the W-gated and Se-gated conditions were examined at a substrate temperature of 470 °C. In the case of gated W, the Se precursor was continuously flowing and the W precursor was gated for several periods of 12 minutes. We observed from XRF that when the W precursor was off both W and Se intensities are stalled and there was little change in the ratio of Se to W over the entire growth (~1.74 ± 0.01). Se-gated experiments revealed that when Se precursor is gated, intensities evolved in opposite directions: W intensity increased and Se intensity decreased as the dose of W(CO)$_6$ continued. As a result, the Se/W ratio dropped significantly in the Se-gated periods and was ended at ~1.05 ± 0.01 (lower than that of W-gated experiment).

The samples were then transferred to an ultrahigh vacuum (UHV) chamber in Olin 312 for *ex situ* XPS. All the samples were exposed to air before loading in and were analyzed as-received. In Fig. 8-1 we display an XPS survey scan for the W-gated experiment. We identify the following elements in the film: W, Se, C, and O. We point out that air exposure is one of the sources of C and O detected in the WSe_2|HOPG samples, in addition to those elements in the W precursor (C, O) and the substrate (C). In Fig. 8-2(a) we display the XP spectrum of the W(4f) region for a WSe_2|HOPG sample that is grown with gated W at $T_s = 470\,°C$. The W(4f) spectrum can be fitted as a mixture of Se-bound and O-bound W, with $4f_{7/2}$ binding energies of 32.5 and 35.9 eV, respectively. W(4f) spectra of both W-containing species were fit assuming a spin-orbit doublet separation of 2.1 eV [1], [2] with a fixed ratio of 3:4 for the $4f_{5/2}$ to $4f_{7/2}$ peak area. Binding energies of Se-bound and O-bound W are in good agreement with those of WSe_2 [1], [3]–[6] and WO_3 [4], [5], [7]. In Fig. 8-2(b) we display the XP spectrum of the Se(3d) region for a WSe_2|HOPG sample that is grown with gated W at $T_s = 470\,°C$. We note that no signature of SeO_2, $Se(3d_{5/2})$ peak at ~59 eV [8], [9], was observed in the Se(3d) region by *ex situ* XPS. This suggests that the WSe_2 film is W-terminated, consistent with the crystal structures of transitional metal dichalcogenides, so that only the surface W atoms were oxidized due to their contact with ambient air [10], [11].
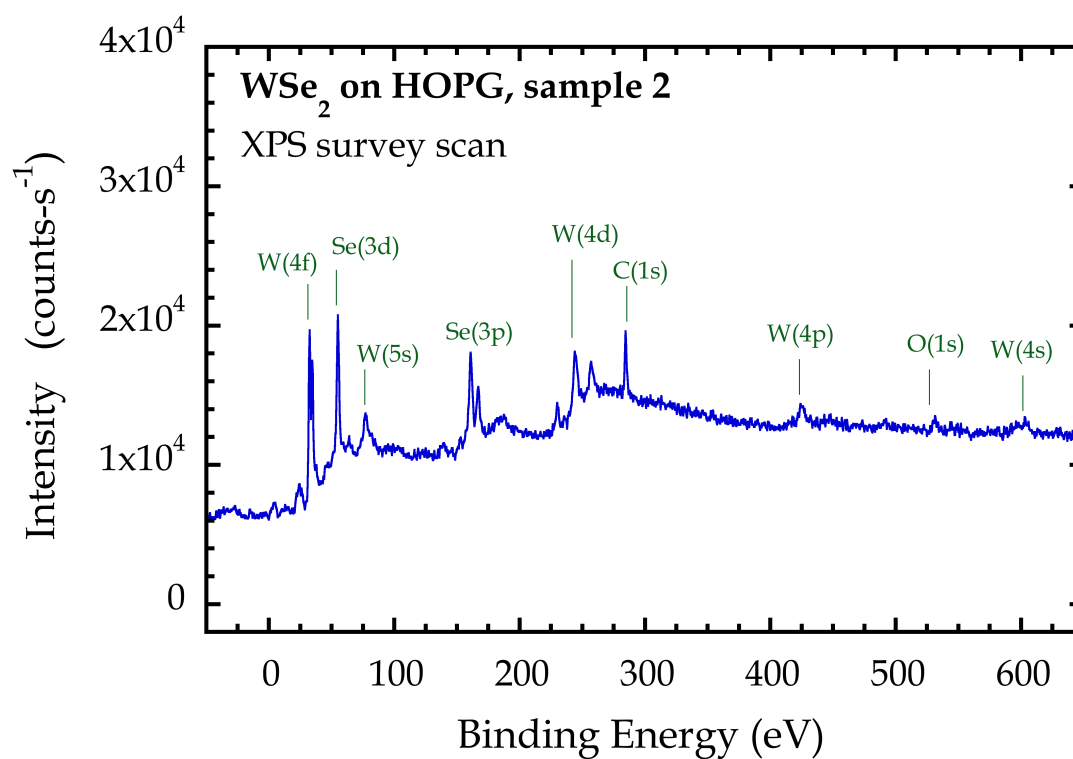
Figure 8-1: X-ray photoelectron spectrum of a survey scan on WSe$_2$|HOPG grown with gated W at T$_s$ = 470 °C.
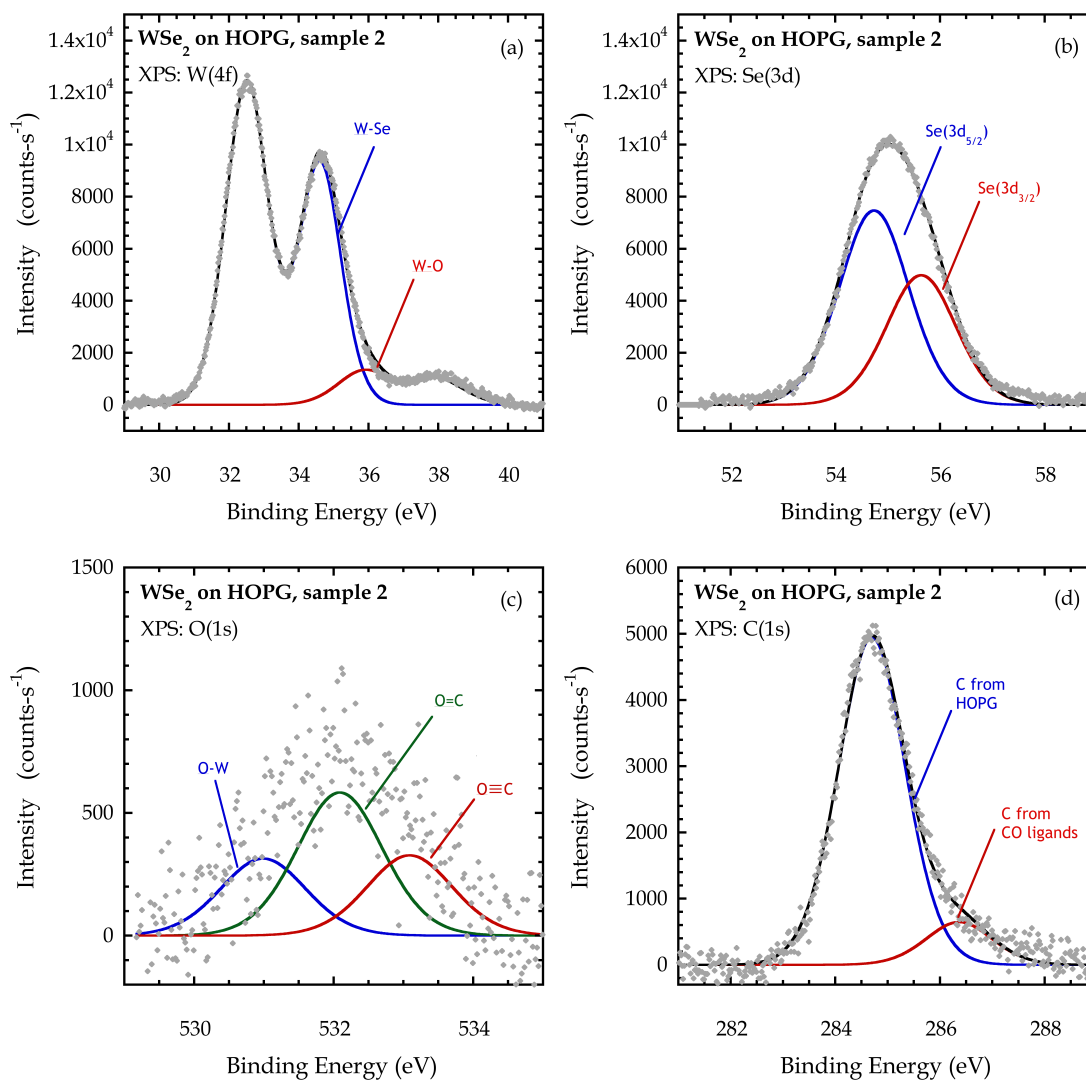
Figure 8-2: X-ray photoelectron spectra of the **(a)** W(4f), **(b)** Se(3d), **(c)** O(1s) and **(d)** C(1s) regions for WSe$_2$|HOPG grown with gated W at T$_s$ = 470 °C.

In Fig. 8-2(c) we display the XP spectrum of the O(1s) region for a WSe$_2$|HOPG sample that is grown with gated W at T$_s$ = 470 °C. A broad feature from ~530 to 534 eV is observed in the O(1s) region, which can be assigned to multiple O-containing species. For example, the O(1s) spectrum can be fitted as a mixture of W-bound and C-bound O. O(1s) binding energy of ~531.0 eV for W-bound O for was in good agreement with that of WO$_3$ [7]. Multiple binding environment between C and O are possible, and here we fitted the spectrum with two peaks that represent C=O and C-O bonds. O(1s) binding energies of ~532.1 and 533.1 eV for C=O and C-O bonds matches those of oxygen-containing functional groups on carbon nanotube surfaces resulting from surface oxidation [12]. In Fig. 8-2(d) we display the XP spectrum of the C(1s) region for a WSe$_2$|HOPG sample that is grown with gated W at T$_s$ = 470 °C. The C(1s) spectrum can be fitted with three peaks at 284.7, 286.1 and 287.5 eV that represents the bulk HOPG substrate, C-O, and C=O surface functional group [12], [13]. Based on the above XPS analysis, the sample contains WSe$_2$ film on HOPG, oxidized W (WO$_3$) surface from the film and oxidized C surface from the substrate. This corresponds to an observation on the morphology of the WSe$_2$ film, from both atomic force microscopy and scanning electron microscopy, that the WSe$_2$ films nucleate around the step edges of the HOPG substrate and that a large portion of the HOPG surface is exposed to ambient air.

To calculate the Se/W atomic ratio we compare the integrated intensity of the Se(3p$_{3/2}$) peak to that of the W(4f$_{7/2}$) peak [14] and account for the relative photoionization cross-sections, σ_{Se}/σ_W = 0.46 [15], analyzer transmission function, T(E$_{Se}$)/T(E$_W$)=(1093 eV/ 1222 eV)$^{-1}$=1.12, the attenuation length of the photoelectrons, λ_{Se}/λ_W =(1093 eV/ 1222 eV)$^{1/2}$=0.95. The sample that is grown with gated W at T$_s$ = 470 °C has a Se/W ratio of

1.79 using total $W(4f_{7/2})$ and $Se(3p_{3/2})$ peak areas. More importantly, using the $W(4f_{7/2})$ area from the Se-bound W peak only we obtained a Se/W ratio of 2.03, which is in good agreement with the stoichiometry of WSe_2 film. This again supports the observation of the growth of stoichiometric WSe_2 film based on binding energies of $W(4f_{7/2})$ and $Se(3p_{3/2})$ peaks. Deposition of stoichiometric WSe_2 film by MOMBE were further confirmed by *ex situ* Raman spectroscopy and X-ray Diffraction. Using the same method, the Se/W ratio the film grown with gated Se at $T_s = 470\ °C$ is 1.87 using the $W(4f_{7/2})$ area from the Se-bound W peak only. We confirmed that, with a gated Se precursor dose, a nearly stoichiometric WSe_2 film is deposited at the end of the experiment despite the oscillation of total Se/W ratio during the experiment.

We also conducted the gated experiments at substrate temperature of 400 °C and 540 °C, respectively for investigating the effect of substrate temperature, and the results are summarized in Table 8-1. Stoichiometric WSe_2 films are deposited in the W-gated and Se-gated experiments at $T_s = 400\ °C$, same as what we observed at $T_s = 470\ °C$. By contrast, W-rich films were observed in the W-gated and Se-gated experiments at $T_s = 540\ °C$ with an overall Se/W ratio of 0.85 and 0.25, respectively. We postulated that at $T_s = 540\ °C$ the desorption rate of elemental selenium is so high that only a fraction of surface W is selenized during the dose of selenium and that non-stoichiometric WSe_x film consisting of unbound and/or partially-bound W, is deposited. This hypothesis is supported by the fact that the percentages of the oxidized W for $T_s = 540\ °C$ reached an averaged ~36%, as compared to the average of ~15% for $T_s = 400\ °C$ and for $T_s = 470\ °C$. Se/W atomic ratios calculated from XPS and XRF (recorded after the exposure) results were displayed in Fig. 8-3.

Table 8-1: Calculated Se/W atomic ratio and the percentage of oxidized W of six samples using peak areas from *in situ* XPS

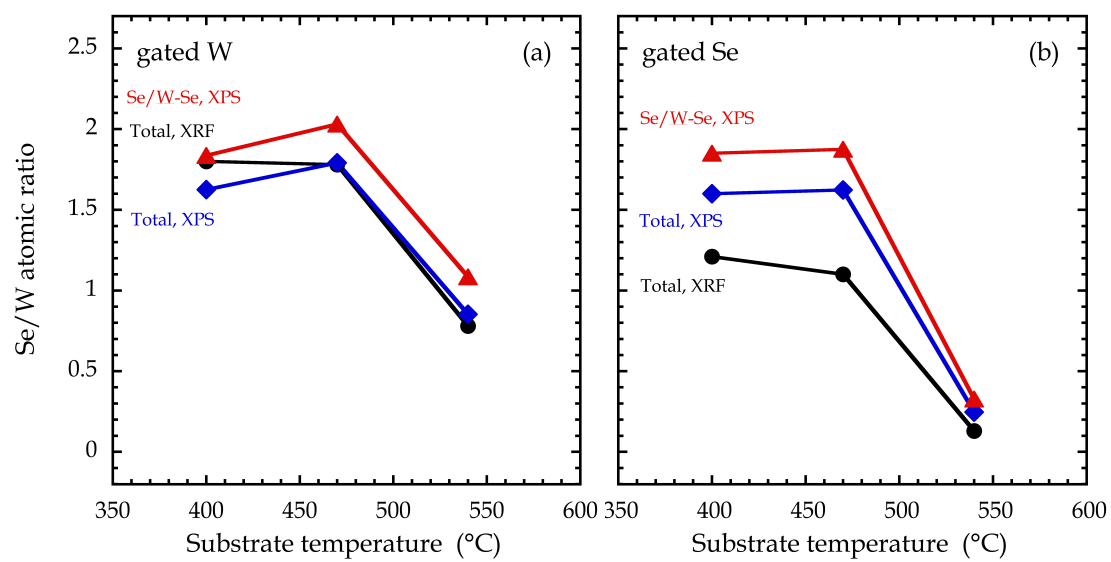| Sample No.	Se/W atomic ratio		Percentage of oxidized W out of total W
	Using total W(4f) peak area	Using W(4f) peak area from Se-bound W	
1	1.63	1.84	12%
2	1.79	2.03	14%
3	0.85	1.08	34%
4	1.60	1.85	22%
5	1.62	1.87	17%
6	0.25	0.33	38%

Figure 8-3: Se/W atomic ratios calculated from XPS and XRF (recorded after the exposure) results in **(a)** gated W and **(b)** gated Se experiments.

8.2 XPS on iodine-treated PbS nanocrystals

Surface states of colloidal nanocrystals are typically created when organic surfactants are removed. We report a chemical process that reduces surface traps and tunes the interparticle coupling in PbS nanocrystal thin films after the surfactant ligands have been stripped off. This process produces PbS/PbI$_2$ core/shell nanocrystal thin films *via* a combined ammonium sulfide and iodine treatment [16]. Interparticle coupling of post-treatment nanocrystal thin films is tunable by controlling the iodine treatment process. Optical studies reveal that this method can produce PbS nanocrystal thin films superior in both coupling and surface quality to nanocrystals linked by small molecules such as 1,2 – ethanedithiol or 3-mercaptopropionic acid.

The presence of iodide in the post-treatment PbS NC thin film (in 0.005 mM I$_2$/CCl$_4$ solution for 720 mins) is confirmed by X-ray photoelectron spectroscopy (XPS). The signal is mainly from the top few layers of NC thin film due to the inelastic mean free path of Pb(4f) and I(3d) photoelectrons in PbS (0.8 – 1.8 nm). Iodide is observed with binding energies of 619.2 eV for I(3d$_{5/2}$) and 630.7 eV for I(3d$_{3/2}$) [Fig. 8-4(a)]. The Pb 4f spectrum can be fitted as a mixture of S-bound and I-bound Pb, with 4f$_{7/2}$ binding energies of 137.6 and 138.1 eV, respectively [Fig. 8-4(b)]. Formation of Pb-I bonds is supported by the fact that both Pb(4f) and I(3d) binding energies are in good agreement with those of PbI$_2$ [17].
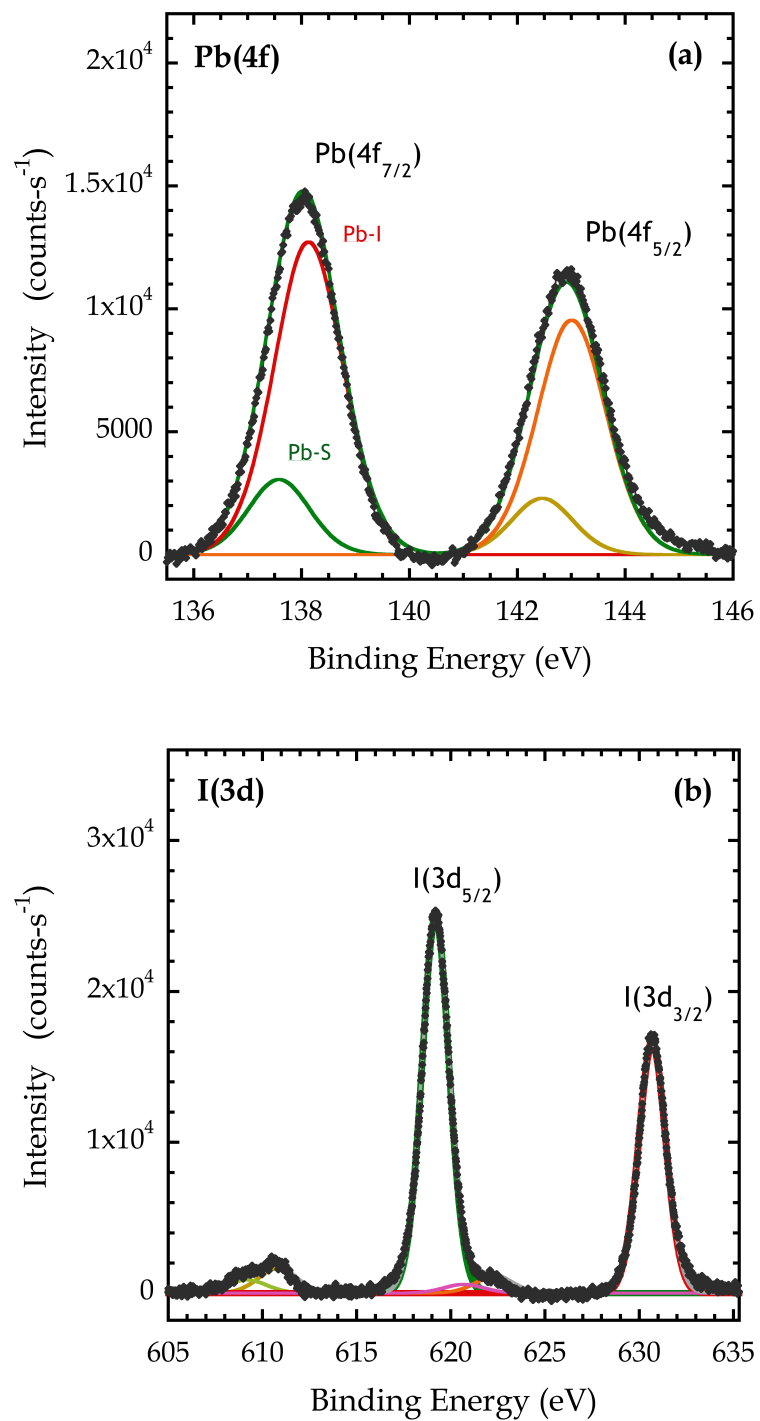
Figure 8-4: X-ray photoelectron spectra of **(a)** I(3d) and **(b)** Pb(4f) regions for PbS NC thin film treated in 0.005 mM I_2/CCl_4 solution for 720 mins.

The samples were exposed to air before loading in and was analyzed as-received. XPS data were collected using an Omicron Sphera U5 concentric hemispherical electron energy analyzer (Omicron Nanotechnology USA, Eden Prairie, MN), operated at a constant pass energy of 50 eV. Nonmonochromated MgKα X-rays (1253.6 eV excitation energy) were produced using an Omicron DAR 400 twin anode source operated at 300 W (15 kV anode potential X 20 mA emission current). CasaXPS software (version 2. 3. 15) was used for analyzing XP spectra.

Pb(4f) spectra were fit assuming a spin-orbit doublet separation of 4.9 eV with a fixed ratio of 3:4 for the $4f_{5/2}$ to $4f_{7/2}$ peak area [18]. I(3d) spectra were fit assuming a spin-orbit doublet separation of 11.5 eV with a fixed ratio of 2:3 for the $3d_{3/2}$ to $3d_{5/2}$ peak area [19]. Satellite lines, originated from the nonmonochromated X-ray source, were included in fitting I(3d) spectrum [20].

8.3 Addition of the micro-reactor probe and the reactant delivery system to the Olin Hall 312 system

8.3.1 LabVIEW codes for flow, pressure and valve control

As we mentioned in Section 3.3.3 complex dosing sequences can be generated using the gas delivery system consisting of three independent panels in a "vent-run" configuration. For a single experimental condition we need full control over valve configurations, the reactor pressure and flow rates, and each of them is regulated by

individual electronics of control systems from different suppliers. We therefore developed LabVIEW programs that integrate all the controlling interfaces of the above functions. We also developed three models of the control interfaces for three distinct categories of experiments that can be conducted using the micro-reactor system, including (i) a manual model for simpler experiments such as selective chemisorption; (ii) an automated, 4-step model for regular ALD experiments (A – purge – B – purge); and (iii) an automated, 6-step model for modified ALD experiments. The time series of the reactor pressure is automatically recorded and saved as a separate file in all three models. In Fig. 8-5 we display front panels of the three models in LabVIEW. Drivers of the throttle valve controller and the 8-channel MFC controller (MKS Instruments) for control over the reactor pressure and flow rates were adopted. The block diagram of the manual model is shown in Fig. 8-6.

8.3.2   Design of sliding panels

Reactant delivery system accompanied with the micro-reactor system underwent two major renovations. The first generation included a reactant delivery system in a vented enclosure for extra safety. Although it was able to generate complex dosing sequences for up to three chemicals, considerable difficulty in delivering reactive species such as ALD precursor was encountered due to long tube length from the bubbler outlet to the end the reactor ($\sim$ 630 cm) in the early stage of the competitive adsorption studies. It also caused $\sim$ 30 s delay from valve actuation to exposure to the substrate for every step, which made the experiments excessively longer.
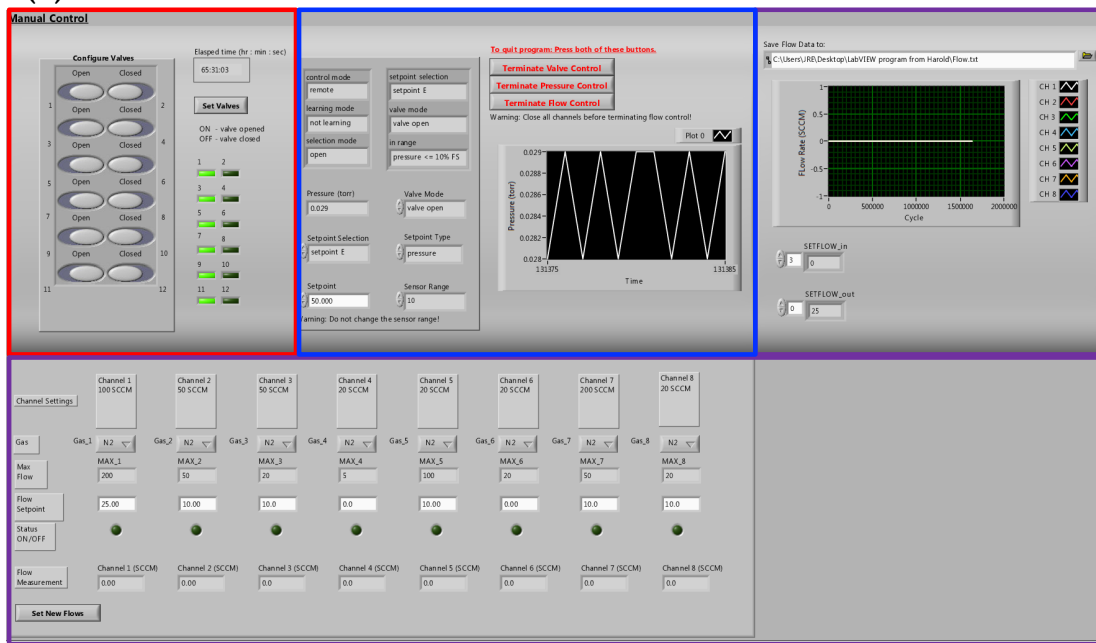
Figure 8-5: Front panels of **(a)** the manual model, **(b)** the automated, 4-step model and **(c)** the automated, 6-step model in LabVIEW. Each of the models includes parts for control over valve configuration (in the red box), reactor pressure (in the blue box) and flow rates (in the purple box).

(b)

Figure 8-5, continued: Front panels of **(a)** the manual model, **(b)** the automated, 4-step model and **(c)** the automated, 6-step model in LabVIEW. Each of the models includes parts for control over valve configuration (in the red box), reactor pressure (in the blue box) and flow rates (in the purple box).
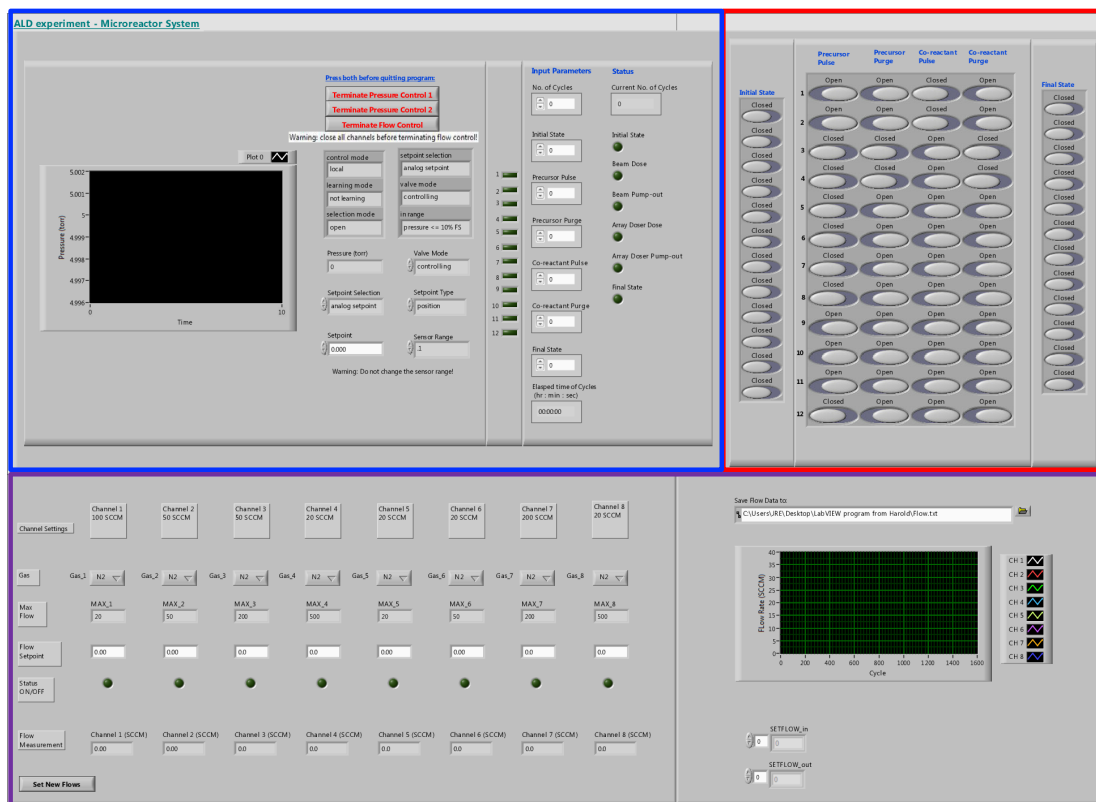
(c)

Figure 8-5, continued: Front panels of **(a)** the manual model, **(b)** the automated, 4-step model and **(c)** the automated, 6-step model in LabVIEW. Each of the models includes parts for control over valve configuration (in the red box), reactor pressure (in the blue box) and flow rates (in the purple box).
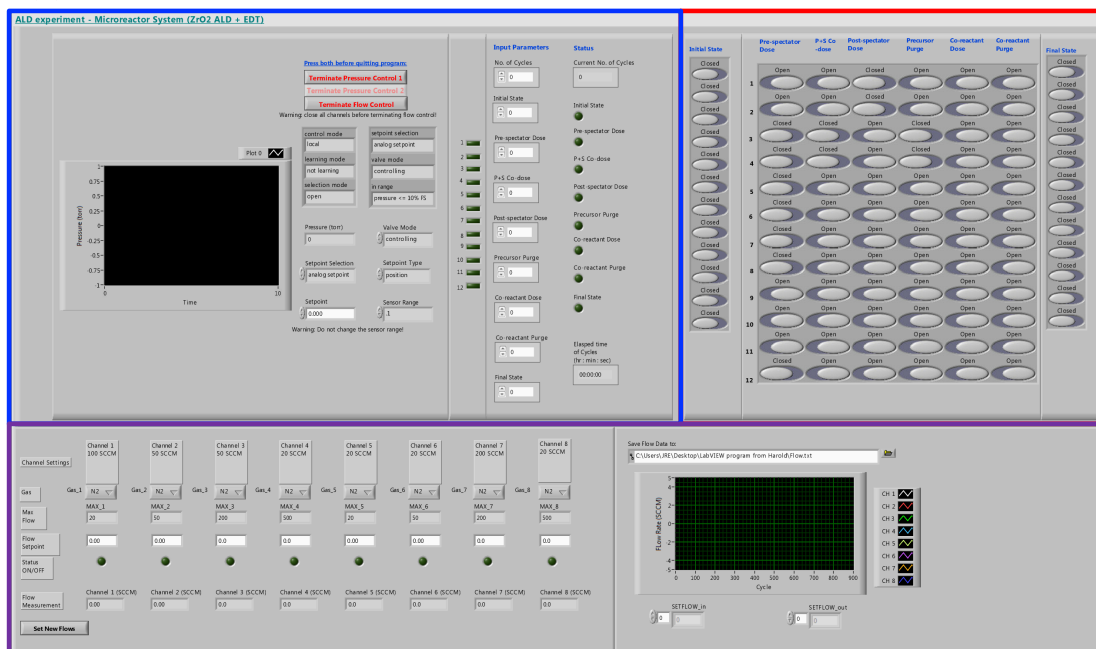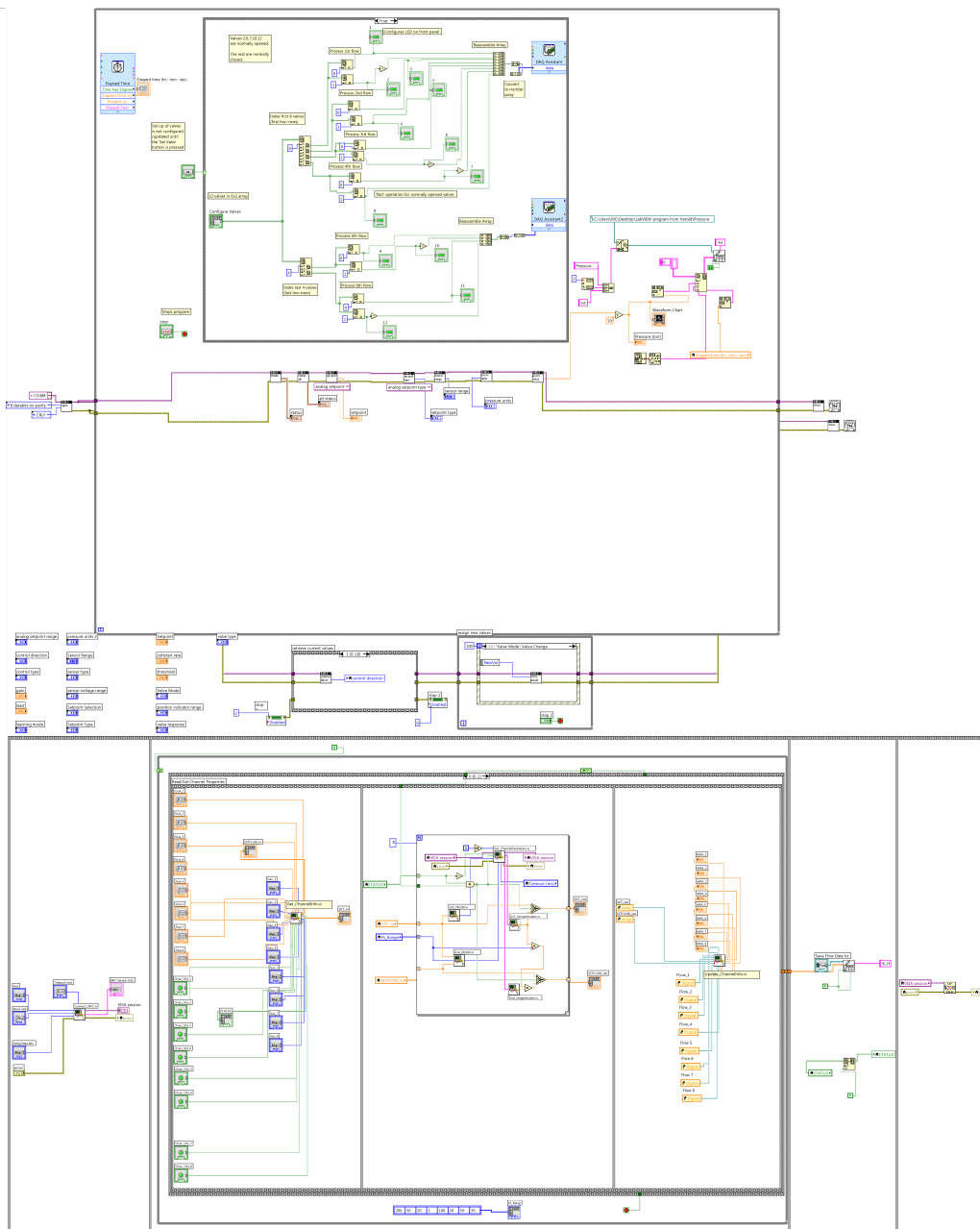
Figure 8-6: Block diagram of the manual model in LabVIEW.

To resolve this issue, two hanging panels that are much closer to the 312 chamber was built. The stationary panels were anchored to the ceiling, and metal hoses (~ 91 cm) were used to deliver reactants from the panel to the reactor.

However, as the micro-reactor traveled all the hoses moved along and their shapes were consequently changed. This caused additional issues for heat tracing the delivery lines in order to eliminate any cold spot. From the user experience of the two early systems, we determined that panels should move along with the reactor during the experiments so that the hose length can be greatly reduced. The third generation of the reactant delivery system consists of three independent panels that are mounted on a sliding surface. The surface, under which four ball-bearing carriages (THK HSR series) are fastened, slides along two parallel rails (THK LM series, 82 cm long). A short metal hose ~ 15 cm used in each of the three panels, so the sliding panel system is much more compact and has a tube length from the bubbler outlet to the end of the micro-reactor of ~ 100 cm (an approximately six times reduction as compared to the vented enclosure system). The sliding panels are installed on a ~ $86 \times 89 \times 91$ cm^3 table made from struts. Each panel has a toggling network for one reactant and its associated purge, as shown in Fig. 8-7.

8.3.3 Methods of removing thiol residue in the reactor

Engstrom research group has historically used thiol molecules twice in 312 chamber system; $1,2-$ ethanedithiol (EDT) and benzenethiol (BT) have been introduced to both supersonic molecular beam system and the micro-reactor system. Sulfur was detected by XPS in the experiments in which thiol was not involved. Thiol was used as a

co-adsorbate in the competitive adsorption studies, so the thiol liquid was contained in a stainless steel bubbler that is attached to one of the panels in the reactant delivery system.

All the sections between the bubbler and the exhaust pump in the micro-reactor are contaminated and thus need to be cleaned, including the bubbler, the panel, the micro-reactor system, the exhaust lines and the mechanical pump itself. All parts in the supersonic molecular beam (the delivery panel, the tube and the nozzle) also requires thiol removal treatment. Kim et al. reported that standard clean No. 1 (SC-1), a solution process of RCA (Radio Corporation of America) clean, can effectively remove self-assemble monolayers of 11-Mercapto-1-undecanol (thiol) on gold surface [21]. SC-1 is widely used in semiconductor industry for removing organics and particles on silicon wafers before processing. Three solution steps comprise of the SC-1 clean: first in NH_4OH–H_2O_2–H_2O solution for an hour, followed by acetone and isopropyl alcohol (30 mins each step). An extra step of 50% nitric acid cleaning is performed for parts with a large quantity of residual thiol. All the above solution processes take place in a 4L glass beaker that can contain any of the contaminated parts, and all the solutions are sonicated to facilitate sulfur removal. One need to repeat the above process until no signature of S is observed. Pump oil change is required for removing sulfur in the mechanical pump.
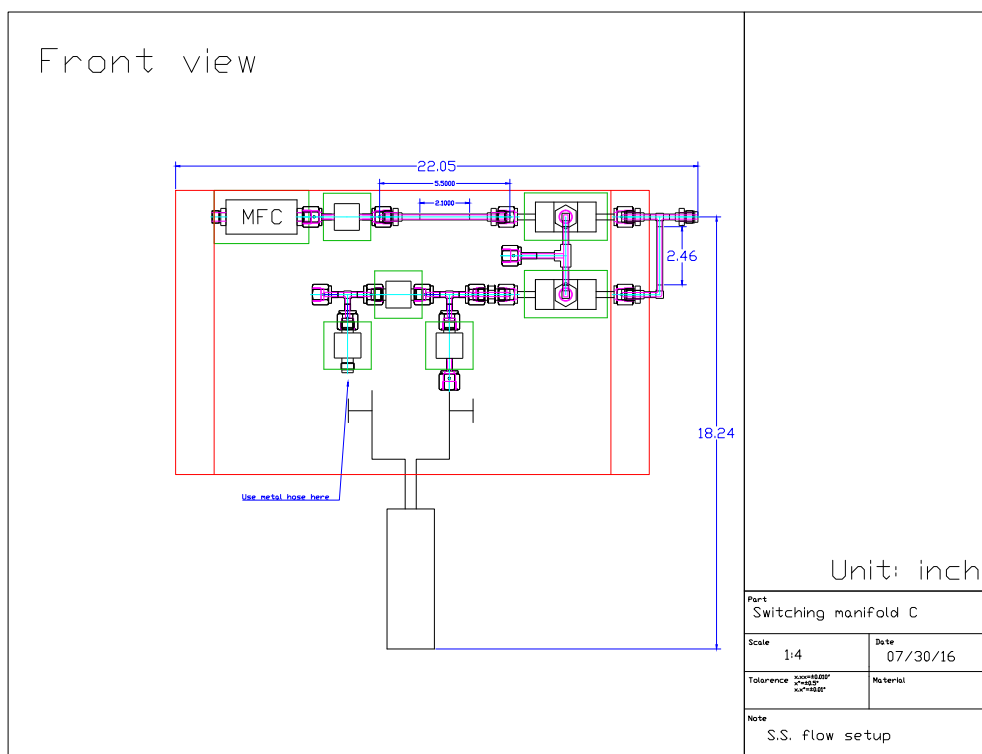
Figure 8-7: Schematic representation of a sliding panel in the reactant delivery system

8.3.4 Design aspects of the concentric micro-reactor

In the early stages of design project, we set dimensional limitations for all the components to be purchased, including the gate valve, the linear translator and a double-sided flange, to make sure we can operate the final assembly without difficulty under practical constraints (Fig. 8-8).

The micro-reactor system is constructed entirely of bakeable materials so that it can undergo a long bake (> 24 h) at ~ 150 °C and of vacuum compatible materials for being a part of an UHV system. PTFE O-rings (for both ¼" and ½" OD tubes) that are bakeable at 150 °C were used in both sides of the central fluidic feedthrough. High-purity alumina tubes (Accuratus, 5/32" OD × 3/32" ID × 12" long) for positioning the spring-loaded probes were machined to exact lengths by Glenn Swan. Each spring-loaded probe (ECT SPA-3D-1, up to 550 °F) was coupled to its receptacle (SPR-3W). The positon of the press ring on the receptacle, along with the lengths of the two alumina tubes covering each side of the receptacle, fully determined the position of the probe / receptacle assembly. Silver-plated vented screws (U-C C-612-A and C-614-A) were used in the micro-reactor for not affecting the operation of the UHV chamber.

Full details of the concentric micro-reactor design, including the mounting flange, central fluidic feedthrough and the micro-reactor head are shown from Fig. 8-9.
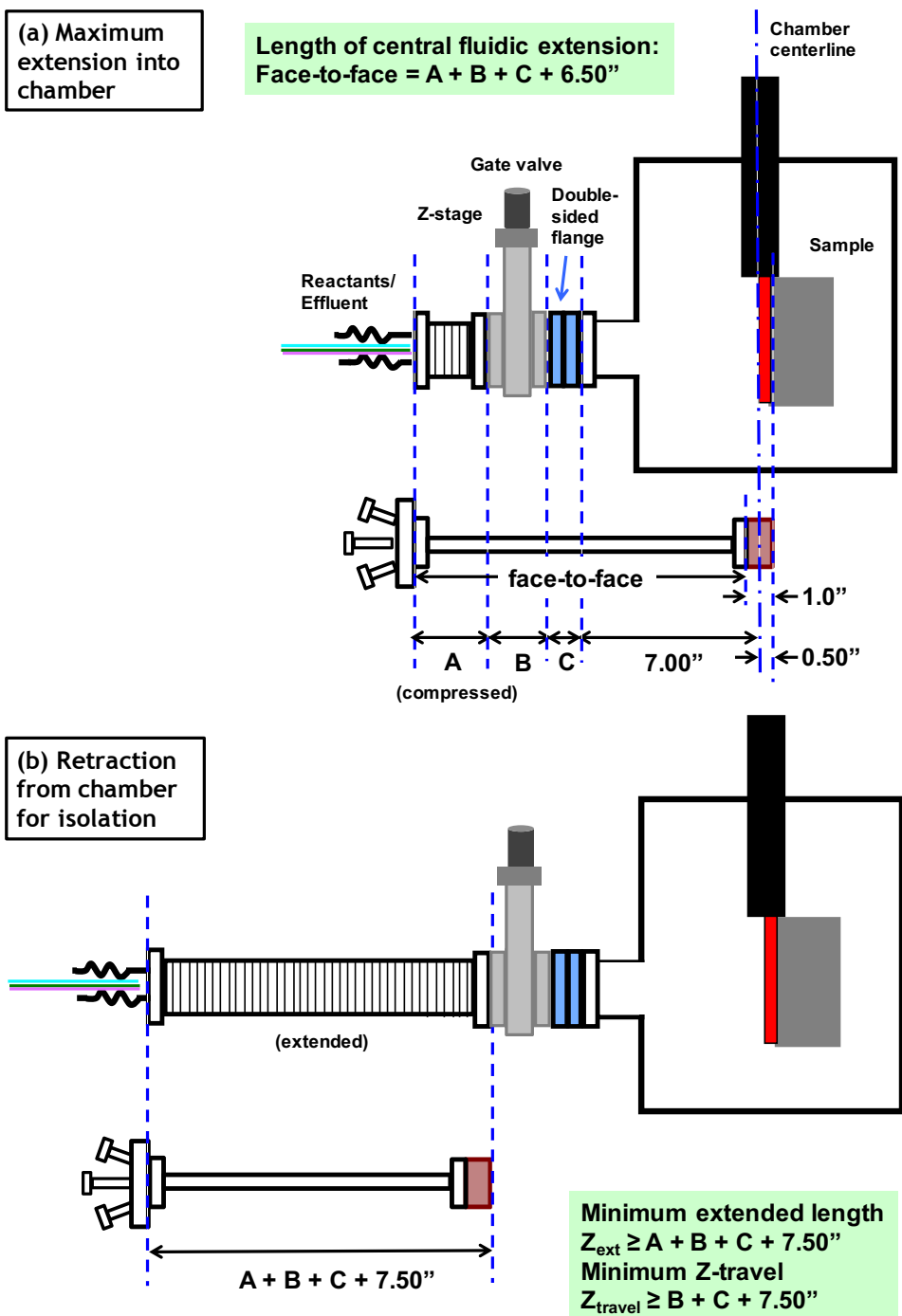
Figure 8-8: Schematic representation of the dimensional limitation of the components in the micro-reactor system in the conditions of **(a)** maximum extension into chamber and **(b)** retraction from chamber for isolation.

(a)

Figure 8-9: Drawings of the concentric microeactor system composed of **(a-b)** a microreactor head**, (c-e)** a central fluidic feedthrough and **(f)** a fluidic and electrical feedthrough.

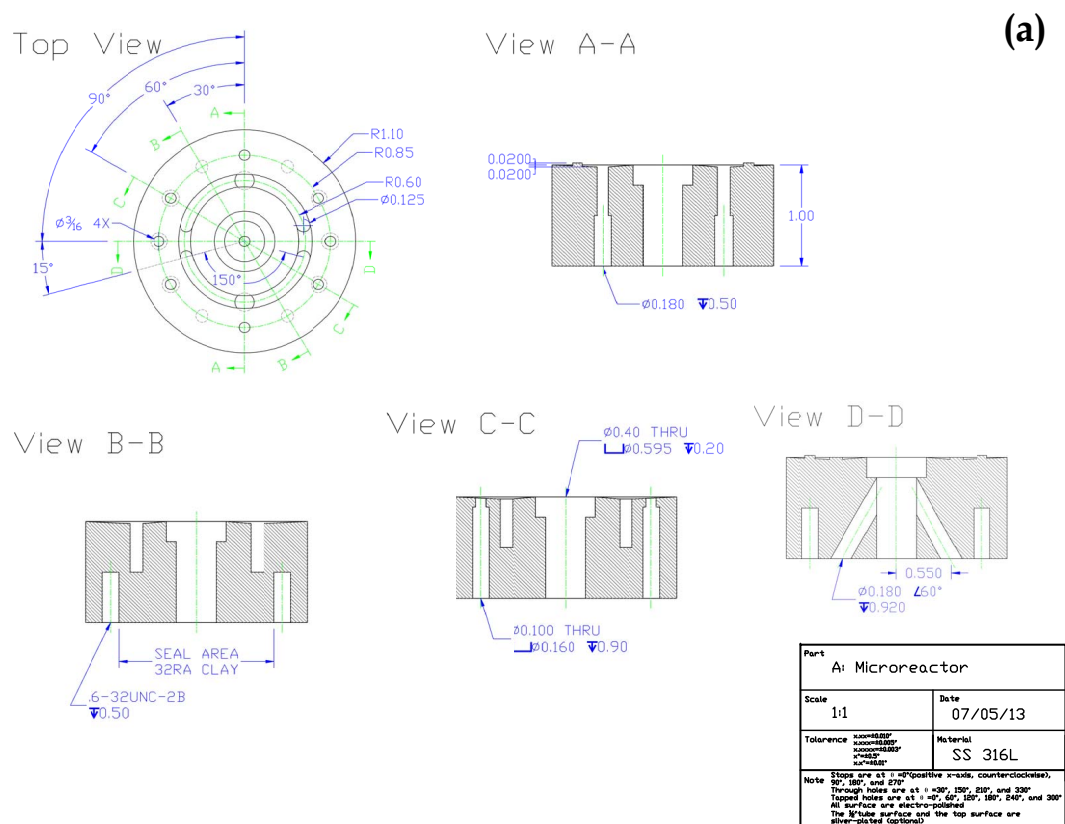**Figure 8-9, continued**: Drawings of the concentric microeactor system composed of **(a-b)** a micro-reactor head**, (c-e)** a central fluidic feedthrough and **(f)** a fluidic and electrical feedthrough.

Figure 8-9, continued: Drawings of the concentric microeactor system composed of **(a-b)** a micro-reactor head**, (c-e)** a central fluidic feedthrough and **(f)** a fluidic and electrical feedthrough.
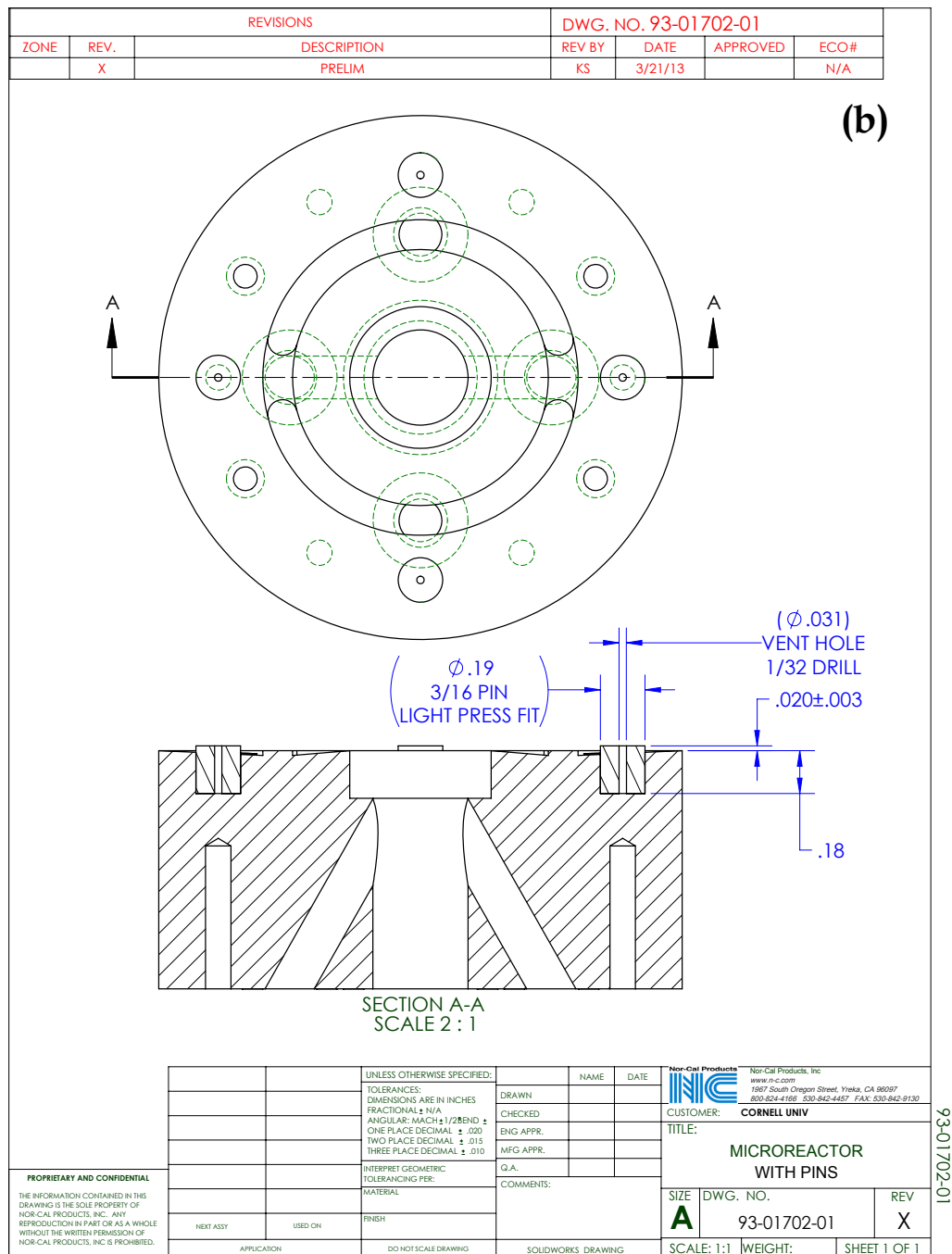
(d)

Figure 8-9, continued: Drawings of the concentric microeactor system composed of **(a-b)** a micro-reactor head**, (c-e)** a central fluidic feedthrough and **(f)** a fluidic and electrical feedthrough.
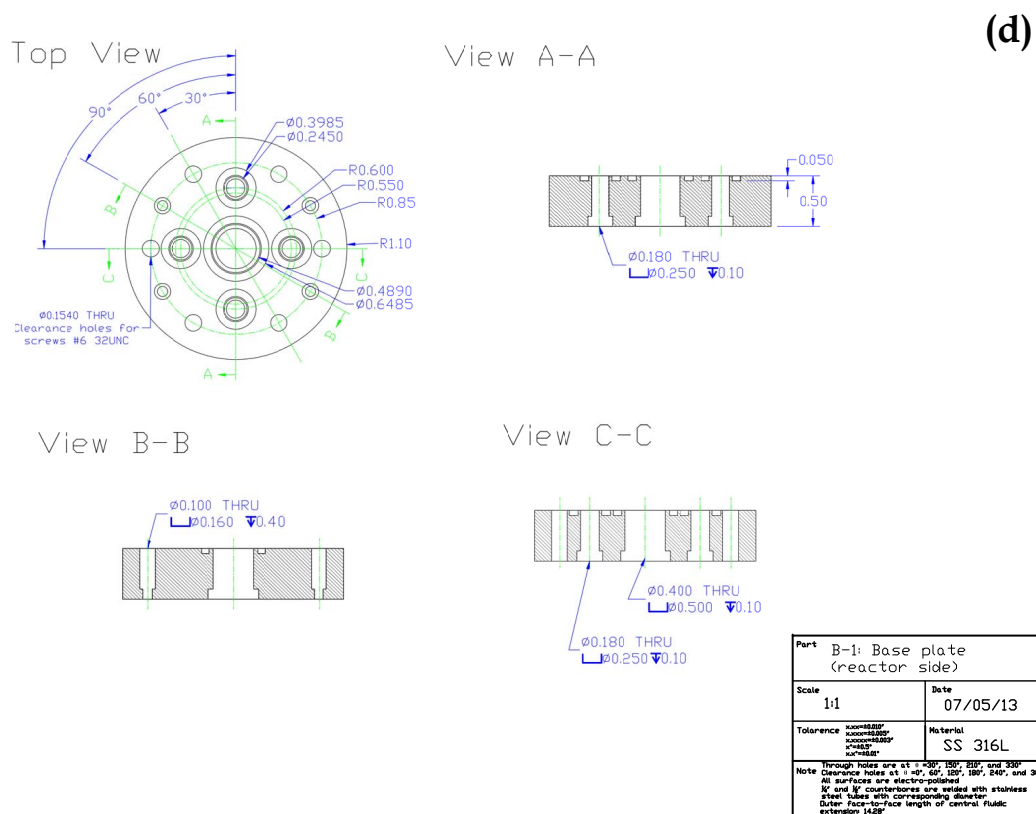
(e)

Figure 8-9, continued: Drawings of the concentric microeactor system composed of **(a-b)** a micro-reactor head**, (c-e)** a central fluidic feedthrough and **(f)** a fluidic and electrical feedthrough.
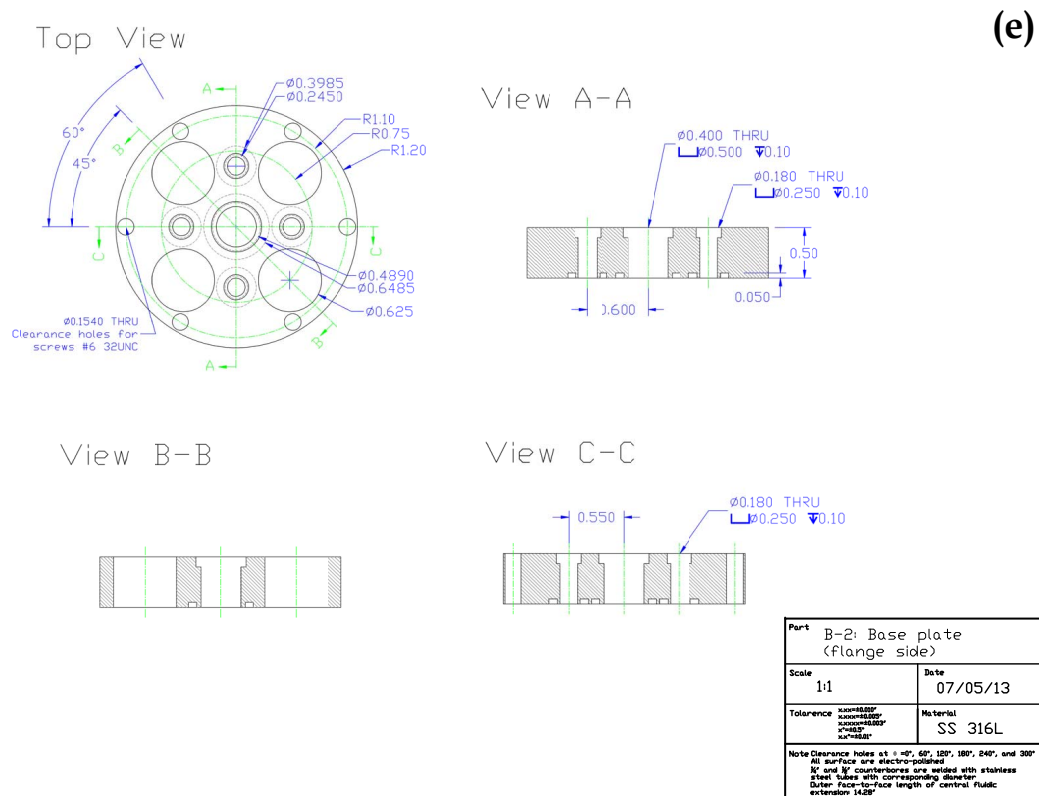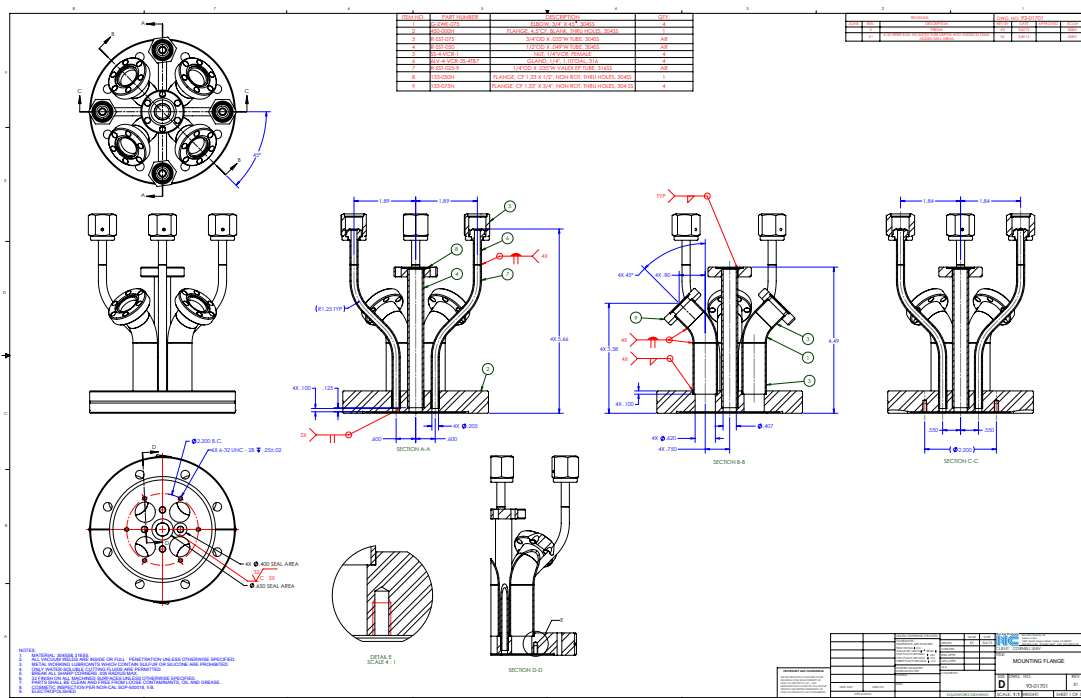
Figure 8-9, continued: Drawings of the concentric microeactor system composed of **(a-b)** a micro-reactor head**, (c-e)** a central fluidic feedthrough and **(f)** a fluidic and electrical feedthrough.

8.4 References

[1] G. Salitra, G. Hodes, E. Klein, and R. Tenne, "Highly oriented WSe$_2$ thin films prepared by selenization of evaporated WO$_3$," *Thin Solid Films*, vol. 245, no. 1–2, pp. 180–185, Jun. 1994.

[2] R. Nyholm, A. Berndtsson, and N. Martensson, "Core level binding energies for the elements Hf to Bi (Z=72-83)," *Journal of Physics C: Solid State Physics*, vol. 13. pp. L1091–L1096, 1980.

[3] M.-H. Chiu, C. Zhang, H.-W. Shiu, C.-P. Chuu, C.-H. Chen, C.-Y. S. Chang, C.-H. Chen, M.-Y. Chou, C.-K. Shih, and L.-J. Li, "Determination of band alignment in the single-layer MoS$_2$/WSe$_2$ heterojunction," *Nat. Commun.*, vol. 6, no. May, p. 7666, Jul. 2015.

[4] N. D. Boscher, C. J. Carmalt, and I. P. Parkin, "Atmospheric pressure chemical vapor deposition of WSe$_2$ thin films on glass—highly hydrophobic sticky surfaces," *J. Mater. Chem.*, vol. 16, no. 1, pp. 122–127, 2006.

[5] H. Wang, D. Kong, P. Johanes, J. J. Cha, G. Zheng, K. Yan, N. Liu, and Y. Cui, "MoSe$_2$ and WSe$_2$ nanofilms with vertically aligned molecular layers on curved and rough surfaces," *Nano Lett.*, vol. 13, no. 7, pp. 3426–3433, 2013.

[6] A. Schellenberger, R. Schlaf, T. Mayer, E. Holub-Krappe, C. Pettenkofer, W. Jaegermann, U. . Ditzinger, and H. Neddermeyer, "Na adsorption on the layered semiconductors SnS$_2$ and WSe$_2$," *Surf. Sci.*, vol. 241, no. 3, pp. L25–L29, Jan. 1991.

[7] O. Y. Khyzhun, Y. M. Solonin, and V. D. Dobrovolsky, "Electronic structure of hexagonal tungsten trioxide: XPS, XES, and XAS studies," *J. Alloys Compd.*, vol.

320, no. 1, pp. 1–6, May 2001.

[8] J. Katari, V. Colvin, and A. Alivisatos, "X-ray photoelectron spectroscopy of CdSe nanocrystals with applications to studies of the nanocrystal surface," *J. Phys. Chem.*, vol. 98, pp. 4109–4117, 1994.

[9] P. J. Sebastian and V. Sivaramakrishnan, "Oxygen adsorption on the surface of CdSe(x) Te (1 − x) thin films," *Vacuum*, vol. 41, no. 1–3, pp. 647–649, Jan. 1990.

[10] Q. H. Wang, K. Kalantar-Zadeh, A. Kis, J. N. Coleman, and M. S. Strano, "Electronics and optoelectronics of two-dimensional transition metal dichalcogenides," *Nat. Nanotechnol.*, vol. 7, no. 11, pp. 699–712, Nov. 2012.

[11] M. Xu, T. Liang, M. Shi, and H. Chen, "Graphene-Like Two-Dimensional Materials," *Chem. Rev.*, vol. 113, no. 5, pp. 3766–3798, May 2013.

[12] S. Kundu, Y. Wang, W. Xia, and M. Muhler, "Thermal Stability and Reducibility of Oxygen-Containing Functional Groups on Multiwalled Carbon Nanotube Surfaces: A Quantitative High-Resolution XPS and TPD/TPR Study," *J. Phys. Chem. C*, vol. 112, no. 43, pp. 16869–16878, Oct. 2008.

[13] S. J. Schmieg and D. N. Belton, "Highly Oriented Pyrolytic Graphite by XPS," *Surf. Sci. Spectra*, vol. 1, no. 4, pp. 333–336, Dec. 1992.

[14] K. J. Hughes, A. Dube, M. Sharma, and J. R. Engstrom, "Initial Stages of Atomic Layer Deposition of Tantalum Nitride on SiO_2 and Porous Low-κ Substrates Modified by a Branched Interfacial Organic Layer: Chemisorption and the Transition to Steady-State Growth," *J. Phys. Chem. C*, vol. 116, no. 41, pp. 21948–21960, Oct. 2012.

[15] J. Scofield, "Hartree-Slater Subshell Photoionization Cross-Sections at 1254 and

1487 eV," *J. Electron Spectros. Relat. Phenomena*, vol. 8, pp. 129–137, 1976.

[16] H. Zhang, J. Yang, J.-R. Chen, J. R. Engstrom, T. Hanrath, and F. W. Wise, "Tuning of Coupling and Surface Quality of PbS Nanocrystals via a Combined Ammonium Sulfide and Iodine Treatment," *J. Phys. Chem. Lett.*, pp. 642–646, Feb. 2016.

[17] V. I. Nefedov, Y. V. Salyn, and K. Keller, "X-Ray Electron Studies of Lead and Mercury Compounds," *Zhurnal Neorg. Khimii*, vol. 24, no. 9, pp. 2564–2566, 1979.

[18] R. Nyholm and N. Martensson, "Core level binding energies for the elements Zr-Te (Z=40-52)," *J. Phys. C Solid State Phys.*, vol. 13, no. 11, pp. L279–L284, Apr. 1980.

[19] C. Godet, S. Ababou-Girard, B. Fabre, Y. Molard, a. B. Fadjie-Djomkam, S. Députier, M. Guilloux-Viry, and S. Cordier, "Surface immobilization of Mo_6I_8 octahedral cluster cores on functionalized amorphous carbon using a pyridine complexation strategy," *Diam. Relat. Mater.*, vol. 55, pp. 131–138, 2015.

[20] J. E. Castle, "Practical surface analysis by Auger and X-ray photoelectron spectroscopy," *Surf. Interface Anal.*, vol. 6, no. 6, pp. 302–302, Dec. 1984.

[21] D. J. Kim, R. Pitchimani, D. E. Snow, and L. J. Hope-Weeks, "A simple method for the removal of thiols on gold surfaces using an NH_4OH-H_2O_2-H_2O solution.," *Scanning*, vol. 30, no. 2, pp. 118–22, 2008.